Head Office: Università degli Studi di Padova

Department of Industrial Engineering

Ph.D. COURSE IN: INDUSTRIAL ENGINEERING
CURRICULUM: MATERIALS ENGINEERING
CYCLE: XXXII

WASTE-DERIVED GLASS-CERAMIC PRODUCTS WITH NOVEL FUNCTIONALITIES

Thesis written with the financial contribution of European Union's Horizon 2020 research and innovation programme under the Marie Sklodowska-Curie grant agreements No. 721185 "NEW-MINE" (EU Training Network for Resource Recovery through Enhanced Landfill Mining)

Coordinator: Prof. Paolo Colombo
Supervisor: Prof. Enrico Bernardo

Ph.D. student: Patricia Rabelo Monich

ABSTRACT

Vitrification of waste is an effective method to produce a safe waste-based material. However, this process is only economical viable if the vitrified residue is further valorised into new materials, such as glass-ceramics. In this PhD thesis, vitrified residues, such as a glass from the gasification/vitrification of solid recovered fuel ('Plasmastone') and vitrified MSWI bottom ash, were converted into safe building materials with high-added values, by sinter-crystallisation. Dense glass-ceramics (with properties comparable to those of commercial tiles) as well as lightweight aggregates (developed to increase the thermal insulation of cement-based products) were produced mainly with mixtures of Plasmastone with soda-lime glass. Furthermore, highly porous inorganic materials for thermal and acoustic insulation were developed by alkali activation, followed by gel-casting and sinter-crystallisation of vitrified residues or partially crystallised residues (e.g. polishing stoneware residue and plasma processed asbestos-containing waste). In specific conditions, soda-lime glass was also added in order to improve hardening and sintering by viscous flow, as in the case of glasses prone to crystallisation, such as Plasmastone, and of partially crystallised residues. Interestingly, the addition of waste glass enabled to recycle powders of vitrified bottom ash-based glass-ceramics into even stronger foams. In addition, the chemical stability of Plasmastone/soda-lime glass foams was considered a critical point, due to high leaching of heavy metals. This was adjusted by using boro-alumino-silicate glass instead of soda-lime-glass or by firing in nitrogen. Besides stabilisation of heavy metals, firing in an inert atmosphere also promoted functionalities in Plasmastone-based porous glass-ceramics: foams fired at low temperature exhibited shielding properties, whereas foams fired at a higher temperature presented dielectric characteristics. A waste-derived glass-ceramic exhibiting multifunctionalities (e.g. insulation coupled with shielding properties) is essential to justify costs and environmental impact of the firing treatment.

AKNOWLEDGEMENTS

I would like to aknowldge and express my gratitude to:

The European Union for financial support in the framework of the European Union's Horizon 2020 research and innovation programme under the Marie Sklodowska-Curie "NEW-MINE" (EU Training Network for Resource Recovery through Enhanced Landfill Mining, grant agreements No. 721185).

My supervisor Prof. Enrico Bernardo, for his guidance, patience and support.

The NEW-MINE members, particularly Peter Tom Jones, Lieven Machiels and Piet Wostyn for providing support for the project; Hugo Lucas for supplying materials and Giovanna Sauve for the life cycle assessment studies.

Prof. Paolo Colombo, for coordinating the doctoral school of Industrial Engineering.

The Advanced Ceramics and Glasses group, particularly Acacio Rincón, Hamada Elsayed, Giorgia Franchin, Kai Huang, Karine Goulart de Oliveira, Renata Botti, Useche Inchauspe, Paolo Scanferla, Durgaprasad Ramteke and Filippo Gobbin, for all help and support.

Federico Bottaro, Fulden Dogrul, Antonio Morra and Nicola Ostoich for experimental assistance during their study projects.

All coworkers, technicians and administration staff from the Universitiy of Padova, particularly Giulia Zanmarchi for the ICP analysis; Mauro Gobin and Sirio Galletto for all the assistance at the laboratoy; Elena Colusso for assistance at FTIR analysis; Prof. Desideri for electromagnetism tests, as well as Lorella Bortolato and Franco Fiorani for all administrative assistance.

Prof. Daniel Vollprecht and the AWAW members, particularly Alexia Aldrian and Bastian Küppers, for assistance during my secondment at Montanuniversität Leoben, as well as Federica Zaccarini for electron microprobe analysis.

Prof. Yiannis Pontikes and the SREMAT group, particularly Roberto Murillo, Georgia Flesoura, Tobias Hertel, Michiel Giels, Arne Peys, Pavel Lopez, Jessica Gordillo, Remus Iacobescu and Theodoros Karachalios, for all help during my secondment at KU Leuven.

Italcementi i.lab employees, particularly Monica Segata, Alessandro Morbi, Aronne Carminati, Guilherme Ascenção and Maurizio Marchi, for assistance during my secondment at Italcementi i.lab.

And I especially would like to thank my family for have always supported me, now and then.

TABLE OF CONTENTS

PART I - General introduction

Chapter 1. Overall introduction: NEW-MINE project

Part of this chapter is based on: P. Rabelo Monich, A. Rincon Romero, D. Höllen, E. Bernardo, Porous glass-ceramics from alkali activation and sinter-crystallization of mixtures of waste glass and residues from plasma processing of municipal solid waste, Journal of Cleaner Production, 188, 871-878 (2018). DOI: 10.1016/j.jclepro.2018.03.167; P. Rabelo Monich, D. Vollprecht, E. Bernardo, Dense glass-ceramics by fast sinter-crystallization of mixtures of waste-derived glasses, International Journal of Applied Ceramic Technology (2019). DOI: 10.1111/ijac.13332; P. Rabelo Monich, F. Dogrul, H. Lucas, B. Friedrich, E. Bernardo, Strong porous glass-ceramics from alkali activation and sinter-crystallization of vitrified MSWI bottom ash. Detritus (2019) in press

1.1 Introduction

The quantity of municipal solid waste (MSW) produced worldwide has never been higher and it will only tend to dramatically increase within the next years. According to the World of Bank report, 2.01 billion tons of municipal solid waste were produced in 2016 and this number is expected to increase by 70% by 2050 (Kaza et al., 2018). European waste management policies recommend firstly the prevention and reuse of waste, followed by recycling and then incineration with energy recovery, rather than landfilling (Cucchiella et al., 2014). However, many countries of the world still adopt this practice as a low-cost way for waste management (Krook et al., 2012). In the EU 28, almost 30% of MSW produced is still being landfilled, with significantly different rates among European countries (Cucchiella et al., 2017). It is known that landfilling can provoke serious environmental problems, such as groundwater and soil contamination, as well as risks to human health and contribution to global warming due to release of greenhouse gases (El-Fadel et al., 1997; Krook et al., 2012; Manfredi et al., 2009).

Based on this, the EU Landfill Directive of 1999 was created in order to minimise the negative effects that landfilling can provoke, by compiling strict requirements for waste and landfills (EU Landfill Directive, 1999). However, Europe still contain between 150.000 and 500.000 landfills, from which 90% could be non-sanitary landfills (created before this directive) (NEW-MINE, 2016). These older landfills usually do not present environmental protection technology and could cause future environmental and health problems. Therefore, remediation measures will need to be applied in order to manage these landfills (Jones et al., 2013).

Enhanced landfill mining (ELFM) could be an interesting alternative for remediation strategies of older landfills (Jones et al., 2013). In addition, ELFM could also consist of a solution for current problems related to limited availability of raw materials, energy production and to reclaim land (Jones et al., 2013). In *ex-situ* ELFM, landfills are first excavated and then applied as a source of fuels and other resources. Resources (such as metals) are recovered from

the excavated waste, whereas the fraction of waste that cannot be recovered can be further used as a solid recovered fuel (SRF) to generate energy by several technologies such as plasma gasification (Jones et al., 2013; Machiels et al., 2017).

In plasma gasification, the SRF is converted into a synthetic gas ('syngas'), whereas the inorganic fraction melts. The melt actually consists of two phases: the liquid metal alloy (extracted from the bottom of the plasma reactor) and a vitreous by-product of the plasma heating process (cooled down as Plasmastone) (Machiels et al., 2017). When compared to municipal solid waste incineration (MSWI) bottom ash, Plasmastone presents lower contents of volatile heavy metals (Pb, Zn), due to higher temperatures. In addition, Cu and Ni can be directed to the metallic phase when reducing conditions are applied (Machiels et al., 2017). Moreover, it is not justifiable to apply Plasmastone directly as a building material (e.g. as an aggregate) due to an increased effort of plasma gasification (Winterstetter et al., 2015). For a true 'zero waste' condition and enhanced economical sustainability for ELFM projects, added value products must be obtained from Plasmastone (Jones et al., 2013; Machiels et al., 2017), such as alkali-activated materials (Machiels et al., 2017) and glass-ceramics for building applications.

Plasmastone may contain a high quantity of iron oxide (Machiels et al., 2017), according to the composition of the SRF and to the conditions applied in the plasma gasificator. Iron oxides present high solubility in molten glasses, which decreases once the temperature decreases. On the other hand, iron oxides remain dissolved in the glass by quenching an iron-rich silicate melt. If this iron-rich glass is heated, iron oxides may separate, thus promoting crystallisation (Chinnam et al., 2013; Höland and Beall, 2012). In addition, the possible phase separation upon firing, may bring new functionalities to the material, such as ferri-magnetism (Ponsot et al., 2014).

Regarding the fresh MSW that is produced daily worldwide, incineration could represent a solution for managing the fraction of waste that cannot be recycled, depending on the country. This is due to a result of public pressure, stricter legislations and more efficient technologies for gas cleaning (Cucchiella et al., 2017; Vehlow, 2015). This thermo-chemical process is able to reduce the quantity of waste in up to 90 vol%, generating mainly exhaust gas (which is used to produce energy), and bottom ash and fly ash (Hjelmar, 1996).

Bottom ash corresponds to more than 98% of the incineration outputs (Joseph et al., 2018), which also needs to be addressed (Chimenos et al., 1999). Bottom ash is usually treated using mechanically using screeners, crushers, magnets, eddy current separators, sorting technologies and washers, in order to extract the metallic fraction and clean as much as possible the mineral fraction (Sabbas et al., 2003). The treated bottom ash can be further applied as a secondary product such as aggregates for road paving or construction (Dou et al., 2017; Silva et al., 2019). Furthermore, previous studies indicated that the treated bottom ash could also be valorised into

other products such as tiles, bricks and alkali-activated materials (Silva et al., 2017). However, it is crucial to perform an environmental impact assessment of bottom ash-derived materials, as bottom ash can still contain hazardous metals, chlorides, sulphates and other pollutants (Silva et al., 2019). Indeed, due to environmental issues that could be caused by bottom ash, this residue is still being mainly landfilled (He et al., 2017). As an example, in the EU, national guidelines or regulatory quality criteria for unbound applications are related to maximum limit values allowed for certain substances and leachable conditions. MSWI bottom ash cannot fulfil all these criteria, due to the existence of Zn, Pb, Cd, Mo, SO_4, Cl, Cu or Cr (Saveyn et al., 2014). Bottom ash can also be screened to remove the fraction below 1-2 mm, in order to reduce the content of hazardous elements (Saveyn et al., 2014). However, in countries such as Switzerland and Austria, which present stricter regulation concerning the maximum content of harmful compounds, MSWI bottom ash is always landfilled (Saveyn et al., 2014).

Instead of landfilling the residue that does not fulfil the criteria for the reuse of mineral waste, bottom ash can be vitrified, producing a stable glass with metal recovery (Ecke et al., 2000; Xiao et al., 2008; Zhang et al., 2014). Vitrification of waste allows the immobilisation of pollutants in the glass structure and reduction of waste volume, producing a glass that can be safely disposed or applied as aggregates (Colombo et al., 2003). However, as this process is very expensive due to high energy consumption, vitrification is only economically viable and environmentally sustainable if the vitrified residue is further upcycled into high-added value products, such as glass-ceramics (Colombo et al., 2003; Rincón et al., 2016) and alkali-activated materials (Machiels et al., 2017). According to the composition of the glass, the vitrified residue can be converted into safe and strong building materials, such as foams, tiles and aggregates (Rawlings et al., 2006; Rincón et al., 2016). Besides the economic benefits of commercialising waste-derived products, the landfilling of vitrified residues and the mining of natural raw materials could be also avoided (Rincón et al., 2016).

1.2 The European project NEW-MINE

The EU Training Network for Resource Recovery Through Enhanced Landfill Mining (NEW-MINE, 2016) has been founded through European Union's Horizon 2020 research and innovation programme under the Marie Sklodowska-Curie grant agreements No. 721185 "NEW-MINE". The main objective of the NEW-MINE project is to train 15 early-stage researchers (ESRs) in all aspects of ELFM, in order to develop profitable and sustainable ELFM practices and regulatory frameworks.

Figure 1-1 illustrates the Scenario "New-MINE" and compares it to other scenarios for managing older non-sanitary landfills. The Scenario "Do-Nothing" is only acceptable for well monitored landfills. The Scenario "Classic remediation with relandfill", on the other hand, consists of excavating landfills and re-landfilling the excavated waste. Finally, the Scenario

"Classic landfill mining" refers to excavation of landfills and separation of the excavated waste into recyclables and a refuse-derived fuel (RDF). In contrast, in the Scenario "New-MINE", a large part of excavated waste is converted into higher-added-value products (e.g. hydrogen and glass-ceramics) (Jones et al., 2013).

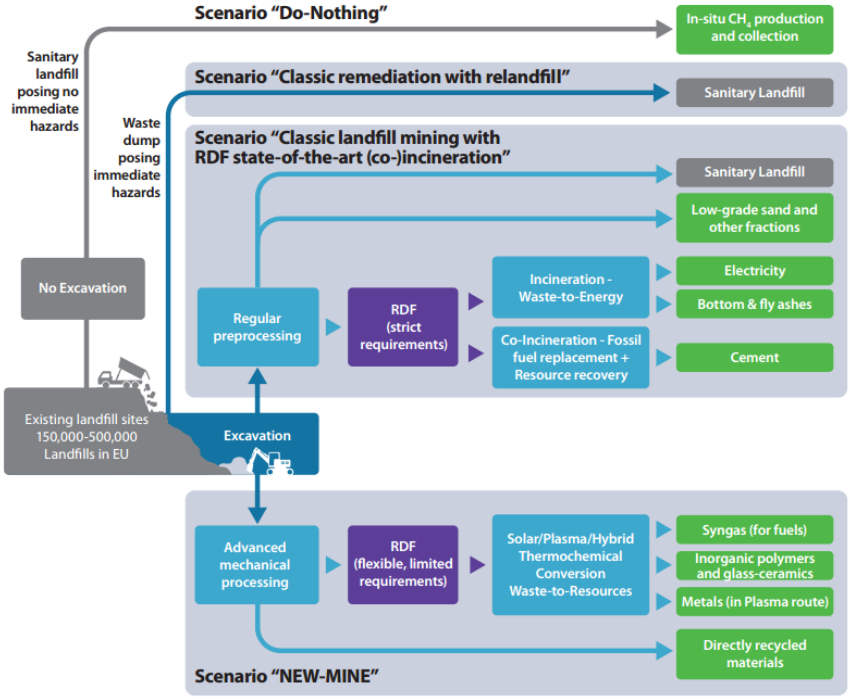

Figure 1-1. The NEW-MINE scenario compared to other scenarios for landfills (figure from the NEW-MINE Grant Agreement).

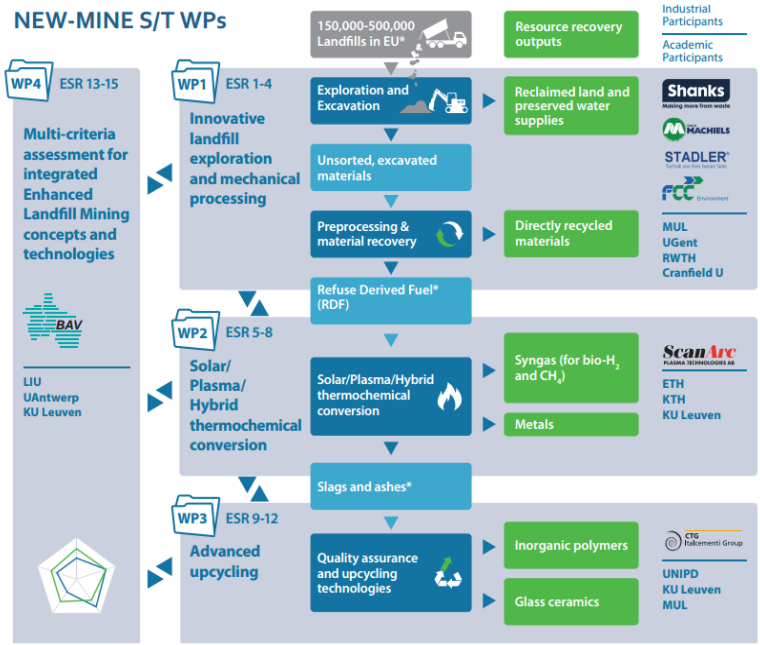

Figure 1-2. Work Packages from NEW-MINE as well as the beneficiaries and partners from the project (figure from the NEW-MINE Grant Agreement).

The 15 ESR's are divided in four work packages (see Figure 1-2), which covers all aspects from ELFM: from advanced landfill exploration to mechanical processing of excavated waste (Work Package 1, 'WP1'), plasma thermochemical conversion techniques (Work Package 2, 'WP2'), vitrification of municipal solid waste-derived residues (e.g. bottom ash) and upcycling of by-products (Work Package 3, 'WP3') and multi-criteria assessments (Work Package 4, 'WP4') (NEW-MINE, 2016).

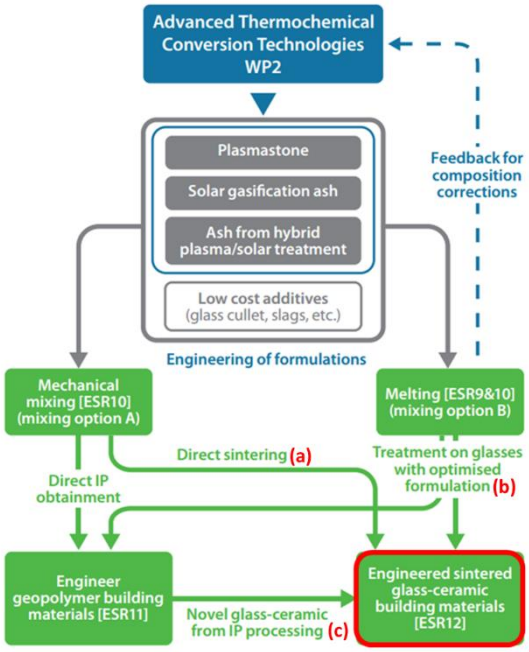

Figure 1-3. Collaborations within the Work Package 3 of NEW-MINE (figure adapted from the NEW-MINE Grant Agreement).

This thesis reports the studies performed by the PhD candidate as ESR12 from Work Package 3 of NEW-MINE. The main goal of this project was to valorise vitreous by-products (produced within NEW-MINE) into innovative building materials, with a low carbon footprint, chemically stable and exhibiting multiple functionalities. Figure 1-3 illustrates well the collaborations of ESR12 (marked in red) within Work Package 3. The first one (marked as 'a' in Figure 1-3) consisted of valorising Plasmastone directly into glass-ceramics by addition of low-cost additives (e.g. soda-lime glass), which is reported in Part III of this thesis. The second one (marked as 'b' in Figure 1-3), referred to applying the conditioned MSWI bottom ash developed by ESR9&10 into glass-ceramics. The results regarding the valorisation of vitrified residues produced by ESR9 and 10 are presented in Part IV and in the Appendix, respectively. Finally, the third collaboration (marked as 'c' in Figure 1-3), included the conversion of alkali-activated materials produced by ESR11 into glass-ceramics by firing treatments. The results of part of this

study are also presented in the Appendix. In addition, Chapter 11 also reports the conversion of alkali-activated materials into glass-ceramics.

Furthermore, the milestones required by the NEW-MINE project for ESR12 consisted of developing dense or porous glass-ceramics with high specific strength (specific bending strength above 2 MPa cm^3/g for dense products; specific compressive strength above 5 MPa cm3/g for cellular products with porosity higher than 70 vol%) as well as products with magnetic functionality established.

This thesis also reports in Part V the valorisation of partially crystalline residues (polishing stoneware residue and plasma processed asbestos-containing waste) which do not match strictly with the concept of ELFM. However, the conversion of other residues into building materials may represent a model for the last operation of ELFM projects, which require the reuse of by-products generated in order to achieve a full 'circularity'.

1.3. References

Chimenos, J.M., Segarra, M., Fernández, M.A., Espiell, F., 1999. Characterization of the bottom ash in municipal solid waste incinerator. J. Hazard. Mater. 64, 211–222. https://doi.org/10.1016/S0304-3894(98)00246-5

Chinnam, R.K., Francis, A.A., Will, J., Bernardo, E., Boccaccini, A.R., 2013. Review. Functional glasses and glass-ceramics derived from iron rich waste and combination of industrial residues. J. Non. Cryst. Solids 365, 63–74. https://doi.org/10.1016/j.jnoncrysol.2012.12.006

Colombo, P., Brusatin, G., Bernardo, E., Scarinci, G., 2003. Inertization and reuse of waste materials by vitrification and fabrication of glass-based products. Curr. Opin. Solid State Mater. Sci. 7, 225–239. https://doi.org/10.1016/j.cossms.2003.08.002

Cucchiella, F., D'Adamo, I., Gastaldi, M., 2017. Sustainable waste management: Waste to energy plant as an alternative to landfill. Energy Convers. Manag. 131, 18–31. https://doi.org/10.1016/j.enconman.2016.11.012

Cucchiella, F., D'Adamo, I., Gastaldi, M., 2014. Strategic municipal solid waste management: A quantitative model for Italian regions. Energy Convers. Manag. 77, 709–720. https://doi.org/10.1016/j.enconman.2013.10.024

Dou, X., Ren, F., Nguyen, M.Q., Ahamed, A., Yin, K., Chan, W.P., Chang, V.W.-C., 2017. Review of MSWI bottom ash utilization from perspectives of collective characterization, treatment and existing application. Renew. Sustain. Energy Rev. 79, 24–38. https://doi.org/10.1016/j.rser.2017.05.044

Ecke, H., Sakanakura, H., Matsuto, T., Tanaka, N., Lagerkvist, A., 2000. State-of-the-art treatment processes for municipal solid waste incineration residues in Japan. Waste Manag. Res. 18, 41–51. https://doi.org/10.1034/j.1399-3070.2000.00097.x

El-Fadel, M., Findikakis, A.N., Leckie, J.O., 1997. Environmental impacts of solid waste landfilling. J. Environ. Manage. 50, 1–25. https://doi.org/10.1006/jema.1995.0131

EU Landfill Directive, 1999. http://ec.europa.eu/environment/waste/landfill_index.htm (accessed 9.20.07).

He, P.J., Pu, H.X., Shao, L.M., Zhang, H., 2017. Impact of co-landfill proportion of bottom ash and municipal solid waste composition on the leachate characteristics during the acidogenesis phase. Waste Manag. 69, 232–241. https://doi.org/10.1016/j.wasman.2017.08.021

Hjelmar, O., 1996. Disposal strategies for municipal solid waste incineration residues. J. Hazard. Mater. 47, 345–368. https://doi.org/10.1016/0304-3894(95)00111-5

Höland, W., Beall, G.H., 2012. Glass-Ceramic Technology. John Wiley & Sons, Inc., Hoboken, NJ, USA.

Jones, P.T., Geysen, D., Tielemans, Y., Van Passel, S., Pontikes, Y., Blanpain, B., Quaghebeur, M., Hoekstra, N., 2013. Enhanced Landfill Mining in view of multiple resource recovery: A critical review. J. Clean. Prod. 55, 45–55. https://doi.org/10.1016/j.jclepro.2012.05.021

Joseph, A., Snellings, R., Van den Heede, P., Matthys, S., De Belie, N., 2018. The Use of Municipal Solid Waste Incineration Ash in Various Building Materials: A Belgian Point of View. Materials (Basel). 11, 141. https://doi.org/10.3390/ma11010141

Kaza, S., Yao, L.C., Bhada-Tata, P., Van Woerden, F., 2018. What a Waste 2.0 : A Global Snapshot of Solid Waste Management to 2050, Urban Development. World Bank Group, Washington, DC.

Krook, J., Svensson, N., Eklund, M., 2012. Landfill mining: A critical review of two decades of research. Waste Manag. 32, 513–520. https://doi.org/10.1016/j.wasman.2011.10.015

Machiels, L., Arnout, L., Yan, P., Jones, P.T., Blanpain, B., Pontikes, Y., 2017. Transforming Enhanced Landfill Mining Derived Gasification/Vitrification Glass into Low-Carbon Inorganic Polymer Binders and Building Products. J. Sustain. Metall. 3, 405–415. https://doi.org/10.1007/s40831-016-0105-1

Manfredi, S., Tonini, D., Christensen, T.H., Scharff, H., 2009. Landfilling of waste: accounting of greenhouse gases and global warming contributions. Waste Manag. Res. 27, 825–836. https://doi.org/10.1177/0734242X09348529

NEW-MINE - EU Training Network for Resource Recovery Through Enhanced Landfill Mining, 2016. http://new-mine.eu/ (accessed 9.20.07).

Ponsot, I.M.M.M., Pontikes, Y., Baldi, G., Chinnam, R.K., Detsch, R., Boccaccini, A.R., Bernardo, E., 2014. Magnetic glass ceramics by sintering of borosilicate glass and inorganic waste. Materials (Basel). 7, 5565–5580. https://doi.org/10.3390/ma7085565

Rawlings, R., Wu, J., Boccaccini, a, 2006. Glass-ceramics: Their production from wastes - A Review. J. Mater. Sci. 41, 733–761. https://doi.org/10.1007/s10853-006-6554-3

Rincón, A., Marangoni, M., Cetin, S., Bernardo, E., 2016. Recycling of inorganic waste in monolithic and cellular glass-based materials for structural and functional applications. J. Chem. Technol. Biotechnol. 91, 1946–1961. https://doi.org/10.1002/jctb.4982

Sabbas, T., Polettini, A., Pomi, R., Astrup, T., Hjelmar, O., Mostbauer, P., Cappai, G., Magel, G., Salhofer, S., Speiser, C., Heuss-Assbichler, S., Klein, R., Lechner, P., 2003. Management of municipal solid waste incineration residues. Waste Manag. 23, 61–88. https://doi.org/10.1016/S0956-053X(02)00161-7

Saveyn, H., Eder, P., Garbarino, E., Muchova, L., Hjelmar, O., Sloot, H., Comans, R., Zomeren, A., Hyks, J., Oberender, A., 2014. Study on methodological aspects regarding limit values for pollutants in aggregates in the context of the possible development of end-of-waste criteria under the EU Waste Framework Directive. European Commission Joint Research Centre Institute for Prospective Technological Studies: Rep. No. JRC91036. https://doi.org/http://dx.doi.org/10.2791/1125

Silva, R.V., de Brito, J., Lynn, C.J., Dhir, R.K., 2017. Use of municipal solid waste incineration bottom ashes in alkali-activated materials, ceramics and granular applications: A review. Waste Manag. 68, 207–220. https://doi.org/10.1016/j.wasman.2017.06.043

Silva, R. V., de Brito, J., Lynn, C.J., Dhir, R.K., 2019. Environmental impacts of the use of bottom ashes from municipal solid waste incineration: A review. Resour. Conserv. Recycl. 140, 23–35. https://doi.org/10.1016/j.resconrec.2018.09.011

Vehlow, J., 2015. Air pollution control systems in WtE units: An overview. Waste Manag. 37, 58–74. https://doi.org/10.1016/j.wasman.2014.05.025

Winterstetter, A., Laner, D., Rechberger, H., Fellner, J., 2015. Framework for the evaluation of anthropogenic resources: A landfill mining case study - Resource or reserve? Resour. Conserv. Recycl. 96, 19–30. https://doi.org/10.1016/j.resconrec.2015.01.004

Xiao, Y., Oorsprong, M., Yang, Y., Voncken, J.H.L., 2008. Vitrification of bottom ash from a municipal solid waste incinerator. Waste Manag. 28, 1020–1026. https://doi.org/10.1016/j.wasman.2007.02.034

Zhang, Z., Li, G.Q., Yang, Y.X., Xiao, Y.P., 2014. Thermodynamics of the Vitrified Bottom Ash Slag from Municipal Solid Waste Incinerators-Phase Relations of CaO-SiO2-Na2O Oxide System. Adv. Mater. Res. 881–883, 574–578. https://doi.org/10.4028/www.scientific.net/AMR.881-883.574

Chapter 2. Valorisation of waste-based glasses into glass-ceramics

Part of this chapter was based on A. Rincon Romero, P. Rabelo Monich, E. Bernardo, Recycling of inorganic waste in monolithic and cellular glass-based materials for structural and functional applications, Proceedings of the 4th Enhanced Landfill Mining Symposium (ELFM 2018), Mechelen (Belgium), 5-6 February 2018, 255-270; and on P. Rabelo Monich, A. Rincon Romero, D. Höllen, E. Bernardo, Porous glass-ceramics from alkali activation and sinter-crystallization of mixtures of waste glass and residues from plasma processing of municipal solid waste, Journal of Cleaner Production, 188, 871-878 (2018). DOI: 10.1016/j.jclepro.2018.03.167

2.1. Vitrification of waste and valorisation into glass-ceramics

According to Colombo et al. (Colombo et al., 2003), vitrification is considered one of the safest options to manage hazardous waste (e.g. MSW fly ash, coal fly ash, muds, ferrous and non-ferrous slags), which usually involves the dissolution of metal oxides in molten glass, at high temperatures. Once the molten glass is cooled down, the metals ions remain trapped inside the vitreous structure, producing a homogeneous silicate glass with high chemical stability (Bernardo et al., 2017; Colombo et al., 2003; Rincón et al., 2016). In specific cases, the stabilisation of hazardous waste does not involve dissolution of pollutants, but thermal destruction of hazardous morphology, as in the case of asbestos-based waste (Bernardo et al., 2017; Rincón et al., 2016).

Besides inertisation of hazardous waste and waste volume reduction, another advantage of vitrification includes the flexibility to vitrify hazardous wastes of a range of forms (e.g. solid, mud, liquid) and composition (Colombo et al., 2003). In the case of mud and liquid waste, it may also be necessary to apply a pre-treatment before vitrification (Colombo et al., 2003). The only requirement for vitrification consist of a minimum content of silica, which is essential for glass formation (Bernardo et al., 2017; Rincón et al., 2016). In addition, if the silica content is too low, the chemical durability of the developed vitrified residue may be affected (Colombo et al., 2003). Silica-rich waste materials such as coal fly ash can be directly vitrified by themselves or by adding minor amounts of additives to reduce the viscosity. In the case of hazardous waste with limited silica content, on the other hand, minerals or glass cullets could also be added to obtain an adequate amount of silica (Bernardo et al., 2017; Rincón et al., 2016).

Generally, vitrification of waste is not economically and environmentally viable if the vitrified waste is simply landfilled (Bernardo et al., 2017; Colombo et al., 2003). Indeed, a life cycle assessment comparing different management options for air pollution control residues from waste incineration indicated the highest global warming potential for vitrification followed by landfilling, when compared to other waste management options (Fruergaard et al., 2010).

This was mainly related to the high energy consumption needed for vitrification (Fruergaard et al., 2010). Therefore, in order to mitigate the economical and environmental impacts associated to vitrification, besides avoiding landfill charges, it is essential that the vitrified residue is valorised into high-value products (Bernardo et al., 2017), as mentioned in Chapter 1. Examples of these products include waste-derived glass-ceramics, such as dense glass-ceramics for structural applications (as an alternative to natural stones or ceramic tiles), as well as foams (for thermal and acoustic insulation) (Rawlings et al., 2006; Rincón et al., 2016).

It is also important to highlight that the valorisation of vitrified residues into glass-ceramics will also depend on the application of a secondary thermal treatment, which will generate extra costs. However, it must also be considered that the applied thermal treatment could bring extra-revenues, such as production of energy and recovery of metals (as in the case of plasma technology and vitrification of MSWI bottom ash) which can help to increase the costs/benefits of the process (Gomez et al., 2009; Rincón et al., 2016; Zhang et al., 2014). In addition, waste-derived glass-ceramics can also be engineered to present functional properties, which would certainly increase the added value of the product (Rincón et al., 2016).

2.2. Monolithic waste-derived glass-ceramics

Glass-ceramics consist of materials obtained from the controlled sinter-crystallisation of glass with a suitable composition (Höland and Beall, 2012). This class of material presents one or more crystalline phases embedded in a residual glass phase, which accounts from 5 to 50 vol% of the microstructure (Höland and Beall, 2012; Rawlings et al., 2006). In addition, glass-ceramics generally present remarkable and superior properties than the parent glass and can even present superior properties (e.g. thermal) than of metals and organic polymers of the same area of application (Höland and Beall, 2012).

Only proper glass compositions can be crystallised, by firstly heating the already shaped glass component to the temperature of maximum nucleation (‘nucleation stage’), in which nucleation of crystals is favoured by separation of nucleating agents (Rincón et al., 2016). Thereafter, the temperature is slightly increased to the temperature of maximum crystal growth (‘growth stage’). The glass component is submitted to a holding time at each of these temperatures and then cooled down. This technology was discovered in the late 1950s and has been employed in the production of waste-derived glass-ceramics since the early 1960s (Colombo et al., 2003; Höland and Beall, 2012; Rawlings et al., 2006; Rincón et al., 2016).

The valorisation of inorganic waste into waste-derived glass-ceramics is supported by extensive literature and industrial production (Rawlings et al., 2006; Rincón et al., 2016). In the case of industrial production, examples of commercialised waste-derived glass-ceramics include ‘Slagceram’ and ‘Slag sitals’. These two types of glass-ceramic products were developed from slags of ferrous and non-ferrous metallurgy, ashes and waste of mining and chemical industries,

in which it was only necessary to apply some minor composition adjustments (e.g. addition of a glass-forming oxide) (Rawlings et al., 2006; Rincón et al., 2016). Slagceram products were the first commercialised waste-derived glass-ceramics, produced by the British Iron and Steel Research Association in the late 1960s. This product belonged to system $CaO\text{-}MgO\text{-}Al_2O_3\text{-}SiO_2$ (CMAS) and it was manufactured following a two-stage heat treatment (Colombo et al., 2003; Rawlings et al., 2006). Slag sitals, on the other hand, referred to waste derived glass-ceramics produced in the late USSR, from the crystallisation of slags, also by a two-stage heat treatment. These waste-derived glass-ceramics belonged to the systems $CaO\text{-}Al_2O_3\text{-}SiO_2$ (CAS), and were known to present high strength and chemical durability (Höland and Beall, 2012). In addition, it is estimated that more than twenty billion square meters of sheeted and pressed slag sital products have already been manufactured for construction (Colombo et al., 2003).

Vitrified residues can present high variability of composition due to the waste origin, which can be adjust by modifying the ratios between different types of waste (Colombo et al., 2003; Rincón et al., 2016). In addition, modifications in the overall glass composition can also be tolerated when the type of precipitated crystalline phase is taken into account. Generally, the main crystalline phases found in waste-derived glass-ceramics consist of calcium silicates (wollastonite, $CaO{\cdot}SiO_2$) and calcium feldspar (anorthite, $CaO{\cdot}Al_2O_3{\cdot}2SiO_2$). Furthermore, secondary phases usually include other silicates and alumino-silicates, such as pyroxenes, melilites and gehlenite ($2CaO{\cdot}Al_2O_3{\cdot}SiO_2$) and its solid solutions. It is also possible that secondary phases replace the main ones (and also the other way round), depending on the glass composition. Different ions can also be accommodated in the same crystal, based on the vitrified residue composition, by precipitation of complex solid solutions, such as pyroxenes (Rincón et al., 2016). The pyroxenes are, in fact, one of the biggest mineral groups, with more than twenty different minerals, such as diopside ($CaMgSiO_6$), hedenbergite ($CaFe^{2+}SiO_6$ and augite ($(Ca,Na)(Mg,Fe,Al)(Si,Al)O_6$). Pyroxenes can form several solid solutions between the end-members because of their simple chain silicate structure, which can incorporate different cations (Karamanov et al., 2014).

Glass-ceramics can be produced by a wide range of vitrified wastes, due to their high tendency to crystallisation (Colombo et al., 2003). In contrast to non-waste-based glasses, it is not necessary to add nucleating agents in the processing of waste-derived glass-ceramics, as waste-based glasses already present nucleating agents (e.g. iron oxides) in their composition (Rincón et al., 2016).

The classical method to produce glass-ceramics based on two-stage heat treatment may not be the most convenient to process waste-derived glass-ceramics due to high costs associated to the heating treatment (Rincón et al., 2016). Based on this, two alternative processes could be applied. The first one refers to the Petrurgic process: the glass component is first shaped at high temperatures and then cooled down, with a holding step at an intermediate temperature. The

cooling down is usually quite slow, whereas the holding step may be avoided for specific glass components. During cooling, both nucleation and crystal growth will occur (Rawlings et al., 2006; Rincón et al., 2016). The second process refers to sinter-crystallisation, in which glass frits are sintered by viscous flow, with concurrent crystallisation. This method was firstly applied in the 1970s, for the production of 'marble-like' tiles ('Neoparies') and was then progressively used to produce waste-derived glass-ceramics (Bernardo et al., 2017; Rincón et al., 2016). In fact, this process offers advantages when compared to other processes to produce waste-derived glass-ceramics, such as energy savings: waste-based glasses usually present a darker colouration due to the presence of heavy metals, and, therefore, may present low thermal conductivity by radiation. Based on this, it is usually necessary to apply high temperatures and long holding times in order to remove glass bubbles from the glass melt. In addition, the crystallisation process may difficult the removal of pores from the glass component, which is detrimental to mechanical properties (Bernardo et al., 2017; Rincón et al., 2016).

In the sinter-crystallisation process, on the other hand, it is not necessary to refine the glass melt before casting into a frit, which decreases costs and gaseous emissions: vitrification can even be applied in smaller plants at reduced time, which is benefit for capturing components that may be vaporised during longer heating treatments (Rincón et al., 2016). The glass frit is then milled and further pressed and heated to a temperature at which viscous flow and crystallisation will take place (Rincón et al., 2016). In addition, it is possible to produce glass-ceramics in reduced time with a relatively high degree of crystallisation, whereas the surface of the glass is the preferred site for nucleation (Rincón et al., 2016). This process can even be applied with fast heating rates or by directly inserting the green compacted glass powder inside the furnace already configured at the processing temperature ('fast sinter-crystallisation') (Bernardo, 2008; Rincón et al., 2016).

In order to obtain quite dense waste-derived glass-ceramics from the sinter-crystallisation process, it is necessary a balance between viscous flow sintering and surface crystallisation. If the crystallisation at the vitrified residue surface is too intensive, densification will be affected and thus the final product will present excessive porosity (see Figure 2-1a). In contrast, glasses not prone to surface crystallisation (e.g. soda-lime glass, boro-alumino-silicate glass) can be very well densified by viscous flow sintering (see Figure 2-1b). The actual optimal balance between viscous flow sintering and surface crystallisation is presented in Figure 2-1c. This can be achieved 'a priori', by reviewing the chemical composition of a glass submitted to sinter-crystallisation (the composition of slag sitals can be used as a reference) or even 'a posteriori', by mixing a glass with high tendency to crystallisation with a glass less prone to devitrification, which will offer extra liquid phase upon firing (Bernardo et al., 2010; Rincón et al., 2016). In this way, components that could represent an issue for the processing of waste-derived glass-

ceramics (e.g. iron oxides), can be turned into an opportunity for extending the functionalities of the final glass-ceramic products.

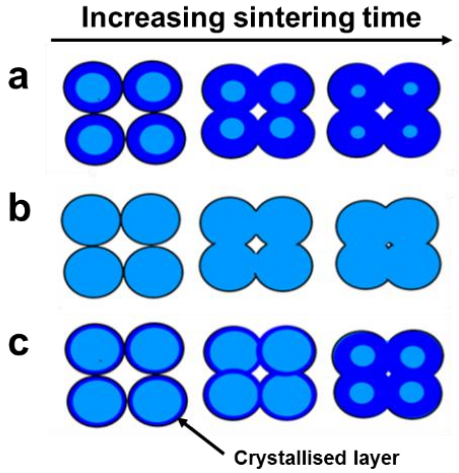

Figure 2-1. Mechanism of sinter-crystallisation: a) excessive crystallisation; b) only glass sintering; c) optimised condition. Adapted from (Rincón et al., 2016).

2.3. Porous waste-derived glass-ceramics

Glass foams presents a series of interesting properties such as high surface area, high permeability, low density and specific heat, high thermal and acoustic insulation and high chemical resistance (Scarinci et al., 2006). Furthermore, glass foams are non-flammable and flame resistant, chemically inert and not toxic, unlike polymeric foams (Rincón et al., 2016; Scarinci et al., 2006). Therefore, this type of inorganic material could potentially replace polymeric foams as building insulation materials, thus minimising damages in case of fire.

However, when compared to polymer foams, glass foams are currently more expensive, due to specific process used. The most established method to produce glass foams consists of mixing glass powders with a foaming agent, followed by firing. During the firing treatment, glass powders soften and form a 'pyroplastic' mass, which is foamed due to gas evolution from the additive. The foaming process will depend on decomposition or oxidation reactions of the foaming agent. Decomposition reactions are those provided by carbonates (mainly Na-carbonates and Ca-carbonates) or sulphates, which leads to the release of CO_2 or SO_x. In addition, a special variant refers to oxides of metals undergoing transition from high to low valence state, thus releasing oxygen gas, such as MnO_2 being transformed into MnO. Oxidation reactions, on the other hand, cause the release of carbon monoxide or carbon dioxide from carbon-containing compounds (e.g. carbon black, graphite, SiC, organic substances), by reacting with oxygen from the atmosphere. Decomposition and oxidation reaction can actually also overlap, as in the case of nitrides, which are transformed into oxides with release of nitrogen (Scarinci et al., 2006). In addition, the control of viscous flow sintering and foaming

phenomena is quite delicate for glass foams production. The situation is even more delicate for glass-ceramic foams, as viscous flow sintering and gas evolution must be combined with crystallisation (Rincón et al., 2016; Scarinci et al., 2006).

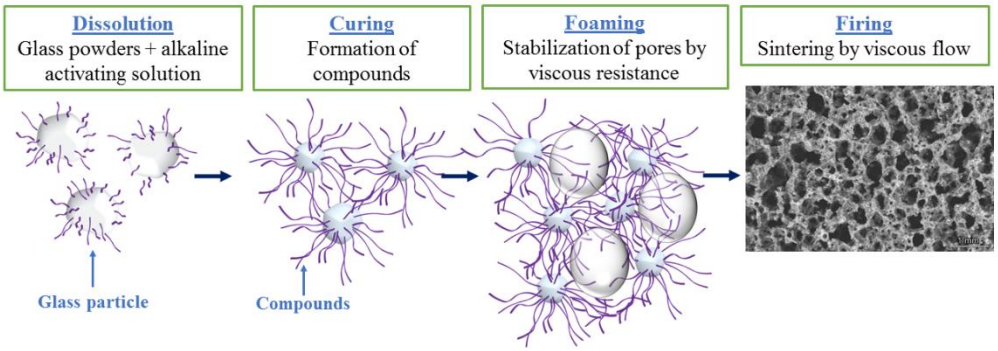

Figure 2-2. Process of alkali activation, gel-casting and sinter-crystallisation. Adapted from (Monich et al., 2018).

Based on this, a new technique was developed by Rincón et al. (Rincón et al., 2017) in an effort to decrease the costs for glass and glass-ceramic foams production. In contrast to the tradition methods for production of glass foams, this technique separates foaming from sintering (or sinter-crystallisation, in the case of glass-ceramics). This process is based on alkali activation combined with gel-casting and firing (see Figure 2-2): suspensions of fine glass powders mixed with an alkaline solution presented marked pseudoplasticity, due to partial dissolution of glass and gelation of corrosion products. This 'gelified' slurry was then submitted to intensive mechanical stirring, in which air was incorporated with the support of a surfactant (4 wt% Triton X-100), at high shear rates and low viscosity. Once stirring stops, the air bubbles formed remained 'frozen', due to viscous resistance, configuring 'inorganic gel casting'. The foamed suspension was finally dried at low temperature and then fired, in order to sinter the material by viscous flow. As foaming is achieved at low temperature, the consolidation of soda-lime glass foams may occur at only 700 °C (Rincón et al., 2017). In conventional glass foams production, on the other hand, it is necessary to apply higher processing temperatures (850-1000 °C) for the foaming reactions to occur (Rincón et al., 2017). Another advantage of the method based on gel-casting involves the production of panels, as there is no geometrical limitation for the low temperature foaming: the 'gelified' slurry can be simply foamed in a beaker and subsequently poured into a mould (Romero et al., 2019).

The procedure of gel-casting applied for soda-lime glass (Rincón et al., 2017) was similar to the one applied for geopolymer foams (Strozi Cilla et al., 2014). However, the activation was much weaker and the gels formed due to alkali activation were also different: in geopolymers, the hardening is originated from the formation of a three-dimensional network structure, from the polymerisation of smaller units, which is in turn provided by the complete dissolution of

alumino-silicate raw materials (e.g. metakaolin) (Cyr et al., 2012). On the other hand, the hardening of soda-lime glass based suspensions was associated to the formation and interlocking at the surface of glass powders of calcium silicate hydrates (C-S-H) compounds, analogous with conventional Portland cement (Garcia-Lodeiro et al., 2016; Rincón et al., 2017).

Table 2-1. Foams made by alkali activation followed by gel-casting and firing.

Formulation	**Firing temperature (°C)**	**Main hardening mechanism**	**Total porosity (vol.%)**	**Compressive strength (MPa)**	**Estimated bending strength (MPa)***	**Ref.**
Soda-lime glass foam, amorphous	700	C-S-H compounds	86	3.2 ± 0.5	89.7	(Rincón et al., 2017)
Ca-Mg silicate glass (bioactive glass), crystallised	900	C-S-H compounds	75	2.4 ± 0.2	102.9	(Elsayed et al., 2017)
80% soda-lime glass/20% Cu slag, crystallised	900	C-S-H compounds	82	1.3 ± 0.1	30.0	(Rincón et al., 2018)
Vitrified MSWI BA, crystallised	900	Carbonates	81	6.2 ± 0.7	374.3	(Rincon Romero et al., 2018)
Boro-alumino-silicate glass, amorphous	700	Hydrated boro-alumino-silicate gel	68	7.7 ± 0.4	212.7	(Romero et al., 2018)
76% coal fly ash/24% soda-lime glass, crystallised	800	Geopolymer-like gel	67	5.1 ± 0.3	134.5	(Romero et al., 2019)

*Calculated by assuming the shape factor is equal to 1 for all foams except for soda-lime glass and 80% soda-lime glass/20% Cu slag foams. In these two cases, the shape factor was considered as 0.8.

The technique based on alkali-activation followed by gel-casting and firing was successfully extended to other types of waste-based materials (Rincón et al., 2018; Rincon Romero et al., 2018; Romero et al., 2019, 2018) and even bioactive glasses (Elsayed et al., 2017) (see Table 2-1). The precipitation of crystals during the firing treatment could prevent significant viscous

flow, maintaining the open-celled structure, in the case of porous glass-ceramics, besides improving mechanical properties. In addition, these investigations showed that the hardening mechanism of the 'gelified' slurry was not always associated to the formation of C-S-H compounds, as it can be seen in Table 2-1.

2.4. Waste-derived lightweight aggregates

Lightweight aggregates (LWA) are other type of building materials that can be produced with vitrified residues. They are known to decrease the thermal conductivity of cement-based products (e.g. lightweight concrete, lightweight mortar) (Cheeseman and Virdi, 2005; Mueller et al., 2008), thus reducing the energy required for heating and cooling in buildings (Ferrándiz-Mas et al., 2014). Furthermore, LWA should present low density (typically between 0.8 to 2 g/cm^3), a porous and strong core, round shape (in order to increase the properties of the fresh cement-based material), and preferably a dense external surface ('shell', in order to minimise water absorption) (Cheeseman and Virdi, 2005; González-Corrochano et al., 2011). These types of building materials can be made from natural raw materials (e.g. clay, perlite) or even from waste materials (e.g. waste glass, fly ash, paper sludge ash, polystyrene, sewage sludge ash) (Cheeseman and Virdi, 2005; Ferrándiz-Mas et al., 2014; Mueller et al., 2008). Regarding waste materials, more specifically, it can even be more economically advantageous to process waste materials into LWA, rather than applying these residues directly as (normal weight) aggregates, due to increase in value added (Cheeseman and Virdi, 2005).

Waste-based lightweight aggregates can be produced by the fast firing treatment of materials containing substances (e.g. organic matter, calcium carbonate) which will release gasses at high temperatures ('bloating'). Furthermore, a phase with proper plasticity also needs to be formed in order to trap the released gasses (Ducman et al., 2002; González-Corrochano et al., 2009). Waste glass can also be mixed with waste materials to produce LWA (Kourti and Cheeseman, 2010; Tuan et al., 2013). In fact, previous studies showed that a proper amount of waste glass could reduce sintering temperature and water absorption, as well as increase mechanical properties and the bloating effect (Kourti and Cheeseman, 2010; Tuan et al., 2013).

In the case of expanded waste glass aggregates, more specifically, LWA are usually manufactured by mixing fine glass powders with an expansive (bloating) agent. A firing treatment is then applied above the softening point of the glass, but still at a temperature in which the viscosity of the glass is high enough to trap the released gasses (Ducman et al., 2002).

Table 2-2 presents examples of LWA produced with waste-based materials. As a reference, the commercially produced LWA Lytag presents mean density between 1.34 and 1.43 g/cm^3, water absorption between 13% and 17% and compressive strength of 6.3 MPa (Cheeseman and Virdi, 2005; Kourti and Cheeseman, 2010).

Table 2-2. Properties of waste-based LWA.

Composition	Firing conditions	Properties LWA	Reference
50% sewage sludge / 50% waste glass	20 min at 930 °C, kiln	Bulk density < 1.3 g/cm^3; water absorption: < 1.54%	(Tuan et al., 2013)
60% lignite coal fly ash / 40% waste glass (organic binder addition)	1120 °C, rotary furnace	Density:1.35 g/cm^3; water absorption: ~16%; compressive strength: 7.3 MPa	(Kourti and Cheeseman, 2010)
Sewage sludge ash (clay or organic binder addition)	1060 °C, rotary furnace	Density:1.35 g/cm^3; water absorption: ~8%	(Cheeseman and Virdi, 2005)
Waste glass (expansive agent addition)	880 °C, rotary kiln	Apparent density: 0.15-0.18 g/cm^3; water absorption: 11.0%	(Ducman et al., 2002)
95% weathered MSWI BA / 5% rice husk (expansive agent)	5 min at 1100 °C	Apparent particle density: 0.61 g/cm^3; water absorption: ~5%; compressive strength: 1.4 MPa	(Giro-Paloma et al., 2019)
85% red clay / 15% sludge from wastewater treatment plant from brewery industry	60 min at 1000 °C, laboratory electrical kiln	Bulk density: 1.16 g/cm^3; water absorption: 28.32%; total porosity: 49.61%	(Farias et al., 2017)

2.5. Structural and functional properties of waste-derived glass-ceramics

Porous glass-ceramics can present a balance between low thermal conductivity and high strength. In fact, the strength of the porous glass-based materials will be dependent on the cell morphology and crystallisation. Generally, the compressive strength of a foam (σ_{comp}) will depend on the bending strength of the solid phase (σ_{bend}), with a scaling factor. The scaling factor is a function of the relative density (ρ_{rel}, which is the ratio between the density of the foam and the density of the solid phase), according to the Gibson and Ashby's model (Gibson and Ashby, 1999; Rincón et al., 2016):

$$\sigma_{comp} = \sigma_{bend} \cdot [0.2(\phi\rho_{rel})^{3/2} + (1-\phi)\rho_{rel})]$$

The shape factor ϕ refers to the fraction of solid at the cell edges, whereas (1-φ) refers to the fraction of solid at the cell faces. Open-celled foams presents ϕ equals to 1, and therefore the linear term is neglected. On the other hand, foams with closed-cell morphology presents a significant contribution from the linear term (Gibson and Ashby, 1999; Rincón et al., 2016). The Gibson and Ashby's model can be applied on the basis of the measured σ_{comp}, to estimate

σ_{bend}, as a 'quality factor' of the developed porous glass-ceramics, as shown by Table 2-1 (as a reference, 'strong' glass-ceramics ideally present bending strength above the one of soda-lime glass, which is between 70-75 MPa (Mecholsky et al., 1974)).

For foams made with glasses prone to surface crystallisation, the estimated bending strength of the solid phase may increase due to crystallisation. However, crystallisation can also enhance the apparent viscosity of the glass. This can limit the reshaping of pores during the firing treatment, leading to heterogeneous materials, which may compromise the reinforcing effect. Finally, the strength of a cellular material depends also on a size effect: smaller pore size leads to stronger struts (Rincón et al., 2016).

Crystallisation can also provide functional properties, depending on the phases formed. For example, magnetite (Fe_3O_4) is a ferri-magnetic and also highly conductive material, which could bring novel functionalities to the material associated to magnetic, optical or electrical properties (Chinnam et al., 2013). According to Voogt et al. (Voogt et al., 1999), magnetite presents such interesting properties, because of the presence of Fe cations as Fe^{2+} (ferrous) and Fe^{3+} (ferric) ions, which are found in tetrahedral or octahedral sites for inverse spinel structure. Half of Fe^{3+} ions are presented in 12.5% of the tetrahedral sites, while the other half of Fe^{3+} ions (and the same amount of Fe^{2+} ions) occupy 50% of the octahedral sites. The octahedral sites occupied by ferrous and ferric ions are connected in strings in all [110] directions. The high conductivity at room temperature presented by magnetite is attributed by a fast electron hopping between ferrous and ferric ions in these strings. The ferri-magnetism presented by magnetite, on the other hand, is originated from the magnetic moments of the iron ions (Voogt et al., 1999).

The presence of magnetite in specific iron-rich waste-derived glass-ceramics can be exploited for electromagnetic shielding in order to minimise human exposure to electromagnetic fields and also to avoid electromagnetic interferences (Kumari et al., 2017; Maschio et al., 2016). According to Chung (Chung, 2001, 2000), materials for electromagnetic interference shielding reflects or absorbs electromagnetic radiation, thus acting as a shield. Reflection of electromagnetic radiation consists in one of the main mechanisms for electromagnetic interference shielding. In this case, the material should present electrons or holes ('mobile charge carriers') which will interact with the electromagnetic fields in the radiation. Therefore, electrical conductors can act as shields based on reflection. A second mechanism for electromagnetic interference shielding is based on absorption, for which the material should present magnetic and/or electric dipoles in order to interact with the electromagnetic fields in the radiation. Finally, another mechanism for electromagnetic interference shielding is multiple reflections, based on reflections at different surfaces of interfaces in the material. A shield for multiple reflections should present large surface area or interface area, such as in the case of foams (Chung, 2001, 2000).

The reflection and absorption losses are based on σ/μ and σ·μ, respectively (σ refers to the electrical conductivity relative to copper, whereas μ refers to the relative magnetic permeability). Increase in frequency decreases reflection losses, while it increases absorption losses. The losses (either from reflection, absorption or multiple reflections) are usually represented in dB. The shielding effectiveness consist of the sum of all losses, in dB (Chung, 2001, 2000).

Therefore, based on different mechanisms for electromagnetic interference shielding, waste-derived glass-ceramic foams containing magnetite could be potentially applied in this field based on reflection and/or absorption losses, as well as multiple reflections. As an example, waste-derived glass-ceramic foams made with 80% soda-lime glass/20% copper slag (see Table 2-1) exhibited some potential in electromagnetic shielding due to the presence of magnetite. The assessment of shielding effectiveness indicated not negligible values between 2 and 2.6 GHz, with a marked peak (about 7 dB) near 2.4 GHz (Rincón et al., 2018).

The presence of magnetite in waste-derived glass-ceramics has already been explored for other applications. Ponsot et al. (Ponsot et al., 2014) developed glass-ceramics made with recycled borosilicate glass mixed with iron-rich slags (from the copper and lead metallurgy), which presented magnetite as main crystal phase. Induction heating tests indicated that these samples could reach 300 °C after application of an alternating magnetic field for 60 s. This was attributed to the presence of magnetite which provided ferri-magnetism. Therefore, taking into account the resistance to thermal shock and the chemical stability presented by these materials, the developed glass-ceramics could potentially be applied as novel heating elements (e.g. for cooking tops) (Ponsot et al., 2014).

Finally, the presence of iron-rich phases in iron-rich glass-ceramics will depend on the composition of the glass, heating treatment (firing temperature, atmosphere, holding time, heating and cooling rates) and particle size (in the case of frits) (Rincón et al., 2016).

2.6. Chemical durability of waste-derived glass-ceramics

Any possible commercialisation of waste-derived glass-ceramics should include an assessment of the potential hazardous effect presented by these materials. This may be done by means of standard chemical durability tests, as well as cell toxicity tests (Rawlings et al., 2006). In order to present a high chemical durability, waste derived glass-ceramic should present stable residual glass phase, as well as stable crystal phases. Waste-derived glass-ceramics can even present superior chemical resistance than the parent glass, depending on the stability of the phases formed (Pisciella et al., 2001).

Pisciella et al. (Pisciella et al., 2001) studied the chemical durability (assessed by means of toxic characterisation leaching procedure, TCLP) of two types of glass-ceramics produced with glasses containing 40% or 50% jarosite. The glass made with 40% jarosite presented the

following main composition (in wt%): SiO_2: 52.90; Fe_2O_3: 23.90; Na_2O: 6.40; CaO: 5.20; Al_2O_3: 4.10; ZnO: 2.70; MgO: 1.80; PbO: 1.70. In contrast, the main composition of the glass made with 50% jarosite is listed as follows (in wt%): SiO_2: 47.38; Fe_2O_3: 28.33; Na_2O: 6.00; CaO: 4.70; Al_2O_3: 3.37; ZnO: 3.25; PbO: 2.05; MgO: 1.76. For glass-ceramics made with lower content of jarosite, chemical durability increased when compared to the parent glass. This was attributed to the formation of pyroxene as the main phase, which is a stable crystal. On the other hand, the glass-ceramic made with higher content of jarosite presented magnetite and franklinite spinel as the major crystal phases. The chemical durability assessment of this glass-ceramic indicated a decrease of chemical durability in acidic conditions when compared to the parent glass. A possible explanation for this could be associated to a higher solubility of magnetite type spinel in acidic conditions, thus reducing the chemical durability of the glass-ceramic (Pisciella et al., 2001).

Besides magnetite, hematite may also affect durability. The surface crystallisation of hematite was already attributed to decrease the durability of vitrified lead-rich waste after annealing for inhibiting the formation of the stable crystal phase magnetoplumbite and for decreasing the quantity of Fe^{3+} ions from the vitreous network. This led to an enrichment of the glass modifiers Fe^{2+} and Pb^{+} in the volume of the amorphous matrix, which may have weakened the matrix, thus promoting the leaching of lead (Kavouras et al., 2003b, 2003a).

Furthermore, as previously mentioned, the stability of the residual glass phase will also be a key factor regarding the chemical durability of waste-derived glass-ceramics. Bernardo et al. (Bernardo et al., 2006) attributed a higher chemical durability of a waste-derived glass-ceramic made with vitrified mixtures of panel glass, lime and mining residues to certain factors such as crystallisation of only wollastonite, which in turn increased the alumina content of the residual glass phase. An alumina-rich residual glass phase may present a high chemical durability, as the substitution of Si^{4+} with Al^{3+} enhances the connectivity of the glass-structure and immobilises the alkali ions for charge balance, thus avoiding glass dissolution (Bernardo et al., 2006; Sinton and Lacourse, 2001).

Finally, if the waste-derived glass-ceramic presents low chemical durability, this could be also adjusted ‘a priori’ by following a composition similar to the one of slag sitals (due to their high chemical durability) (Höland and Beall, 2012) or ‘a posteriori’ by mixing stable materials (e.g. boro-alumino-silicate glass) with the vitrified residue.

2.7. References

Bernardo, E., 2008. Fast sinter-crystallization of a glass from waste materials. J. Non. Cryst. Solids 354, 3486–3490. https://doi.org/10.1016/j.jnoncrysol.2008.03.021

Bernardo, E., Bonomo, E., Dattoli, A., 2010. Optimisation of sintered glass-ceramics from an industrial waste glass. Ceram. Int. 36, 1675–1680.

https://doi.org/10.1016/j.ceramint.2010.02.047

Bernardo, E., Scarinci, G., Colombo, P., 2017. Vitrification of Waste and Reuse of Waste-Derived Glass, in: Meyers, R.A. (Ed.), Encyclopedia of Sustainability Science and Technology. Springer New York, New York, NY, pp. 1–34. https://doi.org/10.1007/978-1-4939-2493-6_96-3

Bernardo, E., Varrasso, M., Cadamuro, F., Hreglich, S., 2006. Vitrification of wastes and preparation of chemically stable sintered glass-ceramic products. J. Non. Cryst. Solids 352, 4017–4023. https://doi.org/10.1016/j.jnoncrysol.2006.07.001

Cheeseman, C.R., Virdi, G.S., 2005. Properties and microstructure of lightweight aggregate produced from sintered sewage sludge ash. Resour. Conserv. Recycl. 45, 18–30. https://doi.org/10.1016/j.resconrec.2004.12.006

Chinnam, R.K., Francis, A.A., Will, J., Bernardo, E., Boccaccini, A.R., 2013. Review. Functional glasses and glass-ceramics derived from iron rich waste and combination of industrial residues. J. Non. Cryst. Solids 365, 63–74. https://doi.org/10.1016/j.jnoncrysol.2012.12.006

Chung, D.D.L., 2001. Electromagnetic interference shielding effectiveness of carbon materials. Carbon N. Y. 39, 279–285. https://doi.org/10.1016/S0008-6223(00)00184-6

Chung, D.D.L., 2000. Materials for Electromagnetic Interference Shielding. J. Mater. Eng. Perform. 9, 350–354. https://doi.org/10.1361/105994900770346042

Colombo, P., Brusatin, G., Bernardo, E., Scarinci, G., 2003. Inertization and reuse of waste materials by vitrification and fabrication of glass-based products. Curr. Opin. Solid State Mater. Sci. 7, 225–239. https://doi.org/10.1016/j.cossms.2003.08.002

Cyr, M., Idir, R., Poinot, T., 2012. Properties of inorganic polymer (geopolymer) mortars made of glass cullet. J. Mater. Sci. 47, 2782–2797. https://doi.org/10.1007/s10853-011-6107-2

Ducman, V., Mladenovič, A., Šuput, J.S., 2002. Lightweight aggregate based on waste glass and its alkali–silica reactivity. Cem. Concr. Res. 32, 223–226. https://doi.org/10.1016/S0008-8846(01)00663-9

Elsayed, H., Romero, A.R., Ferroni, L., Gardin, C., Zavan, B., Bernardo, E., 2017. Bioactive glass-ceramic scaffolds from novel “inorganic gel casting” and sinter-crystallization. Materials (Basel). 10. https://doi.org/10.3390/ma10020171

Farias, R.D., García, C.M., Palomino, T.C., Andreola, F., Lancellotti, I., Barbieri, L., 2017. Valorization of agro-industrial wastes in lightweight aggregates for agronomic use: Preliminary study. Environ. Eng. Manag. J. 16, 1691–1699. https://doi.org/10.30638/eemj.2017.184

Ferrándiz-Mas, V., Bond, T., García-Alcocel, E., Cheeseman, C.R., 2014. Lightweight mortars containing expanded polystyrene and paper sludge ash. Constr. Build. Mater. 61, 285–292. https://doi.org/10.1016/j.conbuildmat.2014.03.028

Fruergaard, T., Hyks, J., Astrup, T., 2010. Life-cycle assessment of selected management options for air pollution control residues from waste incineration. Sci. Total Environ. 408, 4672–4680. https://doi.org/10.1016/j.scitotenv.2010.05.029

Garcia-Lodeiro, I., Aparicio-Rebollo, E., Fernández-Jimenez, A., Palomo, A., 2016. Effect of calcium on the alkaline activation of aluminosilicate glass. Ceram. Int. 42, 7697–7707. https://doi.org/10.1016/j.ceramint.2016.01.184

Gibson, L.J., Ashby, M.F., 1999. Cellular solids: structure and properties. Cambridge University Press, Cambridge, UK.

Giro-Paloma, J., Mañosa, J., Maldonado-Alameda, A., Quina, M.J., Chimenos, J.M., 2019. Rapid sintering of weathered municipal solid waste incinerator bottom ash and rice husk for lightweight aggregate manufacturing and product properties. J. Clean. Prod. 232, 713–721. https://doi.org/10.1016/j.jclepro.2019.06.010

Gomez, E., Rani, D.A., Cheeseman, C.R., Deegan, D., Wise, M., Boccaccini, A.R., 2009. Thermal plasma technology for the treatment of wastes: A critical review. J. Hazard. Mater. 161, 614–626. https://doi.org/10.1016/j.jhazmat.2008.04.017

González-Corrochano, B., Alonso-Azcárate, J., Rodas, M., 2009. Production of lightweight aggregates from mining and industrial wastes. J. Environ. Manage. 90, 2801–2812. https://doi.org/10.1016/j.jenvman.2009.03.009

González-Corrochano, B., Alonso-Azcárate, J., Rodas, M., Barrenechea, J.F., Luque, F.J., 2011. Microstructure and mineralogy of lightweight aggregates manufactured from mining and industrial wastes. Constr. Build. Mater. 25, 3591–3602. https://doi.org/10.1016/j.conbuildmat.2011.03.053

Höland, W., Beall, G.H., 2012. Glass-Ceramic Technology. John Wiley & Sons, Inc., Hoboken, NJ, USA.

Karamanov, A., Maccarini Schabbach, L., Karamanova, E., Andreola, F., Barbieri, L., Ranguelov, B., Avdeev, G., Lancellotti, I., 2014. Sinter-crystallization in air and inert atmospheres of a glass from pre-treated municipal solid waste bottom ashes. J. Non. Cryst. Solids 389, 50–59. https://doi.org/10.1016/j.jnoncrysol.2014.02.009

Kavouras, P., Kaimakamis, G., Ioannidis, T.A., Kehagias, T., Komninou, P., Kokkou, S., Pavlidou, E., Antonopoulos, I., Sofoniou, M., Zouboulis, A., Hadjiantoniou, C.P., Nouet, G., Prakouras, A., Karakostas, T., 2003a. Vitrification of lead-rich solid ashes from incineration of hazardous industrial wastes. Waste Manag. 23, 361–371. https://doi.org/10.1016/S0956-053X(02)00153-8

Kavouras, P., Komninou, P., Chrissafis, K., Kaimakamis, G., Kokkou, S., Paraskevopoulos, K., Karakostas, T., 2003b. Microstructural changes of processed vitrified solid waste products. J. Eur. Ceram. Soc. 23, 1305–1311. https://doi.org/10.1016/S0955-2219(02)00289-3

Kourti, I., Cheeseman, C.R., 2010. Properties and microstructure of lightweight aggregate

produced from lignite coal fly ash and recycled glass. Resour. Conserv. Recycl. 54, 769–775. https://doi.org/10.1016/j.resconrec.2009.12.006

Kumari, P., Tripathi, P., Parkash, O., Kumar, D., 2017. Electromagnetic interference shielding effectiveness of MgO−Al2 O3 −SiO2 glass–ceramic system. Bull. Mater. Sci. 40, 1497–1501. https://doi.org/10.1007/s12034-017-1505-y

Maschio, A., Bernardo, E., Desideri, D., Marangoni, M., Ponsot, I., Pontikes, Y., 2016. Shielding effectiveness of construction materials. Int. J. Appl. Electromagn. Mech. 52, 137–144. https://doi.org/10.3233/JAE-162089

Mecholsky, J.J., Rice, R.W., Freiman, S.W., 1974. Prediction of Fracture Energy and Flaw Size in Glasses from Measurements of Mirror Size. J. Am. Ceram. Soc. 57, 440–443. https://doi.org/10.1111/j.1151-2916.1974.tb11377.x

Monich, P.R., Romero, A.R., Höllen, D., Bernardo, E., 2018. Porous glass-ceramics from alkali activation and sinter-crystallization of mixtures of waste glass and residues from plasma processing of municipal solid waste. J. Clean. Prod. 188, 871–878. https://doi.org/10.1016/j.jclepro.2018.03.167

Mueller, A., Sokolova, S.N., Vereshagin, V.I., 2008. Characteristics of lightweight aggregates from primary and recycled raw materials. Constr. Build. Mater. 22, 703–712. https://doi.org/10.1016/j.conbuildmat.2007.06.009

Pisciella, P., Crisucci, S., Karamanov, A., Pelino, M., 2001. Chemical durability of glasses obtained by vitrification of industrial wastes. Waste Manag. 21, 1–9. https://doi.org/10.1016/S0956-053X(00)00077-5

Ponsot, I.M.M.M., Pontikes, Y., Baldi, G., Chinnam, R.K., Detsch, R., Boccaccini, A.R., Bernardo, E., 2014. Magnetic glass ceramics by sintering of borosilicate glass and inorganic waste. Materials (Basel). 7, 5565–5580. https://doi.org/10.3390/ma7085565

Rawlings, R.D., Wu, J.P., Boccaccini, A.R., 2006. Glass-ceramics: Their production from wastes-A Review. J. Mater. Sci. 41, 733–761. https://doi.org/10.1007/s10853-006-6554-3

Rincón, A., Desideri, D., Bernardo, E., 2018. Functional glass-ceramic foams from ‘inorganic gel casting’ and sintering of glass/slag mixtures. J. Clean. Prod. 187, 250–256. https://doi.org/10.1016/j.jclepro.2018.03.065

Rincón, A., Giacomello, G., Pasetto, M., Bernardo, E., 2017. Novel ‘inorganic gel casting’ process for the manufacturing of glass foams. J. Eur. Ceram. Soc. 37, 2227–2234. https://doi.org/10.1016/j.jeurceramsoc.2017.01.012

Rincón, A., Marangoni, M., Cetin, S., Bernardo, E., 2016. Recycling of inorganic waste in monolithic and cellular glass-based materials for structural and functional applications. J. Chem. Technol. Biotechnol. 91, 1946–1961. https://doi.org/10.1002/jctb.4982

Rincon Romero, A., Salvo, M., Bernardo, E., 2018. Up-cycling of vitrified bottom ash from MSWI into glass-ceramic foams by means of ‘inorganic gel casting’ and sinter-

crystallization. Constr. Build. Mater. 192, 133–140. https://doi.org/10.1016/j.conbuildmat.2018.10.135

Romero, A.R., Tamburini, S., Taveri, G., Toušek, J., Dlouhy, I., Bernardo, E., 2018. Extension of the “inorganic gel casting” process to the manufacturing of boro-alumino-silicate glass foams. Materials (Basel). 11, 1–12. https://doi.org/10.3390/ma11122545

Romero, A.R., Toniolo, N., Boccaccini, A.R., Bernardo, E., 2019. Glass-ceramic foams from “weak alkali activation” and gel-casting of waste glass/fly ash mixtures. Materials (Basel). 12. https://doi.org/10.3390/ma12040588

Scarinci, G., Brusatin, G., Bernardo, E., 2006. Glass Foams. Cell. Ceram. Struct. Manuf. Prop. Appl. 158–176. https://doi.org/10.1002/3527606696.ch2g

Sinton, C.W., Lacourse, W.C., 2001. Experimental survey of the chemical durability of commercial soda-lime-silicate glasses. Mater. Res. Bull. 36, 2471–2479. https://doi.org/10.1016/S0025-5408(01)00724-3

Strozi Cilla, M., Colombo, P., Raymundo Morelli, M., 2014. Geopolymer foams by gelcasting. Ceram. Int. 40, 5723–5730. https://doi.org/10.1016/j.ceramint.2013.11.011

Tuan, B.L.A., Hwang, C.L., Lin, K.L., Chen, Y.Y., Young, M.P., 2013. Development of lightweight aggregate from sewage sludge and waste glass powder for concrete. Constr. Build. Mater. 47, 334–339. https://doi.org/10.1016/j.conbuildmat.2013.05.039

Voogt, F.C., Fujii, T., Smulders, P.J.M., Niesen, L., James, M.A., Hibma, T., 1999. NO2 - assisted molecular-beam epitaxy of Fe3O4, Fe3−δO4, and γ−Fe2O3 thin films on MgO(100) . Phys. Rev. B 60, 11193–11206. https://doi.org/10.1103/physrevb.60.11193

Zhang, Z., Li, G.Q., Yang, Y.X., Xiao, Y.P., 2014. Thermodynamics of the Vitrified Bottom Ash Slag from Municipal Solid Waste Incinerators-Phase Relations of CaO-SiO2-Na2O Oxide System. Adv. Mater. Res. 881–883, 574–578. https://doi.org/10.4028/www.scientific.net/AMR.881-883.574

PART II - Experimental procedures

Chapter 3. Materials and methods

3.1. Materials

3.1.1. Plasmastone

Plasmastone was produced in a pilot vitrification unit and was kindly provided by Scanarc (Sweden) ("Scanarc," 2017). The production of this glass is described by Machiels et al. (Machiels et al., 2017). Furthermore, according to Machiels et al., Plasmastone was produced under a CO/CO_2 gas mixtures in order to guarantee that Fe is mainly present as Fe^{2+}.

This vitrified reside was dried overnight at 100 °C and milled at 360 rpm until particle size was below 75 µm. The chemical composition of Plasmastone was determined by X-Ray fluorescence and it is reported in Table 3-1. In addition, this vitrified residue also contained metals like Cu (7124 ppm), Cr (406 ppm) and Ni (203 ppm) which are above the Austrian limit values for recycled building materials (RIS - Recycling-Baustoffverordnung (Austrian Recycling Building Materials Ordinance)).

Table 3-1. Composition of Plasmastone.

Oxide (wt%)	Plasmastone
SiO_2	34.2 - 37.3
CaO	23.0 - 23.2
Fe_2O_3	20.9 - 24.8
Al_2O_3	12.8 - 14.8
MgO	1.18 - 2.40
TiO_2	0.60 - 0.67
K_2O	0.32 - 0.51
Na_2O	0.26 - 1.10
MnO	0.11 - 0.15
P_2O_5	0.03 - 0.18

3.1.2. Soda-lime glass

Soda-lime glass powders (medium particle size equal to 30 µm) were kindly provided by SASIL SpA (Brusnengo, Biella, Italy), as the residual waste glass fraction which is essentially not employed due to the presence of ceramic contaminations (Rincón et al., 2017). Table 3-2 presents the composition of soda-lime glass:

Table 3-2. Composition of soda-lime glass.

Oxide (wt%)	Soda-lime glass (Rincón et al., 2017)
SiO_2	71.9
Na_2O	14.3
Al_2O_3	1.2
CaO	7.5
MgO	4
K_2O	0.4
Fe_2O_3	0.3
TiO_2	0.1
Sum of contents	99.7

3.1.3. Boro-alumino-silicate glass

Boro-alumino-silicate glass, from disposed pharmaceutical vials, was kindly provided by Nuova OMPI (Piombino Dese, Padova, Italy). This glass was received in form of coarse fragments and it was ground into powders below 45 μm, by ball milling (Bernardo and Scarinci, 2004). The chemical composition of this glass is shown in Table 3-3:

Table 3-3. Composition of boro-alumino-silicate glass.

Oxide (wt%)	Boro-alumino-silicate glass (Bernardo and Scarinci, 2004)
SiO_2	72
B_2O_3	12
Al_2O_3	7
Na_2O	6
K_2O	2
CaO	1
Sum of contents	100

3.1.4. Vitrified MSWI bottom ash

MSWI bottom ash was kindly provided by the company AVR (Netherlands) and dried at 200 °C for 24h. Four different strategies were employed before the smelting in order to recover metallic fractions. In the first strategy (S1), no mechanical separation was applied before vitrification. On the other hand, in the second strategy 2 (S2), the ferrous particles were extracted by a magnet. In the third strategy (S3), an eddy-current separator was employed in order to extract the non-ferrous particles from this residue. Finally, in strategy 4 (S4), both ferrous and non-ferrous particles were extracted from MSWI bottom ash. Thereafter, the treated

bottom ash was added to a graphite crucible and smelted in a lab-scale electric arc furnace at around 1450 °C. The melt bottom ash was finally quenched in water, dried and ground below 75 µm, by ball milling at 360 rpm. The glasses were produced by ESR9 Hugo Lucas (NEW-MINE Project) at RWTH Aachen.

The chemical composition of vitrified bottom ash from the four strategies (Table 3-4) was measured by a PANanalytical WDXRF spectrometer. Generally, the main composition of the four glasses lies inside the range of composition of slag sitals. These waste derived glass-ceramics were known to present high strength and chemical durability (Höland and Beall, 2012), as reported in Chapter 2. Therefore, the similar chemical composition of vitrified bottom ash with slag sitals indicate the suitability of all four glasses in the production of waste-derived glass-ceramics. Finally, the cleaning steps performed before smelting influenced the composition of the glasses, especially regarding the quantities of Al_2O_3.

Table 3-4. Main chemical composition of vitrified bottom ash produced by different strategies.

Oxide (wt%)	Strategy 1	Strategy 2	Strategy 3	Strategy 4
SiO_2	50.3	49.2	51.0	50.1
CaO	20.9	18.8	19.7	23.6
Al_2O_3	19.0	19.9	16.8	14.5
Na_2O	4.59	4.14	4.71	3.21
MgO	2.65	2.59	2.54	2.44
TiO_2	0.85	0.86	1.08	1.43
K_2O	0.75	0.85	0.92	0.73
CuO	0.21	0.30	0.19	0.23
BaO	0.18	0.18	0.22	0.22
Fe_2O_3	0.14	1.43	0.77	0.30
MnO	0.13	0.07	0.21	0.23
SrO	0.11	0.07	0.08	0.10
ZrO2	0.06	0.21	0.20	0.05
Cr_2O_3	0.05	0.05	0.05	0.05
P_2O_5	0.02	0.17	0.05	0.02
SO_3	0.00	1.13	1.47	2.70
Sum of contents	99.9	100	100	99.9

3.1.5. Conditioned bottom ash-red mud

MSWI bottom ash was kindly provided by the company AVR (Netherlands), whereas red mud was kindly provided by the company Aluminum of Greece S.A. Both residues were dried at 150 °C for 24h and no mechanical separation was applied before smelting. Thereafter, bottom ash was first smelted using a submerged arc furnace (SAF) for 30 minutes at around 1450-1500 °C. After 30 minutes, 33% red mud was added to the furnace and treated together with bottom ash for another 30 minutes. The total time in this two-step treatment was 60 minutes including the feeding time for bottom ash (15 minutes) and red mud (10 minutes). Thereafter, the molten mixture of residues was quenched in water and dried at 150 °C for 24h. The obtained glass was milled using a planetary ball mill at 360 rpm until the particle size was below 75 µm. The glass was produced by ESR9 Hugo Lucas (NEW-MINE Project) at RWTH Aachen.

The chemical composition of conditioned bottom ash-red mud was measured using a PANanalytical WDXRF spectrometer Axios:

Table 3-5. Main chemical composition of conditioned bottom ash-red mud (VBARM).

Oxide (wt%)	VBARM
SiO_2	36.6
Al_2O_3	19.6
CaO	17.2
Fe_2O_3	16.5
TiO_2	3.35
Na_2O	3.24
MgO	1.42
K_2O	0.66
CuO	0.6
Cr_2O_3	0.23
BaO	0.19
MnO	0.13
P_2O_5	0.06
C	0.05
ZnO	0.01
Sum of contents	99.8

3.1.6. Partially crystallised residues

Two types of partially crystallised residues (with main particle size below 75 µm) were applied in this study: one from the industrial polishing of porcelain stoneware tiles, recovered from a landfill site in Emilia-Romagna (Italy). The second residue refers to plasma processed asbestos-containing waste (‘cofalit’), obtained from the vitrification of asbestos by means of

plasma technology. Cofalit was kindly provided by Inertam-Europlasma (France) and it actually consists of a partially crystallised residue due to low and uncontrol cooling rate of the molten residue (Bernardo et al., 2011).

Table 3-6 shows the chemical composition of the polishing stoneware residue and of cofalit:

Table 3-6. Chemical composition of the partially crystallised residues.

Oxide (wt%)	Polishing stoneware residue (Bernardo et al., 2009)	Cofalit (Bernardo et al., 2011)
SiO_2	64.1	35.7
Al_2O_3	16.5	7.4
CaO	1.4	35.1
Na_2O	4.4	<0.05
MgO	4.6	12.6
Fe_2O_3	0.5	7
K_2O	2.1	0.1
TiO_2	0.5	1.5
ZrO_2	1.1	
Sum of contents	95.2	99.4

3.2. Methods

3.2.1. General characterisations

Mineralogical analysis

The mineralogical analysis was conducted on fine powders by means of X-ray diffraction (XRD) (Bruker D8 Advance, Karlsruhe, Germany), using CuKα radiation, 0.15418 nm, 40 kV–40 mA, 2θ = 10-70°, step size of 0.02° and counting time of 0.5 - 2 s (0.5 s for fired materials and 2 s for as received residues or activated residues), with a position sensitive detector (LinxEye, Bruker AXS, Karlsruhe, Germany). In Chapters 4, 5, 6, 7, and 9, the crystalline phase assemblage of powdered glass-ceramics was investigated by XRD (Bruker D8 Advance, Karlsruhe, Germany) employing step size of 0.5° and counting time of 2 s.

The crystalline phases were identified by means of the Match!® program package (Crystal Impact GbR, Bonn, Germany), supported by data from Powder Diffraction File (PDF)-2 database (International Centre for Diffraction Data, Newtown Square, PA, USA).

Thermal analysis

Differential thermal analysis and thermogravimetric analysis (DTA/TGA, STA409, Netzsch Gerätebau GmbH) were done on Plasmastone powders in air, with a heating rate of 10 °C/min.

Differential scanning calorimetry (DSC, 3+ STARe System, Mettler Toledo, Columbus, OH, USA), were performed on vitrified bottom ash powders, in air. The heating rate applied was also 10 °C/min.

Morphological and microstructural characterisations

The morphological and microstructural characterisations of the developed samples (polished up to 5 µm finish by using diamond tools) was assessed by means of an optical stereomicroscopy (AxioCam ERc 5 s Microscope Camera, Carl Zeiss Microscopy, Thornwood, New York, USA) or of a scanning electron microscopy (FEI Quanta 200 ESEM, Eindhoven, The Netherlands).

Environmental impact assessment

Leaching test were performed on the waste-derived samples following norm EN 12457-4 ("Norm EN 12457-4," 2002). The materials were firstly crushed and sieved below 10 mm. The sieved fragments were then added to a plastic flask with pure distilled water (liquid/solid ratio of 10), which was submitted to mixing at room temperature for 24h. The eluate was obtained by filtering and centrifuging the suspension. Inductively coupled plasma (ICP; SPECTRO Analytical instruments GmbH, Germany) was used to measure the heavy metals content of the eluate. The leachate values of the eluate were compared to the values allowed for waste acceptable at landfills for inert waste and non-hazardous waste (Directive 2003/33/EC, 2003).

In Chapters 4 and 5, inductively coupled plasma mass spectrometry (ICP-MS, Agilent 7500 cx) and ion chromatography (IC, Dionex ICS 2000) were used to measure the contents of heavy metals and anions, respectively, in the leachates. In these studies, the Austrian Recycling Building Materials Ordinance was used as a reference ("RIS - Recycling-Baustoffverordnung (Austrian Recycling Building Materials Ordinance),"). Furthermore, it was also tested commercial samples (a commercial tile and glass foam in chapters 4 and 5, respectively) as a control. The Austrian Waste Management regulation of 2002 specifies that it must be assessed if the environmental impact of a recycled product is not worse than that of a competing product from primary raw materials. In addition, selected waste-derived samples were analysed at an electron microprobe (Jeol JXA 8200 Superprobe), after polishing (using 1 µm-sized diamond suspension and diamond spray) and coating with a thin carbon layer, in order to correlate the leaching of pollutants with the mineralogical phases formed.

Shielding effectiveness

Shielding effectiveness was determined on hollow cylindrical samples in the frequency range 0.1 MHz-3 GHz (Chapters 4 and 6) or 100 kHz- 3 GHz (Chapter 7): the sample was placed in a coaxial holder with a continuous inner conductor, connected to a vector network analyser, This setup yielded the S_{21} parameter, in turn leading to the shielding effectiveness $SE_{dB} = - S_{21dB}$ (Maschio et al., 2016; Rincón et al., 2018; Tamburrano et al., 2014).

3.2.2. Characterisation of dense glass-ceramics

Water absorption and density

The water absorption and density of the fired samples were assessed according to the boiling and Archimedes method, respectively.

Mechanical properties

The mechanical properties of the dense samples were measured by firstly cutting the tiles and polishing the obtained beams up to 5 μm finish by using diamond tools. The edges of the beams were carefully polished to remove any surface defects. The polished dense glass-ceramics presented approximately the following dimensions: 34.3-48.0 mm x 3.4-5.3 mm x 2.6-3.9 mm.

Dynamic elastic modulus was assessed by non-destructive dynamic resonance and vickers microhardness was measured by applying a load of 9.8 N.

The four-point bending test (32 mm outer span, 8 mm inner span) was done by employing an Instron 1121 UTS instrument (Instron, Danvers, MA) on at least 9 samples with cross-head speed of 1 mm/min. Weibull statistics was applied according to Barsoum (Barsoum, 2003): firstly, the bending strength data were ordered and associated, one by one, to survival probability equal to $P_{s,j} = [(j - 0.3)/(N + 0.4)]$, where j is the number of the sample and N is the total number of samples. The Weibull modulus (m) and the characteristic strength (σ_0^{4pt}) were then calculated by linear regression of strength and probability data in a $\ln[\ln(1/Ps)]/\ln \sigma$ graph) (Barsoum, 2003). Furthermore, the equivalent strength for three-point configuration was estimated by applying scaling equations based on Weibull modulus, with hypothesis of flaws occurring with a volume (Vf) or surface (Sf) distribution (Quinn, 2003).

Porosity

The porosity of the dense glass-ceramics was estimated by using the software ImageJ ("ImageJ") on scanning electron microscopy images binarized by a proper threshold.

3.2.3. Characterisation of panels

FTIR analysis

Fourier-transform infrared spectra (FTIR) were assessed with Jasco 4200 FTIR spectrometer (Jasco, Japan) equipped with an attenuated total reflection (ATR) attachment (ZnSe crystal) on finely crushed samples. In the case of Plasmastone-based porous materials (Chapter 5), the FTIR spectra was measured using a FTIR model 2000 (Perkin Elmer Waltham, MA).

The developed foams were firstly cut into cubes of approximate dimensions of 10 mm x 10 mm x 10 mm. These samples were then applied for mechanical and morphological characterisation, as well as for densities measurements.

Density measurement

The bulk density of the foams was calculated by weight-to-volume ratio of each foam: the mass of the cube was measured by using a digital balance, while the volume of the sample was calculated by measuring the lengths of the cube with a caliper. The true density of the finely crushed powder and the apparent density of the foams were measured by He gas pycnometer (Micromeritics AccuPyc 1330, Norcross, GA). The true density ideally refers to the density of the solid without any pore and the apparent density ideally refers to the density of the solid still comprising closed cells.

Mechanical properties

The compressive strength of the foams was determined by using an Instron 1121 UTM (Instron Danvers, MA). The mechanical test was performed at room temperature with a cross-head speed of 1 mm/min. In general, 5 to 12 individual tests were conducted for each group of samples.

Furthermore, the bending strength of the solid phase (σ_{bend}) was estimated, according to the Gibson-Ashby model (see Chapter 2) (Gibson and Ashby, 1999) for the scaling of compressive strength with relative density. The relative density was defined as 1-(P/100), where P refers to the total porosity of foams. The shape factor ϕ (amount of solid at the cell edges) was assumed to be equal to 1, for foams with limited closed porosity.

Conductivity and relative permittivity

In Chapter 7, the conductivity of foams fired in nitrogen was assessed on disc samples (diameter in the range 35 - 55 mm and height in the range 5.6 - 8.2 mm). As indicated by Figure 3-1a, upper and lower areas were first painted with a silver conductive paint (SCP) in order to form about two parallel conductive layers and then connected with electrical wires, by means of copper tape with conductive adhesive (3M Copper Foil Tape 1181). Figure 3-1b shows the

equivalent model of the electrical configuration applied in the analysis: an inductance L, due to the thread connections, in series with a parallel between a resistance R and a capacitance C, due to the cylindrical sample put between parallel layers.

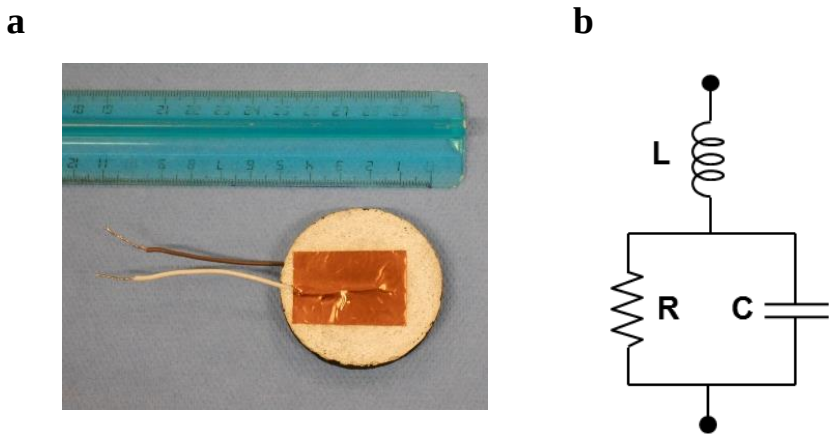

Figure 3-1. a) Sample coated with conductive paint and connected with threads: b) equivalent electrical model.

The DC value of R was measured by means of a Fluke 23 III multimeter. A GW INSTEK LCR-819 precision LCR meter (frequency range: 12 Hz – 100 kHz) and an Agilent 4285 precision LCR meter (frequency range: 75 kHz – 30 MHz) were used for AC measurements. The measured resistance R, given the geometry of the samples and according to Ohm's law, provided an estimation of the electrical conductivity. The measured capacitance C, given the geometry and by applying the relation of parallel plates capacitor configuration, provided an estimation of the relative permittivity.

3.2.4. Characterisation of lightweight aggregates

The particle density and water absorption of the aggregates was measured after a soaking period of 24h, following the EN 1097-6.

The particle size distribution of the aggregates was measured by Dynamic Image Analysis (Haver CPA 3-2, HAVER & BOECKER, Germany).

4. References

Barsoum, M.W., 2003. Fundamentals of ceramics. Inst. Phys. Publ.

Bernardo, E., Esposito, L., Rambaldi, E., Tucci, A., 2011. Sintered glass ceramic articles from plasma vitrified asbestos containing waste. Adv. Appl. Ceram. 110, 346–352. https://doi.org/10.1179/1743676111y.0000000020

Bernardo, E., Esposito, L., Rambaldi, E., Tucci, A., Pontikes, Y., Angelopoulos, G.N., 2009. Sintered esseneite-wollastonite-plagioclase glass-ceramics from vitrified waste. J. Eur.

Ceram. Soc. 29, 2921–2927. https://doi.org/10.1016/j.jeurceramsoc.2009.05.017

Bernardo, E., Scarinci, G., 2004. Sintering behaviour and mechanical properties of Al2O3 platelet-reinforced glass matrix composites obtained by powder technology. Ceram. Int. 30, 785–791. https://doi.org/10.1016/j.ceramint.2003.09.013

Directive 2003/33/EC, 2003. , Official Journal of the European Communities.

Gibson, L.J., Ashby, M.F., 1999. Cellular solids: structure and properties. Cambridge University Press, Cambridge, UK.

Höland, W., Beall, G.H., 2012. Glass-Ceramic Technology. John Wiley & Sons, Inc., Hoboken, NJ, USA.

ImageJ. https://imagej.nih.gov/ij/ (accessed 7.20.06).

Machiels, L., Arnout, L., Yan, P., Jones, P.T., Blanpain, B., Pontikes, Y., 2017. Transforming Enhanced Landfill Mining Derived Gasification/Vitrification Glass into Low-Carbon Inorganic Polymer Binders and Building Products. J. Sustain. Metall. 3, 405–415. https://doi.org/10.1007/s40831-016-0105-1

Maschio, A., Bernardo, E., Desideri, D., Marangoni, M., Ponsot, I., Pontikes, Y., 2016. Shielding effectiveness of construction materials. Int. J. Appl. Electromagn. Mech. 52, 137–144. https://doi.org/10.3233/JAE-162089

Norm EN 12457-4, 2002.

Ponsot, I.M.M.M., Pontikes, Y., Baldi, G., Chinnam, R.K., Detsch, R., Boccaccini, A.R., Bernardo, E., 2014. Magnetic glass ceramics by sintering of borosilicate glass and inorganic waste. Materials (Basel). 7, 5565–5580. https://doi.org/10.3390/ma7085565

Quinn, G.D., 2003. Standardized Rectangular Flexure Specimens. J. Am. Ceram. Soc. 10, 508–510.

Rincón, A., Desideri, D., Bernardo, E., 2018. Functional glass-ceramic foams from ‘inorganic gel casting’ and sintering of glass/slag mixtures. J. Clean. Prod. 187, 250–256. https://doi.org/10.1016/j.jclepro.2018.03.065

Rincón, A., Giacomello, G., Pasetto, M., Bernardo, E., 2017. Novel ‘inorganic gel casting’ process for the manufacturing of glass foams. J. Eur. Ceram. Soc. 37, 2227–2234. https://doi.org/10.1016/j.jeurceramsoc.2017.01.012

RIS - Recycling-Baustoffverordnung (Austrian Recycling Building Materials Ordinance) https://www.ris.bka.gv.at/GeltendeFassung.wxe?Abfrage=Bundesnormen&Gesetzesnummer=20009212 (accessed 4.11.19).

Scanarc, 2017.

Tamburrano, A., Desideri, D., Maschio, A., Sabrina Sarto, M., 2014. Coaxial waveguide methods for shielding effectiveness measurement of planar materials Up to 18 GHz. IEEE Trans. Electromagn. Compat. 56, 1386–1395. https://doi.org/10.1109/TEMC.2014.2329238

PART III - Valorisation of Plasmastone

Chapter 4. Dense Plasmastone-based glass-ceramics by sinter-crystallisation

This chapter was based on: P. Rabelo Monich, D. Vollprecht, E. Bernardo, Dense glass-ceramics by fast sinter-crystallisation of mixtures of waste-derived glasses, International Journal of Applied Ceramic Technology (2019). DOI: 10.1111/ijac.13332

4.1. Introduction

In this chapter, Plasmastone was valorised into dense glass-ceramics to be applied as tiles. The dense glass-ceramics were produced by cold pressing and sinter-crystallisation of Plasmastone mixed with different amounts of recycled soda-lime glass. Kaolin clay was also added as a binder after optimisation of the composition. Based on the results of water absorption (which is related to the amount of residual open porosity) and density of the dense glass-ceramics, several optimisations regarding the composition and the heating treatment were performed. These optimisations were done in order to improve the properties of the dense materials and to apply an approach more compatible to the ceramic industry. The optimised glass-ceramic samples were finally characterised by means of mechanical tests, environmental impact assessment and physical and morphological analyses. Further characterisations were also done in glass-ceramics fired at lower temperature (800 °C): despite presenting low mechanical properties, firing at low temperature was found to maximise the precipitation of magnetite, which could in turn bring novel functionalities to the dense glass-ceramics (Chinnam et al., 2013), as mentioned in Chapter 2.

4.2. Experimental procedure

The dense glass-ceramics were made by uniaxially pressing at 50 MPa fine powders of pure Plasmastone (particle size smaller than 75 μm) or Plasmastone mixed with soda-lime glass (mean particle size of 30 μm). Soda-lime glass was added in the following quantities: 10 wt%, 20 % or 50 wt%.

The samples were fired at 800 °C, 900 °C or 1000 °C, with different heating rates (10 °C/min or 40 °C/min), different holding times (30 min or 60 min) and different cooling rates (normal cooling of the furnace or fast cooling induced by opening the furnace door after the thermal treatment was completed). Furthermore, dense samples made with a fine mixture of powders of 45 wt% Plasmastone/45 wt% soda-lime glass/10 wt% kaolin clay were also produced. In this case, kaolin clay was firstly mixed with distilled water (40 wt% of the total solid content) using a mechanical stirrer at 400 rpm. Thereafter, Plasmastone and soda-lime glass were added to the suspension, which was then mixed for 30 minutes and dried overnight at 75 °C. After drying, the powder mixture was milled with an agate mortar and sieved below 125

µm. The fine powder mixture was finally pressed at 50 MPa and dried overnight at 75 °C before firing.

4.3. Results and discussion

The DTA (Figure 4-1a) performed on fine (<75 µm) and on coarse (1 mm) Plasmastone powders indicates the first crystallisation peak (T_c) shifted to lower temperatures with particle size reduction. This indicates that Plasmastone is sensitive to surface crystallisation (Rincón et al., 2016). Furthermore, fine Plasmastone powder presents three crystallisations peaks: T_c at 800 °C, and two other crystallisation peaks around 900 °C and 1050 °C. These findings were used as a reference for the firing experiments made with Plasmastone-derived materials. Finally, the glass transition temperature (T_g) of fine Plasmastone lies around 625 °C, which is quite close to T_c. This indicates the high crystallisation tendency of Plasmastone upon firing (Karamanov et al., 2000), which may hinder sintering by viscous flow (Rincón et al., 2016).

The TGA curve (Figure 4-1b) performed on fine powder of Plasmastone shows a weight gain of around 1.5 wt% after 530 °C. This weight gain can be attributed to the oxidation of Fe^{2+} into Fe^{3+} (Karamanov et al., 2000; Marangoni et al., 2016). Furthermore, this effect is promoted by the high surface-to-volume ratio of the fine Plasmastone powder (Marangoni et al., 2016).

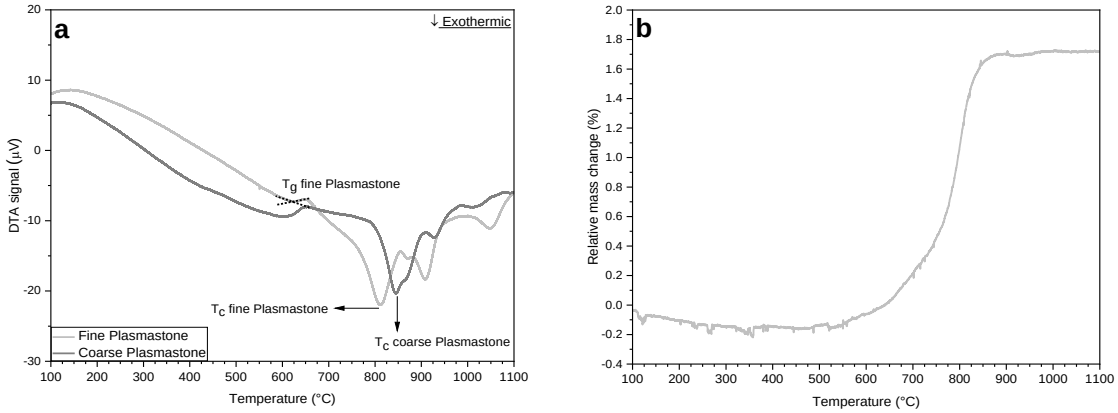

Figure 4-1. DTA (a) and TGA (b) curves of Plasmastone.

Figure 4-2 illustrates the optimisations made to produce dense Plasmastone derived glass-ceramics based on the water absorption and density of the samples. These optimisations were made regarding firstly the firing temperature (Figure 4-2a), then the addition of soda-lime glass combined with firing at two different temperatures (Figures 4-2b and c) and finally the heating treatment (Figure 4-2d). In the case of Plasmastone samples (Figure 4-2a), the increase in firing temperature indicates a slight improvement in densification: by enhancing the firing temperature from 800 °C to 1000 °C, the density increased 10%. However, the water absorption for the Plasmastone samples fired at 1000 °C (12.89%) was still too high for tiles, which should be

below 2%, for optimised frost resistance (Rincón et al., 2016). The densification of pure Plasmastone samples was affected by the high crystallisation tendency of Plasmastone, which hindered viscous flow during firing, thus affecting the densification of the material. Furthermore, the oxidation of Fe^{2+} (as indicated in Figure 4-1b) may also increase the viscosity of the liquid glass phase, thus affecting the densification of Plasmastone (Karamanov et al., 2014, 2004).

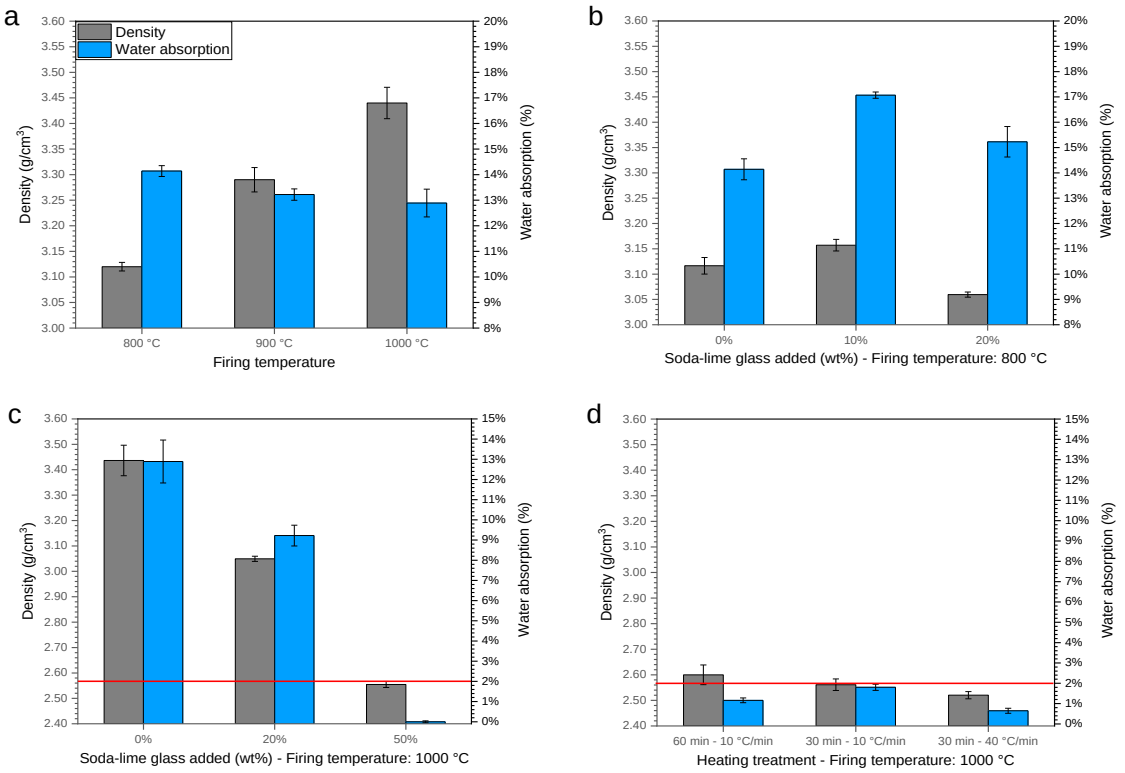

Figure 4-2. Water absorption and density measurements of: a) Plasmastone fired at different temperatures; b) Plasmastone mixed with different contents of soda-lime glass, fired at 800 °C; c) Plasmastone mixed with different contents of soda-lime glass, fired at 1000 °C; d) 45 wt% Plasmastone/45 wt% soda-lime glass/10 wt% kaolin clay samples, fired at 1000 °C with different heating treatments.

Recycled soda-lime glass was then mixed with Plasmastone in order to promote viscous flow (Bernardo et al., 2010). The addition of up to 20 wt% soda-lime glass followed by firing at 800 °C (Figure 4-2b) or 1000 °C (Figure 4-2c) was not enough to obtain dense samples with low water absorption, despite some changes with firing temperature. The optimal content of soda-lime glass to be mixed with Plasmastone was found to be 50 wt%: as exhibited by Figure 4-2c, samples with nearly zero water absorption could be finally developed with addition of 50 wt% soda-lime glass, followed by firing at 1000 °C. In this case, there was also a decrease in density. This could be firstly attributed to simple density variations of the glasses (soda-lime glass is lighter than Plasmastone: 2.5 g/cm^3 against 3.1 g/cm^3). Secondly, the contribution from

bloating must also be considered: at higher temperatures, Fe^{3+} can be partially reduced to Fe^{2+}, releasing oxygen which may remain trapped inside the viscous mass, thus decreasing the sample density (Appendino et al., 2004). This phenomenon may have been more evident for 50 wt% Plasmastone/50 wt% soda-lime glass samples fired at 1000 °C, as the quantity of glass phase was greater and less viscous, which enhanced the medium available for foaming (Ponsot et al., 2014).

After selecting the optimal quantity of soda-lime glass to be mixed with Plasmastone, 10 wt% kaolin clay was also added as a binder in order to improve the pressing step and to reduce demoulding flaws (Marangoni et al., 2014). Figure 4-2d shows that the samples fired following a slower heating schedule (10 °C/min, holding time of 60 min) presented water absorption of 1.16%. Thereafter, other optimisations (Figure 4-2d) were performed in order to apply a thermal treatment comparable to the one applied by the ceramic industry. Firstly, the holding time was reduced from 60 min to 30 min, which increased the water absorption to 1.80%. Then, the heating and cooling rates were increased in order to simulate industrial production (Marangoni et al., 2014). Fast heating treatments are more economical, and, in this case, the water absorption was decreased to 0.65%. Higher heating rates can prevent extensive crystallisation upon heating, thus promoting viscous flow and decreasing the water absorption of the samples (Bernardo, 2008; Karamanov et al., 2003; Lu et al., 2014). Based on these results, the group of samples 45 wt% Plasmastone/45 wt% soda-lime glass/10 wt% kaolin clay fired at 1000 °C fired following a fast heating and cooling rate was considered the optimal one and applied for most of the following characterisations.

The X-ray diffraction patterns (Figure 4-3) illustrate the phase evolution taking place upon firing. In the case of pure Plasmastone (Figure 4-3a), it can be observed that this material presents the characteristic amorphous 'halo' of glasses. Once this vitrified residue is fired, Plasmastone is prone to crystallisation, as previously indicated by Figure 4-1a. Plasmastone samples fired at 800 °C present signals mainly consistent to those of Ca-Fe rich pyroxene (hedenbergite, $Ca(Fe_{0.821}Al_{0.179})(SiAl_{0.822}Fe_{0.178}O_6)$, PDF#78-1546). For firing above 900 °C, andradite ($Ca_3Fe_2(SiO_4)_3$, PDF#84-1935) was also detected. This indicates that the first peak in DTA (Figure 4-1a) is most probably attributed to the crystallisation of pyroxenes while the second peak (at around 900 °C) refers to the crystallisation of andradite.

The addition of soda-lime glass promoted the precipitation of wollastonite ($CaSiO_3$, PDF#84-0655), already in samples fired at 800 °C (Figure 4-3b). For samples fired at 1000 °C (Figure 4-3c), the introduction of 50 wt% soda-lime glass decreased the crystallisation of Ca-Fe silicates. In fact, signals consistent to those of andradite are extremely weak for Plasmastone/soda-lime glass samples. Regarding the sample made with 45 wt% Plasmastone/45 wt% soda-lime glass/10 wt% kaolin clay and fired at 1000 °C, quartz (SiO_2, PDF#83-0539) and

cristobalite (SiO_2, PDF#89-3607) were also detected, probably due to contaminations of kaolin clay.

Finally, peaks of the Ca-Fe silicates phases overlapped with those of hematite "H" (Fe_2O_3, PDF#89-2810) and magnetite "M" (Fe_3O_4, PDF#89-0691). The presence of magnetite for samples fired at 800 °C (Figures 4-3a and b) cannot be excluded, as these samples were attracted by a permanent magnet.

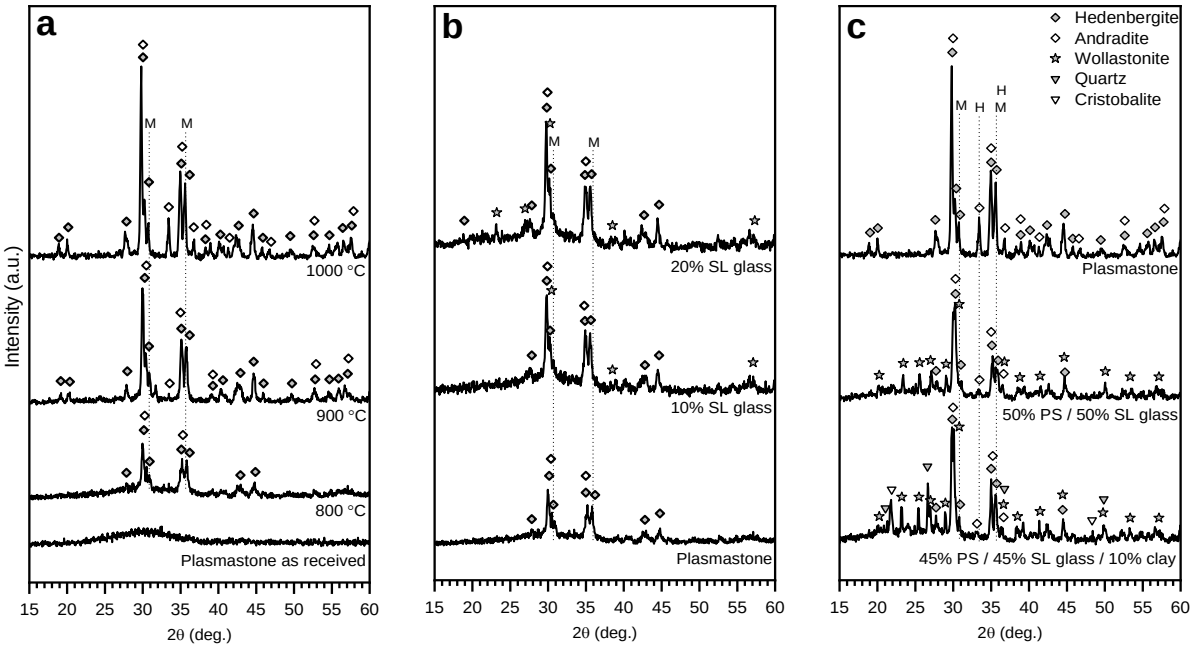

Figure 4-3. XRD patterns of a) Plasmastone as received and fired at 800 °C, 900 °C or 1000 °C; b) Plasmastone-derived glass-ceramics fired at 800 °C; c) Plasmastone-derived glass-ceramics fired at 1000 °C.

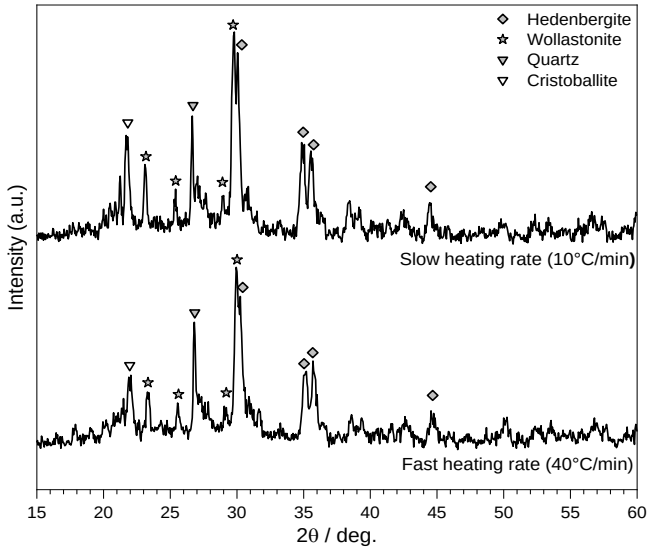

Figure 4-4. 45 wt% Plasmastone/45 wt% soda-lime glass/10 wt% kaolin clay fired at 900 °C for 5 min at different heating rates.

Figure 4-4 presents the XRD patterns made on 45 wt% Plasmastone/45 wt% soda-lime glass/10 wt% kaolin clay samples fired at 900 °C for 5 minutes, by fast (40 °C/min) or slow heating rate (10 °C/min). These thermal treatments were done in order to support the data presented on Figure 4-2d, which shows that water absorption was affected by the heating rate. Indeed, the XRD patterns show that crystallisation of hedenbergite and wollastonite is slightly promoted when applying a slow heating rate (when one considers the difference of heights of the peaks). On the other hand, when a fast heating rate is applied, crystallisation is more hindered, thus promoting viscous flow. This results in samples more densified, with lower water absorption, as observed in Figure 4-2d.

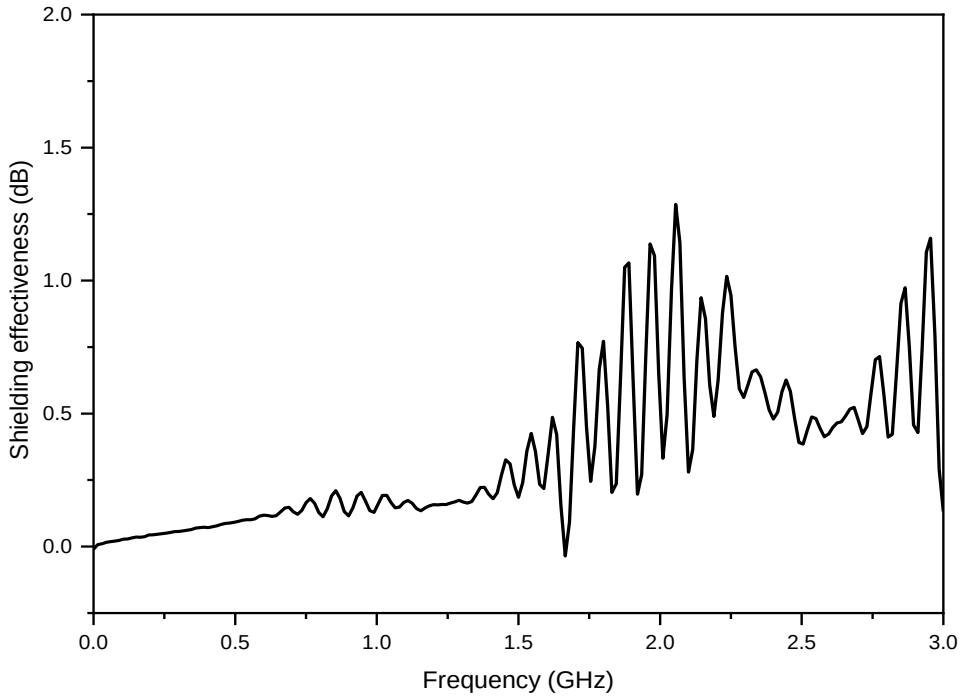

Figure 4-5. Electromagnetic shielding effectiveness made on hollow cylindrical samples (external diameter of 34.3 mm, internal diameter of 7 mm and thickness of 5.2 mm) of 90% Plasmastone/10% soda-lime glass fired at 800 °C.

In order to explore the magnetic behaviour of the dense samples, shielding effectiveness was measured on sample made with 90 wt% Plasmastone/10 wt% soda-lime glass and fired at 800 °C (Figure 4-5). This sample was selected for electromagnetic shielding studies, as it was attracted by a permanent magnet. The measured shielding effectiveness was particularly low (below 1 dB) for lower frequencies. This preliminary study indicates that Plasmastone-based samples made with lower content of soda-lime glass and fired at lower temperature present indeed exhibited some magnetic behaviour. However, other optimisations would then need to be

applied in order to increase the electromagnetic shielding of this group of samples (e.g. firing under an inert atmosphere).

The mechanical properties of the optimised sample and of dense materials fired at a lower temperature with less soda-lime glass are presented in Table 4-1. The results indicate that the optimised sample presents properties similar to other commercial tiles: the elastic modulus is comparable to the one of a commercial porcelain stoneware (Buchner et al., 2011). In addition, the scaling of strength estimated that the equivalent strength σ_{eq}^{3pt} in a three-point configuration of the optimised sample with standard geometry (cross-section of 3 mm x 4 mm and loading span of 40 mm) is 76 MPa, while the equivalent strength for bigger tiles σ_{eq}^{L} (cross-section of 8 mm x 300 mm and loading span of 300 mm) is above the lower strength limit (35 MPa) for tiles of the BI_a group (*BS EN 14411:2016*). Moreover, the specific bending strength for the optimised sample was 16 MPa cm^3/g (considering σ_{eq}^{L}), which is much superior than the one required by the Milestones (see Chapter 1). Regarding the materials fired at 800 °C made with 10 wt% or 20 wt% soda-lime glass, the mechanical properties were much lower. However, one must consider that the bending strength is comparable to the reference minimum value (15 MPa for tiles with thickness below 7.5 mm) of highly porous tiles from the BIII group (*BS EN 14411:2016*).

Table 4-1. Physical and mechanical properties of Plasmastone derived glass-ceramics.

Group of samples	Elastic modulus (GPa)	*M*	Strength (MPa)[1]		
			σ_0^{4pt}	σ_{eq}^{3pt}	σ_{eq}^{L}
45 wt% Plasmastone/45 wt% soda-lime glass/10 wt% kaolin clay	76.8 ± 2.5	10.9	69.8	76.6^{Vf}	39.3^{Vf}
				76.4^{Sf}	43.1^{Sf}
80 wt% Plasmastone/20 wt% soda-lime glass, fired at 800 ° C	48.5 ± 4.5	7.4	20.0	22.8^{Vf}	8.6^{Vf}
				22.6^{Sf}	9.8^{Sf}
90 wt% Plasmastone/10 wt% soda-lime glass, fired at 800 ° C	38.9 ± 2.5	4.7	13.1	15.6^{Vf}	3.3^{Vf}
				15.1^{Sf}	4.0^{Sf}

A series of other types of characterisations were also done on the optimised sample, due to a better performance in the mechanical tests, combined with low water absorption: the microhardness was equal to 5.3 ± 0.04 GPa, which is similar to the micro-hardness of other waste-derived glass-ceramics (Bernardo and Dal Maschio, 2011; Ponsot et al., 2014). Furthermore, the coefficient of thermal expansion was equal to 9.5 10^{-6} $°C^{-1}$, which was also found to be comparable to the ones already measured in waste derived glass-ceramic materials (Bernardo and Dal Maschio, 2011).

[1] Standard deviation is not mentioned, as we applied Weibull statistics in order to consider the size dependance of bending strength.

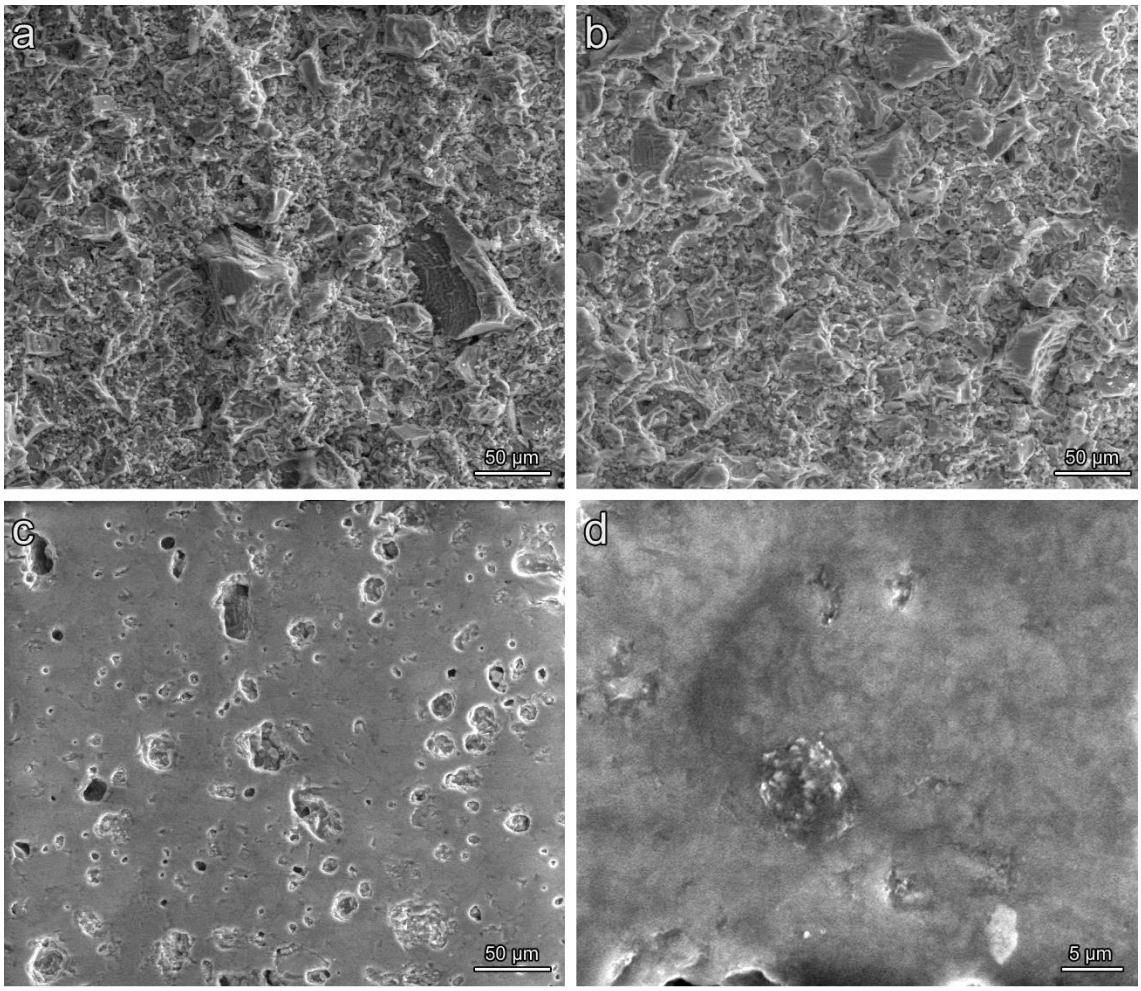

Figure 4-6. Micrographs of Plasmastone derived glass-ceramics: a) 90 wt% Plasmastone/10 wt% soda-lime glass fired at 800 °C; b) 80 wt% Plasmastone/20 wt% soda-lime glass fired at 800 °C; c and d) optimised sample.

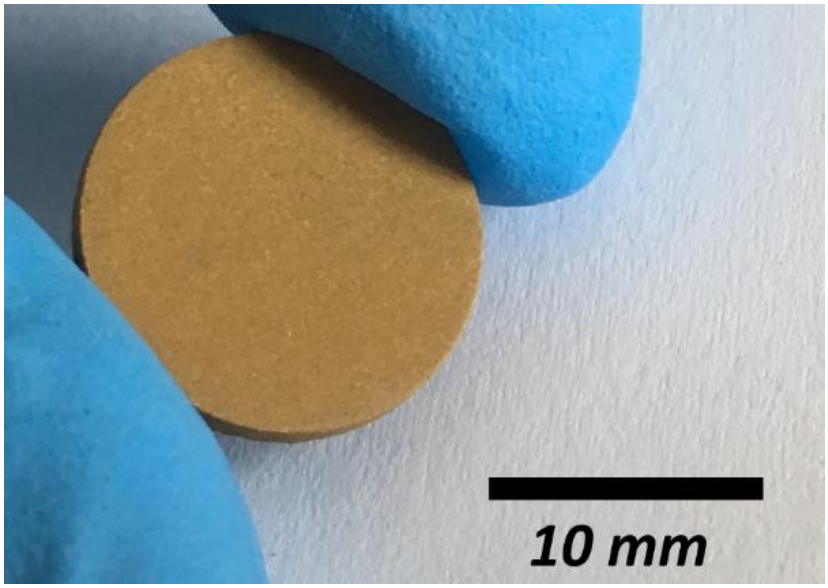

Figure 4-7. Aesthetic appearance of the optimise waste-derived glass-ceramic.

The micrographs of Plasmastone/soda-lime glass samples fired at lower temperature (Figures 4-6a and b) help to understand their low mechanical performance: these groups of samples were poorly densified, as already indicated by the water absorption results (see Figure 4-2b). In contrast, the optimised sample (Figures 4-6c and d) was well densified by viscous flow, with an estimated porosity equal to 5%. Furthermore, the presence of coarser pores indicates that the bloating phenomenon took place upon heating (Appendino et al., 2004), as previously mentioned. Finally, the appearance of the optimise waste-derived glass-ceramic can be seen in Figure 4-7.

Leaching test (Table 4-2) was done on the optimised sample, in order to assess its chemical stability, as well as on a commercial tile for control. The results indicate that the optimised sample is within the Austrian regulation for classes U-A and U-B (quality classes for recycled construction materials used in unbound or hydraulically/bituminously bound applications as aggregate) with respect to leachate content, even if the total contents of Cu, Cr and Ni exceeded the Austrian limit values for recycled building materials. On the other hand, the optimised sample cannot be classified as Class D (relevant for slags) due to high quantity of Mo leached. In addition, the control sample cannot be classified as Class D either, due to leaching values of Co and W above the ones accepted by Class D.

Table 4-2. Leaching test results of the control and optimised samples (mg/kg DM).

	Austrian regulation			**Control sample**	**Optimised sample**
	U-A	**U-B**	**D**		
Cr	0.6	1.0	0.3	0.017	0.088
Cu	1.0	2.0		0.19	0.33
Ni	0.4	0.6		0.042	0.019
Cl	800	1000		5.9	3.4
SO_4	2500	6000		19	32
Ba			20	0.029	0.13
Cd			0.04	0.001	0.0015
Co			1	2.9	0.018
Mo			0.5	0.12	1.5
Tl			0.1	<0.0010	0.0041
V			1	0.26	0.064
W			1.5	2.8	0.18
F			10	4.2	2.6

In order to understand better the relation between mineralogical phases and leaching, the optimised sample was analysed in an electron microprobe. Firstly, the phases of the samples

were identified (Figure 4-8) based on the measured chemical composition of a determined area and on the XRD pattern of 45 wt% Plasmastone/45 wt% soda-lime glass/10 wt% kaolin clay fired at 1000 °C (Figure 4-3c). Figure 4-8 shows that the crystalline phases are embedded in the residual glass phase, which aids in sealing hedenbergite (‘1’). Silica (‘3’) and iron oxide (‘4’) were also identified. The residual glass/wollastonite zone is indicated by ‘2’ in Figure 4-8, where it is possible to see the needle-shaped crystals attributed to wollastonite embedded in the residual glass phase. Finally, the porosity is closed and similar to the one of ceramic tiles.

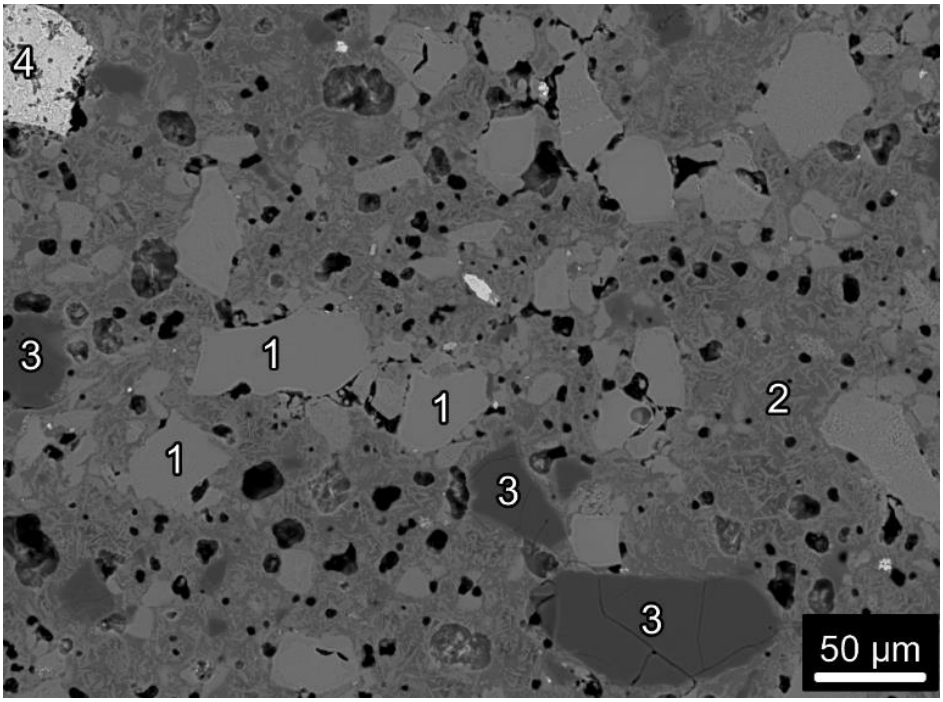

Figure 4-8. Micrograph of the optimised sample: 1) hedenbergite; 2) glass/wollastonite zone; 3) silica; 4) iron oxide.

Table 4-3. Results of the electron microprobe analyses performed on the optimised sample.

Phase	Mo (%)	Fe (%)	Cu (%)	Ba (%)	Zn (%)	V (%)	Cr (%)
1. Hedenbergite	0.01	13.3	0.20	0.03	0.06	0.04	0.13
2. Residual glass/wollastonite	0.03	3.50	0.25	0.03	0.05	0.01	0.03
3. Silica	0.01	0.18	0.01	0.00	0.00	0.00	0.00
4. Iron Oxide	0.00	62.1	0.41	0.00	0.03	0.02	0.10

After the identification of the phases, several metals were quantified by electron microprobe analyses (Table 4-3). The results of this study help to understand the low leaching of heavy metals due to their incorporation in stable mineral phases: Cu is mainly present in iron oxide, which is consistent to the incorporation of Cu in this phase (Piatak and Seal, 2012). Cr and V,

on the other hand, were bonded among hedenbergite, a chemical stable phase (Pisciella et al., 2001). Indeed, examples of the incorporation of these metals in pyroxenes can be found in the literature (Karner et al., 2008; Lottermoser, 2002; Simon et al., 2007). Furthermore, Zn and Ba are evenly distributed among hedenbergite and the glass/wollastonite zone (it was not possible to perform the quantitative analysis separately in these phases, due to the insufficient spatial resolution of the electron microprobe). Finally, Mo was mainly present among the glass/wollastonite zone. The high leaching of this metal (above Class D) may be associated to the crystallisation of wollastonite during firing (as observed in Figure 4-3c), which increased the alkali content of the residual glass phase. This can favour network dissolution, releasing pollutants such as Mo (Bunker, 1994).

4.4. Conclusions

Dense Plasmastone/soda-lime glass/kaolin clay glass-ceramics could be produced by cold-pressing and fast sinter-crystallisation. These samples presented low water absorption, low leachability and high mechanical properties when compared to commercial ceramic tiles. These results indicate that Plasmastone mixed with soda-lime glass and kaolin clay may be valorised into tiles, with a possible commercial exploitation.

In addition, the high amount of iron oxide in Plasmastone was responsible for two effects in the dense glass-ceramic: firstly, crystallisation was promoted thus affecting sintering by viscous flow. Secondly, bloating was favoured in samples with a higher quantity of glass phase with low viscosity, thus decreasing the density of the sample.

Finally, the addition of soda-lime glass as well as optimisations regarding the thermal treatment were applied in order to produce dense samples with quite low water absorption, by promoting sintering by viscous.

4.5. References

Appendino, P., Ferraris, M., Matekovits, I., Salvo, M., 2004. Production of glass-ceramic bodies from the bottom ashes of municipal solid waste incinerators. J. Eur. Ceram. Soc. 24, 803–810. https://doi.org/10.1016/S0955-2219(03)00264-4

Bernardo, E., 2008. Fast sinter-crystallization of a glass from waste materials. J. Non. Cryst. Solids 354, 3486–3490. https://doi.org/10.1016/j.jnoncrysol.2008.03.021

Bernardo, E., Bonomo, E., Dattoli, A., 2010. Optimisation of sintered glass-ceramics from an industrial waste glass. Ceram. Int. 36, 1675–1680. https://doi.org/10.1016/j.ceramint.2010.02.047

Bernardo, E., Dal Maschio, R., 2011. Glass-ceramics from vitrified sewage sludge pyrolysis residues and recycled glasses. Waste Manag. 31, 2245–2252. https://doi.org/10.1016/j.wasman.2011.06.018

BS EN 14411:2016 - Ceramic tiles — Definition, classification, characteristics, assessment and verification of constancy of performance and marking, 2016.

Buchner, S., Mikowski, A., Lepienski, C.M., Ferreira, E.B., Zanotto, E.D., Torres, R.D., Soares, P., 2011. Mechanical and tribological properties of a sintered glass-ceramic compared to granite and porcelainized stoneware. Wear 271, 875–880. https://doi.org/10.1016/j.wear.2011.03.022

Bunker, B.C., 1994. Molecular mechanisms for corrosion of silica and silicate glasses. J. Non. Cryst. Solids 179, 300–308. https://doi.org/10.1016/0022-3093(94)90708-0

Chinnam, R.K., Francis, A.A., Will, J., Bernardo, E., Boccaccini, A.R., 2013. Review. Functional glasses and glass-ceramics derived from iron rich waste and combination of industrial residues. J. Non. Cryst. Solids 365, 63–74. https://doi.org/10.1016/j.jnoncrysol.2012.12.006

Karamanov, A., Maccarini Schabbach, L., Karamanova, E., Andreola, F., Barbieri, L., Ranguelov, B., Avdeev, G., Lancellotti, I., 2014. Sinter-crystallization in air and inert atmospheres of a glass from pre-treated municipal solid waste bottom ashes. J. Non. Cryst. Solids 389, 50–59. https://doi.org/10.1016/j.jnoncrysol.2014.02.009

Karamanov, A., Pelino, M., Hreglich, A., 2003. Sintered glass-ceramics from Municipal Solid Waste-incinerator fly ashes-part I: The influence of the heating rate on the sinter-crystallisation. J. Eur. Ceram. Soc. 23, 827–832. https://doi.org/10.1016/S0955-2219(02)00210-8

Karamanov, A., Pisciella, P., Cantalini, C., Pelino, M., 2000. Influence of Fe^{3+}/Fe^{2+} Ratio on the Crystallization of Iron-Rich Glasses Made with Industrial Wastes. J. Am. Ceram. Soc. 83, 3153–3157. https://doi.org/10.1111/j.1151-2916.2000.tb01697.x

Karamanov, A., Taglieri, G., Pelino, M., 2004. Sintering in nitrogen atmosphere of iron-rich glass-ceramics. J. Am. Ceram. Soc. 87, 1354–1357. https://doi.org/10.1111/j.1151-2916.2004.tb07734.x

Karner, J.M., Papike, J.J., Sutton, S.R., Shearer, C.K., Burger, P., McKay, G., Le, L., 2008. Valence state partitioning of V between pyroxene-melt: Effects of pyroxene and melt composition, and direct determination of V valence states by XANES. Application to Martian basalt QUE 94201 composition. Meteorit. Planet. Sci. 43, 1275–1285. https://doi.org/10.1111/j.1945-5100.2008.tb00697.x

Lottermoser, B.G., 2002. Mobilization of heavy metals from historical smelting slag dumps, north Queensland, Australia. Mineral. Mag. 66, 475–490. https://doi.org/10.1180/0026461026640043

Lu, J., Lu, Z., Peng, C., Li, X., Jiang, H., 2014. Influence of particle size on sinterability, crystallisation kinetics and flexural strength of wollastonite glass-ceramics from waste glass and fly ash. Mater. Chem. Phys. 148, 449–456.

https://doi.org/10.1016/j.matchemphys.2014.08.013

Marangoni, M., Arnout, L., Machiels, L., Pandelaers, L., Bernardo, E., Colombo, P., Pontikes, Y., Jantzen, C., 2016. Porous, Sintered Glass-Ceramics from Inorganic Polymers Based on Fayalite Slag. J. Am. Ceram. Soc. 99, 1985–1991. https://doi.org/10.1111/jace.14224

Marangoni, M., Ponsot, I., Kuusik, R., Bernardo, E., 2014. Strong and chemically inert sinter crystallised glass ceramics based on Estonian oil shale ash. Adv. Appl. Ceram. 113, 120–128. https://doi.org/10.1179/1743676113Y.0000000132

Piatak, N.M., Seal, R.R., 2012. Mineralogy and environmental geochemistry of historical iron slag, Hopewell Furnace National Historic Site, Pennsylvania, USA. Appl. Geochemistry 27, 623–643. https://doi.org/10.1016/j.apgeochem.2011.12.011

Pisciella, P., Crisucci, S., Karamanov, A., Pelino, M., 2001. Chemical durability of glasses obtained by vitrification of industrial wastes. Waste Manag. 21, 1–9. https://doi.org/10.1016/S0956-053X(00)00077-5

Ponsot, I.M.M.M., Pontikes, Y., Baldi, G., Chinnam, R.K., Detsch, R., Boccaccini, A.R., Bernardo, E., 2014. Magnetic glass ceramics by sintering of borosilicate glass and inorganic waste. Materials (Basel). 7, 5565–5580. https://doi.org/10.3390/ma7085565

Rincón, A., Marangoni, M., Cetin, S., Bernardo, E., 2016. Recycling of inorganic waste in monolithic and cellular glass-based materials for structural and functional applications. J. Chem. Technol. Biotechnol. 91, 1946–1961. https://doi.org/10.1002/jctb.4982

Simon, S.B., Sutton, S.R., Grossman, L., 2007. Valence of titanium and vanadium in pyroxene in refractory inclusion interiors and rims. Geochim. Cosmochim. Acta 71, 3098–3118. https://doi.org/10.1016/j.gca.2007.03.027

Chapter 5. Porous Plasmastone-based glass-ceramics by alkali activation and sinter-crystallisation

This chapter is based on: P. Rabelo Monich, A. Rincon Romero, D. Höllen, E. Bernardo, Porous glass-ceramics from alkali activation and sinter-crystallisation of mixtures of waste glass and residues from plasma processing of municipal solid waste, Journal of Cleaner Production, 188, 871-878 (2018). DOI: 10.1016/j.jclepro.2018.03.167

5.1. Introduction

The previous chapter indicated the possibility of applying Plasmastone as a raw material in the production of dense waste-derived glass-ceramics by cold-pressing and sinter-crystallisation. In this chapter, on the other hand, Plasmastone was applied in the production of porous glass-ceramics by the technique based on alkali activation, followed by gel-casting and firing, which was previously described in Chapter 2.

Plasmastone has already been valorised by means of alkali activation to produce inorganic binders as an alternative to Ordinary Portland Cement (OPC) (Machiels et al., 2017). In contrast to the present study, Plasmastone was submitted to a 'stronger' alkali activation (high amounts of alkali hydroxides or alkali silicates added), leading to a substantial dissolution of the vitrified residue and condensation ('polymerisation') of the dissolution product. After a drying step at 20 °C, it was obtained an alkali-activated mortar (Machiels et al., 2017).

In the present study, however, Plasmastone was submitted to a 'weaker' alkali activation, which did not lead to products directly usable after processing at low temperature, but consisted of a fundamental processing step in the manufacturing of glass-ceramic or glass foams (Rincón et al., 2018; Romero et al., 2018). After alkali activation and the gelation step, it was obtained a 'gelified' slurry with marked pseudo-plasticity, due to the formation of gels just at the surface of glass particles, by partial dissolution. The glass suspension was easily foamed by intensive mechanical stirring (with the help of surfactant) and remained 'frozen' when the stirring stopped, due to viscous resistance. A drying step at low temperature and a firing treatment were then finally applied, thus obtaining a highly porous glass-ceramic.

In addition, it was also necessary to produce foams made with Plasmastone mixed with waste glass powders (soda-lime silicate glass or boro-alumino-silicate glass), in order to improve sintering by viscous flow of the solid phase, as observed in the previous chapter. The Plasmastone-based foams were also fired at different temperatures in order to assess the influence of the firing temperature on the final properties of the material, including porosity, mechanical properties, crystalline phases and chemical stability.

5.2. Experimental procedure

The porous materials were prepared following the technique developed by Rincón et al. (Rincón et al., 2017) (see Chapter 2): firstly, fine powders of Plasmastone and soda-lime glass (quantities of 0-40 wt%) were added to an alkaline solution of 2.5 M NaOH/KOH (ratio 1:1). The overall solid loading content was of 68 wt%. After 3h of partial dissolution at 400 rpm, the slurry was poured in a closed polystyrene mould (60 mm diameter) and cured at 75 °C to undergo hardening (4h for suspension containing only Plasmastone). Thereafter, 4 wt% Triton X-100 (polyoxyethylene octyl phenyl ether – $C_{14}H_{22}O(C_2H_4O)_n$, n = 9–10, Sigma-Aldrich, Gillingham, UK) surfactant, which was selected based on the studies from Strozi et al. (Strozi Cilla et al., 2014) and Rincón et al. (Rincón et al., 2017), was added to the partially 'gelified' slurry. The slurry was then submitted to intensive mechanical stirring at 2000 rpm. The foamed structure was then dried at 40 °C, for 48 h, before being demoulded. A firing treatment was finally applied at 800-1000 °C with a heating rate of 10 °C/min and a holding time of 1h, in order to stabilise the foams (Rincón et al., 2017).

Foams made with Plasmastone mixed with soda-lime glass (SL) or boro-alumino-silicate glass (BAS) were also produced following the same process, but with different hardening times at 75 °C: 3h for soda-lime glass-containing mixtures and 6h for boro-alumino-silicate glass-containing mixtures. In this chapter, these groups of samples will be referred to as XSL for soda-lime glass-containing mixtures, in which X corresponds to the amount of glass mixed with Plasmastone. In the case of BAS-containing mixtures, it was only produced samples made with 70 wt% Plasmastone/30 wt% boro-alumino-silicate glass (30BAS), which were fired at only 1000 °C.

5.3. Results and discussion

The FTIR spectra (Figure 5-1) of activated Plasmastone helps to understand the origin of the hardening mechanism in Plasmastone-based slurries: it is possible to observe an absorption band consisting to C-S-H compounds at around 3400 cm^{-1}, which increases with addition of soda-lime glass. This is most probably attributed to an increase in the CaO content of the system, which promoted the formation of these hydrated compounds. Indeed, not fired foams made by mixtures of soda-lime glass were much easily handled than foams made with only Plasmastone. The not fired foams also present bands corresponding to carbonates (at 1400 cm^{-1}) and also vibrations of C-H bonds (C-H_2 stretch at around 2800 cm^{-1}). This latter band is present due to the addition of surfactant.

The firing treatment led to the disappearance of all mentioned bands, which were also not present in the not-activated glasses. The decomposition of C-S-H compounds and carbonates upon firing may lead to a secondary foaming, contributing to the cellular structure. The

decomposition of surfactants, on the other hand, does not provide any contribution, as the decomposition temperature of Triton is below 400 °C (Rincón et al., 2017).

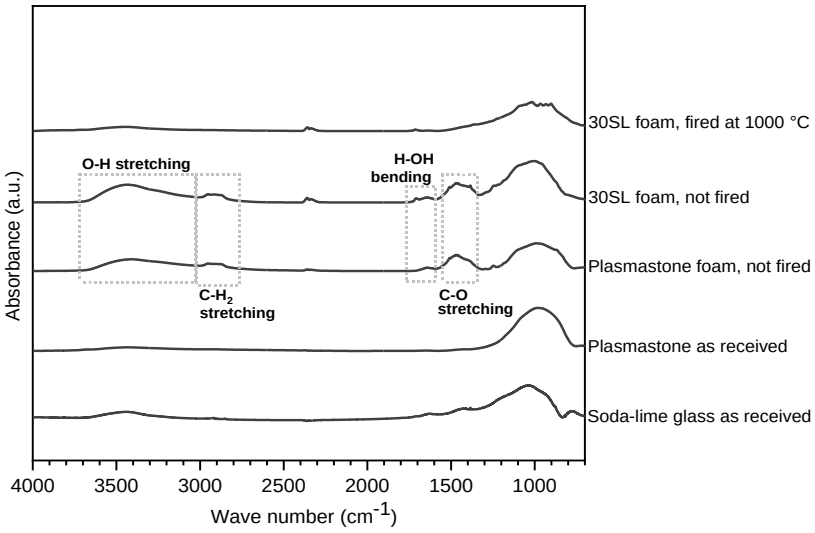

Figure 5-1. FTIR spectra of soda-lime glass, Plasmastone and Plasmastone-derived materials.

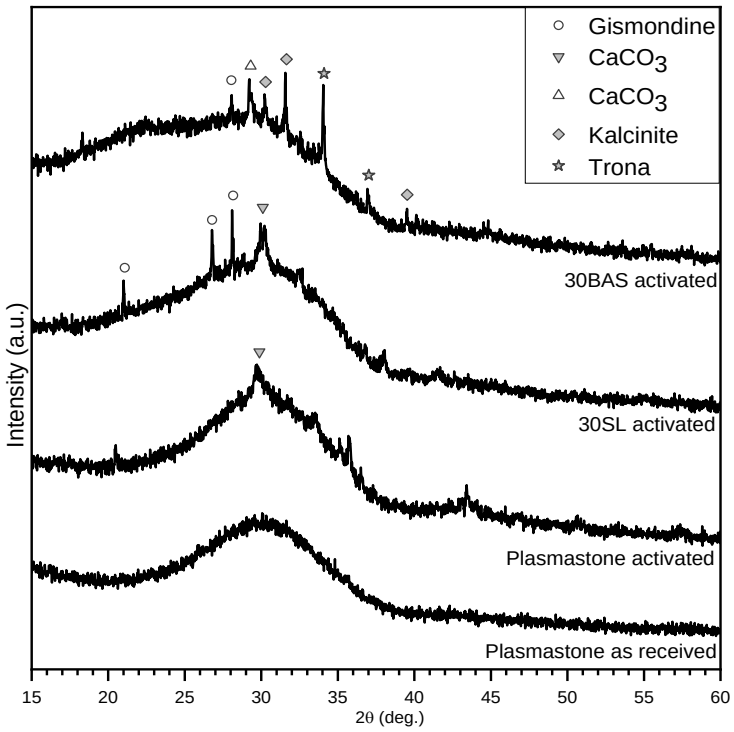

Figure 5-2. XRD patterns of Plasmastone and of green foams.

The XRD patterns of Plasmastone and of not fired foams (Figure 5-2) show that the addition of waste glass improved the formation of more phases on Plasmastone/waste glass mixtures. For Plasmastone pure foams, it was only possible to detect calcium carbonates ($CaCO_3$, PDF#72-

1650), which were also present on 30SL foams. Gismondine ($CaAl_2Si_2O_8 \cdot 4H_2O$, PDF#00-039-1373), which has already been detected by Lancellotti et al. (Lancellotti et al., 2013) in incinerator bottom ash geopolymers, was also present in 30SL. This hydrated phase was also detected in 30BAS, but only in traces. One reason for this could be the higher CaO content in Plasmastone containing soda-lime glass mixtures, which promoted the formation of this phase upon hardening. Finally, besides gismondine, it was also possible to detect another type of calcium carbonate ($CaCO_3$, PDF#86-2342), as well as kalicinite high ($K(HCO_3)$, PDF#01-082-1447) and trona ($Na_3H(CO_3)_2\ (H_2O)_2$, PDF#01-075-1195) on 30BAS foams.

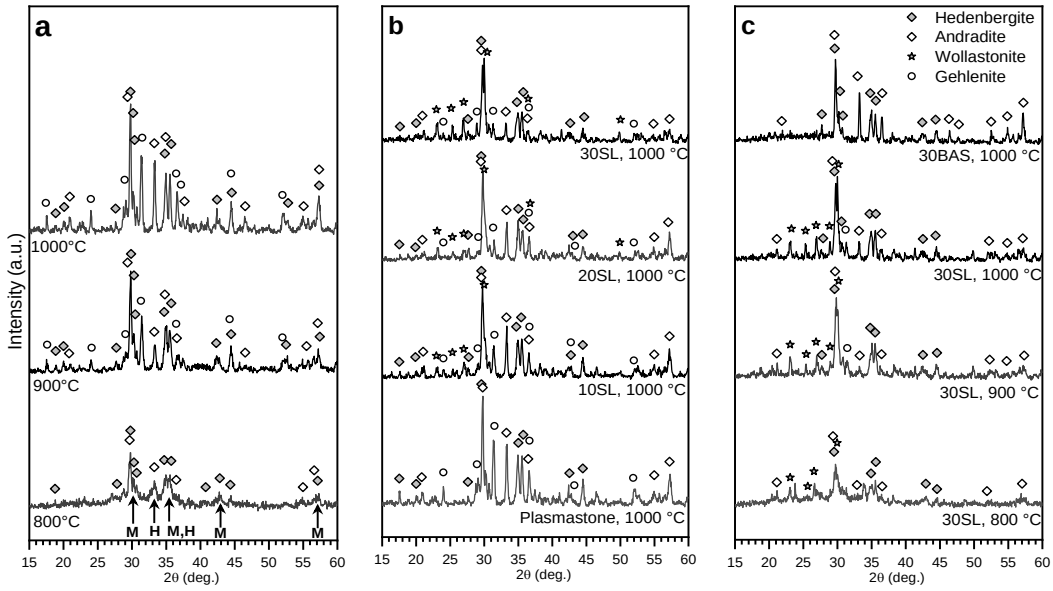

Figure 5-3. XRD patterns of the glass-ceramic foams: a) Plasmastone, fired at different temperatures; b) Plasmastone mixed with different amounts of soda-lime glass, fired at 1000 °C; c) Plasmastone mixed with 30% of recycled glass (soda-lime glass or boro-alumino-silicate glass), fired at different temperatures.

The firing treatments of Plasmastone-derived foams (Figure 5-3) led to substantial changes in the phase assemblage, with a remarkable crystallisation starting already at 800 °C. The XRD patterns show a quite complex overlapping of contributions from Fe-rich silicates, such as hedenbergite, $Ca(Fe_{0.821}Al_{0.179})(SiAl_{0.822}Fe_{0.178})O_6$, PDF #78-1546) and andradite ($Ca_3Fe_2(SiO_4)_3$, PDF#84-1935, as observed in Chapter 4. Furthermore, Figure 5-3a reveals that the major peaks of the iron-rich silicates overlapped (see arrows) with those of magnetite (Fe_3O_4, PDF#89-0691) and hematite (Fe_2O_3, PDF#89-2810). We cannot exclude the presence of magnetite for foams fired at 800 °C, since these samples were attracted by a permanent magnet. As previously mentioned, iron oxides are soluble in molten glass, at high temperature. The solubility decreases at lower

temperatures, which justifies their role as nucleating agents, especially for iron-rich pyroxenes (Höland and Beall, 2002; Karamanov et al., 2004b, 2000; Pisciella and Pelino, 2005).

The increase of firing temperature enhanced crystallisation and promoted the precipitation of Mg- and Fe-doped bearing gehlenite ($(Ca_{1.96}Na_{.05})(Mg_{.24}Al_{.64}Fe_{.12})(Si_{1.39}Al_{.61}O_7)$, PDF#72-2128). As presented in Chapter 4, the intensive crystallisation of Plasmastone upon firing affected densification due to limited viscous flow (indeed foams made with Plasmastone were very brittle). Recycled soda-lime glass was therefore mixed with Plasmastone to adjust the crystallisation/flow balance, by offering extra liquid phase upon firing (Bernardo et al., 2010). Figure 5-3b shows that the addition of soda-lime glass for foams fired at 1000 °C led to reduction of gehlenite and andradite, while the precipitation of wollastonite ($CaSiO_3$, PDF#84-0655) was promoted.

Table 5-1. Physical and mechanical properties of Plasmastone-based glass-ceramic foams.

Formulation	Pure Plasmastone			Plasmastone + Recycled glass				
Recycled glass amount (wt%)	-			10	20	30	40	30
Glass type	-			SL				BAS
Firing Temperature (°C)	800	900	1000	1000				
Density determinations								
ρ_{geom} (g/cm^3)	0.81 ± 0.01	0.98 ± 0.02	0.60 ± 0.01	0.67 ± 0.01	0.58 ± 0.03	0.65 ± 0.02	0.51 ± 0.01	0.78 ± 0.00
$\rho_{apparent}$ (g/cm^3)	2.83 ± 0.06	3.11 ± 0.10	3.32 ± 0.01	3.18 ± 0.03	3.01 ± 0.02	2.92 ± 0.02	2.71 ± 0.02	2.62 ± 0.04
ρ_{true} (g/cm^3)	3.17 ± 0.01	3.31 ± 0.01	3.32 ± 0.01	3.19 ± 0.01	3.07 ± 0.01	3.20 ± 0.01	3.10 ± 0.01	3.04 ± 0.01
Porosity distribution								
Total porosity (vol%)	74.4	70.4	81.9	79.1	81.2	79.6	83.7	74.5
Open porosity (vol %)	71.3	68.5	81.9	79.0	80.8	77.6	81.3	70.4
Closed porosity (vol%)	3.1	2.9	0	0.1	0.4	2.0	2.4	4.1
Strength determinations								
σ_{comp} (MPa)	0.4 ± 0.1	0.6 ± 0.1	0.3 ± 0.0	0.6 ± 0.1	1.0 ± 0.1	1.4 ± 0.2	1.1 ± 0.1	2.2 ± 0.2
σ_{bend} (MPa)[2]	18.4	20.5	20.1	30.5	62.7	75.4	82.0	84.1

[2]Standard deviation is not reported as the Gibson and Ashby's model was applied in order to have an estimation of the strength of the solid phase.

Table 5-1 reports the density and porosity of Plasmastone-derived foams fired at different temperatures: the developed glass-ceramics are highly porous, with total porosity higher than 70 vol%. In addition, the porosity is mostly open, given the close matching between apparent and true densities. The increase of the firing temperature from 800 °C to 900 °C reduced the porosity. This was probably associated to the increased viscous flow of the glass phase. Interestingly, the increase in firing temperature to 1000 °C increased the porosity, This may be attributed to secondary foaming phenomena, such as reduction of ferric ions to ferrous ions, with oxygen evolution (Ponsot et al., 2014) and decomposition of compounds formed due to alkali activation (Rincón et al., 2017).

The density data of foams from the addition of recycled glasses fired at 1000 °C is also shown in Table 5-1. The overall porosity remained at about 80 vol%, mostly open for samples made with soda-lime glass. The change in recycled glass to boro-alumino-silicate glass led to a small decrease in total porosity.

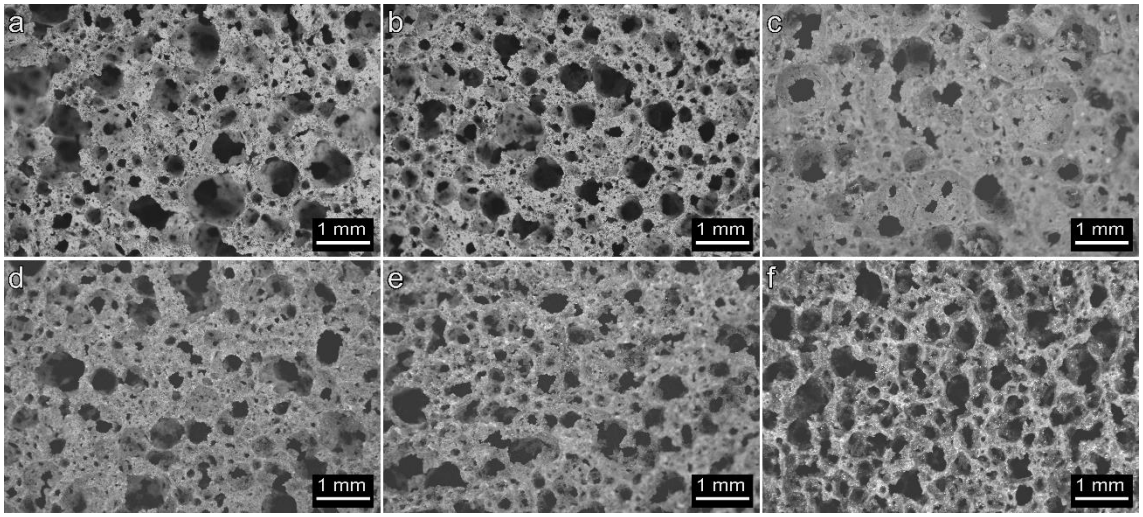

Figure 5-4. Micrographs of Plasmastone-derived foams fired at 1000 °C: a) Pure Plasmastone; b) 10SL; c) 20SL; d) 30SL; e) 40SL; f) 30BAS.

The microstructures from the Plasmastone-based foams fired at 1000 °C (Figure 5-4) confirm their similarity, despite the quantity and type of recycled glass added. On the other hand, regarding mechanical properties (Table 5-1), the addition of recycled glass added led to significant improvements, by changing the typology of crystal phases and the composition of the residual glass phase.

The estimated bending strength of the solid phase (σ_{bend}), for foams made with at least 30 wt% recycled glass is consistent with the strength values of most glasses (Bernardo et al., 2004). These foams could be potentially applied in buildings, as thermal and acoustic insulators, given their high porosity.

The results of the leaching test of Plasmastone/soda-lime glass foams are presented in Table 5-2, along with the leaching test results performed on a commercial glass foam (control sample). For the tests, it was considered foams made with 30 wt% soda-lime glass fired at different temperatures in order to assess the impact of the firing temperature on the leachate values. Furthermore, foams made with 20 wt% soda-lime glass (fired at 1000 °C) were also analysed in order to evaluate a possible influence of the composition on the leaching results. In all groups of samples, the leaching of Cr, Mo and V were above the limit values for classes U-A (aggregate for unbound or hydraulically or bituminously bound applications with end-of-waste status prior to recycling), U-B (like U-A, but end-of-waste not before recycling) and D (relevant for slags) from the Austrian Recycling Construction Materials Ordinance. In the case of Cr, the leaching decreased with firing temperature and increased with addition of soda-lime glass. In the case of Mo and V, the leachate values were quite similar for samples fired at different temperatures, while the leachate values decreased with addition of soda-lime glass.

Table 5-2. Results of the leaching tests made on the control sample and on Plasmastone derived glass-ceramics (mg/kg DM).

	Reference limits			*Leaching values*				
	U-A	*U-B*	*D*	**Control**	**30SL, 800 °C**	**30SL, 900 °C**	**30SL, 1000 °C**	**20SL, 1000 °C**
Cr	*0.6*	*1*	*0.3*	0.062	23	18	2.8	1.7
Cu	*1*	*2*		0.42	0.022	<0.001	0.067	0.054
Ni	*0.4*	*0.6*		0.15	0.0041	0.0033	0.0085	0.0029
Cl	*800*	*1000*		2.7	2.4	0.94	16	15
SO_4	*2500*	*6000*		56	38	58	52	26
Ba			*20*	0.16	0.091	0.23	0.13	0.0055
Cd			*0.04*	0.017	<0.001	0.0013	0.004	0.001
Co			*1*	0.082	0.015	0.013	0.028	0.018
Mo			*0.5*	0.072	4.1	5	3.7	7
Tl			*0.1*	<0.001	0.0041	0.0041	0.0041	0.0041
V			*1*	0.011	1.5	1.8	1.8	3.6
W			*1.5*	0.99	0.79	0.37	0.24	0.44
F			*10*	0.55	0.78	0.58	0.76	1

Microprobe analyses were performed on 70 wt% Plasmastone/30 wt% soda-lime glass foams fired at different temperatures, in order to understand the high leachate values of Cr, Mo

and V, based on the incorporation of these pollutants by determined phases. In contrast to glasses, glass-ceramics do not present a 'homogeneous' chemical behaviour: a significant leaching could be related to the solubility of a determined crystal phase or residual glass phase, as mentioned in Chapter 2.

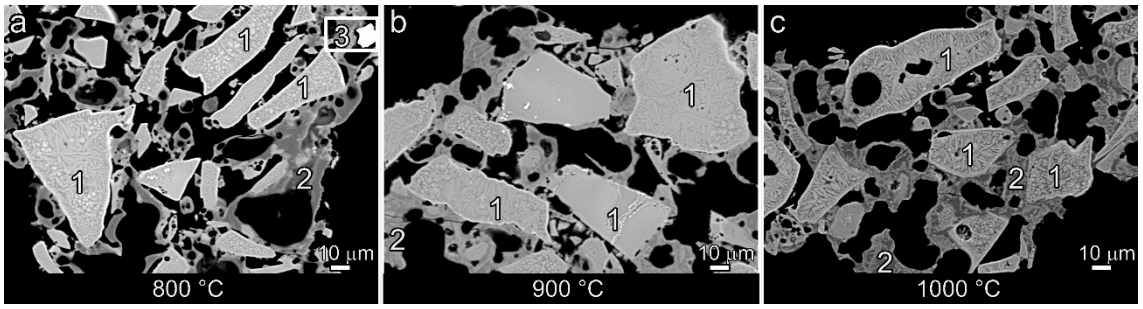

Figure 5-5. Micrographs of 70 wt% Plasmastone/30 wt% soda-lime glass foams fired at: a) 800 °C; b) 900 °C; c) 1000 °C; '1': iron silicate zone; '2': glass/wollastonite zone; '3': inclusion.

Table 5-3 shows that the Cr concentration was quite constant in the iron silicate-rich zones ('1' in Figure 5-5) for samples fired at different temperatures. Indeed, a previous study show that Cr can be incorporated in pyroxene (Li et al., 2017). This is consistent with phase separation in iron-rich glasses; Cr can form Cr-based spinels (the same crystal structure of magnetite), on which pyroxene crystals grow epitaxially (Goel et al., 2008; Karamanov et al., 2004a). In the case of the glass/wollastonite zones ('2' in Figure 5-5), the amount of Cr decreased with firing temperature. Therefore, the reduced leaching of Cr with firing temperature is consistent to the increased crystallisation (see Figure 5-3c).

Table 5-3. Microprobe analysis of selected zones of 70 wt% Plasmastone/30 wt% soda-lime glass foams fired at different temperatures.

Firing temperature	Zone	Mo (%)	Fe (%)	Cu (%)	Ba (%)	Zn (%)	V (%)	Cr (%)
800 °C	Iron silicates	0.03	15.4	0.003	0.002	0.002	0.037	0.010
900 °C		0.01	15.7	0.012	0.008	0.001	0.036	0.013
1000 °C		0.01	15.2	0.051	0.003	0.001	0.039	0.012
800 °C	Residual glass/wollastonite	0.01	1.88	0.099	0.018	0.007	0.007	0.027
900 °C		0.01	2.57	0.083	0.024	0.014	0.009	0.016
1000 °C		0.01	3.81	0.052	0.022	0.002	0.009	0.009

On the other hand, the concentration of V practically did not change with firing temperature in the iron silicate-rich zones nor in the glass/wollastonite zones; whereas the amount of Mo in iron silicate-rich zone was reduced with firing temperature. These findings indicate that the

chemical stability of the residual glass phase was the critical point, as previously observed in Chapter 4. As indicated by Figure 5-3b, the addition of soda-lime glass promoted the precipitation of wollastonite, resulting in an alkali enrichment in the residual glass phase. This reduced the stability of the residual glass phase, as alkali-rich highly depolymerized glasses are more prone to ionic diffusion (Bunker, 1994). Interestingly, Cu and Ba were also concentrated in the glass-wollastonite zone, but presented low leachates values. This was attributed to their incorporation by another "crystal host", such as Ba-containing copper zinc silicate inclusions ('3', Figure 5-5a).

Foams made with Plasmastone mixed with at least 30 wt% soda-lime glass and fired at 1000 °C were considered as thermal and acoustic insulators in buildings. However, the high leachate values of Cr, Mo and V constrained the application of these materials: the foams could only be applied in dry conditions or embedded in a more chemically stable matrix. An example could be the cladding with a geopolymeric paste, thus configuring sandwich structures. This possible suggestion is based on the easy low temperature processing and the high chemical stability of geopolymers (Lancellotti et al., 2010).

Furthermore, 'a priori' modifications of Plasmastone could also be considered to increase the chemical stability of Plasmastone-based glass-ceramics, such as a revision of the overall formulation. Indeed, the plasma processing conditions could be adjusted in order to increase the separation of metals, that could include relevant metals, such as Cr, Mo and V.

In the present study, in any case, 'a posteriori' modifications were applied: boro-alumino-silicate glass, from pharmaceutical vials, was used instead of soda-lime glass, mixed with Plasmastone (70 wt% Plasmastone/30 wt% boro-alumino-silicate glass). The 'zero waste' approach was maintained, as discarded or end-of-use pharmaceutical vials constitute a specific kind of waste, for not being applied in the manufacturing of new vials (Ponsot et al., 2014). The change of glass resulted in longer hardening steps, due to the reduced CaO content in boro-alumino-silicate glass. The process also led to homogeneous cellular structures after firing at 1000 °C, as shown by Figure 5-4f.

In addition, the change in glass added also modified the phase assemblage. Figure 5-3c shows that the firing at 1000 °C of 30BAS foams led to the precipitation of only hedenbergite and andradite. In contrast to foams made with soda-lime glass, which decreased the amount of andradite, the addition of boro-alumino-silicate glass favoured its recovery. There is also an increase in the amorphous background, which is consistent with the shiny glassy appearance of cell walls in Figure 5-4f. The new phase assemblage was advantageous for the mechanical properties (see Table 5-1), with increased in both compressive strength and estimated bending strength of the solid phase.

Finally, the leaching tests performed on this group of foams indicated a very good stabilisation of any heavy metal. Figure 5-6 exhibits the leachate values of the critical pollutants

(Cr, Mo and V) of Plasmastone mixed with 30 wt% boro-alumino-silicate glass and Plasmastone mixed with different amounts of soda-lime glass (20 wt%, 30 wt% or 40 wt%), which were normalised by the Class D (relevant for slags) thresholds of the Austrian regulation. There was a great reduction of more than one order of magnitude in the overall releases of critical elements. Therefore, glass-ceramic foams made with Plasmastone mixed with boro-alumino-silicate glass can be considered as safe.

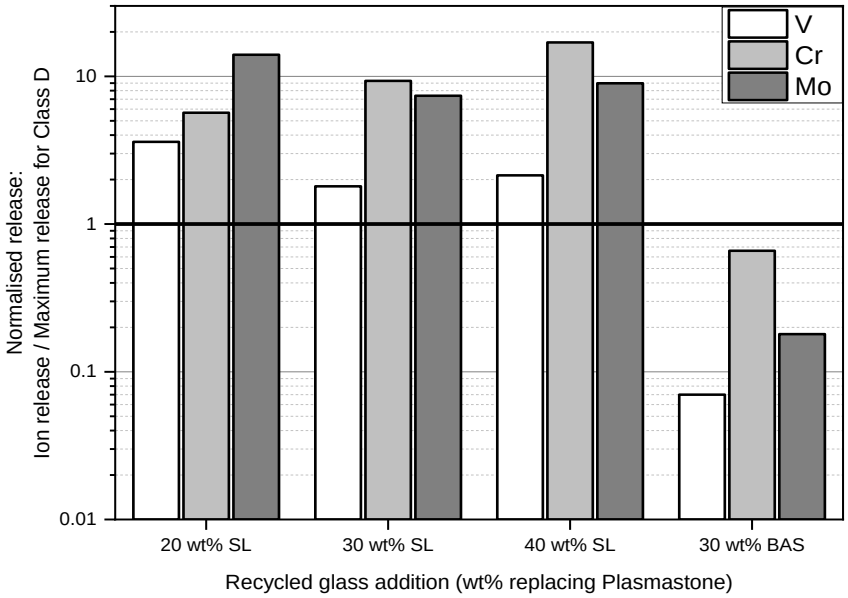

Figure 5-6. Leaching results of Cr, Mo and V normalised by the limits of Class D (Austrian Regulation).

5.4. Conclusions

The combined technique of alkali activation, gel-casting and sinter-crystallisation could be successfully applied to produce highly porous Plasmastone-based glass-ceramics, with total porosity exceeding 75 vol%. Furthermore, the addition of waste glass helped in promoting the gelation process by increasing the formation of compounds.

The increase in firing temperature and in the content of soda-lime glass increased the strength of the solid phase. For foams made with 70 wt% Plasmastone/30 wt% soda-lime glass, the increase in firing temperature helped overall in stabilising the heavy metals due to crystallisation, with some exceptions. Applying boro-alumino-silicate glass as glass additive (instead of soda-lime glass) helped to increase the stability of foams fired at 1000 °C, by particularly reducing the leaching of critical metals (Cr, Mo and V). The high porosity and high strength of the solid phase was maintained for these foams.

5.5. References

Bernardo, E., Bonomo, E., Dattoli, A., 2010. Optimisation of sintered glass – ceramics from an industrial waste glass. Ceram. Int. 36, 1675–1680. https://doi.org/10.1016/j.ceramint.2010.02.047

Bernardo, E., Scarinci, G., Maddalena, A., Hreglich, S., 2004. Development and mechanical properties of metal-particulate glass matrix composites from recycled glasses. Compos. Part A Appl. Sci. Manuf. 35, 17–22. https://doi.org/10.1016/j.compositesa.2003.09.022

Bunker, B.C., 1994. Molecular mechanisms for corrosion of silica and silicate glasses. J. Non. Cryst. Solids 179, 300–308. https://doi.org/10.1016/0022-3093(94)90708-0

Goel, A., Tulyaganov, D.U., Kharton, V. V., Yaremchenko, A.A., Ferreira, J.M.F., 2008. The effect of Cr2O3 addition on crystallization and properties of La2O3-containing diopside glass-ceramics. Acta Mater. 56, 3065–3076. https://doi.org/10.1016/j.actamat.2008.02.036

Höland, W., Beall, G.H., 2002. Glass ceramic technology. The American Ceramic Society, Ohio.

Karamanov, A., Arrizza, L., Matekovits, I., Pelino, M., 2004a. Properties of sintered glass-ceramics in the diopside-albite system. Ceram. Int. 30, 2129–2135. https://doi.org/10.1016/j.ceramint.2003.11.019

Karamanov, A., Pisciella, P., Cantalini, C., Pelino, M., 2000. Influence of Fe3+/Fe2+ ratio on the crystallisation of Iron-rich glasses made with industrial wastes. J. Th 83, 3153–3157. https://doi.org/10.1111/j.1151-2916.2000.tb01697.x

Karamanov, A., Taglieri, G., Pelino, M., 2004b. Iron-Rich Sintered Glass-Ceramics from Industrial Wastes. J. Am. Ceram. Soc. 82, 3012–3016. https://doi.org/10.1111/j.1151-2916.1999.tb02195.x

Lancellotti, I., Kamseu, E., Michelazzi, M., Barbieri, L., Corradi, A., Leonelli, C., 2010. Chemical stability of geopolymers containing municipal solid waste incinerator fly ash. Waste Manag. 30, 673–679. https://doi.org/10.1016/j.wasman.2009.09.032

Lancellotti, I., Ponzoni, C., Barbieri, L., Leonelli, C., 2013. Alkali activation processes for incinerator residues management. Waste Manag. 33, 1740–1749. https://doi.org/10.1016/j.wasman.2013.04.013

Li, J., Liu, B., Zeng, Y., Wang, Z., 2017. Mineralogical determination and geo-chemical modeling of chromium release from AOD slag: Distribution and leachability aspects. Chemosphere 167, 360–366. https://doi.org/10.1016/j.chemosphere.2016.10.020

Machiels, L., Arnout, L., Yan, P., Jones, P.T., Blanpain, B., Pontikes, Y., 2017. Transforming Enhanced Landfill Mining Derived Gasification/Vitrification Glass into Low-Carbon Inorganic Polymer Binders and Building Products. J. Sustain. Metall. 3, 405–415. https://doi.org/10.1007/s40831-016-0105-1

Pisciella, P., Pelino, M., 2005. FTIR spectroscopy investigation of the crystallisation process in

an iron rich glass. J. Eur. Ceram. Soc. 25, 1855–1861. https://doi.org/10.1016/j.jeurceramsoc.2004.06.012

Ponsot, I.M.M.M., Pontikes, Y., Baldi, G., Chinnam, R.K., Detsch, R., Boccaccini, A.R., Bernardo, E., 2014. Magnetic glass ceramics by sintering of borosilicate glass and inorganic waste. Materials (Basel). 7, 5565–5580. https://doi.org/10.3390/ma7085565

Rincón, A., Desideri, D., Bernardo, E., 2018. Functional glass-ceramic foams from 'inorganic gel casting' and sintering of glass/slag mixtures. J. Clean. Prod. 187, 250–256. https://doi.org/10.1016/j.jclepro.2018.03.065

Rincón, A., Giacomello, G., Pasetto, M., Bernardo, E., 2017. Novel 'inorganic gel casting' process for the manufacturing of glass foams. J. Eur. Ceram. Soc. 37, 2227–2234. https://doi.org/10.1016/j.jeurceramsoc.2017.01.012

Romero, A.R., Tamburini, S., Taveri, G., Toušek, J., Dlouhy, I., Bernardo, E., 2018. Extension of the "inorganic gel casting" process to the manufacturing of boro-alumino-silicate glass foams. Materials (Basel). 11, 1–12. https://doi.org/10.3390/ma11122545

Strozi Cilla, M., Colombo, P., Raymundo Morelli, M., 2014. Geopolymer foams by gelcasting. Ceram. Int. 40, 5723–5730. https://doi.org/10.1016/j.ceramint.2013.11.011

Chapter 6. Multifunctional porous Plasmastone-based glass-ceramics fired at low temperature

This chapter is based on: P. Rabelo Monich, D. Desideri, E. Bernardo, Low temperature upcycling of vitreous byproduct of the MSW plasma processing into multifunctional porous glass-ceramics, Advances in Applied Ceramics, 118, 366-371 (2019). DOI: 10.1080/17436753.2019.1595265

6.1. Introduction

The present chapter is dedicated to extend the 'inorganic gel casting' approach to Plasmastone combined with 30 wt% boro-alumino-silicate glass by firing at lower temperature. Chapters 4 and 5 have already indicated that firing Plasmastone-based materials at 800 °C maximised the precipitation of magnetite. The presence of magnetite could in turn could bring interesting functionalities to the material related to magnetic, optical or electrical properties (Chinnam et al., 2013; Ponsot et al., 2014), as mentioned in Chapter 2. In addition, the selection of boro-alumino-silicate glass as a glass additive was based on the previous chapter, which indicated stabilisation of heavy metals only for foams made with boro-alumino-silicate glass fired at 1000 °C.

The shielding effectiveness of the developed waste-derived glass-ceramics was also assessed. A multifunctional material (e.g. a thermal insulator with shielding properties) could certainly enhance the 'value' of waste-derived products, thus contributing to the sustainability of waste processing.

6.2. Experimental procedure

Fine waste glass powders (100 wt% Plasmastone or 70 wt% Plasmastone 30 wt% boro-alumino-silicate glass, 30BAS) were added to an alkaline activating solution of 2.5 M NaOH/KOH (ratio 1:1). The overall solid loading was 68 wt% and the slurries were mechanically stirred at 400 rpm. After 3h of partially dissolution of the fine powders, the slurries were poured in closed polystyrene moulds (diameter of 60 mm). and submitted to hardening at 75 °C (4h for foams with only Plasmastone and 6h for foams with boro-alumino-silicate-glass). 4% Triton X-100 surfactant (Sigma-Aldrich, Gillingham, UK) was added to the gelified slurries, which were further submitted to intensive mechanical stirring at 2000 rpm. Finally, the foamed suspensions were dried at 40 °C for 48 h. The demoulded and dried foams were fired at 800 °C, with heating rate of 10 °C/min and a holding time of 60 min (Rincón et al., 2017).

6.3. Results and discussion

Figure 6-1 exhibits the XRD patterns of Plasmastone and of foams made with 30% boro-alumino-silicate glass sintered at 800 °C. Crystallisation was more evident in porous glass-ceramics made by addition of boro-alumino-silicate glass, which is surprisingly as Plasmastone was 'diluted' by a glass not prone to crystallisation upon firing at 800 °C (Bernardo and Scarinci, 2004). This could be justified by the presence of interfaces between softened Plasmastone and BAS glass, with chemical gradients promoting ionic interdiffusion and modifying the crystallisation sequence.

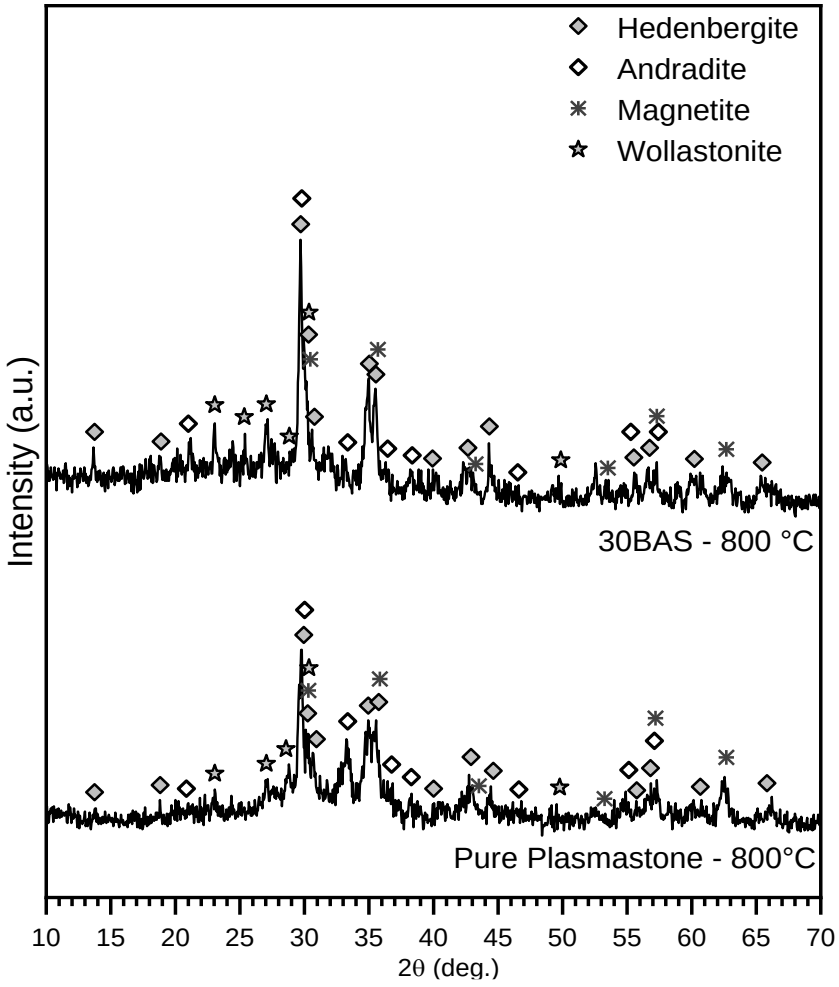

Figure 6-1. Mineralogical characterisation of Plasmastone-based glass-ceramics.

Both samples presented hedenbergite ($Ca(Fe_{0.821}Al_{0.179})(SiAl_{0.822}Fe_{0.178})O_6$, PDF#78-1546), andradite ($Ca_3Fe_2(SiO_4)_3$, PDF#84-1935), wollastonite ($CaSiO_3$, PDF#84-0655) and magnetite (Fe_3O_4, PDF#89-0691). A detailed analysis on the iron oxides presented in 30BAS foams fired at 800 °C is presented in the following chapter. It can also be observed that the addition of boro-alumino-silicate glass decreased andradite peaks, while promoting formation of hedenbergite and wollastonite. In contrast, as presented in Chapter 5, 30BAS foams fired at 1000 °C exhibited phase

assemblages consisting of only hedenbergite and andradite, while pure Plasmastone foams fired at the same temperature featured gehlenite, along with hedenbergite and andradite. Interestingly, for these foams fired at higher temperature, crystallisation was more prominent for pure Plasmastone.

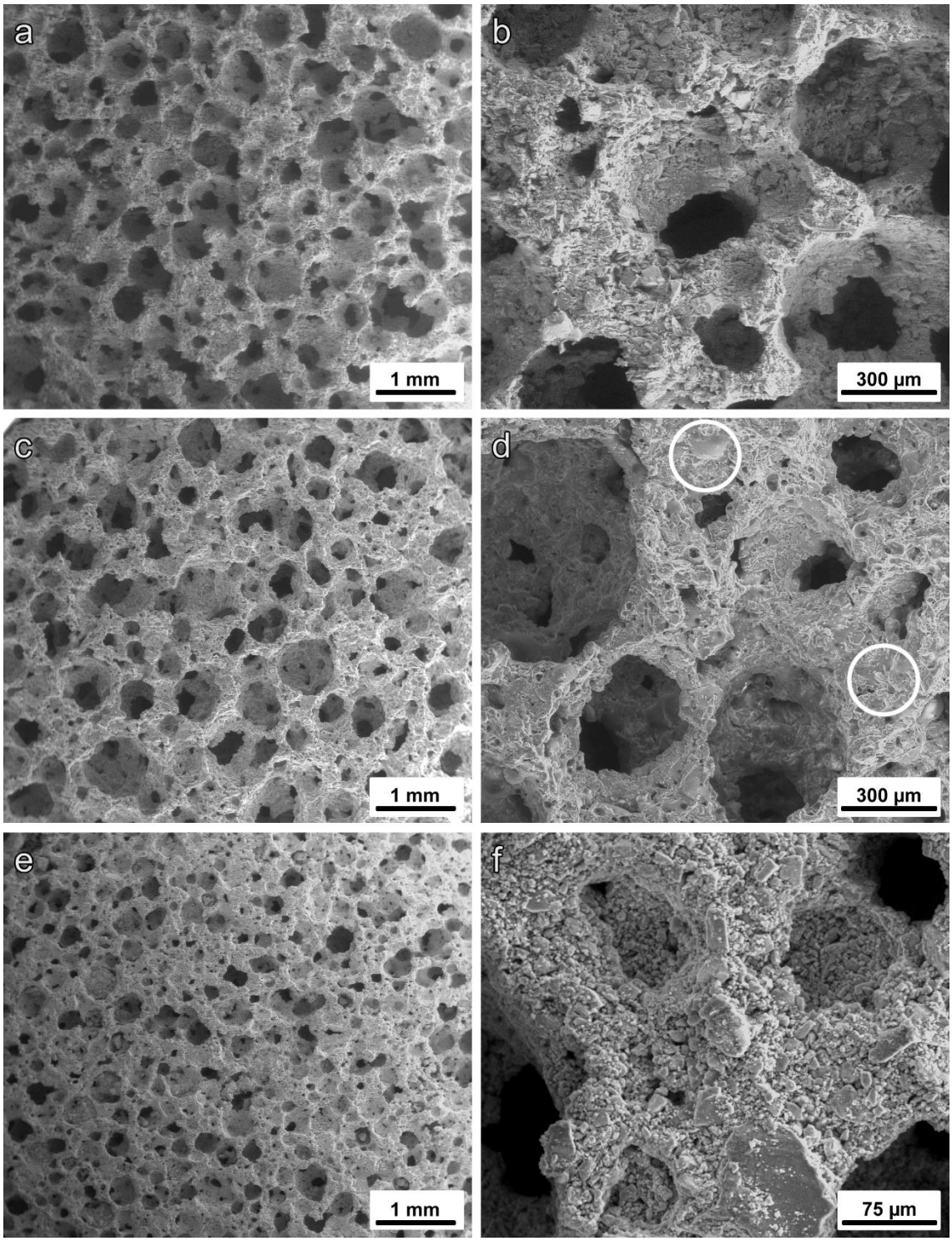

Figure 6-2. Morphology of Plasmastone-based glass-ceramic foams (left: low magnification; right: details): a,b) 30BAS in the green state; c,d) 30BAS fired at 800 °C; e,f) pure Plasmastone fired at 800 °C.

Table 6-1 reports the density and porosity data of fired foams made with pure Plasmastone or with Plasmastone/boro-alumino-silicate glass mixtures. Both foams were highly porous, with porosity exceeding 74 vol%, and mostly open, as evidenced by Figure 6-2. The open-celled morphology of 30BAS foams was originated from low temperature foaming, as indicated by Figures 6-2a and b. In addition, the firing treatment did not lead to any substantial change in the morphology, as evidenced by Figures 6-2c and d.

Table 6-1. Physical and mechanical properties of Plasmastone-based porous glass-ceramics fired at 800 °C.

Group of samples	**Pure Plasmastone**	**30BAS**
Density determinations		
ρ_{geom} (g/cm^3)	0.81 ± 0.01	0.64 ± 0.04
$\rho_{apparent}$ (g/cm^3)	2.83 ± 0.06	2.24 ± 0.04
ρ_{true} (g/cm^3)	3.17 ± 0.01	2.71 ± 0.10
Porosity distribution		
Total porosity (vol%)	74.4	76.2
Open porosity (vol%)	71.3	71.2
Closed porosity (vol%)	3.1	5.0
Strength determinations		
σ_{comp} (MPa)	0.3 ± 0.1	1.9 ± 0.4
σ_{bend} (MPa)	11.4	84.6

The Gibson and Ashby model (see Chapter 2) (Gibson and Ashby, 1999) was applied in order to estimate the bending strength of the solid phase (σ_{bend}), based on the scaling of compressive strength for open-celled materials. As indicated in Chapter 5, foams made with pure Plasmastone were very brittle, exhibiting σ_{bend} slightly above 10 MPa. This is reasonable to the micrographs of pure Plasmastone foams fired at 800 °C (see Figure 6-2f), which indicates poor joining between adjacent particles due to reduced amount of residual glass phase available for sintering. In contrast, the addition of boro-alumino-silicate glass increased σ_{bend} to 84.6 MPa, which is quite similar to the values obtained for foams made with the same composition fired at 1000 °C (from the previous chapter). In addition, this value is comparable to the bending strength of dense waste-derived glass-ceramics (Rawlings et al., 2006). Figure 6-2 illustrates well the change for 30BAS passing from poorly bound powders, before firing (Figure 6-2b), to sintered struts after firing at 800 °C (Figure 6-2d, see the circles indicating the residual glass phase). The high porosity as well as high strength presented by 30BAS foams indicate that these foams could be potentially applied in buildings, as thermal and acoustic insulators.

The assessment of the chemical stability of 30BAS foams by means of leaching test (Table 6-2) indicate a quite limited leaching of heavy metals, below the limit values for inert waste and non-hazardous waste (*Directive 2003/33/EC*, 2003). The samples made with pure Plasmastone were not analysed, due to their low strength. The low leaching of pollutants observed for 30BAS fired at 800 °C, as well as 1000 °C (Chapter 5), indicates that boro-alumino-silicate glass consists of an ideal glass additive for Plasmastone-based foams. Furthermore, strong foams could be obtained even at 800 °C, which is favourably lower than the temperature adopted for commercial glass foams (Chinnam et al., 2013; Rincón et al., 2016).

Table 6-2. Leaching test results made on 30BAS fired at 800 °C (ppm).

	Inert waste	**Non-hazardous waste**	**30BAS, 800 °C**
As	*0.5*	*2*	<0.0049
Ba	*20*	*100*	0.0316
Cd	*0.04*	*1*	<0.0002
Cr total	*0.5*	*10*	0.0153
Cu	*2*	*50*	0.0069
Hg	*0.01*	*0.2*	0.001
Mo	*0.5*	*10*	0.071
Ni	*0.4*	*10*	<0.0014
Pb	*0.5*	*10*	<0.0047
Sb	*0.06*	*0.7*	<0.0099
Se	*0.1*	*0.5*	<0.0122
Zn	*4*	*50*	<0.0203

The low firing temperature could also provide additional functionalities attributed to the presence of magnetite in traces, as indicated by the XRD patterns (see Figure 6-1). In addition, the samples were also attracted by permanent magnets, confirming the presence of this iron oxide phase.

The fired foams 30BAS were further subjected to preliminary electromagnetic shielding studies, analogous to glass-ceramic foams-containing magnetite made from soda-lime glass and metallurgical slag (Rincón et al., 2018). Magnetite is interesting in this specific field for the magnetic behaviour, but also for a distinctive combination of properties (electrical conductivity,

atomic and electronic polarization) (Al-Ghamdi et al., 2012). The measured of shielding effectiveness (Figure 6-3) was lower than 0.1 dB for frequencies below 1.7 GHz, but increased up to 2.8 dB for a frequency of 2.1 GHz. The shielding effect is not quite strong, but one must considers it is dependent only on the type of applied waste, in contrast to electromagnetic shields, based on specific composite design, such as carbon fibres in cement based composites (Zornoza et al., 2010). The developed glass-ceramic foams could contribute to the definition of a new generation of multifunctional building materials by coupling thermal and acoustic insulation (related to the high porosity) with the reduction of human exposure to electromagnetic fields and of electromagnetic interferences.

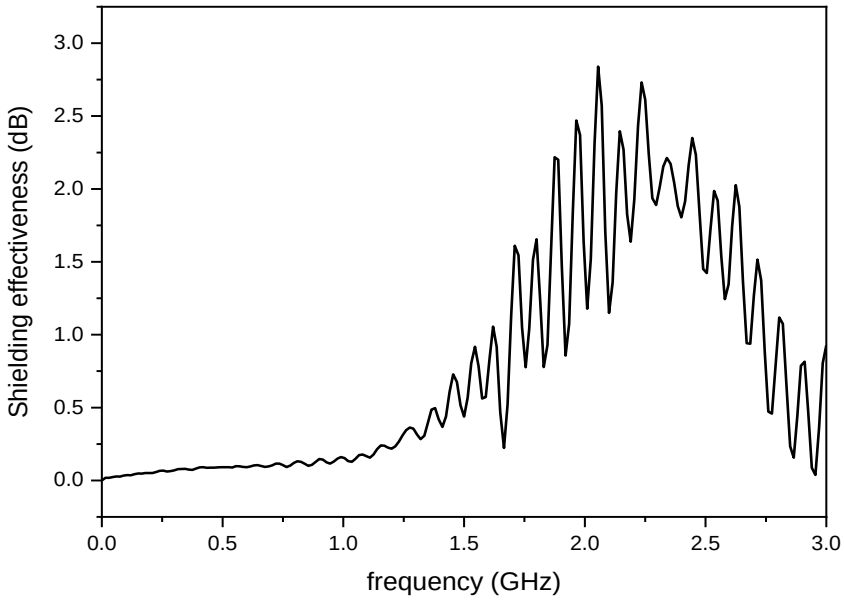

Figure 6-3. Shielding effectiveness measurement of 30BAS800 (external diameter: 36 mm; internal diameter: 7 mm; thickness: 8 mm).

6.4. Conclusions

Boro-alumino-silicate glass has proven to be ideal to be employed as glass additive for Plasmastone-based porous glass-ceramics. It was possible to obtain highly porous and strong foams, with good stabilisation of pollutants, for addition of 30 wt% boro-alumino-silicate glass coupled with firing at only 800 °C. In addition, the firing at low temperature favoured the separation of magnetite, which in turn could bring novel functionalities to the material. Indeed, the foams exhibited some potential in electromagnetic shielding.

6.5. References

Al-Ghamdi, A.A., Al-Hartomy, O.A., Al-Salamy, F., Al-Ghamdi, A.A., El-Mossalamy, E.H., Abdel Daiem, A.M., El-Tantawy, F., 2012. Novel electromagnetic interference shielding effectiveness in the microwave band of magnetic nitrile butadiene rubber/magnetite

nanocomposites. J. Appl. Polym. Sci. 125, 2604–2613. https://doi.org/10.1002/app.36371

Bernardo, E., Scarinci, G., 2004. Sintering behaviour and mechanical properties of Al2O3 platelet-reinforced glass matrix composites obtained by powder technology. Ceram. Int. 30, 785–791. https://doi.org/10.1016/j.ceramint.2003.09.013

Chinnam, R.K., Francis, A.A., Will, J., Bernardo, E., Boccaccini, A.R., 2013. Review. Functional glasses and glass-ceramics derived from iron rich waste and combination of industrial residues. J. Non. Cryst. Solids 365, 63–74. https://doi.org/10.1016/j.jnoncrysol.2012.12.006

Directive 2003/33/EC, 2003. Official Journal of the European Communities.

Gibson, L.J., Ashby, M.F., 1999. Cellular solids: structure and properties. Cambridge University Press, Cambridge, UK.

Ponsot, I.M.M.M., Pontikes, Y., Baldi, G., Chinnam, R.K., Detsch, R., Boccaccini, A.R., Bernardo, E., 2014. Magnetic glass ceramics by sintering of borosilicate glass and inorganic waste. Materials (Basel). 7, 5565–5580. https://doi.org/10.3390/ma7085565

Rawlings, R., Wu, J., Boccaccini, a, 2006. Glass-ceramics: Their production from wastes - A Review. J. Mater. Sci. 41, 733–761. https://doi.org/10.1007/s10853-006-6554-3

Rincón, A., Desideri, D., Bernardo, E., 2018. Functional glass-ceramic foams from ‘inorganic gel casting’ and sintering of glass/slag mixtures. J. Clean. Prod. 187, 250–256. https://doi.org/10.1016/j.jclepro.2018.03.065

Rincón, A., Giacomello, G., Pasetto, M., Bernardo, E., 2017. Novel ‘inorganic gel casting’ process for the manufacturing of glass foams. J. Eur. Ceram. Soc. 37, 2227–2234. https://doi.org/10.1016/j.jeurceramsoc.2017.01.012

Rincón, A., Marangoni, M., Cetin, S., Bernardo, E., 2016. Recycling of inorganic waste in monolithic and cellular glass-based materials for structural and functional applications. J. Chem. Technol. Biotechnol. 91, 1946–1961. https://doi.org/10.1002/jctb.4982

Zornoza, E., Catalá, G., Jiménez, F., Andión, L.G., Garcés, P., 2010. Electromagnetic interference shielding with Portland cement paste containing carbon materials and processed fly ash. Mater. Construcción 60, 21–32. https://doi.org/10.3989/mc.2010.51009

Chapter 7. Multifunctional porous Plasmastone-based glass-ceramics fired in nitrogen

This chapter was based on "P. Rabelo Monich, A. Rincon Romero, D. Desideri, E. Bernardo, Waste-derived glass-ceramics fired in nitrogen: stabilization and functionalization, Construction and Building Materials, 232 (2020). DOI: 10.1016/j.conbuildmat.2019.117265"

7.1. Introduction

Chapters 5 and 6 indicated the potential of adding 30 wt% soda-lime glass or boro-alumino-silicate glass to improve densification of Plasmastone-based foams during firing, in air. However, only foams made with addition of boro-alumino-silicate glass (fired at 800 °C or 1000 °C) led to the stabilisation of pollutants. In addition, firing in air of Plasmastone-based materials at low temperatures also maximised the precipitation of magnetite, leading to materials exhibiting some electromagnetic shielding effectiveness (see Chapters 4 and 6).

The present chapter is dedicated to tune stabilisation of heavy metals and provide functionalities for Plasmastone-based porous glass-ceramics by changing the firing atmosphere from air to nitrogen[3]. Electrical conductivity, relative permittivity and electromagnetic shielding effectiveness were measured on samples made by specific compositions, regarding type of waste glass added and firing temperature applied.

7.2. Experimental procedure

Plasmastone-based foams were produced following the same procedure applied in Chapter 5: after partial dissolution of 70 wt% Plasmastone/30 wt% waste glass mixtures in an alkaline aqueous solution (2.5 M NaOH/KOH, ratio 1:1), the slurry underwent preliminary gelation at 75 °C. The solid content was equal to 68 wt%. Thereafter, the partially gelified suspensions were submitted to intensive mechanical stirring at 2000 rpm, with previous addition of 4 wt% Triton X-100 (polyoxyethylene octyl phenyl ether – $C_{14}H_{22}O(C_2H_4O)_n$, n = 9–10, Sigma-Aldrich, Gillingham, UK) surfactant. The foamed structure was then dried at 40 °C, for 48 h, before being demoulded. In contrast to the previous chapter, the firing treatment was done in flowing nitrogen atmosphere, with a holding time of 1h. Foams made with addition of 30% boro-alumino-silicate glass were fired at only 800 °C ('30BAS800N_2'), whereas foams made with 30% soda-lime glass were fired at 800 °C ('30SL800N_2') or 1000 °C ('30SL1000N_2').

7.3. Results and discussion

7.3.1. Characterisation of Plasmastone-based foams

[3] Firing in low pressure nitrogen flow was conducted in order to provide non-oxidative atmosphere.

Figure 7-1 presents the XRD patterns of foams made with Plasmastone mixed with 30 wt% waste glasses fired in air or in nitrogen at 800 °C or 1000 °C. These two temperatures were considered as reference for the firing treatments, based on the previous chapters. As mentioned in Chapter 4, 800 °C corresponds to the crystallisation temperature of fine powders of Plasmastone, while the increase in firing temperature up to 1000 °C for foams made with addition of waste-glass significantly promoted viscous flow sintering.

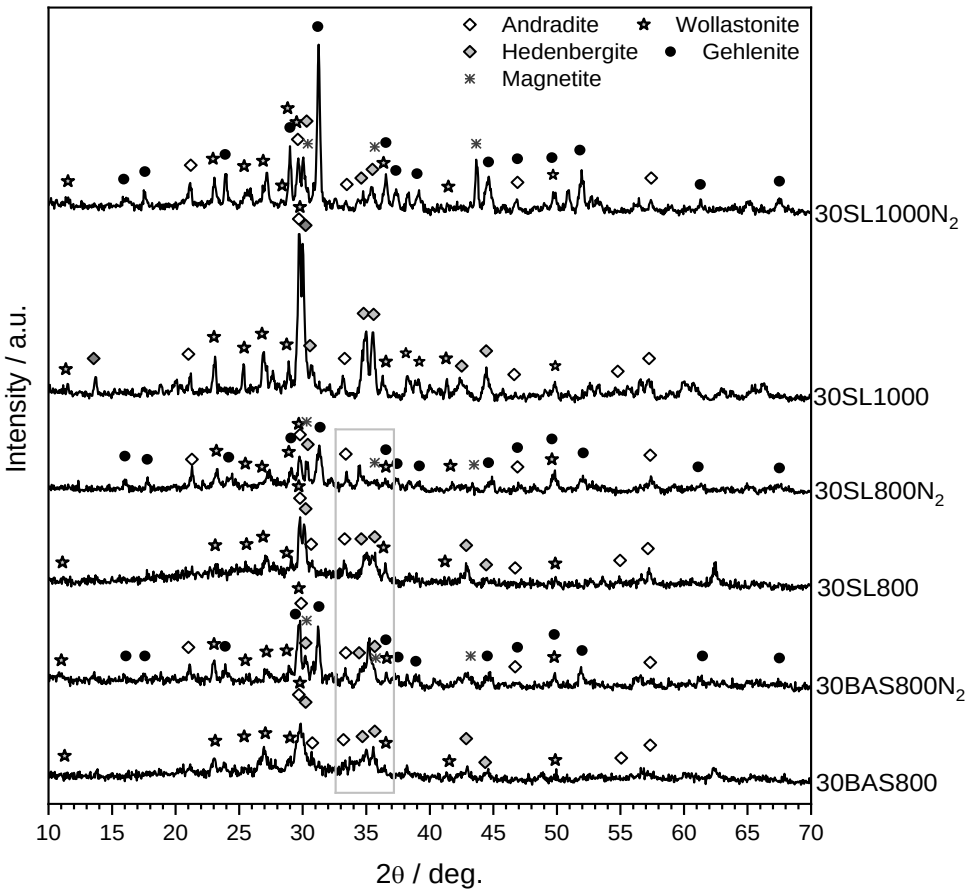

Figure 7-1. Effect of temperature and firing atmosphere on foams made with mixtures of Plasmastone with waste glass (soda-lime glass or boro-alumino-silicate-glass).

The XRD patterns of the samples fired in air (30SL800, 30SL1000 and 30SLBAS) have already been exhibited in Chapters 5 and 6. As previously mentioned, the increase in firing temperature to 1000 °C in air for 30SL samples increased the phases presented already in 30SL800: hedenbergite ($Ca(Fe_{0.821}Al_{0.179})(SiAl_{0.822}Fe_{0.178})O_6$, PDF#78-1546), andradite ($Ca_3Fe_2(SiO_4)_3$, PDF#84-1935) and wollastonite ($CaSiO_3$, PDF#84-0655). On the other hand, firing at 1000 °C in nitrogen ($30SL1000N_2$) promoted the precipitation of Na-Mg-Fe doped gehlenite ($(Ca_{1.96}Na_{.05})(Mg_{.24}Al_{.64}Fe_{.12})(Si_{1.39}Al_{.61}O_7)$, PDF#72-2128), which was already present in minor amount in samples fired at 800 °C in N_2 ($30SL800N_2$). It is quite usual to find solid

solutions of two groups, such as pyroxene (e.g. hedenbergite) and melilite (e.g. gehlenite) in silicate glasses containing iron oxides (Francis, 2005; Rawlings et al., 2006; Williamson et al., 1968).

The oxidation state of iron ions probably decreased by changing the atmosphere to nitrogen, when one considers the reduction of andradite (featuring Fe^{3+}) and the promotion of gehlenite, which presents a particular stoichiometry suggested by the phase identification software Match! (including Fe^{2+} ions). Nonetheless, both pyroxene and melilite solid solutions may contain both Fe^{2+} and Fe^{3+} ions, still leading to some uncertainties (Redhammer, 2006; Žáček et al., 2005). The change of waste glass added passing from soda-lime glass to boro-alumino-silicate glass did not lead to significant effects regarding the phase assemblage, with gehlenite present in traces in both foams fired at 800 °C in nitrogen.

The samples fired in nitrogen were subjected to a more detailed mineralogical analysis, especially concerning the peaks attributed to magnetite (Fe_3O_4, PDF#89-0691). The overlapping of peaks of iron oxides with the previously mentioned silicate phases, in fact, impeded a clear discussion, from Figure 7-1 (especially in the 2θ range marked by the box). Based on this, Figure 7-2 presents the XRD patterns of 30SL800 and 30SL800N_2 (Figure 7-2a), as well as the ones of 30BAS800 and 30BAS800N_2 (Figure 7-2b), exhibiting only peaks consistent to those of different types of iron oxides. Samples fired at 1000 °C made with soda-lime glass are not shown, as it was only possible to detect one type of magnetite polymorph (e.g. the peaks for 2θ~43.5°), in contrast to the foams fired at 800 °C.

In addition to the already mentioned magnetite polymorph (labelled as 'M1'), two other forms were also detected (labelled as 'M2', PDF#89-0951, and 'M3', PDF#89-6466). These three forms have already been recognised in the literature (Bepari et al., 2017; Marciello et al., 2013; Sundar et al., 2014). Furthermore, some peaks are compatible with hematite (Fe_2O_3, PDF#89-2810). The polymorphism of magnetite includes many possible crystal structures passing from cubic inverse spinel to perovskite-based orthorhombic (Liu et al., 2013), with complications related to the varying site occupancy (Fleet, 1982). The forms 'M1' and 'M2' are attributed to a cubic symmetry (Fd-3m space group, according to the PDF-2 records exhibited in Match!), whereas M3 is orthorhombic (Pbcm space group).

It is not possible to consider the intensity of the peaks corresponding to iron oxides as proportional to the relative amounts: as already mentioned, these signals overlapped with the ones of silicate phases. In foams 30SL800 (Figure 7-2a), in particular, the main peak of magnetite 'M1' at 2θ~30° in fact overlaps with the more intense peak of pyroxene, which is formed by epitaxial growth on magnetite nuclei (Feinberg et al., 2004)). Other peaks, such as at 2θ~18°, are more visible in the analogous sample fired in nitrogen (Figures 7-2a and b). Nonetheless, several peaks not indexed in Figure 7-1 (especially around 2θ~35° for samples

fired in nitrogen at 800 °C, see box in the same figure) are consistent to several iron oxide phases. The formation of several polymorphs could be favoured by interaction with the atmosphere. As an example, magnetite-like structures can be formed with Fe^{2+} and Fe^{3+} balanced by oxygen ions mixed with nitrogen ions, instead of simply by oxygen ions (iron oxynitride) (Voogt et al., 2002). The incorporation of nitrogen and the possible replacement of Fe^{2+} and Fe^{3+} ions with other metal ions further complicates the analysis, since solid solutions lead to displacements in the position of diffraction peaks.

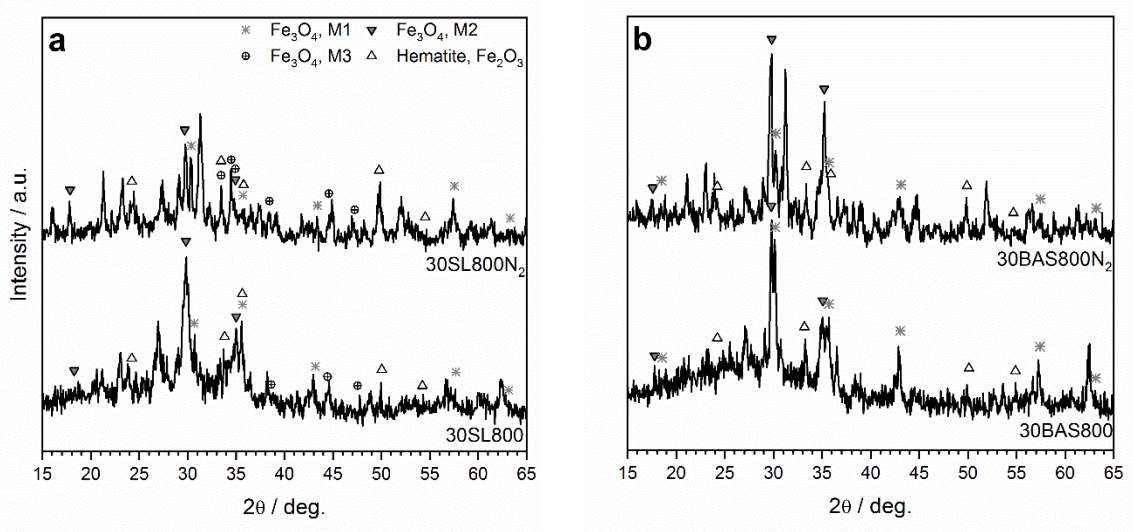

Figure 7-2. XRD diffraction patterns of samples fired at 800 °C with indication of the overlapping with major peaks of iron oxide phases.

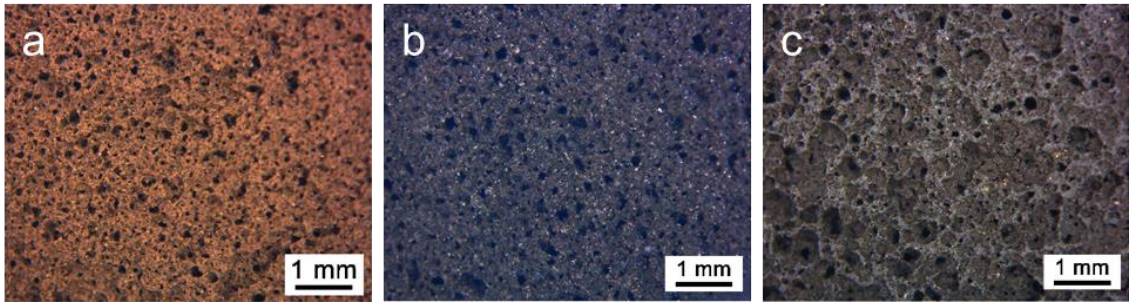

Figure 7-3. Micrographs of Plasmastone/soda-lime glass foams after: a) low temperature hardening; b) firing at 800 °C in nitrogen (30SL800N2); b) firing at 1000 °C in nitrogen (30SL1000N2).

The micrographs of the foams after hardening and after firing in nitrogen are presented in Figures 7-3 (30SL) and 7-4 (30BAS). The different types of compounds formed upon alkali activation (e.g. hydrated compounds, carbonates) for these samples were already reported in Chapter 5. The low temperature hardening resulted in highly porous materials for both foams

30SL and 30BAS. Furthermore, the high amount of porosity was maintained after firing in nitrogen for all groups of foams, which exhibited mainly an open-celled morphology.

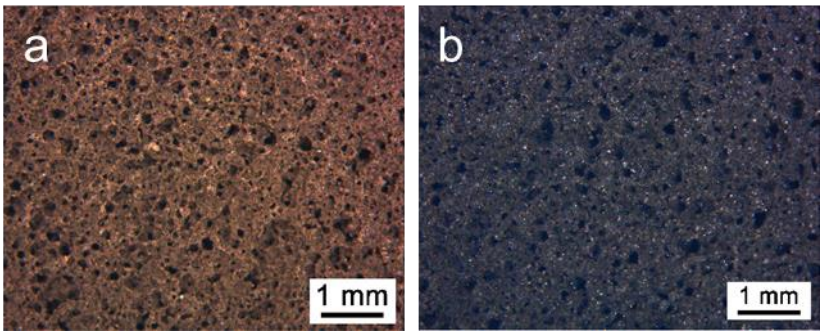

Figure 7-4. Micrographs of Plasmastone/boro-alumino-silicate glass foams after: a) low temperature hardening; b) firing at 800 °C in nitrogen (30BAS800N2).

Table 7-1. Physical and mechanical properties of Plasmastone-based foams fired in nitrogen or in air.

Group of samples	**30BAS 800**	**30BAS 800N$_2$**	**30SL 800**	**30SL 800N$_2$**	**30 SL1000**	**30 SL1000N$_2$**
Glass additive	BAS		SL			
Firing temperature	800 °C		800 °C		1000 °C	
Atmosphere	Air	*N_2*	Air	*N_2*	Air	*N_2*
Density determinations						
ρ_{geom} (g/cm^3)	0.64 ± 0.04	*0.74 ± 0.01*	0.69 ± 0.01	*0.78 ± 0.01*	0.65 ± 0.02	*0.77 ± 0.03*
$\rho_{apparent}$ (g/cm^3)	2.24 ± 0.04	*2.96 ± 0.02*	2.74 ± 0.02	*2.90 ± 0.10*	2.92 ± 0.01	*2.96 ± 0.01*
ρ_{true} (g/cm^3)	2.71 ± 0.10	*3.05 ± 0.01*	2.90 ± 0.01	*2.92 ± 0.01*	3.20 ± 0.01	*2.98 ± 0.01*
Porosity distribution						
Total porosity (vol%)	76.2	*75.7*	76.2	*73.3*	79.7	*74.2*
Open porosity (vol%)	71.2	*75.0*	74.8	*73.1*	77.7	*74.0*
Closed porosity (vol%)	5.0	*0.7*	1.4	*0.2*	2.0	*0.2*
Strength determinations						
σ_{comp} (MPa)	2.0 ± 0.4	*1.3 ± 0.6*	1.7 ± 0.2	*1.4 ± 0.4*	1.4 ± 0.2	*2.3 ± 0.4*
σ_{bend} (MPa)	84.6	*54.4*	73.2	*50.7*	75.4	*87.6*

Table 7-1 presents the densities, porosity and strength (compressive strength, σ_{comp}; and estimated bending strength of the solid phase, σ_{bend}) of foams made with addition of waste glasses fired in air or in nitrogen. The bending strength was estimated by applying the Gibson and Ashby model (see Chapter 2) for open-celled materials (Gibson and Ashby, 1999). In addition, the overall data regarding the foams fired in air were already present in Chapters 5 and 6 and are presented here for comparison.

The increase in firing temperature from 800 °C to 1000 °C for foams made with soda-lime glass slightly increased the overall porosity. This could be attributed to gas evolution from high temperature reduction of Fe^{3+} into Fe^{2+} ($2\ Fe_2O_3 \rightarrow 4\ FeO + O_2$) (Rincón et al., 2018). Interestingly, the porosity of samples fired in nitrogen remain open in all conditions, in contrast to the ones fired in air. The cellular structure developed upon firing in nitrogen probably originated from a substantial 'reshaping' of pores, with contributions to porosity from overlapping phenomena, such as the previously mentioned oxygen release, by reduction of Fe^{3+} into Fe^{2+}.

Regarding the estimated bending strength, firing in nitrogen at 800 °C reduced σ_{bend} when compared to the analogous foams fired in air, for both types of mixtures. On the other hand, foams fired at 1000 °C in nitrogen ($30SL1000N_2$) were stronger than those fired in air (30SL1000). In any case, all developed foams still compare favourably in terms of strength-to-density ratio, with several commercial ceramic foams ("CES EduPack 2018 materials education software").

7.3.2. Assessment of chemical stability

Chapter 5 already showed the low chemical durability of glass-ceramic foams made with mixtures of Plasmastone and soda-lime glass, specially concerning Cr, Mo, and V which exceeded the limits from the Austrian Recycling Building Materials Ordinance. Chemical stable foams were only obtained by employing boro-alumino-silicate glass as glass additive, for foams fired at 1000 °C, or even just at just at 800 °C, as exhibited in Chapters 5 and 6.

The results of the leaching test performed on foams fired in nitrogen (Table 7-2) indicate that all samples present leachate values below the limits for non-hazardous and inert waste (*Directive 2003/33/EC*, 2003). The stabilisation of foams fired in nitrogen could be derived from the mineralogical changes, especially by the formation of gehlenite instead of andradite, verified passing from soda-lime glass and boro-alumino-silicate glass, in air, and, generally, from air to nitrogen as firing atmosphere, for both glass additives. A previous study has already indicated an increased stabilisation of heavy metals due to reduced basicity (CaO/SiO_2 ratio) of the residual glass phase (Romero et al., 2008). This reasonably occurred with the precipitation of gehlenite, which is a relatively 'silica-poor' crystal phase.

Table 7-2. Results of the leaching tests performed on porous glass-ceramics fired in nitrogen (ppm).

	Limits Directive 2003/33/EC		*Foams*		
	Inert waste	**Non-hazardous waste**	**30BAS 800N_2**	**30SL 800N_2**	**30SL 1000N_2**
As	0.5	2	0.015	0.0135	0.0327
Ba	20	100	<0.0000	<0.0000	<0.0000
Cd	0.04	1	<0.0002	<0.0002	<0.0002
Cr	0.5	10	<0.0004	<0.0004	0,0062
Cu	2	50	<0.0001	<0.0001	0.0113
Mo	0.5	10	0.0322	0.3141	<0.0033
Ni	0.4	10	<0.0014	<0.0014	0.0289
Pb	0.5	10	<0.0047	<0.0047	<0.0047
Sb	0.06	0.7	0.0314	0.0378	<0.0099
Se	0.1	0.5	0.0162	<0.0122	<0.0122
Zn	4	50	<0.0203	<0.0203	<0.0203

7.3.3. Assessment of functionalities

Magnetite-containing composites can be a valid solution for electromagnetic shielding (G. Bantsis et al., 2011). Furthermore, magnetite-containing porous waste-derived glass-ceramics have already presented some potential, in electromagnetic shielding (Rincón et al., 2018).

As described in Chapter 2, magnetite is a ferri-magnetic material and an electronic conductor, due to electron exchanges (‘electron hopping’) between iron sites possessing a different charge (Fe^{2+} and Fe^{3+}) (Kündig and Steven Hargrove, 1969; Lazor et al., 2004). Conductive materials are considered good electromagnetic shields (Chung, 2001; Sarto and Tamburrano, 2006).

Figure 7-5 presents the electrical conductivity of samples fired in nitrogen. Foams fired at low temperature (Figures 7-5a and b) exhibited a significant conductivity, with values generally close to those of semiconductors (Levinshtein et al., 1996). In contrast, the foam fired at 1000 °C (30SLN_2, Figure 7-5c) presented electrical conductivity values of about two order of magnitude lower than the ones obtained for firing at 800 °C. The great difference in electrical conductivity passing from 800 °C to 1000 °C for Plasmastone/soda-lime glass mixtures is

probably associated to the available polymorphic variant of magnetite: 30SL1000N_2 only featured one variant, while samples fired at 800 °C presented two additional variants (see Figure 7-2).

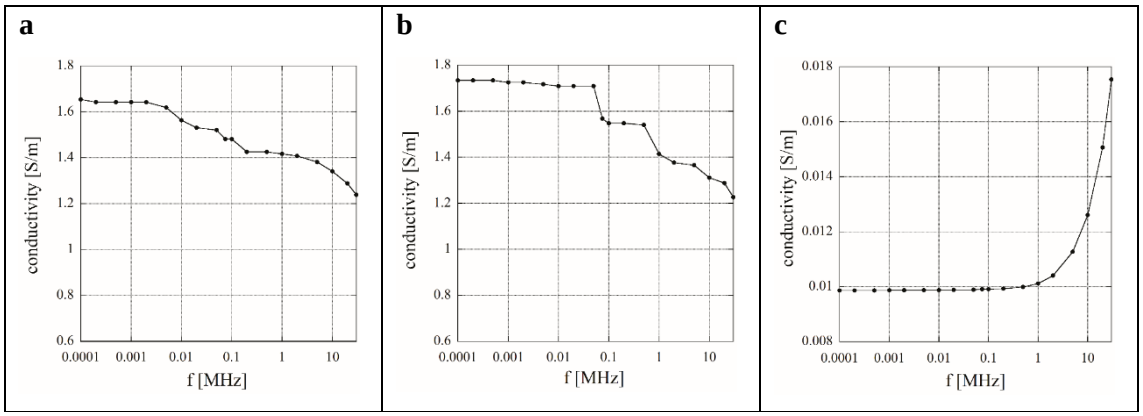

Figure 5. Electrical conductivity of tested samples in function of frequency: a) 30BAS800N2; 30SL800N2; c) 30SL1000N2.

The two samples fired in nitrogen at 800 °C (30SL800N_2 and 30BAS800N_2) exhibited an ohmic-inductive behaviour (negligible capacitance contribution in parallel with R) based on the measurements obtained on these samples. The measured inductance was of the order of 100 nH by applying as model the series of L and R, which is in agreement with the expected value associated with the connection threads from sample to LCR meter. From the experimental R data, it was possible to estimate the electrical conductivity (σ) from Ohm's law ($R=h/(\sigma \cdot A)$), with h and A height and area of top/bottom surface of disc samples).

On the other hand, the sample made with addition of soda-lime glass and fired at 1000 °C in nitrogen (30SL1000N_2) is ohmic-capacitive (parallel of R and C, with negligible contribution from the inductance of the threads). The electrical conductivity was also estimated from the measured resistance R, as done before. The relative permittivity (ε_r) was in turn estimated from the measured capacitance ($C = \varepsilon_0 \cdot \varepsilon_r \cdot A/h$, where ε_0 is the vacuum permittivity).

The data obtained from RLC circuit were confirmed by DC resistance measurements, from which it was possible to infer values of 2.1 S/m and 2.0 S/m for 30BAS800N_2 and 30SL800N_2, respectively, and $9.8 \cdot 10^{-3}$ S/m for 30SL1000N_2. The significant electrical conductivity presented by samples fired at 800 °C, combined with open porosity and presence of iron oxide phases indicate that these waste-derived materials could be potentially applied in electocatalytic reactions.

The shielding effectiveness (Figure 7-6) was higher for samples fired at lower temperature, which presented enhanced electrical conductivity. The sample 30BAS800N_2 (Figure 7-6a) exhibited a shielding effectiveness above 3 dB in all frequency range, with a peak value of about 10 dB near to 3 GHz. Furthermore, 30SL800N_2 (Figure 7-6b) presented a value of

shielding effectiveness below 1-2 dB than the one presented by 30BAS800N_2 in all frequency range, with a peak value of about 8 dB near to 3 GHz. In contrast, 30SL1000N_2 (Figure 7-6c), which was the sample with the lowest electrical conductivity, presented at low frequency a very low value of shielding effectiveness and at high frequency a peak value lower than 2.5 dB.

A previous investigation estimated the experimental error for the shielding effectiveness data: the measurement system without sample and a central slit of 5 mm showed a negligible value of shielding effectiveness for frequencies less than 1.5 GHz and a shielding effectiveness mostly below 1 dB in the frequency range 1.5-3 GHz (Maschio et al., 2016).

A shielding effectiveness above 3 dB, also at low frequency, as exhibited by samples fired at low temperature is significant, considering the results of other waste-derived materials, with shielding effectiveness of about 3 dB for frequencies above 8 GHz (G Bantsis et al., 2011). As previously mentioned, the shielding mechanism is most probably related to both electrical conductivity and 'magnetic' contribution, leading to a significant effect in an extensive frequency range. In contrast, Plasmastone-based foams fired in air at low temperature (Chapter 6) presented a significant shielding effectiveness only in the GHz range.

According to Chung (Chung, 2000), shielding effects due to conductivity are usually observed with a conductivity in the order of at least 0.01 S/m. In the case of conductive thin films, absorption loss is about 0 dB, and reflection plus multiple reflection losses derive from the product of thickness and electrical conductivity (Sarto and Tamburrano, 2006). Absorption losses, in contrast to reflection losses, increase with increasing frequency (Chung, 2000). Based on this, for all the three samples analysed, the shielding effectiveness is most probably due to reflection and multiple reflection losses at low frequency. On the other hand, some absorption due to the ferrimagnetisim of magnetite is the reason of the increase of shielding effectiveness values at high frequency.

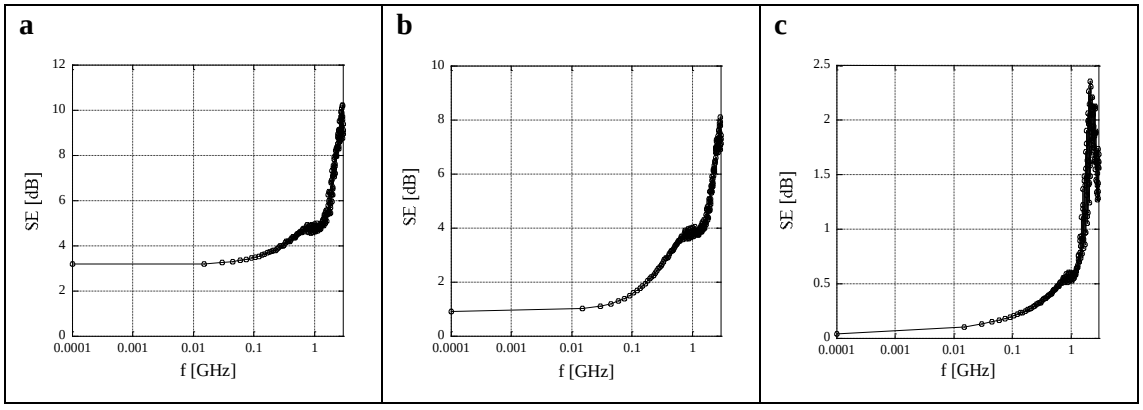

Figure 7-6. Shielding effectiveness of tested samples: a) 30BAS800N2, with thickness about 7 mm; 30SL800N2, with thickness about 7 mm; c) 30SL1000N2, with thickness about 8 mm.

The sample 30SL1000N_2, on the other hand, could be interesting for other applications. Figure 7-7 presents the measured values of relative permittivity, which exhibit a marked increase with decreasing frequency: below 1 kHz, the relative permittivity reached a particularly high level, approaching 1500 at 100 Hz. Magnetite and, in general, complex iron-rich oxides with the same structure (ferrites) have extremely high permittivity values (Abdullah and Yusoff, 1996; Radoń et al., 2018), due to an effect of interfacial polarisation, which is in turn originated from structural inhomogeneities and free charges ('hopping electrons'). The frequency sensitivity is associated to the trapping of the hopping electrons operated by the same inhomogeneities (Abdullah and Yusoff, 1996), at low frequency. Higher frequencies 'unlock' the electron exchanges.

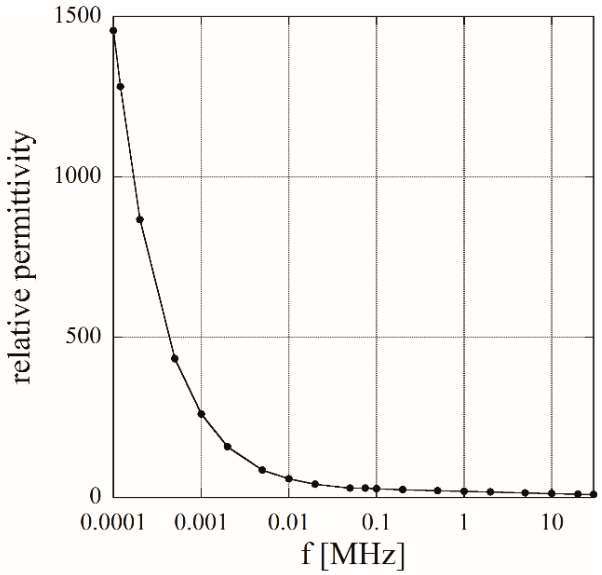

Figure 7-7. Relative permittivity for 30SL1000N_2.

The results presented in this chapter are preliminary. However, the shielding effectiveness of Plasmastone-based samples fired at 800 °C make them interesting as example of a new generation of safe, waste-derived materials that could minimise the human exposure to electromagnetic fields and reduce electromagnetic interferences. On the other hand, Plasmastone-based samples fired at 1000 °C, with particular dielectric characteristics, could be considered for novel electrical devices.

7.4. Conclusions

Fine Plasmastone powders mixed with soda-lime glass or boro-alumino-silicate glass were converted into foams by alkali activation, gel-casting and sintering in nitrogen, instead of air. Despite not representing a straightforward option for waste-derived materials, this study

demonstrated that firing in nitrogen was compensated due to stabilisation of heavy metals as well as to provide novel functionalities.

In contrast to Plasmastone/soda-lime glass-based foams fired in air, firing in nitrogen enhanced stabilisation of heavy metals even for compositions containing soda-lime glass and fired at 800 °C. This was most probably attributed to a different phase assemblage formed with increased silica content in the residual glass phase. Furthermore, firing in nitrogen favoured the precipitation of iron oxide as magnetite, specially at 800 °C: samples fired at this temperature exhibited several polymorphic variants of magnetite. Treatment in nitrogen also promoted functionalities, according to the firing temperature applied. Electrically conductive glass-ceramic foams were obtained by firing at 800 °C. These samples exhibited interesting electromagnetic shielding effectiveness values, in a wide frequency range with remarkable peaks at high frequency (about 8-10 dB for a sample with thickness of about 7 mm). This particular behaviour was probably due to overlapping contributions of magnetite (electrical and magnetic). Furthermore, firing at 1000 °C led to foams with particularly high relative permittivity (1500 at 100 Hz).

7.5. References

Abdullah, M.H., Yusoff, A.N., 1996. Complex impedance and dielectric properties of an Mg-Zn ferrite. J. Alloys Compd. 233, 129–135. https://doi.org/10.1016/0925-8388(96)80044-2

Bantsis, G., Sikalidis, C., Betsiou, M., Yioultsis, T., Bourliva, A., 2011. Ceramic building materials for electromagnetic interference shielding using metallurgical slags. Adv. Appl. Ceram. 110, 233–237. https://doi.org/10.1179/1743676111y.0000000009

Bantsis, G., Sikalidis, C., Betsiou, M., Yioultsis, T., Xenos, T., 2011. Electromagnetic absorption, reflection and interference shielding in X-band frequency range of low cost ceramic building bricks and sandwich type ceramic tiles using mill scale waste as an admixture. Ceram. Int. 37, 3535–3545. https://doi.org/10.1016/j.ceramint.2011.06.010

Bepari, S., Pradhan, N.C., Dalai, A.K., 2017. Selective production of hydrogen by steam reforming of glycerol over Ni/Fly ash catalyst. Catal. Today. https://doi.org/10.1016/j.cattod.2017.01.015

CES EduPack 2018, materials education software.

Chung, D.D.L., 2001. Electromagnetic interference shielding effectiveness of carbon materials. Carbon N. Y. 39, 279–285. https://doi.org/10.1016/S0008-6223(00)00184-6

Chung, D.D.L., 2000. Materials for Electromagnetic Interference Shielding. J. Mater. Eng. Perform. 9, 350–354. https://doi.org/10.1361/105994900770346042

Directive 2003/33/EC, 2003. , Official Journal of the European Communities.

Feinberg, J., Wenk, H.-R., Renne, P., Scott, G., 2004. Epitaxial relationship of clinopyroxene-hosted magnetite determined using electron backscatter diffraction (EBSD) technique,

American Mineralogist. https://doi.org/10.2138/am-2004-2-328

Fleet, M.E., 1982. The structure of magnetite: defect structure II. Acta Crystallogr. Sect. B Struct. Crystallogr. Cryst. Chem. 38, 1718–1723. https://doi.org/10.1107/S056774088200702X

Francis, A.A., 2005. Non-isothermal crystallization kinetics of a blast furnace slag glass. J. Am. Ceram. Soc. 88, 1859–1863. https://doi.org/10.1111/j.1551-2916.2005.00354.x

Gibson, L.J., Ashby, M.F., 1999. Cellular solids: structure and properties. Cambridge University Press, Cambridge, UK.

Kündig, W., Steven Hargrove, R., 1969. Electron Hopping in Magnetite, Solid State Communications. https://doi.org/10.1016/0038-1098(69)90729-7

Lazor, P., Shebanova, O.N., Annersten, H., 2004. High-pressure study of stability of magnetite by thermodynamic analysis and synchrotron X-ray diffraction. J. Geophys. Res. Solid Earth 109, 1–16. https://doi.org/10.1029/2003JB002600

Levinshtein, M., Rumyantsev, S., Shur, M., 1996. Handbook Series on Semiconductor Parameters, World Scientific. WORLD SCIENTIFIC, London. https://doi.org/10.1142/2046-vol2

Liu, Y., Gao, Z.F., Sun, Q., Zeng, Y.P., 2013. The structure-tunable synthesis and magnetic properties of Fe3O4 nanocrystals. Hyperfine Interact. 219, 107–112. https://doi.org/10.1007/s10751-013-0811-z

Marciello, M., Connord, V., Veintemillas-Verdaguer, S., Vergés, M.A., Carrey, J., Respaud, M., Serna, C.J., Morales, M.P., 2013. Large scale production of biocompatible magnetite nanocrystals with high saturation magnetization values through green aqueous synthesis. J. Mater. Chem. B 1, 5995–6004. https://doi.org/10.1039/c3tb20949k

Maschio, A., Bernardo, E., Desideri, D., Marangoni, M., Ponsot, I., Pontikes, Y., 2016. Shielding effectiveness of construction materials. Int. J. Appl. Electromagn. Mech. 52, 137–144. https://doi.org/10.3233/JAE-162089

Radoń, A., Łukowiec, D., Kremzer, M., Mikuła, J., Włodarczyk, P., 2018. Electrical conduction mechanism and dielectric properties of spherical shaped Fe3O4 nanoparticles synthesized by co-precipitation method. Materials (Basel). 11. https://doi.org/10.3390/ma11050735

Rawlings, R.D., Wu, J.P., Boccaccini, A.R., 2006. Glass-ceramics: Their production from wastes-A Review. J. Mater. Sci. 41, 733–761. https://doi.org/10.1007/s10853-006-6554-3

Redhammer, G.J., 2006. Single-crystal X-ray diffraction and temperature dependent 57Fe Mossbauer spectroscopy on the hedenbergite-aegirine (Ca,Na)(Fe2+,Fe3+)Si2O6 solid solution. Am. Mineral. 91, 1271–1292. https://doi.org/10.2138/am.2006.2173

Rincón, A., Desideri, D., Bernardo, E., 2018. Functional glass-ceramic foams from ‘inorganic gel casting’ and sintering of glass/slag mixtures. J. Clean. Prod. 187, 250–256. https://doi.org/10.1016/j.jclepro.2018.03.065

Romero, M., Hernández-Crespo, M.S., Rincón, J.M., 2008. Leaching behaviour of a glassy slag and derived glass ceramics from arc plasma vitrification of hospital wastes. Adv. Appl. Ceram. 108, 67–71. https://doi.org/10.1179/174367608x366337

Sarto, M.S., Tamburrano, A., 2006. Innovative test method for the shielding effectiveness measurement of conductive thin films in a wide frequency range. IEEE Trans. Electromagn. Compat. 48, 331–341. https://doi.org/10.1109/TEMC.2006.874664

Sundar, S., Mariappan, R., Piraman, S., 2014. Synthesis and characterization of amine modified magnetite nanoparticles as carriers of curcumin-anticancer drug. Powder Technol. https://doi.org/10.1016/j.powtec.2014.06.033

Voogt, F.C., Smulders, P.J.M., Wijnja, G.H., Niesen, L., Fujii, T., James, M.A., Hibma, T., 2002. NO2-assisted molecular-beam epitaxy of wustitelike and magnetitelike Fe oxynitride films on MgO(100). Phys. Rev. B 63, 1–11. https://doi.org/10.1103/physrevb.63.125409

Williamson, J., Tipple, J., Rogers, P.S., 1968. Influence of iron oxides on kinetics of crystal growth in CaO-MgO-Al2O3-SiO2 glasses. J. Iron Steel Inst. 206, 898–903.

Žáček, V., Skála, R., Chlupáčová, M., Dvořák, Z., 2005. Ca-Fe3+-rich, Si-undersaturated buchite from Zelenky, North-Bohemian Brown Coal Basin, Czech Republic. Eur. J. Mineral. 17, 623–634. https://doi.org/10.1127/0935-1221/2005/0017-0623

Chapter 8. Waste glass/Plasmastone lightweight aggregates by alkali activation and fast firing

Part of this chapter was based on P. Rabelo Monich, H. Lucas, B. Friedrich, M. Segata, A. Morbi, E. Bernardo, Upcycling of vitrified residues by alkali activation and sinter-crystallization, 17th International Waste Management and Landfill Symposium, Cagliari (Italy), 30 September-04 October 2019.

8.1. Introduction

In this study, the concept of alkali activation of glass powders followed by firing was extended to the development of lightweight aggregates made with Plasmastone mixed with soda-lime glass. The waste-derived glasses aggregates were developed by adding the almost dried 'gelified' suspension of an activated mixture of soda-lime glass/Plasmastone to a granulator, without addition of a surfactant. Fine soda-lime glass powders were then poured in order to evolve the alkali-activated material with a 'shell' of glass. After drying, the aggregates were finally fired by a fast heating treatment. During firing, the compounds formed due to alkali activation were decomposed and remained trapped within the glass structure, leading to the self-foaming of the material.

Soda-lime glass was added in order to improve densification and spheroidization by viscous flow (Toniolo et al., 2018), as well as to increase mechanical and physical properties of the aggregates (Kourti and Cheeseman, 2010; Tuan et al., 2013). Moreover, this glass also increased the formation of compounds upon alkali activation, as indicated by Chapter 5. In this way, a higher quantity of compounds are decomposed during firing, promoting the 'self-foaming' of the material, thus increasing the porosity of the material.

8.2. Experimental procedure

8.2.1. Production of lightweight aggregates

Fine powders of waste glass (70 wt% soda-lime glass/30 wt% Plasmastone) were added to an alkaline solution of 5 M NaOH/KOH (ratio 1:1) and mixed at 400 rpm. The overall solid content of the suspension was 68 wt%. After 2h of mixing, the suspension was cured at 75 °C for 40 min. The almost dried alkali-activated material was then added to a granulator, which was responsible for the spheroidization of the granules. Fine powders of soda-lime glass were also poured to the granules in order to help in the granulation process and to seal the granules. The obtained aggregates were dried overnight at 100 °C and covered with a slurry of metakaolin and water before firing. Finally, the granules were directly introduced inside a furnace at the specified firing temperature for 30 min in order to densify the material and decompose the compounds formed due to alkali activation.

Preliminary firing tests were firstly made to assess the firing temperature of the granules, at 750 °C, 800 °C, 850 °C or 900 °C. The optimal firing temperature was then selected based on particle density and water absorption after soaking period of 24h and on crush test. Four aggregates presenting the same size from each group were submitted to a crush test in order to assess the peak load required to break the samples. These values were taken as an indicative of the materials strength. After selecting the optimal firing temperature, the optimised granules were further characterised and applied in the production of lightweight mortars.

8.2.2. Development and characterisation of lightweight mortars

The lightweight mortars were made by mixing cement (52,5R type I of cement plant of Rezzato, Italy) and water with the developed lightweight aggregates. In addition, the following admixtures were also added: a water reducing agent, a foaming agent and a viscosity modifier agent. The water/cement ratio was equal to 0.67 for both mixtures. The main difference between both mixtures concentrated on the quantity of aggregates and water reducing agent added, as shown by Table 8-1:

Table 8-1. Mass of the materials applied on the production of the mortars.

	Mortar 1	Mortar 2
Cement (g)	1500	1500
Water (g)	1000	1000
Aggregates (g)	1300	2500
Superplasticiser (g)	0.0	7.5
Foaming agent (g)	2.0	2.0
Viscosity modifier (g)	2.0	2.0

The compressive strength, density and thermal conductivity of the mortars were measured after 7 days of drying. The thermal conductivity was assessed by an ISOMET MODEL 2104 heat transfer analyser, while the compression test was performed following the EN UNI 196-1. As retained water in a cementitious material may increase thermal conductivity, the mortars were dried for 2 more days at 105 °C (Ferrándiz-Mas et al., 2014). After this period, the thermal conductivity and density were assessed again.

8.3. Results and discussion

Table 8-2 presents the apparent particle density (ρ_a), oven-dried particle density (ρ_{rd}), saturated surface dried particle density (ρ_{ssd}), water absorption (WA) and peak load of the aggregates fired at different temperatures:

Table 8-2. Particle density, water absorption and peak load of the lightweight aggregates.

Firing temperature	ρ_a (g/cm^3)	ρ_{rd} (g/cm^3)	ρ_{ssd} (g/cm^3)	WA (%)	Peak load (N)
750 °C	0.8	0.7	0.8	9.2	150 ± 2
800 °C	0.8	0.8	0.8	10.2	202 ± 5
850 °C	0.9	0.7	0.9	19.2	174 ± 4
900 °C	0.9	0.7	0.9	26.6	150 ± 2

All four groups of lightweight aggregates were found to be quite light, with particle density below 2 g/cm^3, as required by the Norm EN 13-055 for lightweight aggregates (*BS EN 13055:2016*). The apparent density overall increased with firing temperature, probably due to sinter-crystallisation. Furthermore, these results indicate that the process based on alkali activation, granulation and fast firing is adequate to produce lightweight aggregates, without using an expansive agent responsible for bloating.

Regarding water absorption, the values were comparable to the ones of commercially available lightweight aggregates Lytag, specially for aggregates fired below 800 °C (Cheeseman and Virdi, 2005; Kourti and Cheeseman, 2010). In fact, water absorption actually increased with the firing temperature. A possible explanation for this could be related to the softening of the 'shell' of soda-lime glass with temperature: once the firing temperature increases, the viscosity of the soda-lime glass 'shell' decreases and the solubility of the gases in the glass increases. However, once the samples are removed from the furnace, the solubility of the gases will dramatically decrease due to increase of the viscosity of the glass. This may generate the formation of bubbles in the 'shell', thus increasing the open porosity which is associated to water absorption (Shelby, 2005).

The water absorption should be minimised in order to avoid the formation of micro-cracks in the aggregate/cement interface in early hydration (Lo et al., 1999). Based on this, samples fired at 750 °C or 800 °C would be more convenient. 800 °C was finally selected as the optimal temperature, based on a better performance of aggregates fired at this temperature on the crush test (see Table 8-2).

Figure 8-1. Aggregates made by mixture of soda-lime glass and Plasmastone.

Furthermore, the process of alkali activation followed by granulation and fast firing yielded mostly rounded granules, with a wide particle size distribution (see Figure 8-1). The rounder shaper of the granules was a result of the granulation process and also due to the softening of the soda-lime glass 'shell' during firing.

The particle size distribution (Figure 8-2) is also consistent to a wide distribution of size classes, with a greater volume of granules presenting sizes between 8 and 18 mm:

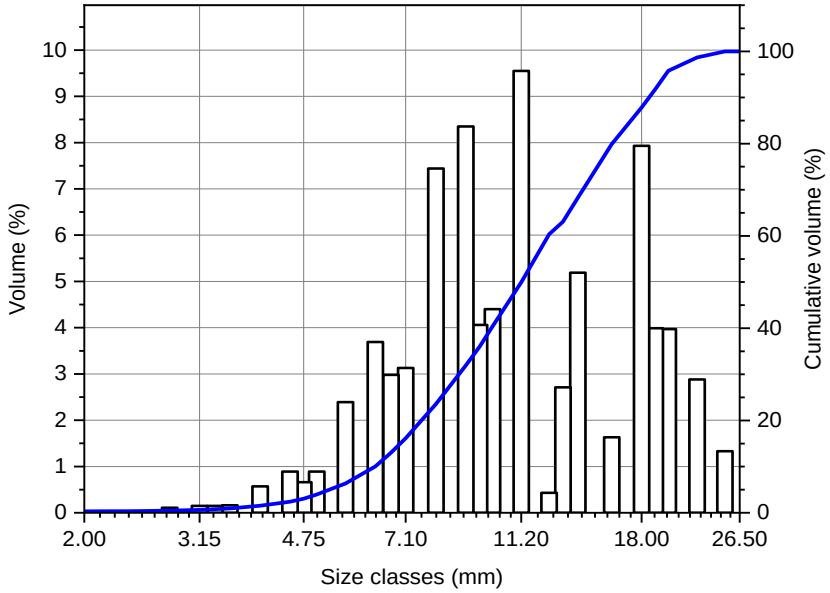

Figure 8-2. Particle size distribution of the aggregates fired at 800 °C.

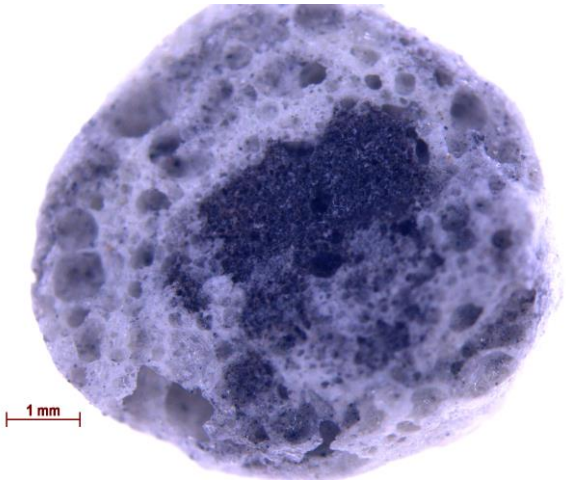

Figure 8-3. Internal structure of the aggregates fired at 800 °C.

Figure 8-3 shows the internal structure of the lightweight aggregates. The darker region corresponds to the mixture of soda-lime glass/Plasmastone which is surrounded by a shell of soda-lime glass (lighter region). In addition, the presence of a porous structure indicates that the

compounds formed due to alkali activation were decomposed during firing, releasing gases responsible for the self-foaming.

The XRD patterns (Figure 8-4) of not fired as well as of fired aggregates indicate that the hardening step was probably originated due to formation of gismondine ($CaAl_2Si_2O_8 \cdot 4H_2O$, PDF#00-039-1373) and calcite ($CaCO_3$, PDF#86-2342), as already observed for Plasmastone/waste-glass green foams (Chapter 5). These two phases were decomposed upon firing at high temperatures, which led to the self-foaming of the material, as observed in Figure 8-3. Quartz (SiO_2, PDF#89-8935) was presented in the fired and not fired aggregates, probably associated to recycled soda-lime glass with quartz traces. Regarding the fired foams, the XRD pattern indicates a highly amorphous content of the sample, due to the fast heating treatment performed at low temperature (only 800 °C), as well as high content of soda-lime glass applied (Rincón et al., 2017). It was only possible to detect wollastonite ($CaSiO_3$, PDF#84-0655), anorthite ($Ca(Al_2Si_2O_8)$, PDF#073-0265) and sodium aluminium silicate ($Na_{1.45}Al_{1.45}Si_{0.55}$, PDF #00-049-0002), in traces.

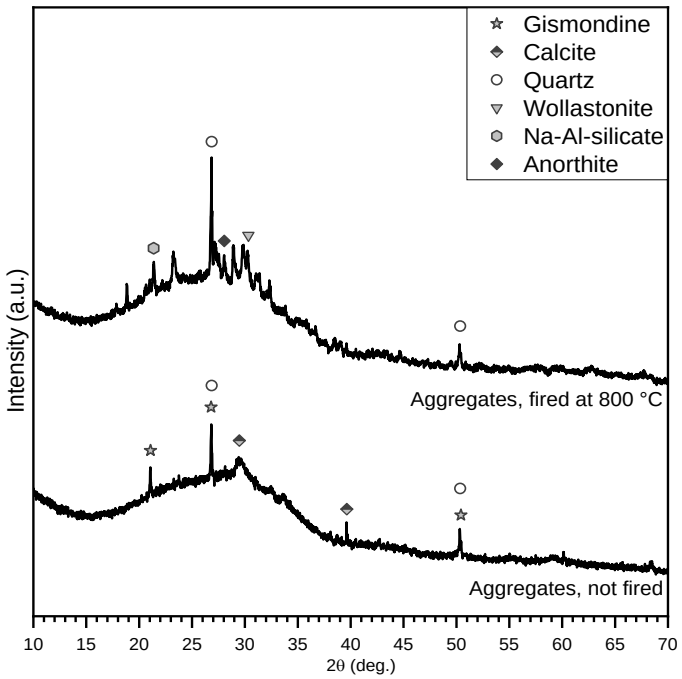

Figure 8-4. XRD patterns of fired and not fired aggregates.

As Plasmastone is a waste-derived glass, it is essential to assess the stability of materials made with this glass. The results of the leaching test (Table 8-3), made on aggregates with particle size below 4 mm, show that the content of heavy metals leached from the lightweight aggregates is within the values allowed for waste acceptable at landfills for non-hazardous and inert waste. The low leaching of heavy metals indicates that the 'shell' of soda-lime glass may have contributed to increase the stability by sealing the surface of the aggregates, thus preventing leaching of pollutants.

Table 8-3. Leaching test results performed on the foams and on the aggregates (ppm).

	Limit values for inert waste	**Limit values for non-hazardous waste**	**Lightweight aggregates**
As	0.5	2	0.0487
Ba	20	100	0.0033
Cd	0.04	1	0.0003
Cr total	0.5	10	0.0144
Cu	2	50	0.0081
Hg	0.01	0.2	<0.0004
Mo	0.5	10	<0.0033
Ni	0.4	10	0.2240
Pb	0.5	10	0.0059
Sb	0.06	0.7	<0.0099
Se	0.1	0.5	<0.0122
Zn	4	50	<0.0203

The properties of the developed lightweight mortars are presented in Table 8-4. Drying for 7 days contributed to decrease the density of Mortars 1 and 2 in 3% and 2%, respectively. By applying the accelerated drying (2 days at 105 °C), the density of Mortars 1 and 2 were decreased in 16% and 13%, respectively.

Regarding the thermal conductivity of the mortars, the values measured were below 0.3 W/mK. These values are below the thermal conductivity of lightweight mortars containing expanded polystyrene and paper sludge ash (Ferrándiz-Mas et al., 2014) and are comparable to mortars made with addition of granulated foam glass (Pichór et al., 2019). Furthermore, the addition of more aggregates to the mixture (Mortar 2) decreased the thermal conductivity of the mortars. Finally, the accelerated drying helped to decrease the thermal conductivity of mortars 1 and 2 in 38% and 35%, respectively. Furthermore, it is possible to build a building wall (60 cm of thickness) with a thermal conductivity of about 0.1 W/mK which complies the energy efficiency standards in almost every European country.

The compressive strength (Table 8-4) was found to be 7.0 MPa for Mortar 1, while the addition of more aggregates (Mortar 2) contributed to decrease the compressive strength to 2.4 MPa. Despite the low strength values of the mortars, one must consider the low thermal

conductivity values for these mortars. Furthermore, mortars with compressive strength of 5 MPa may already be adequate to build a two-floors building. Therefore, Mortar 1 would be a more convenient choice due to its higher compressive strength, despite presenting lower thermal insulation than Mortar 2.

Table 8-4. Properties of the developed lightweight mortars.

	Mortar 1	**Mortar 2**
Density		
Density at fresh state (kg/m^3)	970	800
Density after drying (kg/m^3)	942	786
Density after accelerated drying (kg/m^3)	792	683
Thermal conductivity (λ)		
λ after drying (W/mK)	0.3	0.2
λ after accelerated drying (W/mK)	0.2	0.1
Strength		
Compressive strength after drying (MPa)	7.0	2.4

8.3. Conclusions

Alkali activation followed by granulation and sinter-crystallisation could be successful applied to valorise waste glasses into safe lightweight aggregates with a wide distribution of particle size. The low thermal conductivity of the mortars indicates that the developed lightweight aggregates could be potentially applied in cement-based products to increase the thermal insulation in buildings.

8.4. References

BS EN 13055:2016 Lightweight aggregates, 2016. BSI Standards Publication.

Cheeseman, C.R., Virdi, G.S., 2005. Properties and microstructure of lightweight aggregate produced from sintered sewage sludge ash. Resour. Conserv. Recycl. 45, 18–30. https://doi.org/10.1016/j.resconrec.2004.12.006

Ferrándiz-Mas, V., Bond, T., García-Alcocel, E., Cheeseman, C.R., 2014. Lightweight mortars containing expanded polystyrene and paper sludge ash. Constr. Build. Mater. 61, 285–292. https://doi.org/10.1016/j.conbuildmat.2014.03.028

Kourti, I., Cheeseman, C.R., 2010. Properties and microstructure of lightweight aggregate produced from lignite coal fly ash and recycled glass. Resour. Conserv. Recycl. 54, 769–775. https://doi.org/10.1016/j.resconrec.2009.12.006

Lo, Y., Gao, X.F., Jeary, A.P., 1999. Microstructure of pre-wetted aggregate on lightweight concrete. Build. Environ. 34, 759–764. https://doi.org/10.1016/S0360-1323(98)00060-2

Pichór, W., Kamiński, A., Szołdra, P., Frąc, M., 2019. Lightweight Cement Mortars with Granulated Foam Glass and Waste Perlite Addition. Adv. Civ. Eng. 2019, 1–9. https://doi.org/10.1155/2019/1705490

Rincón, A., Giacomello, G., Pasetto, M., Bernardo, E., 2017. Novel 'inorganic gel casting' process for the manufacturing of glass foams. J. Eur. Ceram. Soc. 37, 2227–2234. https://doi.org/10.1016/j.jeurceramsoc.2017.01.012

Shelby, J.E., 2005. Introduction to Glass Science and Technology, Second Edi. ed. The Royal Society of Chemistry, Cambridge.

Toniolo, N., Romero, A.R., Marangoni, M., Binhussain, M., Boccaccini, A.R., Bernardo, E., 2018. Glass-ceramic proppants from sinter-crystallisation of waste-derived glasses. Adv. Appl. Ceram. 117, 127–132. https://doi.org/10.1080/17436753.2017.1394019

Tuan, B.L.A., Hwang, C.L., Lin, K.L., Chen, Y.Y., Young, M.P., 2013. Development of lightweight aggregate from sewage sludge and waste glass powder for concrete. Constr. Build. Mater. 47, 334–339. https://doi.org/10.1016/j.conbuildmat.2013.05.039

PART IV - Valorisation of MSWI bottom ash-based glasses

Chapter 9. Porous vitrified MSWI bottom ash-based glass-ceramics by alkali activation and sinter-crystallisation

This chapter was based on P. Rabelo Monich, F. Dogrul, H. Lucas, B. Friedrich, E. Bernardo, Strong porous glass-ceramics from alkali activation and sinter-crystallisation of vitrified MSWI bottom ash. Detritus (2019) in press

9.1. Introduction

In this study, the process of alkali activation, gelation and sinter-crystallisation was further extended to produce porous glass-ceramics made with vitrified bottom ash from Strategy 1. In this strategy, no mechanical separation was applied before vitrification of MSWI bottom ash. After the activation of fine powders of vitrified bottom ash glass in a NaOH solution of low molarity (up to 1.5 M), foams were easily produced by intensive mechanical stirring, with the support of a surfactant, and stabilised by gelation. The obtained foamed material was further consolidated by a firing treatment, at 800-900 °C. Furthermore, the addition of recycled soda-lime glass allowed to maintain alkali activation at low molarity and also firing at low temperature. However, the mechanical properties and the stabilisation of heavy metals were reduced. The increase in molarity of the alkaline solution, on the other hand, enhanced the porosity and the strength of foams made with only vitrified bottom ash.

9.2. Experimental procedure

Glass-ceramic foams were developed by firstly mixing at 400 rpm fine powders of vitrified bottom ash or 90 wt% vitrified bottom ash/10 wt% soda-lime glass an alkaline solution of NaOH for 3h. The overall solid loading content applied was of 70 wt%.

Table 9-1. Different approaches applied in the production of samples.

Group of samples	**A**	**B**	**C**	**D**
Alkaline solution	1 M NaOH	1.5 M NaOH	1 M NaOH	1 M NaOH
Soda-lime glass added	-	-	10%	10%
Firing temperature	900 °C	900 °C	900 °C	800 °C

After the partial dissolution of the fine powders, 4 wt% of surfactant (Triton X-100, (polyoxyethylene octyl phenyl ether – $C_{14}H_{22}O(C_2H_4O)_n$, n = 9–10, Sigma-Aldrich, Gillingham, UK) was added to the slurry, which was then submitted to an intensive mechanical stirring at 2000 rpm. The foamed suspension was dried at 40 °C for 48h, demoulded and fired at 800 °C or

900 °C, with heating rate of 10 °C/min and holding time of 1h. Table 9-1 presents the different types of groups developed in the present study.

9.3. Results and discussion

DSC analysis (Figure 9-1) made on fine powders (below 75 µm) of vitrified bottom ash indicates that the crystallisation temperature (T_c) lies around 925 °C. Based on this, firing treatments were performed at 900 °C for foams from groups A, B and C. Foams from group C (made with addition of soda-lime glass) were fired at 800 °C, in order to minimise the energy consumption. Furthermore, the DSC curve of coarse vitrified bottom ash (Figure 9-1) does not present a crystallisation peak. This indicates that this glass is sensitive to surface crystallisation (E. Bernardo, 2008).

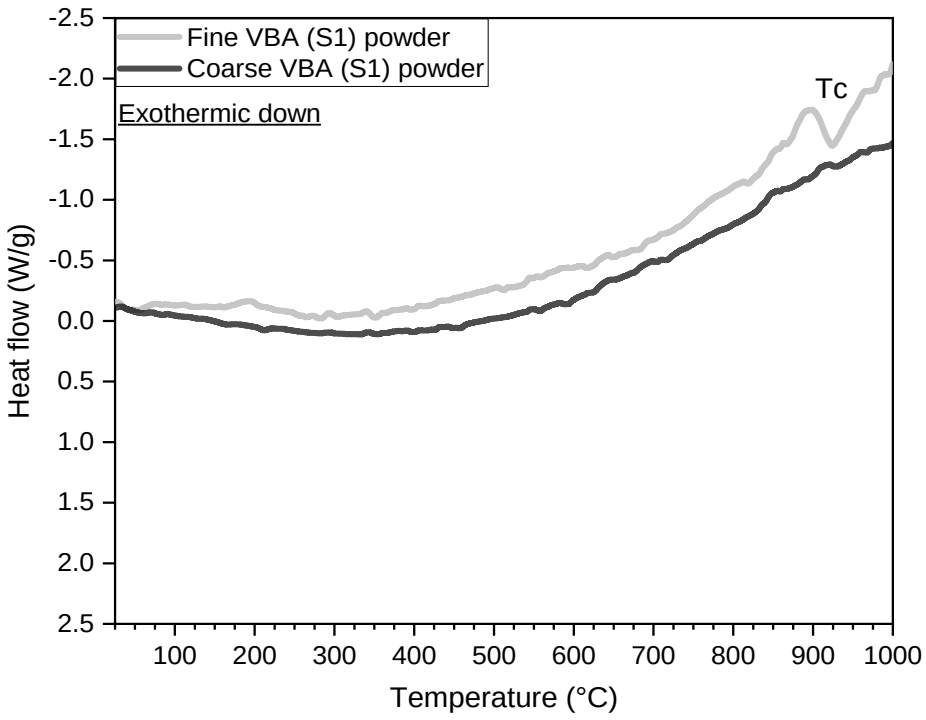

Figure 9-1. DSC curves of fine and coarse powder of vitrified bottom ash (S1).

FTIR analysis performed on not fired foams from groups A, B and C/D (Figure 9-2) helps to understand the hardening mechanism of the suspensions made with vitrified bottom ash. In contrast to FTIR analysis of activated Plasmastone (Chapter 5), signals consistent to the formation of C-S-H compounds (peaks at 3458 cm^{-1} and at 1680 cm^{-1}, corresponding to O-H stretching and O-H bending) are hardly visible, even considering the strongest activation (Group B, 1.5 M NaOH). On the other hand, signals consistent to carbonates (main peak at 1450 cm^{-1}, attributed to the stretching vibration of C-O) were visible in all groups of not fired foams

(Rincon Romero, Salvo, & Bernardo, 2018). This finding is consistent to a previous study (Rincon Romero et al., 2018) in which the hardening of weak alkali activated vitrified bottom ash was mainly attributed to carbonation. Signals consistent to C-H_2 stretching (peak at 2900 cm^{-1}) were also visible in all not fired foams due to the addition of the surfactant. The FTIR spectra of not activated vitrified bottom ash presents a band between 800 cm^{-1} and 1260 cm^{-1} attributed to the asymmetric Si-O-Si stretching vibration (Paola Pisciella & Pelino, 2005). Alkali activation made this band slightly narrower, while firing led to its separation in more peaks (probably due to crystallisation) (Rincon Romero et al., 2018).

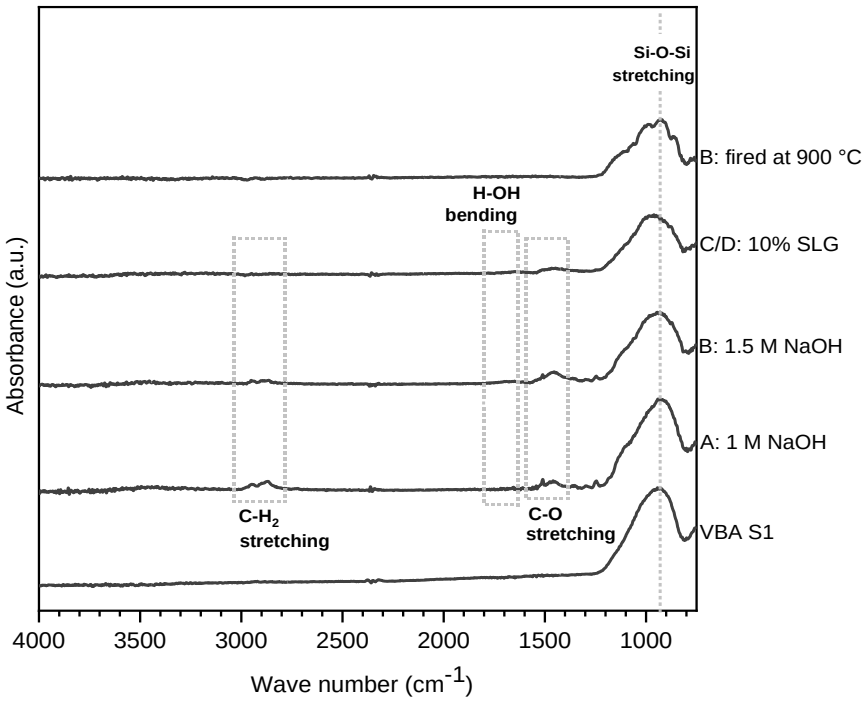

Figure 9-2. FTIR spectra of: vitrified bottom ash, foams from groups A, B and C/D before firing and from group B after firing.

The XRD patterns of not fired materials (Figure 9-3) provided more information on the reaction products formed due to alkali activation. In foams from group A (alkali activation with 1 M NaOH), it was possible to detect only trona ($Na_3H(CO_3)_2 \cdot 2(H_2O)$, PDF#00-029-1447) as a newly formed phase. This is in agreement with a previous study regarding vitrified bottom ash activated by a solution of 2.5 M NaOH (Rincon Romero et al., 2018).

The molarity of the alkali solution was slightly increased to 1.5 M NaOH (Figure 9-3, group B) in order to facilitate the handling of foams upon demoulding. This favoured the formation of more phases, contributing to the hardening: signals consistent to meionite ($(Ca_{3.4}Na_{0.64})(Al_{5.43}Si_{6.59})O_{24}(CO_3)_{0.88}O_{0.12}$, PDF#75-1222), sodium carbonate (Na_2CO_3, PDF#86-0315), tilleyite ($(Ca_5Si_2O_7(CO_3)_2$, PDF#73-2117) and sodium aluminium silicate carbonate

($Na_8Al_6Si_6O_{24}CO_3$, PDF#00-024-1045) were detected. Increasing the molarity of the alkaline solution favoured some dissolution of vitrified bottom ash, which contributed to the incorporation of Ca^{2+}, Al^{3+} and Si^{4+} in carbonates. However, it did not lead to any practical formation of non-carbonate phases.

Foams from group C/D (Figure 9-3) were made with addition of 10 wt% soda-lime glass in order to maintain the low molarity of the alkaline solution (1 M NaOH), simultaneously increasing the strength of the foams in the green state. The addition of recycled glass turned the newly formed phases from being sodium based to being calcium based, as calcium carbonate ($CaCO_3$, PDF#86-2339) was evidently detected. Gismondine ($CaAl_2Si_2O_8 \cdot 4H_2O$, PDF#20-0452) was also detected in traces. This phase has already been found in geopolymers from granulated blast furnace slag (Zhang, Zhao, Li, & Xu, 2008).

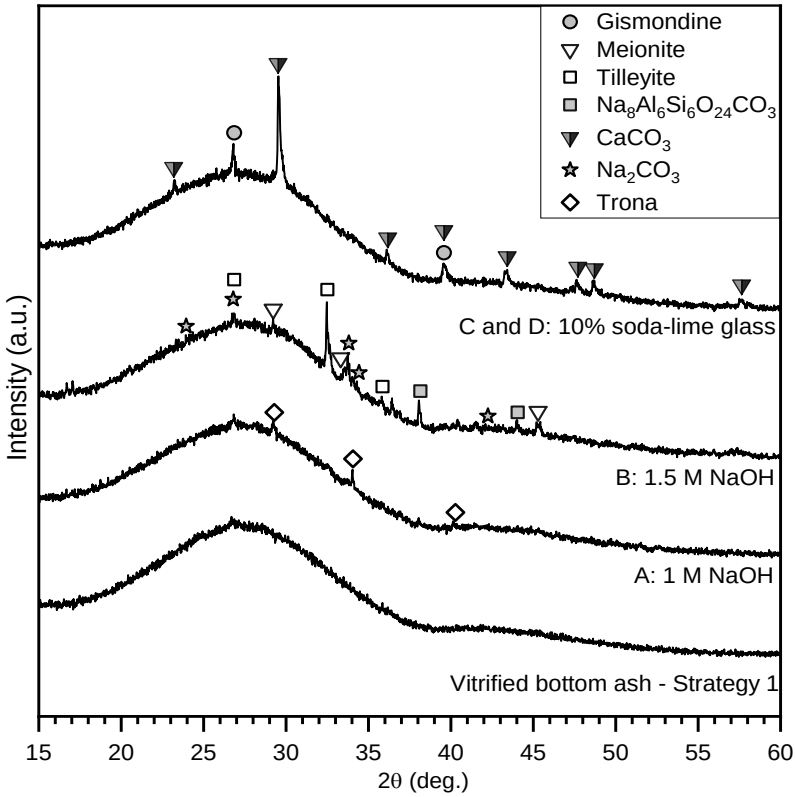

Figure 9-3. XRD patterns of vitrified bottom ash and of not fired foams.

The different formulations applied also had some impacts after firing. The XRD patterns (Figure 9-4) of foams fired at 900 °C indicated signals consistent to those of labradorite ($Ca_{0.64}Na_{0.35}(Al_{1.63}Si_{2.37}O_8)$, PDF#83-1371) and gehlenite ($Ca_2(Al(AlSi)O_7)$, PDF#74-1607). These two phases have already been previously detected in plasma vitrified MSWI fly ashes-derived glass-ceramics (Enrico Bernardo et al., 2011). In addition, an Al-rich pyroxene (augite, $CaMg_{0.7}Al_{0.6}Si_{1.7}O_6$, PDF#78-1392) was also detected in the foams fired at 900 °C. Pyroxene

solid solutions are quite typical in waste-derived glass-ceramics (Park, Moon, & Heo, 2003), as well as plagioclase and melilite solid solutions, which comprise labradorite and gehlenite, respectively.

The increase of molarity of the alkaline solution and the addition of soda-lime glass also influenced the crystallisation: compared to foams from group A, foams made with a stronger alkali activation (group B) and with soda-lime glass addition (group C) presented more marked peaks, with distinctive differences: in group B, all peaks became more intense. On the other hand, in group C, gehlenite had a more significant increase. The enhanced crystallisation is probably associated to an increase of overall alkali content in both groups B (1.5 M NaOH) and C (1 M NaOH, addition of 10% soda-lime glass), which may have decreased the apparent activation energy for crystal growth, as already seen for alkali-rich glasses (Watanabe, Hashimoto, Hayashi, & Nagata, 2008). Finally, the firing below the crystallisation temperature of vitrified bottom ash led simply to amorphous foams (group D).

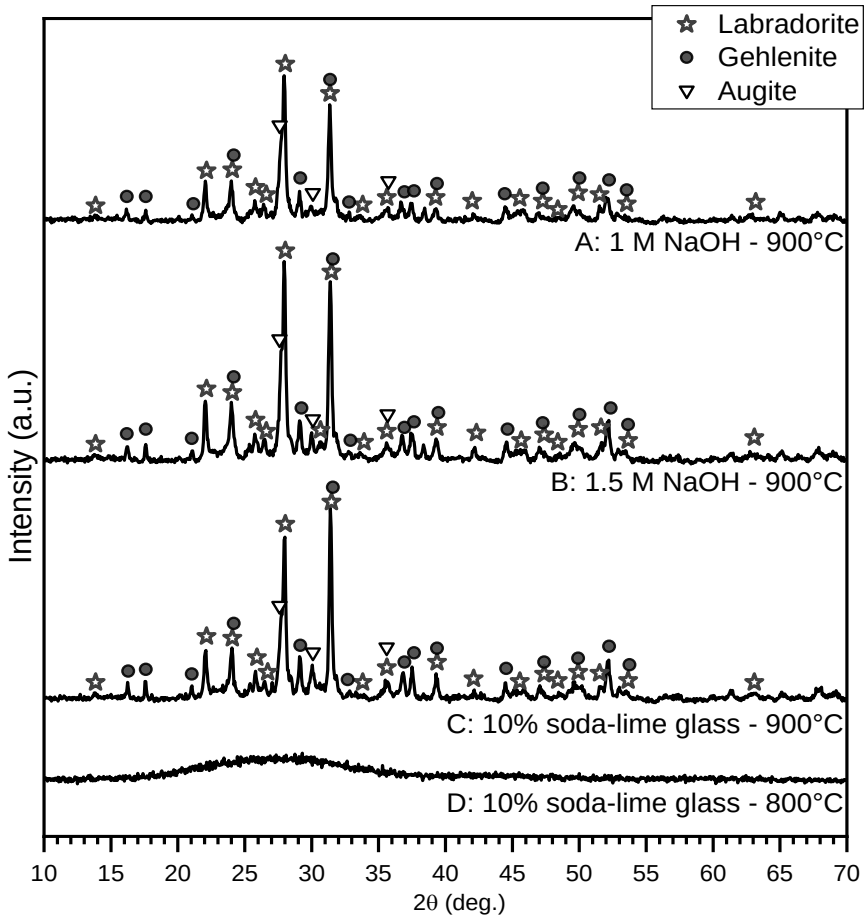

Figure 9-4. XRD patterns of the waste-derived glass-ceramics.

Figure 9-5 presents the micrographs of the four groups of porous glass-ceramics. The foams are highly porous, with interconnected cells. Furthermore, the increase in molarity of the

alkaline solution from 1 M (group A) to 1.5 M (group B) lead to a decrease in the pore size. This can be attributed to the increase in hardening with increase in molarity: as shown by Figure 9-3, foams from group B formed more products due to alkali activation than foams from group A. This means that in foams from group B, the viscosity of the 'gelified' slurry is higher, which helped to prevent more efficiently the collapse of the bubbles entrapped after foaming. This can certainly help to produce foams with smaller pore size.

The firing temperature also influenced the pore size distribution, as shown by porous glass-ceramics made with addition of soda-lime glass (groups C and D): foams fired at 800 °C (group D, Figure 9-5d) present a larger pore size than foams fired at 900 °C (group C, Figure 9-5c). As indicated by the XRD patterns (Figure 9-4), foams from group D were still amorphous. This indicates that the softened glass could have contributed to reshape the pores, before crystallisation. Once the firing temperature was increased to 900 °C (group C), the precipitation of crystals enhanced the viscosity of the softened glass, thus preventing a further reshaping of pores at higher temperatures (Rincón, Giacomello, Pasetto, & Bernardo, 2017).

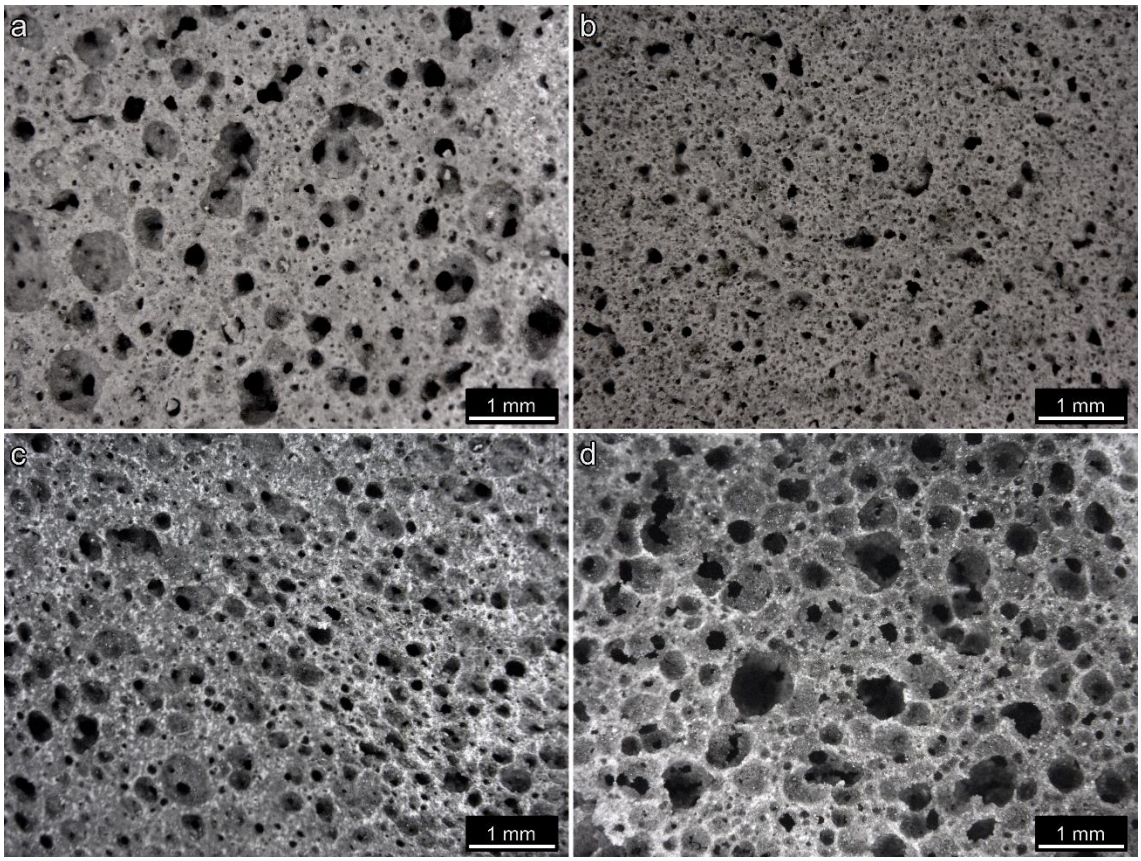

Figure 9-5. Micrographs of porous glass-ceramics from: a) group A; b) group B; c) group C; d) group D.

Table 9-2 is in agreement with the micrographs of the foams (see Figure 9-5): the porous glass-ceramics present porosity higher than 58 vol%, mainly open. In addition, the increase of

molarity of the alkaline solution passing from 1 M (group A) to 1.5 M (group B) increased the porosity in almost 10 vol%. Despite the increase in porosity, foams from group B are still stronger than foams from group A, with compressive strength reaching 8.1 MPa. This could be associated to the decrease of pore size with increase of molarity: as already seen in another study, foams with smaller macro-pore size presented higher compressive strength than foams with a larger macro-pore size up to a certain level of porosity (Liu, 1997).

The increase in firing temperature from 800 °C (group D) to 900 °C (group C) for foams made with soda-lime glass did not change the amount of porosity. However, the compressive strength of the foams increased in 38% due to crystallisation.

Table 9-2. Porosity, density and mechanical properties of the vitrified bottom ash-derived foams.

Group of samples	**A**	**B**	**C**	**D**
Alkaline solution	1 M NaOH	1.5 M NaOH	1 M NaOH	1 M NaOH
Soda-lime glass added	-	-	10%	10%
Firing temperature (°C)	900	900	900	800
Density determinations				
ρ_{geom} (g/cm^3)	1.04 ± 0.08	0.85 ± 0.04	1.03 ± 0.03	1.07 ± 0.09
$\rho_{apparent}$ (g/cm^3)	2.28 ± 0.01	2.59 ± 0.03	2.45 ± 0.04	2.54 ± 0.04
ρ_{true} (g/cm^3)	2.52 ± 0.00	2.62 ± 0.00	2.53 ± 0.01	2.57 ± 0.00
Porosity distribution				
Total porosity (vol%)	58.8	67.4	59.3	58.6
Open porosity (vol%)	54.4	67.0	58	58.1
Closed porosity (vol%)	4.4	0.4	1.3	0.5
Strength determinations				
σ_{comp} (MPa)	7.0 ± 2.7	8.1 ± 1.1	7.3 ± 1.8	5.3 ± 2.0

The very low leaching of heavy metals in vitrified bottom ash from Strategy 1 (Table 9-3) confirms that the vitrification of MSWI bottom ash effectively yielded a safe glass. Regarding foams made with only vitrified bottom ash (groups A and B), the leaching of heavy metals was below the limit values for inert and non-hazardous waste.

On the other hand, foams made with soda-lime glass (groups C and D) could only be accepted as non-hazardous waste, due to high leaching of Sb. This may be associated to the increase in alkalinity of the residual glass, due to the addition of soda-lime glass, thus favouring its dissolution, analogous to what was observed in Chapter 5 for Plasmastone/soda-lime glass foams fired in air (P. Pisciella, Crisucci, Karamanov, & Pelino, 2001).

Table 9-3. Leaching test results of vitrified bottom ash from strategy 1 and of the four groups of porous glass-ceramics (ppm).

	Limit values for inert waste	**Limit values for non-hazardous waste**	**VBA (S1)**	**A**	**B**	**C**	**D**
As	**0.5**	2	0.0076	<0.0049	<0.0049	<0.0049	<0.0049
Ba	**20**	100	0.0054	0.0354	0.0696	0.0041	0.0061
Cd	**0.04**	1	<0.0002	0.0004	<0.0002	<0.0002	<0.0002
Cr total	**0.5**	10	0.0066	0.0072	0.0021	0.0020	0.0146
Cu	**2**	50	0.0219	0.0128	0.0024	0.0003	0.002
Hg	**0.01**	0.2	<0.0004	<0.0004	<0.0004	0.0023	0.0015
Mo	**0.5**	10	0.0184	<0.0033	<0.0033	<0.0033	<0.0033
Ni	**0.4**	10	0.0017	0.0042	<0.0014	<0.0014	<0.0014
Pb	**0.5**	10	0.0068	0.0111	0.0072	<0.0047	<0.0047
Sb	**0.06**	0.7	0.0339	0.0151	0.0320	0.3518	0.2316
Se	**0.1**	0.5	<0.0122	0.0163	0.0221	<0.0122	<0.0122
Zn	**4**	50	<0.0203	<0.0203	<0.0203	<0.0203	<0.0203

9.4. Conclusions

This study showed the feasibility of applying the technique based on alkali activation, gel-casting and firing to produce strong glass-ceramic foams made with vitrified bottom ash. Furthermore, the costs of the process were minimised by applying a low molarity of the alkaline solution and by firing the foams at low temperature. The hardening of suspension has been attributed mainly to the formation of carbonates, unlike previous experiences made with Plasmastone. Furthermore, the slight increase in molarity from 1 M to 1.5 M yielded stronger foams with higher porosity and smaller pore size, which could potentially be applied as thermal and acoustic insulators in buildings. Finally, the incorporation of recycled soda-lime glass allowed to maintain alkali activation at low molarity and sintering at lower temperature. However, this was accompanied with reduction of mechanical properties and increase in leaching of heavy metals.

9.5. References

Bernardo, E. (2008). Fast sinter-crystallization of a glass from waste materials. *Journal of Non-Crystalline Solids*, *354*(29), 3486–3490. http://doi.org/10.1016/j.jnoncrysol.2008.03.021

Bernardo, E., Dattoli, A., Bonomo, E., Esposito, L., Rambaldi, E., & Tucci, A. (2011). Application of an industrial waste glass in “glass-ceramic stoneware.” *International Journal of Applied Ceramic Technology*, *8*(5), 1153–1162. http://doi.org/10.1111/j.1744-

7402.2010.02550.x

Liu, D. M. (1997). Influence of porosity and pore size on the compressive strength of porous hydroxyapatite ceramic. *Ceramics International*, *23*(2), 135–139. http://doi.org/10.1016/S0272-8842(96)00009-0

Park, Y. J., Moon, S. O., & Heo, J. (2003). Crystalline phase control of glass ceramics obtained from sewage sludge fly ash. *Ceramics International*, *29*(2), 223–227. http://doi.org/10.1016/S0272-8842(02)00109-8

Pisciella, P., Crisucci, S., Karamanov, A., & Pelino, M. (2001). Chemical durability of glasses obtained by vitrification of industrial wastes. *Waste Management*, *21*(1), 1–9. http://doi.org/10.1016/S0956-053X(00)00077-5

Pisciella, P., & Pelino, M. (2005). FTIR spectroscopy investigation of the crystallisation process in an iron rich glass. *Journal of the European Ceramic Society*, *25*(11), 1855–1861. http://doi.org/10.1016/j.jeurceramsoc.2004.06.012

Rincón, A., Giacomello, G., Pasetto, M., & Bernardo, E. (2017). Novel 'inorganic gel casting' process for the manufacturing of glass foams. *Journal of the European Ceramic Society*, *37*(5), 2227–2234. http://doi.org/10.1016/j.jeurceramsoc.2017.01.012

Rincon Romero, A., Salvo, M., & Bernardo, E. (2018). Up-cycling of vitrified bottom ash from MSWI into glass-ceramic foams by means of 'inorganic gel casting' and sinter-crystallization. *Construction and Building Materials*, *192*, 133–140. http://doi.org/10.1016/j.conbuildmat.2018.10.135

Watanabe, T., Hashimoto, H., Hayashi, M., & Nagata, K. (2008). Effect of Alkali Oxides on Crystallization in CaO–SiO2–CaF2 Glasses. *ISIJ International*, *48*(7), 925–933. http://doi.org/10.2355/isijinternational.48.925

Zhang, Y. J., Zhao, Y. L., Li, H. H., & Xu, D. L. (2008). Structure characterization of hydration products generated by alkaline activation of granulated blast furnace slag. *Journal of Materials Science*, *43*(22), 7141–7147. http://doi.org/10.1007/s10853-008-3028-9

Chapter 10. Porous glass-ceramics made with vitrified MSWI bottom ash produced by different metallurgical strategies

10.1. Introduction

In this study, MSWI bottom ash was submitted to different strategies to clean the residue and recover the maximum quantity of metals before smelting. In the first strategy (S1), no mechanical separation was applied before vitrification. In the second strategy 2 (S2), the ferrous particles were extracted by a magnet, whereas in the third strategy (S3), an eddy-current separator was employed in order to extract the non-ferrous particles from the residue. Finally, in strategy 4 (S4), both ferrous and non-ferrous particles were extracted from MSWI bottom ash. These four strategies yielded four glasses which were further upcycled into porous glass-ceramics. The technique of alkali activation, gel-casting and sinter-crystallisation could be successfully applied to produce strong, safe and highly porous materials with glasses from all strategies. In contrast to the previous chapter, it was preferred to maintain the molarity of the alkaline solution very low (1 M NaOH), and increase the firing temperature to 1000 °C.

The comparison between the foams produced by different types of vitrified bottom ash concentrated mainly on the porosity (essential for insulation), mechanical strength and leaching resistance. Furthermore, this study also reports a first attempt to recycle the foams into new porous glass-ceramics. This specific study was carried on in order to assess if the developed waste-derived glass-ceramic foams could potentially be applied in the production of new foams after the end of life of the product.

10.2. Experimental procedure

The porous glass-ceramics made with vitrified bottom ash from different strategies (S1, S2, S3 and S4) were developed by firstly mixing at 400 rpm fine powders of glass to an alkaline solution of 1 M NaOH. The overall content of vitrified bottom ash used corresponded to 70 wt% of the slurry. After 3h of weak dissolution of the glass, 4 wt% of surfactant (Triton X-100, (polyoxyethylene octyl phenyl ether – $C_{14}H_{22}O(C_2H_4O)_n$, n = 9–10, Sigma-Aldrich, Gillingham, UK) was introduced to the slurry, which was easily foamed by intensive mechanical stirring at 2000 rpm. Thereafter, the foamed slurry was dried at 40 °C for 48h, demoulded and fired. The firing treatment was performed at 1000 °C, with heating rate of 10 °C/min and a holding time of 1h.

The recycled foams were developed by firstly milling the fired foams made with vitrified bottom ash from Strategy 1. The ground powder was then sieved below 75 μm and applied in the production of new foams by using the same process described previously (1 M NaOH alkali

activation followed by foaming, curing and firing at 1000 °C). Foams made with addition of 30% recycled soda-lime glass were also produced.

10.3. Results and discussion

10.3.1. Vitrified bottom ash-based porous glass-ceramics

The DSC curves of glasses from all strategies (Figure 10-1) show that the crystallisation temperature (T_c) of the glasses from strategies 1, 2 and 3 lies around 940 °C, while the T_c of the glass from Strategy 4 was 20 °C higher. In addition, Figure 10-1 also indicates a decrease in crystallisation tendency from S1 to S4.

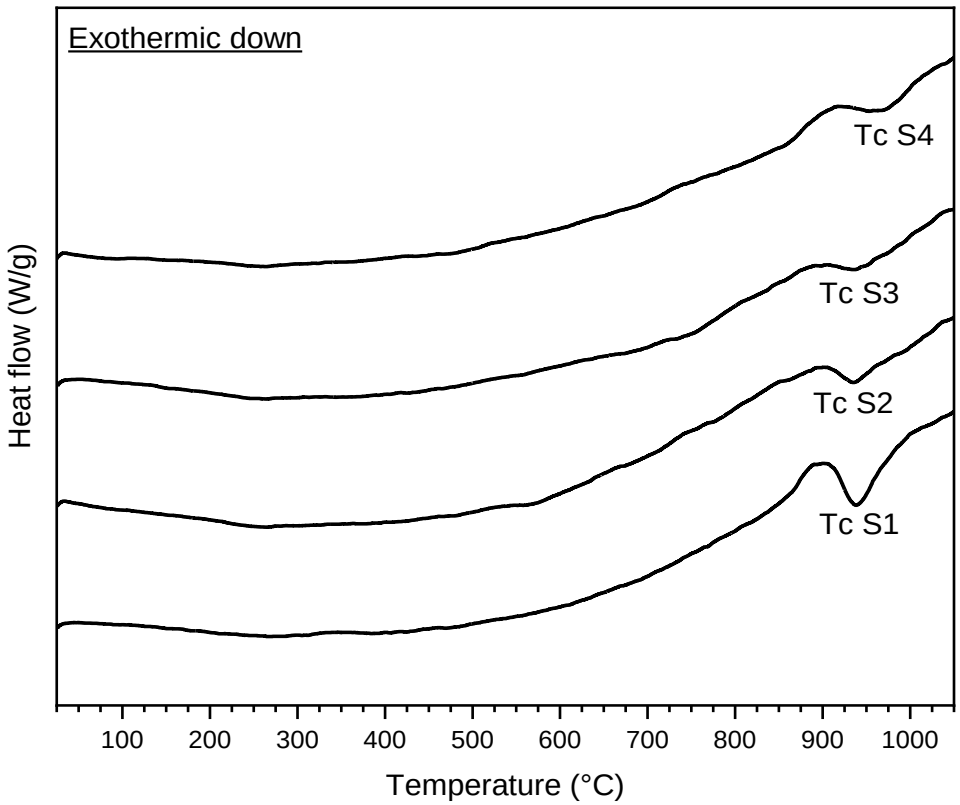

Figure 10-1. DSC curves of vitrified bottom ash produced by different strategies.

The crystallisation temperatures of the glasses were used as a reference for sintering experiments, which were performed at 1000 °C for all foams. Furthermore, the selection of the firing treatment was also supported by preliminary trials: vitrified bottom was from Strategy 3 (not activated) was pressed into discs and fired at 900 °C or 1000 °C and the water absorption of the fired disc was subsequently assessed. The results indicated a decrease by 54% in water absorption by increasing the firing temperature to 1000 °C, which shows improved densification for firing at this temperature.

Figure 10-2 presents the FTIR spectra of vitrified bottom ash from Strategy 1 (as received and after firing at 1000 °C), as well as the spectra of the four types of vitrified residues after alkali activation. The FTIR spectra of vitrified bottom ash as received shows only a band corresponding to the asymmetric Si-O-Si stretching vibration for the range selected for the measurement (Pisciella et al., 2001). The alkali activation and foaming of glasses from all strategies led to the appearance of two other bands: the band between 3030 and 2750 cm^{-1} is associated to the C-H_2 stretching due to the addition of the surfactant (Rincón et al., 2017). The second band between 1530 and 1370 cm^{-1} corresponds to the stretching vibration of C-O, indicating carbonation after alkali activation. In this study, this is probably associated to the carbonation of the pore solution (Nedeljković et al., 2018).

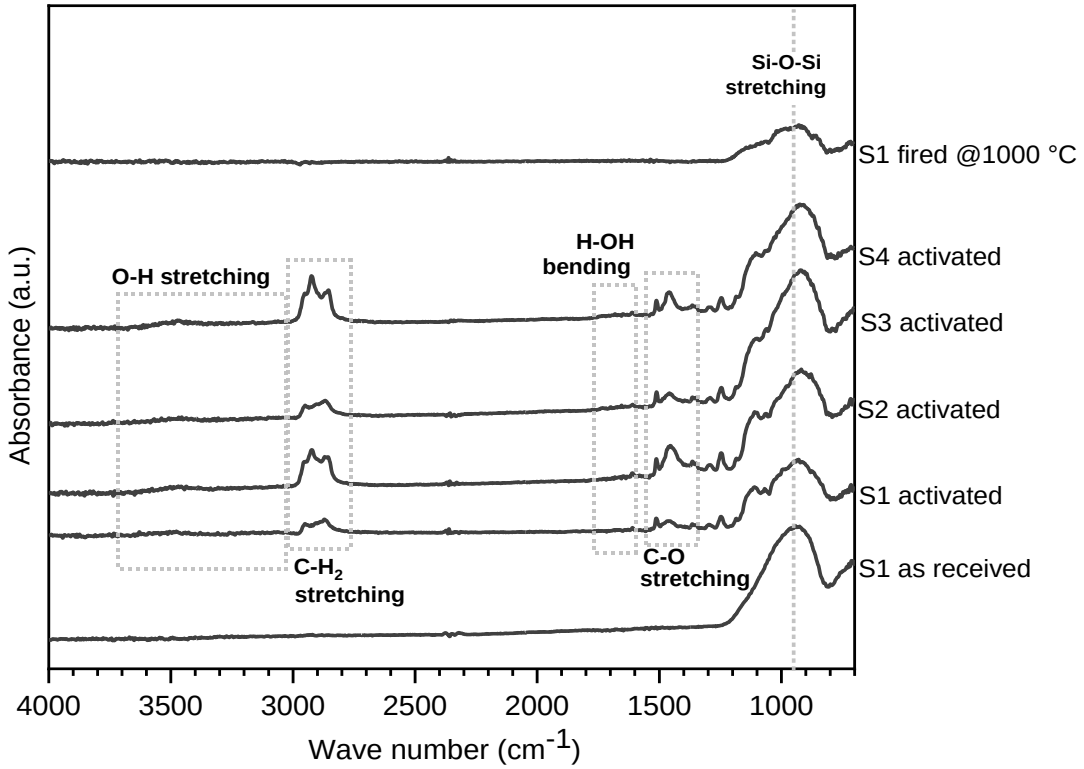

Figure 10-2. FTIR spectra of vitrified bottom ash (S1) as received, foams from all strategies before firing and foam S1 fired at 1000 °C.

Analogous to the FTIR spectra of activated vitrified bottom ash from the previous chapter, bands corresponding to O-H stretching and H-OH binding were hardly detected in not fired foams (see Figure 10-2). This indicates that the molarity of the alkaline solution was too low to form hydration products. Therefore, the hardening of the activated suspension was most likely attributed to the precipitation of carbonates, as already observed in the previous chapter, as well as for foams made by weak alkali activation with vitrified bottom ash (Rincon Romero et al., 2018). Once the foams were fired, the bands formed after alkali activation and foaming

disappeared. The FTIR spectra of not activated glasses and fired foams from all strategies were not presented for the sake of brevity.

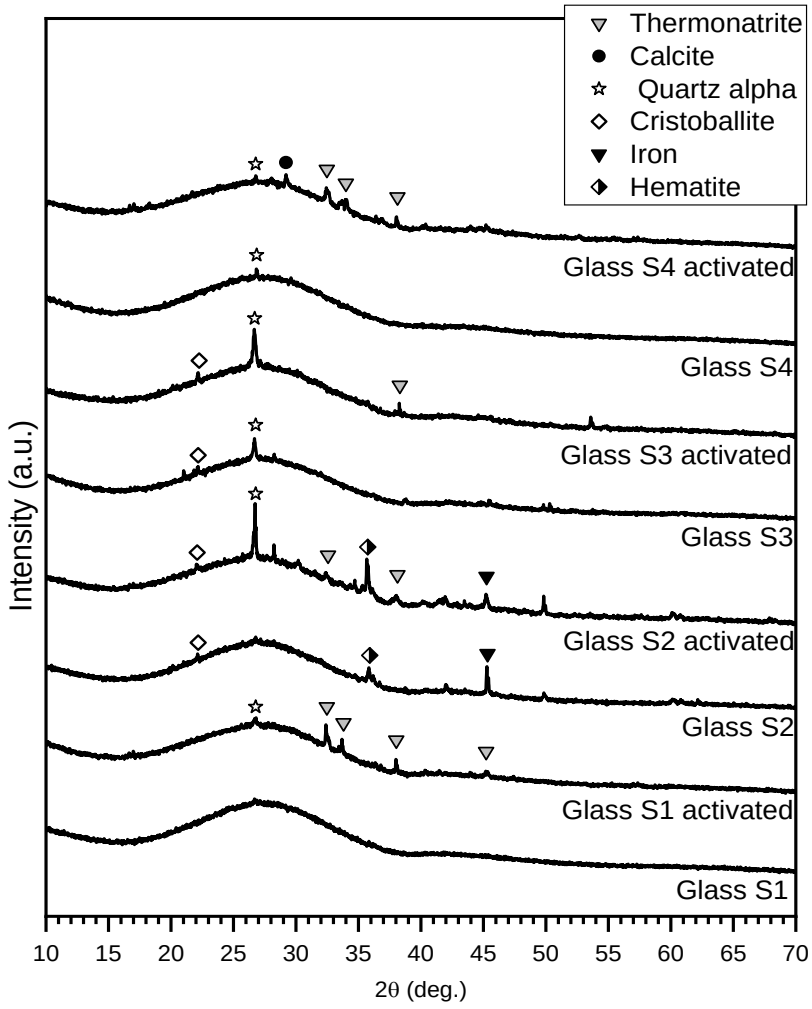

Figure 10-3. XRD patterns of activated and not activated vitrified bottom ash from different strategies.

According to the XRD patterns of not fired materials (Figure 10-3), the only reaction product identified in all activated glasses is consistent to thermonatrite ($Na_2CO_3 \cdot H_2O$, PDF#00-008-0448), which was easily visible in S1 and S4 foams. Furthermore, it was also possible to detect calcite ($CaCO_3$, PDF#86-2342) in the S4 foams. These findings are in agreement with the FTIR analysis, which indicated only the formation of carbonates due to alkali activation.

In addition, quartz (SiO_2, PDF#89-8938) and cristobalite (SiO_2, PDF#82-1232) were present in almost all samples (including the not activated glass). These silica phases are most probably originated from bottom ash. Finally, iron (Fe, PDF#00-001-1267) and hematite (Fe_2O_3, PDF#73-0603) were found in the S2 activated and not activated glasses, in traces. Iron could be originated from the intermediate region between vitrified bottom ash and recovered metals that

were milled together with the glass. Hematite, on the other hand, could correspond to the oxidised metallic part.

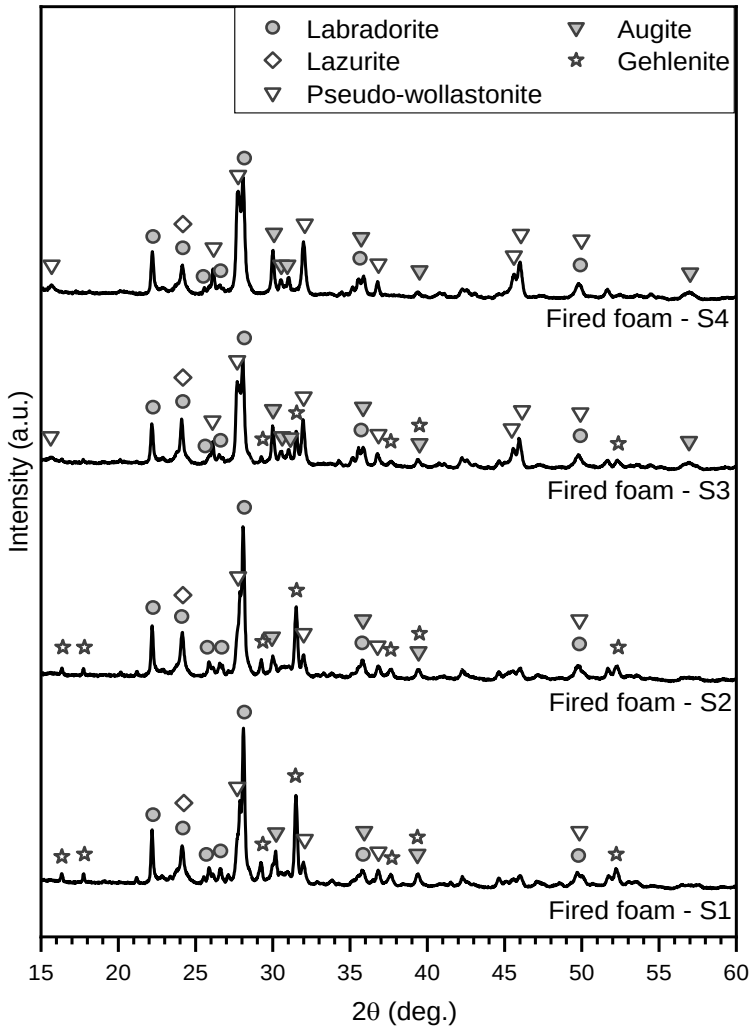

Figure 10-4. XRD patterns of the fired foams.

The different chemical compositions of four glasses influenced the phase assemblage formed upon firing (Figure 10-4). Labradorite (($Ca_{0.64}Na_{0.35}(Al_{1.63}Si_{2.37}O_8)$, PDF#83-1371), augite ($CaMg_{0.7}Al_{0.6}Si_{1.7}O_6$, PDF#78-1392), lazurite ($Na_{8.56}(Al_6Si_6O_{24})(SO_4)_{1.56}S_{.44}$, PDF#77-1702) and pseudo-wollastonite ($Ca_3(Si_3O_9)$, PDF#74-0874) were detected in all glass-ceramics: labradorite was formed in greater quantities in foams from Strategies 1 and 2 (which presented a similar composition), while pseudo-wollastonite was found in higher amount in foams from Strategies 3 and 4. Traces of lazurite and augite where recognized in all fired foams. Finally, gehlenite ($Ca_2Al(AlSiO_7)$, PDF#74-1607) was only detected in foams from Strategies 1, 2 and 3, with increased content only in the foams made with the first two strategies.

These results indicate the influence of the cleaning step performed before smelting on the crystallisation of the glasses: in glasses made without the previous extraction of non-ferrous

particles (Strategies 1 and 2), the Al_2O_3/SiO_2 molar ratio was higher which could have promoted the formation of gehlenite (Bernardo et al., 2010) and labradorite. On the other hand, pseudo-wollastonite was favoured in glasses with a lower Al_2O_3/SiO_2 molar ratio.

The porous glass-ceramics foams from all strategies were highly porous, with porosity higher than 71 vol% (Table 10-1). The porosity was mainly open, with less than 3 vol% of closed porosity. In addition, the fired foams were also quite strong, with compressive strength (σ_{comp}) lying between 2.9 MPa and 4.2 MPa. The estimated values for the bending strength of the solid phase (σ_{bend}, calculated following the Ashby and Gibson model for open-celled materials (Gibson and Ashby, 1999) (see Table 10-1) were higher than 120 MPa. This value is comparable to the bending strength of slag sitals and it is much higher than the bending strength of commercial glass-ceramics Neoparies® (Höland and Beall, 2012). Finally, the required milestones for cellular products (specific compressive strength above 5 MPa cm^3/g and porosity higher than 70%) could be finally achieved by valorisation of vitrified bottom ash.

Table 10-1. Mechanical and physical properties of the porous glass-ceramics.

Group of samples	**S1**	**S2**	**S3**	**S4**
Density determinations				
ρ_{geom} (g/cm^3)	0.76 ± 0.03	0.54 ± 0.01	0.63 ± 0.01	0.66 ± 0.01
$\rho_{apparent}$ (g/cm^3)	2.45 ± 0.00	2.70 ± 0.01	2.50 ± 0.03	2.55 ± 0.01
ρ_{true} (g/cm^3)	2.70 ± 0.00	2.81 ± 0.00	2.68 ± 0.00	2.64 ± 0.01
ρ_{rel}	0.281	0.193	0.233	0.252
Porosity distribution				
Total porosity (vol%)	71.9	80.7	76.7	74.8
Open porosity (vol%)	68.9	79.9	75.0	73.9
Closed porosity (vol%)	2.9	0.8	1.7	0.9
Strength determinations				
σ_{comp} (MPa)	3.8 ± 0.9	3.0 ± 0.5	2.9 ± 0.9	4.2 ± 0.7
σ_{bend} (MPa)	128.5	179.2	130.8	165.8
Specific σ_{comp} (MPa cm^3/g)	5.0	5.6	4.7	6.3

The micrographs of the developed porous glass-ceramics (Figure 10-5) support the data presented in Table 10-1: the foams are highly porous and present mostly open porosity. In addition, the pore size distribution is quite heterogeneous, with well interconnected macro-pores and micro-pores on cell walls. Finally, the struts appear to be very well densified, which probably helped in the high mechanical performance of the foams, as reported by Table 10-1.

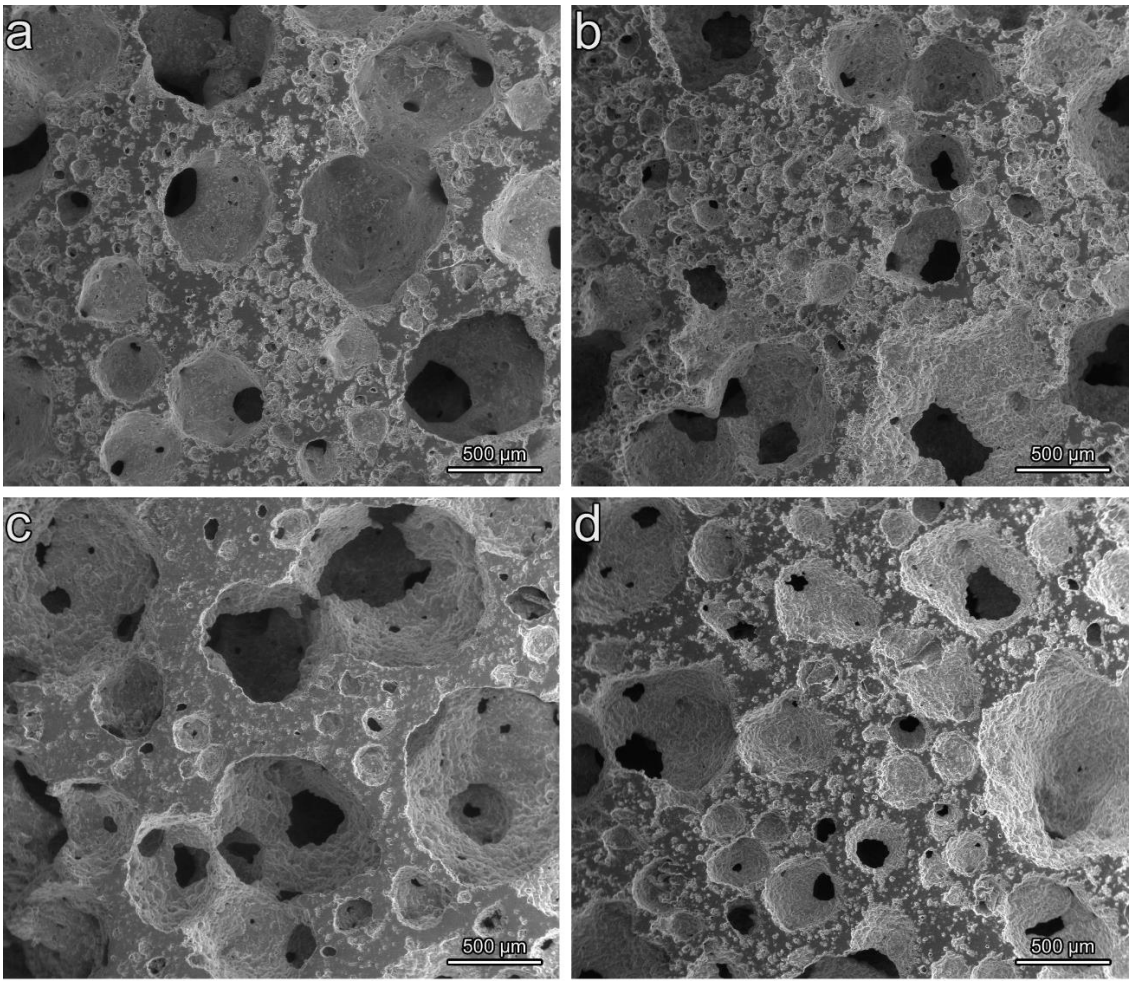

Figure 10-5. Microstructure of the porous glass-ceramics made with vitrified bottom ash from: strategy 1 (a); strategy 2 (b); strategy 3 (c); strategy 4 (d).

Before any possible commercial exploitation of waste-derived products, it is necessary to perform an environmental impact assessment. Leaching tests (Table 10-2) indicate a good stabilisation of heavy metals after firing for all four groups of glass-ceramics: according to the leachate values, the foams can be classified as inert waste (*Directive 2003/33/EC*, 2003). These results suggest that crystallisation did not affect the chemical stability of the glass and that crystalline phases and residual glass phase could immobilise the pollutants. However, one must consider that the different phases formed upon firing and also the composition of the residual glass phase most certainly affected the quantity of pollutants leached from each foam.

The overall results indicate that all four glasses made from the vitrification of bottom ash can be safely valorised into strong and highly porous glass-ceramics. Life cycle assessment (LCA) can be further applied in the future in order to evaluate the environmental impacts and benefits of each resource recovery process and select the strategy with the lowest impact.

Table 10-2. Results of the leaching test of the developed porous glass-ceramics (ppm).

	Limit values for inert waste	**S1**	**S2**	**S3**	**S4**
As	**0.5**	<0.0049	0.0070	0.0086	<0.0049
Ba	**20**	0.0486	0.0346	0.0430	0.1152
Cd	**0.04**	<0.0002	<0.0002	<0.0002	<0.0002
Cr total	**0.5**	0.0025	0.0255	0.0086	0.0028
Cu	**2**	0.0167	0.0493	0.0268	0.0090
Hg	**0.01**	<0.0004	<0.0004	<0.0004	<0.0004
Mo	**0.5**	0.0054	<0.0033	<0.0033	0.0103
Ni	**0.4**	<0.0014	<0.0014	<0.0014	<0.0014
Pb	**0.5**	<0.0047	<0.0047	<0.0047	<0.0047
Sb	**0.06**	0.0155	<0.0099	<0.0099	<0.0099
Se	**0.1**	<0.0122	<0.0122	<0.0122	0.0127
Zn	**4**	<0.0203	<0.0203	<0.0203	<0.0203

10.3.2. Recycling of vitrified bottom ash-based porous glass-ceramics

In order to conduct a LCA comparing the valorisation of vitrified bottom ash with other waste management alternatives (e.g. directly use of vitrified bottom ash as aggregate), it may be necessary to include information about the end of life of the product. Based on this, the recyclability potential of porous glass-ceramics (made with vitrified bottom ash from Strategy 1) was assessed, by employing ground powders of fired foams as raw materials in the production of new foams.

The recycled foams (Table 10-3) present porosity above 74 vol%, mainly open, with very limited closed porosity. In addition, the amount of porosity is even slightly higher than the S1 foams. These results indicate that the alkali activation and gel-casting steps were not substantially affected by a reduced amount of glassy phase.

Regarding the mechanical properties (Table 10-3), on the other hand, the estimated bending strength decreased by 67% with the recycling process without soda-lime glass. This is most probably attributed to the limited amount of glass phase during firing, which affected the densification by viscous flow, thus resulting in brittle foams (Bernardo et al., 2010). Based on these results, 30 wt% soda-lime glass was mixed with the partially crystallised powder of vitrified bottom ash, in order to promote sintering by viscous flow (as reported in Part III). In this case, the compressive strength increased in more than 4 times and the estimated bending strength was far above the one of S1 foams. These results indicate that vitrified bottom ash-

derived foams could be indeed recycled into strong and highly porous materials, when mixed with soda-lime glass.

Table 10-3. Physical and mechanical properties of recycled vitrified bottom ash-derived foams.

Group of samples	**VBA recycled foams**	**70% VBA/30% SL glass recycled foams**
Density determinations		
ρ_{geom} (g/cm^3)	0.68 ± 0.01	0.66 ± 0.00
$\rho_{apparent}$ (g/cm^3)	2.66 ± 0.03	2.59 ± 0.01
ρ_{true} (g/cm^3)	2.72 ± 0.00	2.63 ± 0.00
Porosity distribution		
Total porosity (vol%)	75.0	74.8
Open porosity (vol%)	74.4	74.5
Closed porosity (vol%)	0.6	0.3
Strength determinations		
σ_{comp} (MPa)	1.0 ± 0.1	4.9 ± 1.2
σ_{bend} (MPa)	42.3	196.4

The micrographs of the recycled foams (Figure 10-6) are consistent with the data presented in Table 10-3: it can be observed that the two types of recycled foams are indeed highly porous, with mainly open porosity. Furthermore, the addition of recycled soda-lime glass (Figure 10-6b) helped to slightly decreased the pore size, which may have also helped to increase the strength of the foams, as observed in the previous chapter.

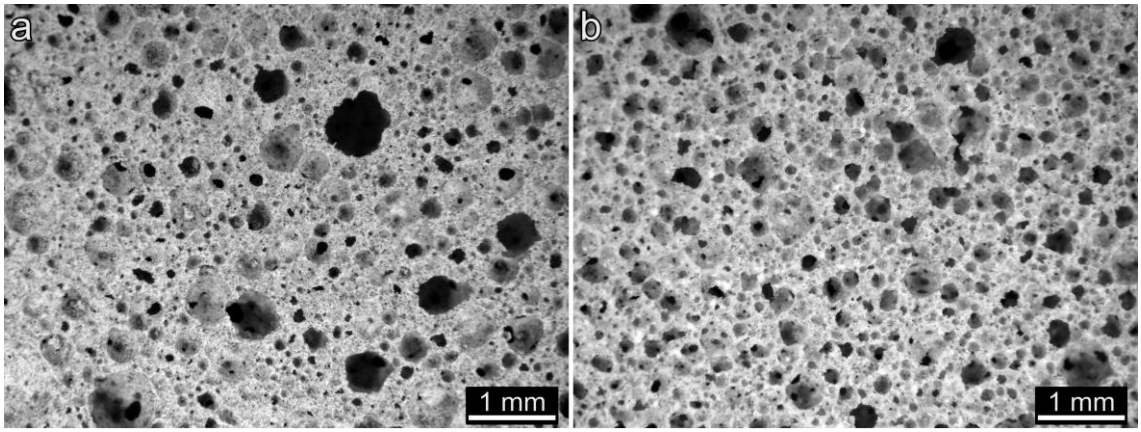

Figure 10- 6. Micrographs of recycled vitrified bottom ash-based foams: a) foams made with only milled S1 foams; b) foams made with addition of 30% soda-lime glass.

10.4. Conclusions

The metallurgical step performed on bottom ash before smelting affected the composition of the produced glass and, consequently, the precipitation of phases upon firing. In addition, the results of this study showed that the technique of alkali activation combined with gel-casting and sinter-crystallisation can be applied to valorise different types of vitrified bottom ash into strong and highly porous glass-ceramics, with low leaching of heavy metals. Finally, the recyclability potential of vitrified bottom ash-based foams has been confirmed. This indicates that the new foams could be continuously regenerated from discarded ones with the addition of soda-lime glass, configuring 'permanent materials'.

10.5. References

Bernardo, E., Bonomo, E., Dattoli, A., 2010. Optimisation of sintered glass-ceramics from an industrial waste glass. Ceram. Int. 36, 1675–1680. https://doi.org/10.1016/j.ceramint.2010.02.047

Directive 2003/33/EC, 2003. Official Journal of the European Communities.

Gibson, L.J., Ashby, M.F., 1999. Cellular solids: structure and properties. Cambridge University Press, Cambridge, UK.

Höland, W., Beall, G.H., 2012. Glass-Ceramic Technology. John Wiley & Sons, Inc., Hoboken, NJ, USA.

Nedeljković, M., Ghiassi, B., Melzer, S., Kooij, C., van der Laan, S., Ye, G., 2018. CO2 binding capacity of alkali-activated fly ash and slag pastes. Ceram. Int. 44, 19646–19660. https://doi.org/10.1016/j.ceramint.2018.07.216

Pisciella, P., Crisucci, S., Karamanov, A., Pelino, M., 2001. Chemical durability of glasses obtained by vitrification of industrial wastes. Waste Manag. 21, 1–9. https://doi.org/10.1016/S0956-053X(00)00077-5

Rincón, A., Giacomello, G., Pasetto, M., Bernardo, E., 2017. Novel 'inorganic gel casting' process for the manufacturing of glass foams. J. Eur. Ceram. Soc. 37, 2227–2234. https://doi.org/10.1016/j.jeurceramsoc.2017.01.012

Rincon Romero, A., Salvo, M., Bernardo, E., 2018. Up-cycling of vitrified bottom ash from MSWI into glass-ceramic foams by means of 'inorganic gel casting' and sinter-crystallization. Constr. Build. Mater. 192, 133–140. https://doi.org/10.1016/j.conbuildmat.2018.10.135

Chapter 11. Vitrified MSWI bottom ash ceramic foams by means of alkali activation

This chapter was based on P. Rabelo Monich, R. Murillo Alarcón, G. Sauve, H. Lucas, B. Friedrich, K. Van Acker, Y. Pontikes, E. Bernardo, Valorisation of conditioned MSWI bottom ash into ceramic foams by means of alkali activation (the manuscript is in submission process). The life cycle assessment analysis was conducted by NEW-MINE ESR Giovanna Sauve (KU Leuven).

11.1. Introduction

Chapters 9 and 10 have already demonstrated the feasibility of producing highly porous and strong vitrified bottom ash-based glass-ceramics, with very good stabilisation of pollutants, by alkali activation, gel-casting and firing. In contrast, this chapter reports other approaches based on alkali activation to valorise vitrified MSWI bottom ash into highly porous and strong glass-ceramics or alkali-activated materials for thermal insulation.

In contrast to glass-ceramics, alkali-activated materials consist of hardened materials obtained from the reaction of an aluminosilicate precursor with an alkaline solution at room temperature (Provis and Bernal, 2014). The strong dissolution of the aluminosilicate precursor promotes the polycondensation of binding phases, which are responsible for the hardening of the material (Ismail et al., 2014; Provis and Bernal, 2014). The type of formed hydrated products will depend mainly on the content of calcium in the system, as well as on the type of alkali activator used (Provis et al., 2015; Provis and Bernal, 2014). Alkali-activated materials are generally referred to as a more sustainable choice than Ordinary Portland Cement (OPC), due to savings in CO_2 emissions, which in turn is mainly related to the use of by-products from the industry as precursors (Provis, 2014). Furthermore, alkali-activated materials could also consist of a less expensive alternative for fired porous ceramics (Provis and Bernal, 2014). Porous alkali-activated materials can be produced by adding a foaming agent to the slurry, such as metallic aluminium powder (Novais et al., 2018) or hydrogen peroxide (Bai et al., 2016). These additives will be responsible for releasing gas once in contact with the alkaline solution, which is then entrapped within the suspension. In this way, a highly porous material can be obtained at low temperature.

The three approaches applied in this study to valorise vitrified bottom ash into ceramic foams are based on alkali activation, followed or not by firing. The first technique is the one reported in the previous chapters based on alkali activation, gel-casting and firing (Scenario 1): after the formation of reaction products on the surface of the glass, the ‘gelified’ slurry is foamed by intensive mechanical stirring with the support of a surfactant and dried at 40 °C. The dried material is finally fired at 1000 °C, obtaining a porous glass-ceramic. In the second

approach (Scenario 2), in contrast, vitrified bottom ash is mostly dissolved by an alkaline solution with higher molarity and converted into a porous alkali-activated-material by addition of metallic aluminium powder followed by curing at 60 °C. Finally, in the third approach (Scenario 3), the porous alkali-activated material obtained in Scenario 2 is fired following the same heating schedule than in Scenario 1, thus obtaining a porous glass-ceramic.

The porous ceramics obtained by these three different approaches were compared based on mechanical properties, porosity and leaching resistance. Furthermore, a life cycle assessment (LCA) was also conducted in order to estimate the environmental impact of each process. LCA is, in fact, a usual tool applied in order to assess the environmental impacts of product systems throughout the whole life cycle.

11.2. Experimental procedure

In this study, it was employed the vitrified bottom ash from Strategy 3 to produce the ceramic foams. The process applied in Scenario 1 is in fact the same one employed in the previous chapter. Therefore, the results from S3 foams are replicated in the present study as Scenario 1 in order to compare it with the other approaches. The foams were produced by adding fine powders of vitrified bottom ash to alkaline solution of 1 M NaOH (approximately 3.01 wt% Na_2O and 96.99 wt% H_2O), configuring a liquid/solid ratio of 0.42. The suspension was mixed at 400 rpm for 3h, and then a surfactant (Triton X-100, (polyoxyethylene octyl phenyl ether – $C_{14}H_{22}O(C_2H_4O)_n$, n = 9–10, Sigma-Aldrich, Gillingham, UK) was added to the activated slurry, The partially 'gelified' suspension was foamed by intensive mechanical stirring at 2000 rpm. The foamed slurry was then poured in a plastic mould and cured at 40 °C for 48h. The porous glass-ceramics were finally obtained by demoulding the green foam and firing it at 1000 °C, with a heating rate of 10 °C/min and a holding time of 1h.

The increase in molarity of the alkaline solution allowed to decrease the process time in Scenario 2. In this approach, the alkaline solution of approximately 5 M Na-silicate (composed of 11.90 wt% Na_2O, 13.27 wt% SiO_2 and 74.84 wt% H_2O) was prepared by mixing NaOH (10 wt%), sodium silicate solution (50 wt%) and water (40 wt%). The SiO_2/ Na_2O molar ratio of the alkaline solution was equal to 1.2. Fine powders of vitrified bottom ash and 0.0375 wt% of surfactant sodium oleate ($(CH_3(CH_2)_7CH=CH(CH_2)_7COONa$, purity 82 %, Sigma-Aldrich) were then added to a laboratory plastic bottle containing the Na-silicate based alkaline solution (liquid/solid ration of 0.45). After 3 min of mixing by using a handheld electric mixer, 0.05 wt% of metallic aluminium powder (purity 99.9 %, particle size range 1 to 5 μm, Atlantic Equipment Engineers) was added to the slurry, which was then mixed for another 30 s (Hertel et al., 2019). Both the surfactant and the aluminium weight percentages were related to the mass of vitrified bottom ash. Once aluminium was added to the alkaline medium, hydrogen gas (together with soluble aluminate ions) was released, increasing the porosity of the material (Novais et al.,

2018). Subsequently, the laboratory bottle was closed and cured at 60 °C. After 24h of curing, the alkali-activated foam was demoulded. In Scenario 3, the alkali-activated foams developed in Scenario 2 were fired following the same heating schedule than in Scenario 1 (1000 °C, with a heating rate of 10 °C/min and a holding time of 1h), thus obtaining a porous glass-ceramic.

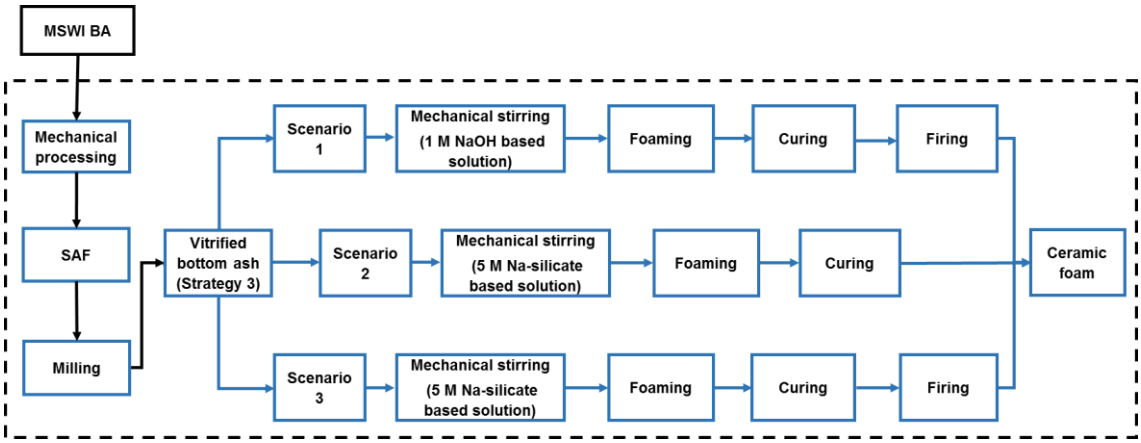

Figure 11-1. Summary of the three different scenarios applied to produce ceramic foams, as well as system boundaries.

A comparative life cycle assessment was conducted in order to analyse, and compare, the environmental impacts of the three different scenarios for valorisation of vitrified bottom ash. The functional unit (FU) select for this study was: "the production of an insulation panel of 1000 cm^3" (as the ceramic foams were developed for building insulation). This FU was selected under the assumption that the three ceramic foams produced in the three scenarios present the same insulation characteristics in terms of thermal conductivity. This parameter was estimated by calculations based on the relative density of the samples and thermal conductivity of the solid phase (Gibson and Ashby, 1999), as it was not possible to measure the thermal conductivity of the ceramic foams at this point of the research. The values obtained for the three groups of ceramic foams were found to be comparable. Therefore, a common thickness of the panel was defined, leading to the overall volume of the insulation panel as presented in the FU. The lifetime of the products was assumed to be the same and equal to the average lifetime of a building. As the ceramic foams produced by the three different approaches presented different densities, the initial amount of vitrified bottom ash required for each process was also different. In order to also consider this difference, the assessment also included the processes required to produce vitrified bottom ash from MSWI bottom ash. The zero-burden approach was instead considered for the MSWI bottom ash. The three scenarios as well as the system boundaries are summarised in Figure 11-1.

Table 11-1. Summary of the life cycle inventory for the three scenarios. All energy and material requirements refer to the amount of foam/material processed in each step for the production of an insulation panel of 1000 cm^3.

Processes inputs and outputs	**Scenario 1**	**Scenario 2**	**Scenario 3**
Vitrified bottom ash (g)	650.2	626.3	622.0
Density of the foam (g/cm^3)	0.63	0.72	0.67
Mechanical stirring			
L/S ratio	0.43	0.45	0.45
Solution (g)	278.61	281.84	279.9
Distilled water (g)	267.88	112.73	111.96
NaOH (g)	10.73	28.18	27.99
Sodium silicate (g)	-	49.32	139.95
Sodium oleate (g)	-	0.23	0.23
Electricity (kWh)	0.075	0.0035	0.0035
Foaming			
Mass input (g)	928.81	908.37	902.13
Surfactant or foaming agent (g)			
Triton X-100	37.15	-	-
Aluminium powder	-	0.31	0.31
Mass loss (%)	5	5	5
Electricity (kWh)	0.01	0.00058	0.00058
Curing			
Mass input (g)	917.66	863.25	857.32
Electricity (kWh)	0.066	0.055	0.058
Emissions (%)			
H_2O	27.2	16.6	16.6
Firing			
Mass input (g)	668.04	-	715.01
Electricity (kWh)	0.66	-	0.63
Emissions (%)			
CO_2	3.8 (decomposition of Triton)	-	-
H_2O	1.9	-	6.3
Mass of insulation panel of 1000 cm^3 (g)	630	720	670

The LCA was conducted with GaBi 8.0, and the Ecoinvent v3.3 database was applied for the life cycle inventory of background processes (e.g. materials and energy production, and waste treatment processes). Process inputs and outputs, in terms of material and energy flows, were obtained from the laboratory experiments. When data was not directly available from the laboratory or from the Ecoinvent database, related literature was investigated. Transportation of materials from the production plants to the lab were not included in this assessment.

The life cycle inventory for the three scenarios (Table 11-1) refers to the data from the laboratory processes and related to an average batch size of 1000 g. The assessment was carried out at lab scale, therefore the upscaling of these processes could have led to optimised parameter values. This should mostly be considered for energy consumption values, as materials usage is determined based on stoichiometric relations (Piccinno et al., 2016). In particular, the energy consumption of the lab machines used was calculated from the related technical data sheets considering the nominal power and adapting it to the process Further considerations are included in the Results and Discussion.

For the life cycle impact assessment (LCIA), the ILCD method was chosen, as it considers the recommended impact assessments methods for each impact category. All impact categories, as defined in the ILCD method and guidelines, were addressed to avoid potentially neglecting impacts: climate change (kg CO2 eq.), acidification (mole of H^+ eq.), ecotoxicity (CTUe), freshwater eutrophication (kg P eq.), marine eutrophication (kg N eq.), terrestrial eutrophication (Mole of N eq.), human toxicity (cancer and non-cancer effects) (CTUh), ionizing radiation (kBq U235 eq.), land use (kg C deficit), ozone depletion (kg CFC-11), particulate matter (kg PM2.5 eq.), photochemical ozone formation (kg NMVOC eq.), resource depletion, water (m^3 eq.), resource depletion, mineral fossils and renewables (kg Sb eq.).

11.3. Results and discussion

11.3.1. Valorisation of vitrified bottom ash results

The FTIR spectra (Figure 11-2) helps to understand the physico-chemical modifications taking place due to alkali activation, as well as sintering. A broad band between 2940 and 3715 cm^{-1} is associated to the O-H stretching, while the one at 1650 cm^{-1} is related to the H-OH vibration of molecular H_2O bound in the hydration products (Bernal et al., 2010; Yu et al., 2004). These two bands are visible almost only in samples made by 5 M Na-silicate alkali activation (Scenario 2). This indicates that the hardening mechanism in 1 M NaOH alkali activation (Scenario 1) is most probably not related to the formation of hydrated gels, as previously mentioned in Chapter 10.

In contrast, bands that can be easily detected are the ones at around 2900 cm^{-1} (only for foams made by 1 M NaOH alkali activation, Scenario 1) and 1450 cm^{-1}. The first band corresponds to the C-H_2 stretching due to the addition of Triton surfactant. On the other hand,

the second band is associated with the stretching vibration of C-O (Rincón et al., 2017), indicating the presence of carbonates. Once CO_2 is dissolved into water, H_2CO_3 is formed which can then interreact with hydration products (Palacios and Puertas, 2006). Furthermore, carbonic acid can also interact with the free ions present in the pore solution (e.g. Ca^+ and Na^+), forming carbonates (Nedeljković et al., 2018; Salman et al., 2015). The carbonation of foams made by 1 M NaOH alkali activation (Scenario 1) is most probably associated to the carbonation of the pore solution, as it was very hard to detect bands corresponding to hydration products. On the other hand, the carbonation of foams made by 5 M Na-silicate alkali activation (Scenario 2) could be due to one or both processes.

The band associated with the asymmetric Si-O-Si stretching vibration was dislocated towards higher wavelengths numbers after 5 M Na-silicate alkali activation (Scenario 2). This indicates a higher degree of polymerisation of silicates, probably due to the formation of hydration products (Bernal et al., 2010). Finally, the firing treatment decomposed this band in more peaks, possibly due to crystallisation (Rincon Romero et al., 2018).

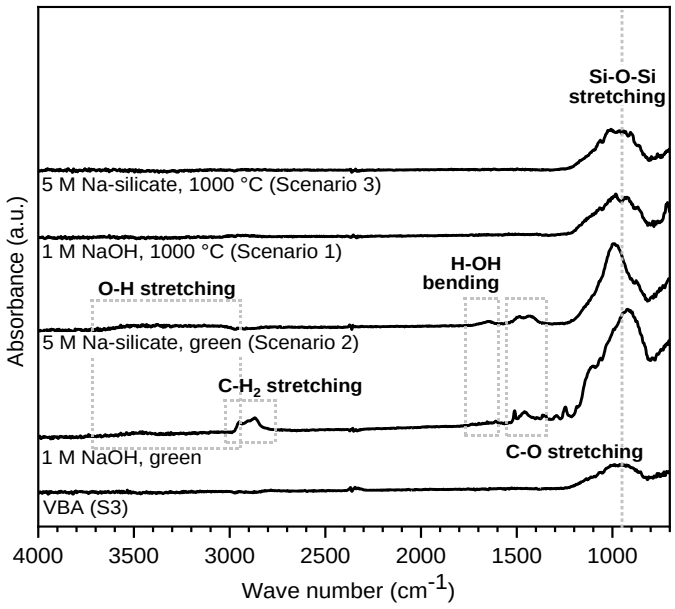

Figure 11-2. FTIR spectra of vitrified bottom ash, green foams as well as foams fired at 1000 °C.

The thermogravimetric analysis (TGA) and the derivative thermogravimetry (DTG) of foams made by 1 M NaOH (Figure 11-3a) and 5 M Na-silicate (Figure 11-3b) alkali activation present two distinct areas of weight losses: below 200 °C, the weight loss are attributed to the evaporation of physically bonded water (Nedeljković et al., 2018). Above this temperature, the weight losses could be attributed to dihydroxylation (Natali Murri et al., 2013), as well as to decomposition of carbonates (Nedeljković et al., 2018). Furthermore, in Figure 11-3a, part of

the weight loss between 250 °C and 400 °C is due to the decomposition of Triton X-100 (Rincón et al., 2017). The total weight loss associated to the decomposition of free water, hydration products and carbonates is higher in foams made by 5 M Na-silicate based solution. This supports the data presented in the FTIR analysis: the formation of gels and carbonates was naturally favoured by an alkaline solution of higher molarity. Finally, it is also possible to observe a slight weight gain above 780 °C, which may be due to the oxidation of metals (such as Fe). These metallic particles correspond to the intermediate region between vitrified bottom ash and recovered metals that were milled together with the glass.

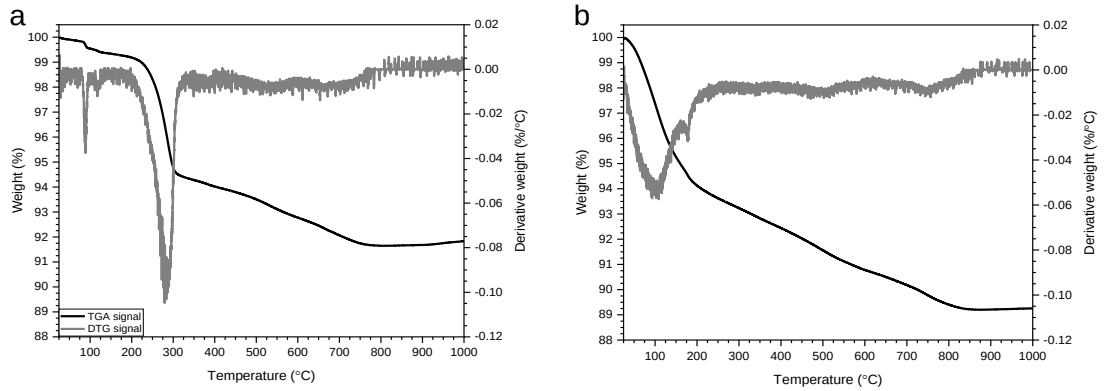

Figure 11-3. TGA and DTG performed on foams made by: a) 1 NaOH alkali activation; b) 5 M Na-silicate alkali activation.

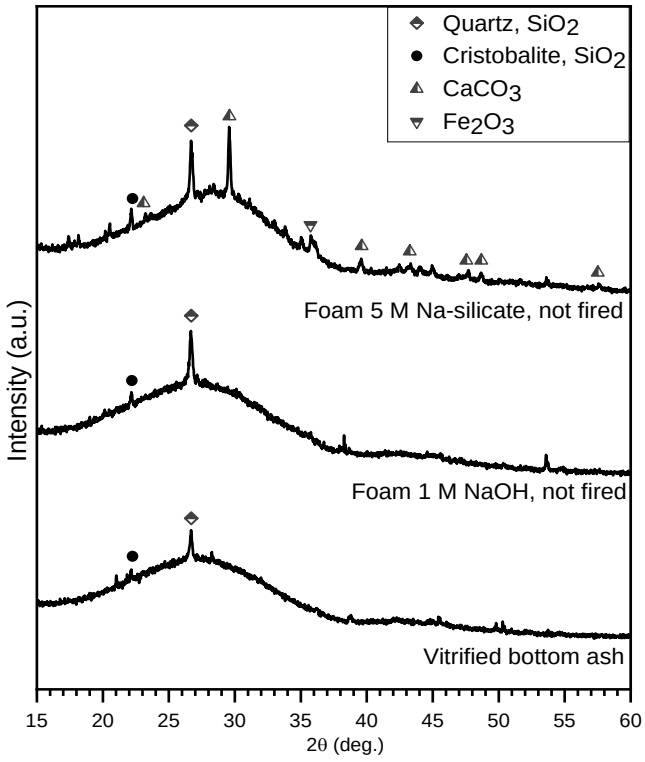

Figure 11-4. XRD patterns of vitrified bottom ash and green foams.

XRD analysis was performed on vitrified bottom ash and on the green foams in order to identify the reaction products formed due to alkali activation. The only detected product was calcium carbonate ($CaCO_3$, PDF#86-2339) in foams made with 5 M Na-silicate. The absence of any crystalline phase containing sodium may suggest that the hardening mechanism was associated to the formation of non-crystalline reaction products (Bernal et al., 2010).

Traces consistent to quartz (SiO_2, PDF#89-8938), cristobalite (SiO_2, PDF#82-1232) and hematite (Fe_2O_3, PDF#73-0603) were also detected. Quartz and cristobalite are originated from MSWI bottom ash, which were most probably not completely dissolved during smelting. The difference in peaks intensities between as received vitrified bottom ash and activated glass is most probably due to a heterogeneous distribution of undissolved quartz and cristobalite among the glass. Hematite, on the other hand, was only found in foams activated with the Na-silicate based solution. The presence of this iron oxide is most probably attributed to the recovered metallic part which was oxidised during the production of vitrified bottom ash.

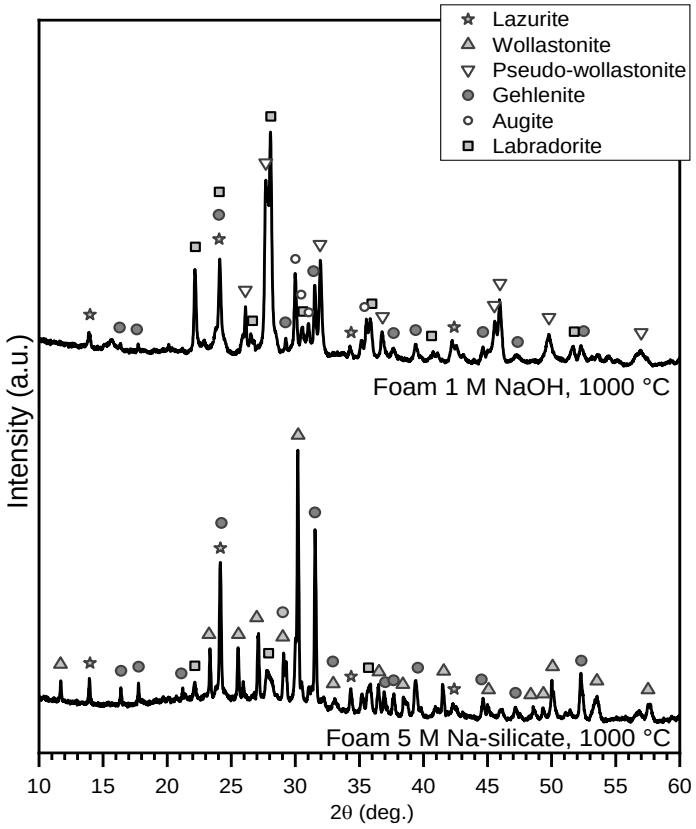

Figure 11-5. XRD patterns of the foams fired at 1000 °C.

The composition of the alkaline solution had a great impact also in the crystallisation of phases (Figure 11-5). For 5 M Na-silicate activated foams fired at 1000 °C, signals consistent to gehlenite ($Ca_2Al(AlSiO_7)$, PDF#74-1607) and wollastonite ($CaSiO_3$, PDF#84-0655) were detected, as well as lazurite ($Na_{8.56}(Al_6Si_6O_{24})(SO_4)_{1.56}S_{.44}$, PDF#77-1702) and labradorite

($Ca_{0.64}Na_{0.35}(Al_{1.63}Si_{2.37}O_8)$, PDF#83-1371), in traces. Interestingly, with an alkali activation of 1 M NaOH, the phase assemblage after firing at 1000 °C was completely different. The main phases consisted of labradorite and pseudo-wollastonite ($Ca_3(Si_3O_9)$, PDF#74-0874). Gehlenite was far less visible, whereas lazurite was also formed. Finally, augite ($Ca(Mg_{0.70}Al_{0.30})((Si_{1.70}Al_{0.30})O_6)$, PDF#78-1392) was also detected.

It is possible that the formation of gehlenite and wollastonite was promoted by the hydration products, in agreement with previous observations on the thermal evolution of C-S-H gel into wollastonite (Tajuelo Rodriguez et al., 2017). Gehlenite, on the other hand, has been attributed as one of the phases originated from the crystallisation of C-A-S-H gel above 600 °C (Park et al., 2016). Labradorite and lazurite probably derive from vitrified bottom ash, being present in both foams fired at 1000 °C.

Table 11-2 shows that the compressive strength (σ_{comp}) of the two glass-ceramics (Scenarios 1 and 3) was nearly the same (nearly 3 MPa), and far higher than the one of alkali-activated foam (Scenario 2). This is even more evident when applying the Gibson-Ashby model (Gibson and Ashby, 1999) for open-celled foams to estimate bending strength of the solid phase (σ_{bend}). The values obtained for fired foams were found to be comparable to the one of commercial glass-ceramics (Shelby, 2005).

Table 11-2. Physical and mechanical properties of the obtained ceramic foams.

Group of samples	**Scenario 1**	**Scenario 2**	**Scenario 3**
Density determinations			
ρ_{geom} (g/cm^3)	0.63 ± 0.01	0.72 ± 0.02	0.67 ± 0.02
$\rho_{apparent}$ (g/cm^3)	2.50 ± 0.03	2.36 ± 0.04	2.42 ± 0.07
ρ_{true} (g/cm^3)	2.68 ± 0.00	2.38 ± 0.00	2.57 ± 0.00
Porosity distribution			
Total porosity (vol%)	76.7	69.9	73.9
Open porosity (vol%)	75.0	69.6	72.3
Closed porosity (vol%)	1.7	0.3	1.6
Strength determinations			
σ_{comp} (MPa)	2.9 ± 0.9	1.6 ± 0.3	2.9 ± 0.4
σ_{bend} (MPa)	130.8	47.91	110.7

The micrographs of the ceramic foams (Figure 11-6) indicate that the foams are highly porous, with mainly open-celled morphology. This is in agreement with the data presented in Table 11-2. The foams made by the addition of aluminium powder present a more homogeneous pore distribution (Figures 11-6a and c). In addition, the microstructure of the alkali-activated

foam (Figure 11-6b) shows unreacted glass (marked as '1') surrounded by the binder phase ('2'). According to the EDS analysis, the binder is rich in Si, Ca, Al and Na. Finally, while the white spot ('3') corresponds to an iron-rich inclusion.

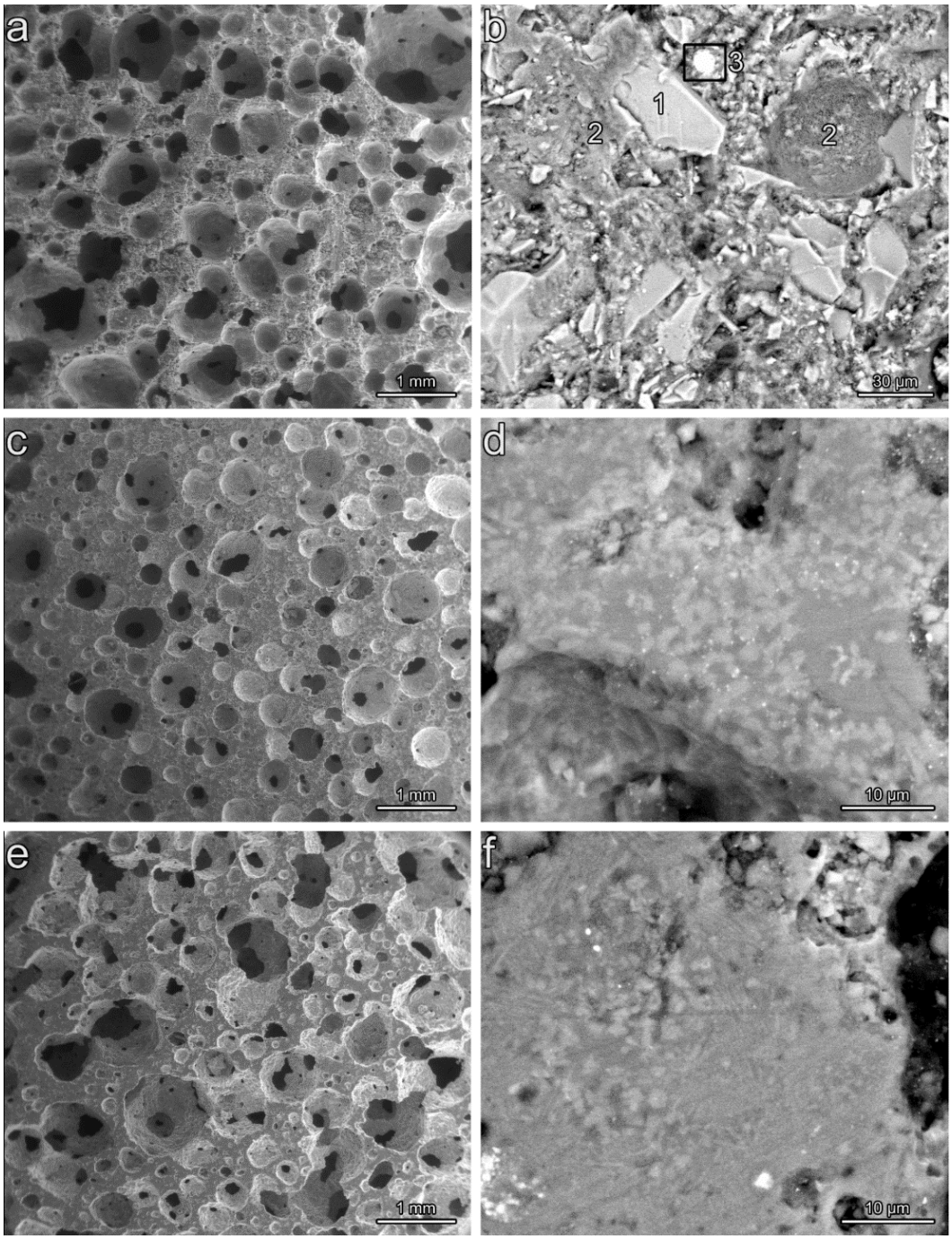

Figure 11-6. Micrographs of the ceramic foams obtained in: a-b) Scenario 2 (5 M Na-silicate alkali activation, not fired); c-d; Scenario 3 (5 M Na-silicate alkali activation, fired); e-f: Scenario (1 M NaOH alkali activation, fired).

Regarding the foams from 5 M Na-silicate activation, after firing (Figures 11-6c and d), the viscous flow determined some sealing of smaller pores. However, the total porosity increased

slightly (see Table 11-2), most probably due to secondary foaming reactions, corresponding to the decomposition of the binding compounds (Rincón et al., 2017).

The fired foams from 1 M NaOH alkali activation (Figures 11-6e and f) presented quite smaller struts than the previous foams. Besides crystallisation, also the viscous flow was conditioned by the formation of an alkali-enriched glass phase from the decomposition of the binding compounds, surrounding not dissolved glass particles. A lower content of binding phase, with lower activation, caused a less significant viscous flow.

Table 11- 3. Results of the leaching test performed on the ceramic foams (ppm), with leaching index values between square parentheses.

	Limit values for inert waste	**Scenario 1**	**Scenario 2**	**Scenario 3**
As	**0.5**	0.0086 [0.0172]	0.0198 [0.0396]	0.0090 [0.0180]
Ba	**20**	0.0430 [0.0022]	0.0806 [0.0040]	0.0643 [0.0032]
Cd	**0.04**	<0.0002 [0.0050]	0.0003 [0.0075]	<0.0002 [0.0050]
Cr	**0.5**	0.0086 [0.0172]	0.0220 [0.0440]	0.0221 [0.0442]
Cu	**2**	0.0268 [0.0134]	0.2904 [0.1452]	0.0103 [0.0052]
Hg	**0.01**	<0.0004 [0.0400]	0.0023 [0.2300]	<0.0004 [0.0400]
Mo	**0.5**	<0.0033 [0.0066]	0.0565 [0.1130]	0.0186 [0.0372]
Ni	**0.4**	<0.0014 [0.0035]	<0.0014 [0.0035]	<0.0014 [0.0035]
Pb	**0.5**	<0.0047 [0.0094]	0.0445 [0.0890]	<0.0047 [0.0094]
Sb	**0.06**	<0.0099 [0.1650]	<0.0099 [0.1650]	<0.0099 [0.1650]
Se	**0.1**	<0.0122 [0.1220]	0.0356 [0.3560]	<0.0122 [0.1220]
Zn	**4**	<0.0203 [0.0051]	<0.0203 [0.0051]	<0.0203 [0.0051]

Leaching tests (Table 11-3) performed on the ceramic foams exhibits leachate values below the limit values for inert waste (*Directive 2003/33/EC*, 2003). This indicates that both alkali activation and sinter-crystallisation could be applied to valorise vitrified bottom ash into stable ceramic foams. Furthermore, the fired foams presented in general the lowest leaching values. This can be attributed to the precipitation of chemical stable phases that immobilised the heavy metals (Pisciella et al., 2001).

11.3.2. Life cycle assessment results

Regarding the LCA, results were analysed for all impact categories at a midpoint level. For a more distinctive interpretation of the results in relation to the three scenarios, and considering the comparative goal of the assessment, only the net differences in impacts for the production of the vitrified bottom ash are reported. The processes from the mechanical treatment of the MSWI bottom ash to the milling of the vitrified bottom ash are in fact the same for the three approaches. The only difference is the amount of vitrified bottom ash required for the three scenarios. Based on this, the impacts related to the common processes are considered only for Scenarios 1 and 2 for the additional amount of vitrified bottom ash required compared to Scenario 3.

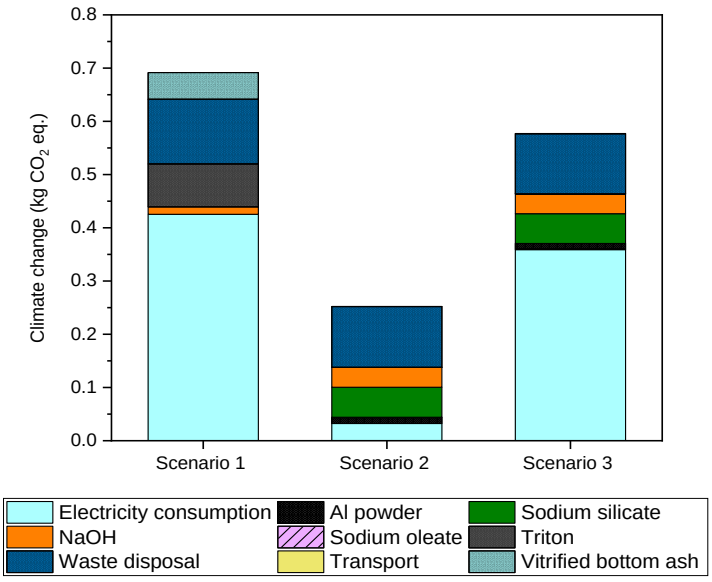

Figure 11-7. Results for the climate change impact category for three scenarios (the results also include the contribution of the main processes to the total impacts on climate change).

For all impact categories, Scenario 2 results in lower impacts compared to Scenarios 1 and 3. In addition, for most impact categories, Scenario 1 exhibits higher impacts than Scenario 3. A

contribution analysis was then performed to understand which processes contributed more to the results and to what extent they affected the different results for the three scenarios.

Results for the climate change impacts are reported in Figure 11-7. The contribution analysis indicates that the major contributing process to the higher impacts to climate change of Scenarios 1 and 3 is the electricity consumption, which can be related to the firing treatment. Similar results have been obtained for most of the other impact categories. The results also indicate how the higher electricity consumption in Scenario 1 leads to overall higher impacts in climate change, even considering the higher impacts in Scenarios 2 and 3 related to the materials used. From the contribution analysis, it can also be assessed how the higher amount of vitrified bottom ash in input also influences the results. The high electricity consumption of the submerged arc furnace (SAF) and milling processes is reflected in the higher impacts of Scenario 1.

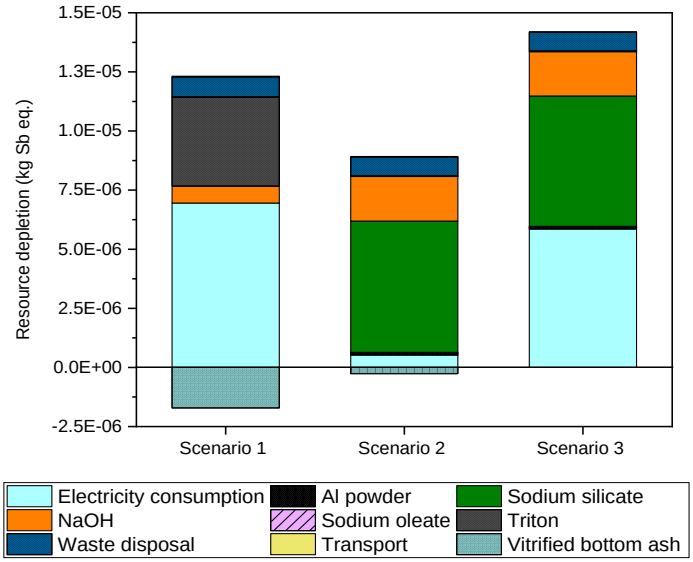

Figure 11-8. Results for the resource depletion impact category for the three scenarios: the results highlight the higher contribution of the materials used in the scenarios to the overall results.

Similar results have also been obtained for all other impact categories, with the exception of ecotoxicity, human toxicity, ozone depletion and resource depletion (Figure 11-8). While the impacts for ecotoxicity are higher in Scenario 1 due to the higher electricity consumption, these are compensated by the higher metal recovery rate, leading Scenario 3 to present higher overall impacts. Impacts to the other three categories are, instead, majorly affected by the material consumption. More specifically, the impacts related to the use of different materials are higher for Scenarios 2 and 3. The main contributor to the impacts related to the use of materials is the production of sodium silicate, in human toxicity and resource depletion, and sodium hydroxide

in ozone depletion. The production of aluminium powder affects the results to a minor extent, while the production of Triton appears to have negligible impacts compared to the other materials. Despite the higher amount of Triton employed in Scenario 1, the impacts related to the use of sodium silicate, sodium hydroxide and aluminium powder in Scenarios 2 and 3 led to higher impacts (when compared to the impacts of the use of Triton and sodium hydroxide in Scenario1). This result is relevant in the mentioned categories, where Scenario 3 results in overall higher impacts. Similar results in terms of higher and lower total impacts were obtained for the categories of human toxicity, and ozone depletion.

The results of the LCA have indicated how, for the analysed scenarios, electricity consumption represents a critical factor, with particular reference to the energy use related to the firing process in Scenarios 1 and 3. Considering the high influence on the total results and conclusions, and also considering that the consumption data was derived from technical data sheets of lab machines and related to the processing of a small amount of material, a sensitivity analysis was conducted. The goal of the sensitivity analysis is to assess how the variation of a parameter or model input (e.g. electricity consumption) affects the results (Laurent et al., 2014b). In particular, a perturbation analysis was here conducted by varying the electricity consumption values estimated in the inventory by ±10. The sensitivity ratio (SR) was then calculated following the equation provided in (Clavreul et al., 2012; Laurent et al., 2014a):

$$SR = \frac{\frac{\Delta result}{initial\ result}}{\frac{\Delta parameter}{initial\ parameter}} \quad (Equation\ 1)$$

In fact, the sensitivity ratio defines how much the results can vary in relation to the variation of the parameter value. In particular, SR>1 indicates that a variation of 10% is obtained in the results for a 10% variation of the parameter. The sensitivity analysis was not applied to the material flows, as chemical relations were used to define the amounts of required materials. Nevertheless, one must consider that these processes have been assessed at a lab scale level and that more optimised processes, in terms of material, energy and waste flows could be achieved.

The obtained sensitivity ratios for all three scenarios have shown how 10% variation of the electricity required for firing could lead to around 3-10% variation in the total results for Scenarios 1, and 1-9% variation in Scenario 3, across all impact categories. A 10% variation in the electricity consumption for the curing process would instead lead to variations in the results between 0-1% for Scenario 1, and 0-6% in Scenario 2. The sensitivity analysis was also performed on the mechanical treatment, SAF and milling processes. In particular, a 10% variation in the energy consumption for the SAF would lead to 2-7% variation in results for all scenarios. All scenarios could also achieve variations in results of 1-8% with a variation in the

energy consumption of the milling processes. The sensitivity ratios obtained for the electricity consumption of the other processes were instead considered negligible as SR<0.01.

The sensitivity analysis results indicate how more detailed data on the electricity consumption of the processes, and in particular of the firing process, could lead to a variation of around 6% in the results. This should mostly be considered in relation to the potential upscaling of the processes to industrial level.

Further considerations can be made on the lack of data for the production of the materials used in the processes. Indeed, the use of literature data and data from the ecoinvent database is not fully representative of the processes and impacts for the production of the specific materials used in the lab. The assumptions and simplifications made need to be considered in the interpretation of the results. However, due to the lack of direct data from the manufacturing companies, the obtained processes and results have been considered acceptable for a first estimation of the environmental impacts of the three approaches.

11.3.3. Weighted properties method

LCA is just one of the elements that needs to be taken into account when comparing different approaches. The technical performances (such as mechanical strength and leachability) should also be considered. Weighted properties method consists of a useful method that can be applied to consider a series of materials properties. In this method, a material property is assigned a certain weight (π), depending on the importance to the performance in service (Farag, 2007). The ranking between different solutions is given by a comparative materials penalty index, calculated by summing the numerical values of the properties multiplied by the weighting factors. The numerical values, in order to combine properties with different units, are in turn considered as 'scaled' values. When the property should decrease (e.g. LCA and leachability), each single property value is normalised in relation to the maximum value in the list. When the property should increase (e.g. strength), the scaled value is obtained dividing the minimum value in the list by the single property value. The most convenient solution is the one exhibiting the minimum penalty index.

In this study, the environmental sustainability assessed by LCA was considered the most important property. Based on this, LCA was attributed a weighting factor of 0.5, from the impact categories discussed above. However, each impact category in the LCA results addresses a specific environmental impact and is characterised by a specific unit. In order to simplify the interpretation of the results and to be able to consider one total impact value for each scenario, normalised results were considered. The normalisation step in LCA consisted in dividing the results of each impact category by related reference information (ISO 14044), such as the average impact of a person over a year. The normalisation was conducted directly in Gabi

software. The resulting normalised impacts all have the common unit of person equivalent (PE) and can be directly compared and summed up.

Both compressive strength and leachability were assigned a weight factor of 0.25. Moreover, the leachability ('L') was considered as the average of leaching indices for all elements, in turn calculated by dividing the leachate value by the threshold value for inert waste (see leaching index values between square parentheses in Table 11-3). Based on this, the overall penalty index (Z) of any type of foam ('f') was calculated as follows:

$$Z_f = 0.5 \cdot \left(\frac{LCA_f}{LCA_{max}}\right) + 0.25 \cdot \left(\frac{L_f}{L_{max}}\right) + 0.25 \cdot \left(\frac{\sigma_{comp,min}}{\sigma_{comp,f}}\right) \quad \text{(Equation 2)}$$

Table 11-4. Normalised data and penalty functions for the tree processes for the valorisation of vitrified bottom ash.

Group of samples	**Scenario 1**	**Scenario 2**	**Scenario 3**
LCA: π = 0.5			
Total LCA results per FU (panel 1000 cm^3)	*0.0031*	0.0014	0.0030
Normalised LCA	*1.00*	*0.46*	*0.96*
Leachability (L): π = 0.25			
L	0.03	0.10	0.04
Normalised L	*0.34*	*1.00*	*0.38*
Compressive strength (σ_{comp}): π = 0.25			
σ_{comp} (MPa)	2.9	1.6	2.9
Normalised σ_{comp}	*0.54*	*1.00*	*0.54*
Penalty (Z)	**0.72**	**0.73**	**0.71**

Table 11-4 indicates that all scenarios are quite similar. This indicates that all scenarios can be applied to valorise vitrified bottom ash into ceramic foams. The glass-ceramic foams (Scenarios 1 and 3) would be preferred when assigning priority to the safety and strength of the waste-derived material. On the other hand, alkali-activated foams (Scenario 2) would be selected when the environmental impact should be reduced.

Scenario 3 presented the lowest penalty according to Table 11-4. However, as previously mentioned, the data from the ecoinvent database may not be fully representative of the processes, as complete data regarding the three scenarios was not available in literature. In addition, the environmental impact of each process could also be reduced, depending on the choice of materials used (e.g. surfactant).

Moreover, the high environmental impact presented by the glass-ceramic foams (Scenarios 1 and 3), could also be mitigated by integrating the incineration of MSW with the production of ceramic foams (sintering operated exploiting heat recovered from the primary step). The chemical composition of vitrified bottom ash could also be revisited. As previously exhibited in Part III, magnetic phases could be precipitated upon firing of iron-rich glasses, thus yielding novel functionalities to the material (Chinnam et al., 2013; Ponsot et al., 2014), such as electromagnetic shielding. An increased cost would be certainly compensated by an increased value of the product.

Regarding Scenario 2, in particular, one of the advantages of using Na-silicate solutions consists of increased properties of the green material when compared to the NaOH activated systems. This could provide the possibility of another process design, in which the silicate-based activator is optimised in order to produce foams with a fairly good performance even without firing.

11.4. Conclusions

Highly porous and chemical stable vitrified bottom ash-based materials were successful obtained from alkali activation (based on different alkaline solutions), alone or combined with firing. Furthermore, the developed glass-ceramic foams presented higher strength and in general lower leaching of heavy metals when compared to the alkali-activated foams. Interestingly, the composition of the alkaline solution (1 M NaOH or 5 M Na-silicate) had a great impact on the phase assemblage observed after hardening and firing.

The LCA highlighted the great impact of firing in most impact categories. In addition, results indicated the influence of materials on the environmental performance of the different scenarios applied to valorise vitrified bottom ash. Finally, an overall penalty index was proposed to compare solutions from different scenarios, considering LCA, leachability and strength. The analysis indicated a quite similar performance for all scenarios. Therefore, the selection of the most convenient process would then depend on the importance assigned for factors such as material properties and environmental impact.

11.5. References

Bai, C., Franchin, G., Elsayed, H., Conte, A., Colombo, P., 2016. High strength metakaolin-based geopolymer foams with variable macroporous structure. J. Eur. Ceram. Soc. 36, 4243–4249. https://doi.org/10.1016/j.jeurceramsoc.2016.06.045

Bernal, S.A., de Gutierrez, R.M., Provis, J.L., Rose, V., 2010. Effect of silicate modulus and metakaolin incorporation on the carbonation of alkali silicate-activated slags. Cem. Concr. Res. 40, 898–907. https://doi.org/10.1016/j.cemconres.2010.02.003

Chinnam, R.K., Francis, A.A., Will, J., Bernardo, E., Boccaccini, A.R., 2013. Review.

Functional glasses and glass-ceramics derived from iron rich waste and combination of industrial residues. J. Non. Cryst. Solids 365, 63–74. https://doi.org/10.1016/j.jnoncrysol.2012.12.006

Clavreul, J., Guyonnet, D., Christensen, T.H., 2012. Quantifying uncertainty in LCA-modelling of waste management systems. Waste Manag. 32, 2482–2495. https://doi.org/10.1016/j.wasman.2012.07.008

Directive 2003/33/EC, 2003. Official Journal of the European Communities.

Farag, M.M., 2007. Materials and Process Selection for Engineering Design, 2nd Editio. ed. CRC Press, Boca Raton. https://doi.org/10.1201/9781420063110

Gibson, L.J., Ashby, M.F., 1999. Cellular solids: structure and properties. Cambridge University Press, Cambridge, UK.

Hertel, T., Novais, R.M., Alarcón, R.M., Labrincha, J.A., Pontikes, Y., 2019. Use of modified bauxite residue-based porous inorganic polymer monoliths as adsorbents of methylene blue. J. Clean. Prod. 227. https://doi.org/10.1016/j.jclepro.2019.04.084

Ismail, I., Bernal, S.A., Provis, J.L., San Nicolas, R., Hamdan, S., Van Deventer, J.S.J., 2014. Modification of phase evolution in alkali-activated blast furnace slag by the incorporation of fly ash. Cem. Concr. Compos. 45, 125–135. https://doi.org/10.1016/j.cemconcomp.2013.09.006

Laurent, A., Bakas, I., Clavreul, J., Bernstad, A., Niero, M., Gentil, E., Hauschild, M.Z., Christensen, T.H., 2014a. Review of LCA studies of solid waste management systems - Part I: Lessons learned and perspectives. Waste Manag. 34, 573–588. https://doi.org/10.1016/j.wasman.2013.10.045

Laurent, A., Clavreul, J., Bernstad, A., Bakas, I., Niero, M., Gentil, E., Christensen, T.H., Hauschild, M.Z., 2014b. Review of LCA studies of solid waste management systems - Part II: Methodological guidance for a better practice. Waste Manag. 34, 589–606. https://doi.org/10.1016/j.wasman.2013.12.004

Natali Murri, A., Rickard, W.D.A., Bignozzi, M.C., van Riessen, A., 2013. High temperature behaviour of ambient cured alkali-activated materials based on ladle slag. Cem. Concr. Res. 43, 51–61. https://doi.org/10.1016/j.cemconres.2012.09.011

Nedeljković, M., Ghiassi, B., Melzer, S., Kooij, C., van der Laan, S., Ye, G., 2018. CO2 binding capacity of alkali-activated fly ash and slag pastes. Ceram. Int. 44, 19646–19660. https://doi.org/10.1016/j.ceramint.2018.07.216

Novais, R.M., Ascensão, G., Ferreira, N., Seabra, M.P., Labrincha, J.A., 2018. Influence of water and aluminium powder content on the properties of waste-containing geopolymer foams. Ceram. Int. 44, 6242–6249. https://doi.org/10.1016/j.ceramint.2018.01.009

Palacios, M., Puertas, F., 2006. Effect of Carbonation on Alkali-Activated Slag Paste. J. Am. Ceram. Soc. 89, 3211–3221. https://doi.org/10.1111/j.1551-2916.2006.01214.x

Park, S.M., Jang, J.G., Lee, N.K., Lee, H.K., 2016. Physicochemical properties of binder gel in alkali-activated fly ash/slag exposed to high temperatures. Cem. Concr. Res. 89, 72–79. https://doi.org/10.1016/j.cemconres.2016.08.004

Piccinno, F., Hischier, R., Seeger, S., Som, C., 2016. From laboratory to industrial scale: a scale-up framework for chemical processes in life cycle assessment studies. J. Clean. Prod. 135, 1085–1097. https://doi.org/10.1016/j.jclepro.2016.06.164

Pisciella, P., Crisucci, S., Karamanov, A., Pelino, M., 2001. Chemical durability of glasses obtained by vitrification of industrial wastes. Waste Manag. 21, 1–9. https://doi.org/10.1016/S0956-053X(00)00077-5

Ponsot, I.M.M.M., Pontikes, Y., Baldi, G., Chinnam, R.K., Detsch, R., Boccaccini, A.R., Bernardo, E., 2014. Magnetic glass ceramics by sintering of borosilicate glass and inorganic waste. Materials (Basel). 7, 5565–5580. https://doi.org/10.3390/ma7085565

Provis, J.L., 2014. Geopolymers and other alkali activated materials: Why, how, and what? Mater. Struct. Constr. 47, 11–25. https://doi.org/10.1617/s11527-013-0211-5

Provis, J.L., Bernal, S.A., 2014. Geopolymers and Related Alkali-Activated Materials. Annu. Rev. Mater. Res. 44, 299–327. https://doi.org/10.1146/annurev-matsci-070813-113515

Provis, J.L., Palomo, A., Shi, C., 2015. Advances in understanding alkali-activated materials. Cem. Concr. Res. 78, 110–125. https://doi.org/10.1016/j.cemconres.2015.04.013

Rincón, A., Giacomello, G., Pasetto, M., Bernardo, E., 2017. Novel ‘inorganic gel casting’ process for the manufacturing of glass foams. J. Eur. Ceram. Soc. 37, 2227–2234. https://doi.org/10.1016/j.jeurceramsoc.2017.01.012

Rincon Romero, A., Salvo, M., Bernardo, E., 2018. Up-cycling of vitrified bottom ash from MSWI into glass-ceramic foams by means of ‘inorganic gel casting’ and sinter-crystallization. Constr. Build. Mater. 192, 133–140. https://doi.org/10.1016/j.conbuildmat.2018.10.135

Salman, M., Cizer, Ö., Pontikes, Y., Snellings, R., Vandewalle, L., Blanpain, B., Balen, K. Van, 2015. Cementitious binders from activated stainless steel refining slag and the effect of alkali solutions. J. Hazard. Mater. 286, 211–219. https://doi.org/10.1016/j.jhazmat.2014.12.046

Shelby, J.E., 2005. Introduction to Glass Science and Technology, Second Edi. ed. The Royal Society of Chemistry, Cambridge.

Tajuelo Rodriguez, E., Garbev, K., Merz, D., Black, L., Richardson, I.G., 2017. Thermal stability of C-S-H phases and applicability of Richardson and Groves’ and Richardson C-(A)-S-H(I) models to synthetic C-S-H. Cem. Concr. Res. 93, 45–56. https://doi.org/10.1016/j.cemconres.2016.12.005

Yu, P., Kirkpatrick, R.J., Poe, B., McMillan, P.F., Cong, X., 2004. Structure of Calcium Silicate Hydrate (C-S-H): Near-, Mid-, and Far-Infrared Spectroscopy. J. Am. Ceram. Soc. 82,

742–748. https://doi.org/10.1111/j.1151-2916.1999.tb01826.x

Chapter 12. Porous conditioned bottom ash-red mud-based glass-ceramics by alkali activation and sinter-crystallisation

12.1. Introduction

The previous chapter highlighted the importance on providing multifunctionalities to waste-derived glass-ceramics in order to environmentally justify high costs associated with firing. Furthermore, Part 3 indicated that magnetite can be precipitated in iron-rich glasses upon firing following specific conditions, such as firing at lower temperature and under inert atmosphere, thus producing a porous glass-ceramic with high thermal and acoustic insulation (due to high porosity), as well as shielding properties (especially for foams fired at low temperature).

Based on this, a new MSWI bottom ash-based glass was developed by ESR9 (NEW-MINE Project) at RWTH Aachen with a higher content of iron oxide, by mixing 66 wt% MSWI bottom ash with 33 wt% red mud. Red mud (or bauxite residue) is a by-product rich in iron oxide generated during alumina production by the Bayer process (Power et al., 2011). The disposal of red mud can generate great environmental concern and must be addressed. Therefore, the conditioning of MSWI bottom ash mixed with red mud offers the possibility to produce a stable glass which can be further valorised into building materials.

In this study, the conditioned bottom ash-red mud glass (VBARM) was applied in the development of porous glass-ceramics by alkali activation, gel-casting and sinter-crystallisation. The present study reports the different conditions applied to produce the porous glass-ceramics regarding composition and firing conditions. Finally, the foams were characterised by means of XRD (in order to identify the phases formed upon hardening and firing), porosity, strength, microstructure and leaching of heavy metals.

12.2. Experimental procedure

The VBARM-based porous glass-ceramics were developed by firstly mixing at 400 rpm fine powders of VBARM or 70 wt% VBARM/30 wt% soda-lime glass to an alkaline solution of 1 M NaOH. The overall solid content corresponded to 70 wt% of the suspension. After 3h of mechanical stirring, 4 wt% of surfactant (Triton X-100, (polyoxyethylene octyl phenyl ether – $C_{14}H_{22}O(C_2H_4O)_n$, n = 9–10, Sigma-Aldrich, Gillingham, UK) was introduced to the suspension, which was easily foamed by intensive mechanical stirring at 2000 rpm. Thereafter, the foamed slurry was dried at 40 °C for 48h, demoulded and fired. The firing treatment was performed at 800 °C or 900 °C, with heating rate of 10 °C/min and a holding time of 1h. In addition, one group of samples was fired in flowing nitrogen atmosphere, at 800 °C with heating rate of 5 °C/min and a holding time of 60 min. Table 12-1 presents the different groups of

samples developed: 0SLG refers to foams made with pure VBARM, whereas 30SLG consist of foams made with addition of 30 wt% soda-lime glass.

Table 12-1. Soda-lime glass content and firing conditions applied for each group of samples.

Group of samples	**0SLG800**	**0SLG900**	**30SLG800**	**30SLG900**	**30SLG800N$_2$**
Soda-lime glass	0 wt%	0 wt%	30 wt%	30 wt%	30 wt%
Firing temperature	800 °C	900 °C	800 °C	900 °C	800 °C
Firing atmosphere	air	air	air	air	nitrogen

12.3. Results and discussion

The crystallisation temperature of fine powders (below 75 µm) of VBARM lies around 850 °C, according to Figure 12-1. This temperature was taken as a reference for the sintering experiments, performed at 800 °C or 900 °C.

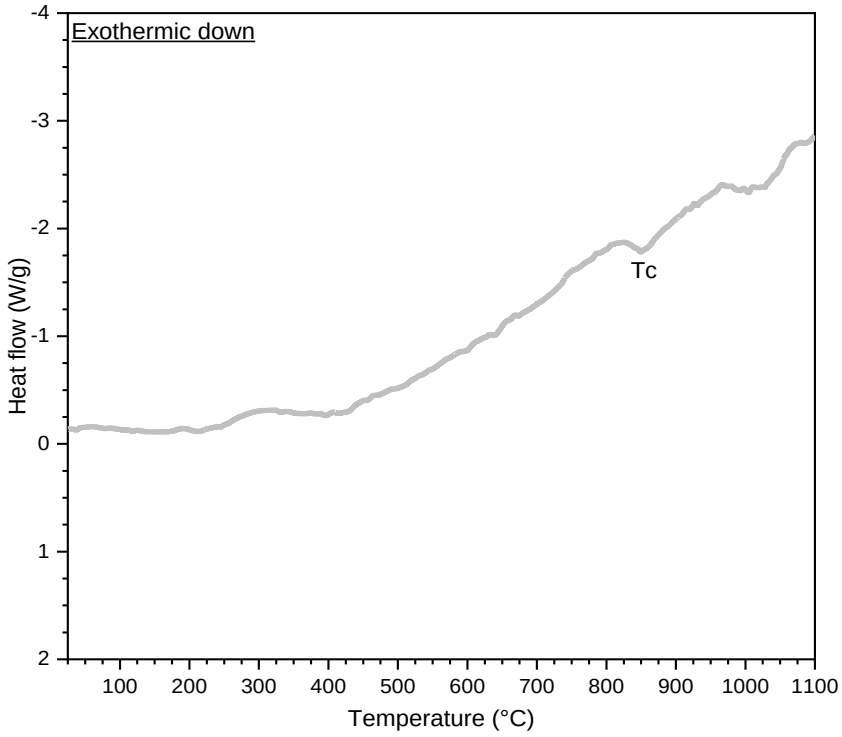

Figure 12-1. DSC curves of conditioned bottom ash-red mud.

XRD analysis (Figure 12-2) indicate the presence of cristobalite (SiO_2, PDF#82-1232) and maghemite (Fe_2O_3, PDF#00-025-1402) in the glass as received. Maghemite could have been

originated from the intermediate region between glass and recovered metals which were milled together with the vitrified residue. Regarding the XRD patterns of not fired foams, thermonatrite ($Na_2CO_3 \cdot H_2O$, PDF#00-008-0448) was detected in 0SLG and 30SLG, while the addition of soda-lime glass favoured formation of gismondine ($CaAl_2Si_2O_8 \cdot 4H_2O$, PDF#00-020-0452). Traces of trona ($Na_3H(CO_3)_2(H_2O)_2$, PDF#75-1195) were also identified in 0SLG. The presence of both thermonatrite and trona could be due to an excess of Na^+ ions (from the alkaline solution) which reacted with atmospheric CO_2.

It was not possible to identify the phase corresponding to the peak at around 38 degrees. However, it can be observed that the addition of soda-lime glass overall promoted the formation of more phases, when compared to the pure VBARM samples This could have influenced the gel-casting step, and, consequently, the porosity of the material (in terms of size and quantity of pores).

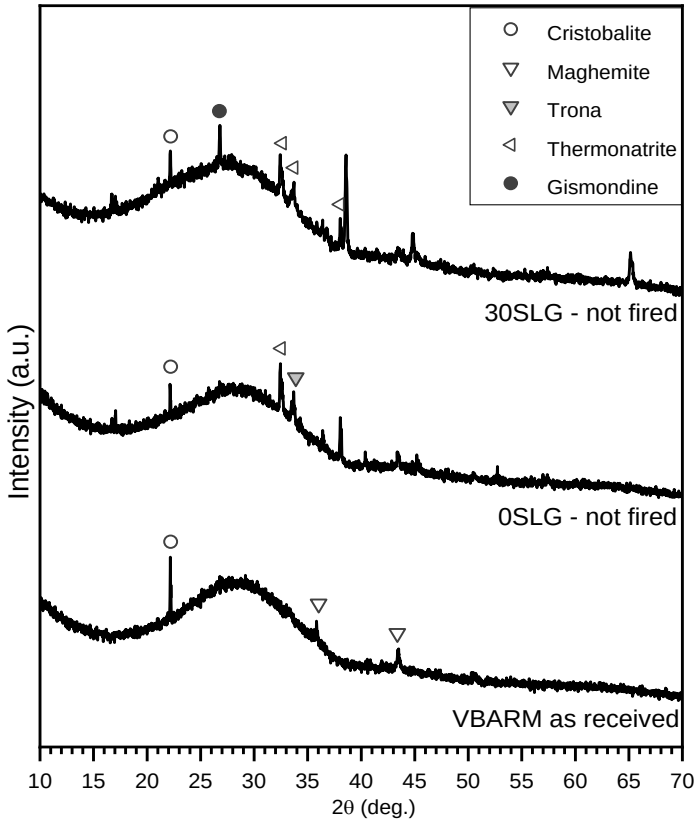

Figure 12-2. XRD patterns of conditioned bottom ash-red mud-based foams and as received glass.

The phase evolution upon firing for samples submitted to different firing conditions are represented in Figure 12-3. The firing below the crystallisation temperature of conditioned bottom ash-red mud (Figure 12-3a, 0SL800) led to the precipitation in traces of hedenbergite ($Ca(Fe_{0.821}Al_{0.179})(SiAl_{0.822}Fe_{0.178}O_6)$, PDF#78-1546), nepheline ($Na_{6.65}Al_{6.24}Si_{9.76}O_{32}$, PDF#83-

2372) and andradite ($Ca_3Fe_2(SiO_4)_3$, PDF#84-1935). The increase in firing temperature to 900 °C (Figure 12-3a, 0SL900) increased the content of crystalline phases and also promoted the formation of gehlenite ($Ca_2Al((Al\ Si)O_7$), PDF#87-0969). Due to the intensive crystallisation of the glass during firing, pure VBARM samples were poorly densified. Analogous to the studies carried on with Plasmastone (Part III), 30 wt% soda-lime glass was added in order to improve sintering by viscous flow. The addition of this waste glass promoted the formation of wollastonite ($CaSiO_3$, PDF#84-0655) and anorthite ($(Ca_{.94}Na_{.06})(Al_{1.94}Si_{2.06}O_8)$, PDF#84-0751), besides increasing the content of nepheline (Figure 12-3a, 30SL900).

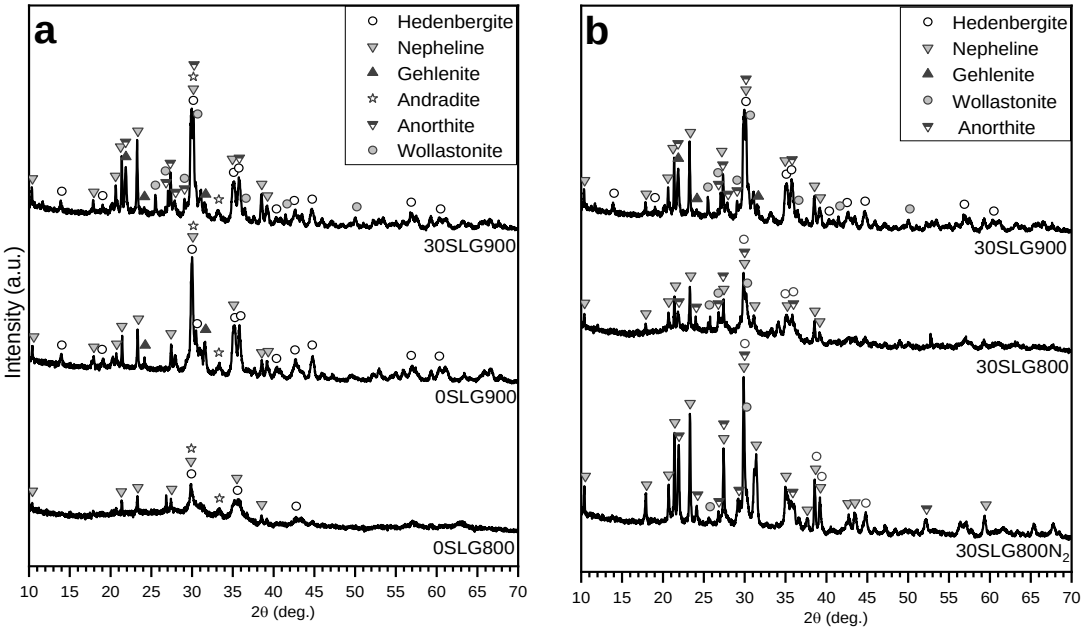

Figure 12-3. XRD patterns of VBARM based glass-ceramics fired in air or in nitrogen.

Interestingly, samples made with addition of soda-lime glass fired at lower temperature, in air, (30SL800, Figure 12-3b) were more crystallised than 0SL800 (Figure 12-3a), similar to what was observed for Plasmastone-based samples fired at low temperature (Chapter 6). The change in firing atmosphere passing from air to nitrogen (30SL800N_2, Figure 12-3b) increased the content of crystalline phases, promoting the formation of especially nepheline and anorthite. This probably decreased the alkali content of the residual glass phase when compared to the other samples. Furthermore, samples fired in nitrogen presented the highest crystalline content from all developed samples. Previous studies have already indicated increase in crystallisation for iron-rich glasses when fired in nitrogen, due to the absence of oxidation of Fe^{2+} to Fe^{3+}. On the other hand, when iron-rich glasses are fired in air, surface oxidation reduces the formation of magnetite, thus reducing the crystallisation degree (Karamanov et al., 2004, 2000). Finally, one must also consider that the heating rate was lower for samples fired in nitrogen, due to

limitations of the furnace used. A lower heating rate could have also promoted crystallisation (Bernardo et al., 2009).

Analogous to Plasmastone-based foams fired in nitrogen (Chapter 7), iron oxide phases were also found in the VBARM based glass-ceramic foams. For an easier visualisation of peaks consistent to those of iron oxide, Figure 12-4 exhibits the XRD patterns identifying these peaks. It was only possible to detect two variants of magnetite (Fe_3O_4): 'M1' (PDF#89-0691) and 'M2' (PDF#89-0951), which could possibly provide novel functionalities to the glass-ceramic foams, as indicated by Chapters 6 and 7. In addition, peaks corresponding to hematite (Fe_2O_3, PDF#89-2810) were hardly detected on samples fired at 800 °C, especially for samples fired in nitrogen.

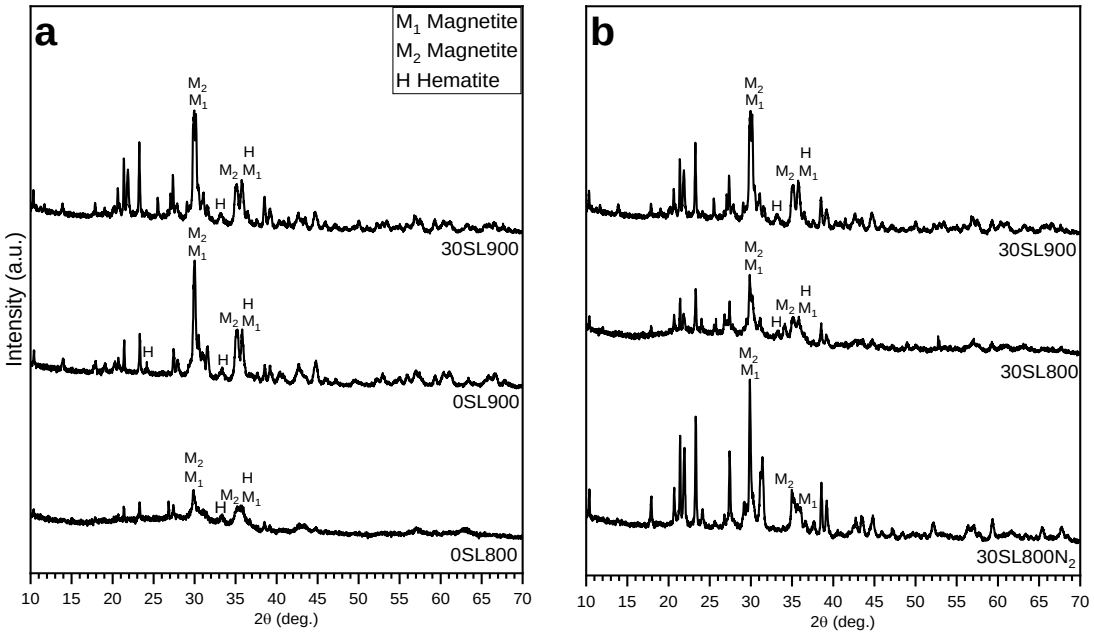

Figure 12-4. XRD patterns of VBARM based glass-ceramics with peaks corresponding to those of iron oxide.

The developed foams are highly porous, with porosity higher than 73 vol%, mainly open (Table 12-2). The high porosity of the foams indicates that these waste-based glass-ceramics could present high acoustic and insulation properties. Furthermore, the compressive strength (σ_{comp}) and estimated bending strength of the solid phase (σ_{bend}, estimated by applying the Gibson and Ashby model, see Chapter 2) (Gibson and Ashby, 1999)) were in general quite low.

Regarding the foams made with pure VBARM, the increase in firing temperature to 800 °C to 900 °C slightly increased the estimated σ_{bend}, due to promotion of viscous flow with temperature. However, 0SL900 foams were still too brittle, due to the high tendency to crystallisation presented by the vitrified residue, as observed in Figure 12-3. Analogous to Plasmastone, viscous flow was affected by increase in viscosity due to precipitation of crystals during firing, hindering densification. The addition of soda-lime glass finally led to stronger

foams, for firing at 900 °C. In addition, considering only 30SL foams fired at 800 °C, the change in atmosphere to nitrogen decreased the estimated σ_{bend} from 34 MPa to 5 MPa. This is most probably associated to poorly densification of foams fired in nitrogen atmosphere due to intensive crystallisation upon firing.

Table 12-2. Physical and mechanical properties of the porous glass-ceramics.

Group of samples	**0SLG 800**	**0SLG 900**	**30SLG 800**	**30SLG 900**	**30SLG 800N$_2$**
Soda-lime glass	0 wt%	0 wt%	30 wt%	30 wt%	30 wt%
Firing temperature	800 °C	900 °C	800 °C	900 °C	800 °C
Firing atmosphere	air	air	air	air	nitrogen
Density determinations					
ρ_{geom} (g/cm^3)	0.51 ± 0.02	0.52 ± 0.06	0.73 ± 0.04	0.71 ± 0.05	0.69 ± 0.02
$\rho_{apparent}$ (g/cm^3)	2.91 ± 0.01	3.00 ± 0.02	2.52 ± 0.02	2.65 ± 0.02	2.80 ± 0.02
ρ_{true} (g/cm^3)	2.91 ± 0.02	3.00 ± 0.01	2.71 ± 0.00	2.78 ± 0.01	2.80 ± 0.00
Porosity distribution					
Total porosity (vol%)	82.6	82.6	73.0	74.5	75.2
Open porosity (vol%)	82.6	82.6	71.0	73.3	75.2
Closed porosity (vol%)	0.0	0.0	2.0	1.2	0.0
Strength determinations					
σ_{comp} (MPa)	0.1 ± 0.0	0.1 ± 0.0	0.9 ± 0.3	2.3 ± 0.1	0.1 ± 0.0
σ_{bend} (MPa)	3.2	6.8	33.9	89.6	5.2

Figure 12-5 shows the micrographs of the glass-ceramic foams. As indicated by Table 12-2, the foams are highly porous, with porosity mainly open. The pore size distribution of 0SL900 (Figure 12-5a) is quite heterogeneous, comprising macro-pores and micro-pores on the cell walls. The foams made with soda-lime glass (Figures 12-5b and d), on the other hand, presented a more homogeneous pore size distribution, with overall smaller pore size than 0SL900. This is most probably associated to an increase of hardening with addition of soda-lime glass (as indicated by Figure 12-2 and as previously observed in Chapter 9). This means that the

'gelified' slurries made with soda-lime glass addition were more viscous, which helped in preventing more efficiently the collapse of the bubbles after the foaming step was ceased (Rincon Romero et al., 2018). The macropores of 0SL900 may be attributed to a possible collapse of bubbles during the drying step of the foamed slurry.

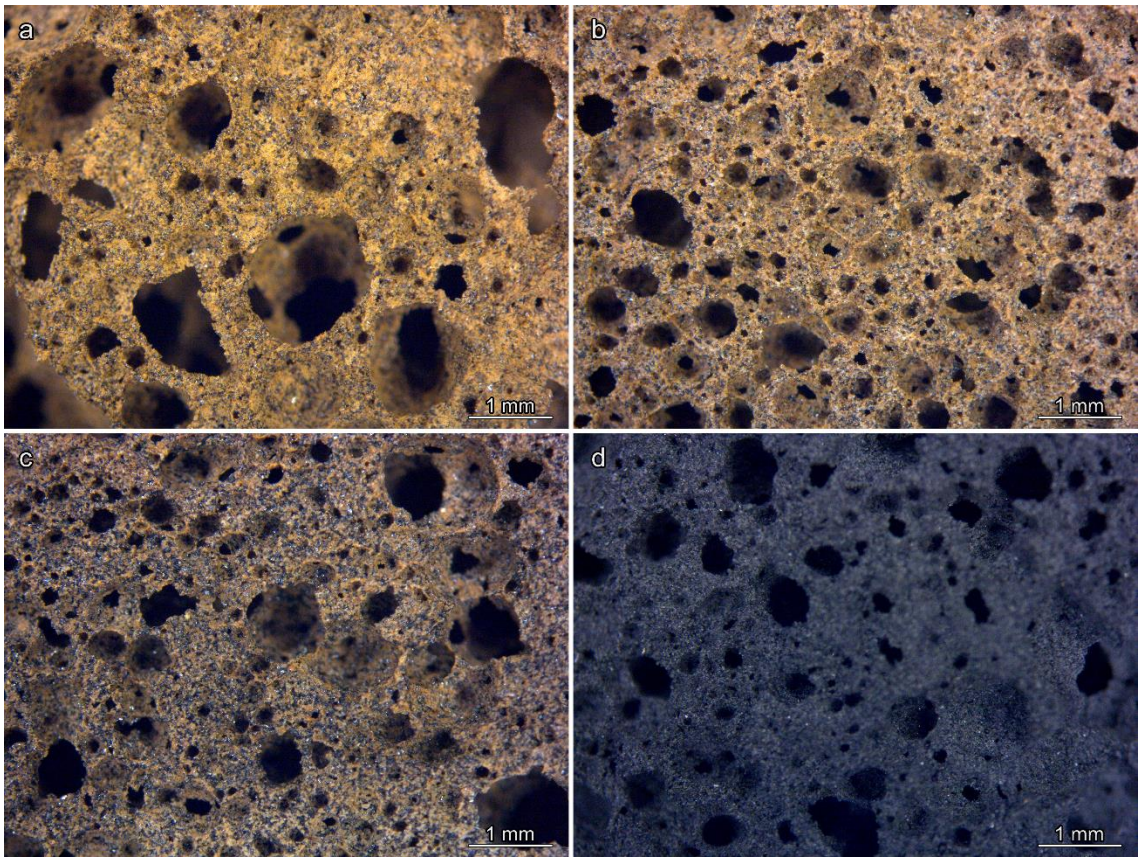

Figure 12-5. Microstructure of the conditioned bottom ash-red mud-based foams: (a) 0SL900; (b); 30SL900 (c); 30SL800; (d) 30SL800N2.

Leaching tests (Table 12-3) were performed in fired samples and also on conditioned bottom ash-red mud. The glass presented low leaching of heavy metals, far below the limit values for inert waste (*Directive 2003/33/EC*, 2003). However, the firing in air of VBARM based foams decrease the stability of pollutants (specially of Cr), which prevented the classification of these waste-derived materials as inert waste. Analogous to Plasmastone-based foams (Chapter 7), stabilisation of Cr could be achieved by changing the firing atmosphere to nitrogen, as a result of the phases assemblage formed. In the present study, the increased chemical stability could be associated to a higher stability of the residual glass phase, due a lower content of alkali in the residual glass phase when compared to the other fired samples. As previously mentioned in Chapter 5, alkali-rich highly depolymerized glasses are more prone to ionic diffusion, which reduces the stability of the residual glass phase (Bunker, 1994).

Table12- 3. Results of the leaching test of the developed porous glass-ceramics (ppm).[4]

	Limit values		**VBARM**	**0SL 800**	**0SL 900**	**30SL 800**	**30SL 800N_2**	**30 SL900**
	Inert waste	**Non-hazardous waste**						
As	**0.5**	**2**	<0.0049	0.0181	0.0223	0.0212	<0.0049	0.0319
Ba	**20**	**100**	0.0044	0.0133	0.0195	0.0126	0.0130	0.0141
Cd	**0.04**	**1**	<0.0002	<0.0002	<0.0002	<0.0002	<0.0002	<0.0002
Cr	**0.5**	**10**	0.0144	>1.746	1.0420	>1.813	0.0049	>1.219
Cu	**2**	**50**	0.0374	0.0154	0.0383	0.0041	0.0042	0.0274
Hg	**0.01**	**0.2**	<0.0004	<0.0004	<0.0004	<0.0004	<0.0004	<0.0004
Mo	**0.5**	**10**	<0.0033	0.3044	0.4668	0.2073	0.5676	0.2382
Ni	**0.4**	**10**	<0.0014	<0.0014	<0.0014	<0.0014	<0.0014	<0.0014
Pb	**0.5**	**10**	0.0052	<0.0047	<0.0047	<0.0047	<0.0047	0.0049
Sb	**0.06**	**0.7**	0.0132	0.0503	0.0179	0.0513	<0.0099	0.0318
Se	**0.1**	**0.5**	<0.0122	<0.0122	<0.0122	<0.0122	<0.0122	<0.0122
Zn	**4**	**50**	<0.0203	<0.0203	<0.0203	<0.0203	<0.0203	<0.0203

12.4. Conclusions

This study presented a first attempt to valorise conditioned bottom ash-red mud into porous glass-ceramics by alkali activation, gel-casting and sinter-crystallisation. The developed foams were highly porous, with porosity mainly open. The development of the foams involved modifications regarding firing temperature, firing atmosphere and composition. Pure VBARM based glass-ceramic foams were too brittle due to limited viscous flow upon firing. The addition of 30 wt% soda-lime glass led to stronger foams, for firing at 900 °C. However, firing in air produced foams with higher leachate values of Cr. Foams fired in nitrogen atmosphere, on the other hand, presented low leachate values of this pollutant as well as high content of crystalline phases. In fact, the high tendency to crystallisation during firing in nitrogen hindered sintering by viscous flow, leading to poorly densified and extremely brittle foams. The foams also exhibited variants of magnetite, which could provide novel functionalities to the material. Future studies can comprise the increase of heating rate and soda-lime glass content in order to produce stronger foams, as well as assessment of novel functionalities.

12.5. References

Bernardo, E., Scarinci, G., Edme, E., Michon, U., Planty, N., 2009. Fast-sintered gehlenite

[4] The reported leachate values presenting '<' are on the basis of instrument sensibility.

glass-ceramics from plasma-vitrified municipal solid waste incinerator fly ashes. J. Am. Ceram. Soc. 92, 528–530. https://doi.org/10.1111/j.1551-2916.2008.02892.x

Bunker, B.C., 1994. Molecular mechanisms for corrosion of silica and silicate glasses. J. Non. Cryst. Solids 179, 300–308. https://doi.org/10.1016/0022-3093(94)90708-0

Directive 2003/33/EC, 2003. , Official Journal of the European Communities.

Gibson, L.J., Ashby, M.F., 1999. Cellular solids: structure and properties. Cambridge University Press, Cambridge, UK.

Karamanov, A., Pisciella, P., Pelino, M., 2000. Crystallization kinetics of iron rich glass in different atmospheres. J. Eur. Ceram. Soc. 20, 2333–2237.

Karamanov, A., Taglieri, G., Pelino, M., 2004. Sintering in nitrogen atmosphere of iron-rich glass-ceramics. J. Am. Ceram. Soc. 87, 1354–1357. https://doi.org/10.1111/j.1151-2916.2004.tb07734.x

Power, G., Gräfe, M., Klauber, C., 2011. Bauxite residue issues: I. Current management, disposal and storage practices. Hydrometallurgy 108, 33–45. https://doi.org/10.1016/j.hydromet.2011.02.006

Rincon Romero, A., Salvo, M., Bernardo, E., 2018. Up-cycling of vitrified bottom ash from MSWI into glass-ceramic foams by means of ‘inorganic gel casting’ and sinter-crystallization. Constr. Build. Mater. 192, 133–140. https://doi.org/10.1016/j.conbuildmat.2018.10.135

PART V - Valorisation of partially crystallised residues

Chapter 13. Ceramic foams by alkali activation and sintering of partially crystalline residues

13.1. Introduction

Chapter 10 indicated the possibility of recycling vitrified bottom ash-based glass-ceramic foams into new foams. Furthermore, the addition of soda-lime glass enabled to increase the densification of the struts, thus producing stronger foams. In this chapter, the approach of alkali activation combined with gel-casting and sintering was further extended to valorise two other types of partially crystallised residues into ceramic foams: polishing stoneware residue and plasma processed asbestos-containing waste ('cofalit').

Polishing stoneware residue refers to the material collected from the polishing of porcelain stoneware tiles. This material is usually disposed in landfills, which can generate environmental concerns due to high quantities of waste landfilled (Rambaldi et al., 2007). An alternative to avoid the landfilling is by valorising polishing stoneware residues into building materials, such as ceramic tiles (Rambaldi et al., 2007) and geopolymers (Ramos et al., 2018).

Cofalit, on the other hand, is a material obtained after the plasma vitrification of asbestos, from Inertam-Europlasma (France) (Bernardo et al., 2011). This thermal treatment is applied in order to destroy the harmful fibrous structure of asbestos, producing an inert material (Inertam; Spasiano and Pirozzi, 2017). After the melting of asbestos, the molten material is poured into containers and submitted to uncontrolled cooling at slow cooling rates. This leads to some crystallisation of the residue, especially due to the composition of the residue. Cofalit can then further applied as building materials, such as aggregates (Inertam). A previous study has indicated that this partially crystalline residue could also be valorised into glass-ceramics, in order to mitigate the high costs associated to plasma vitrification (Bernardo et al., 2011). In this case, the residue was firstly melted and quenched in order to produce an amorphous material, which was then applied in the production of dense or porous glass-ceramics (Bernardo et al., 2011).

In this study, soda-lime glass was also added in order to increase the glass content of the material. In fact, the challenge in applying alkali activation followed by firing to partially crystalline residues may involve the reduced amount of glass phase in these residues. As a comparison, a material with higher amorphous content presents, usually, higher reactivity, and, as a result, a greater amount of hydrated phases can be formed due to alkali activation (Garcia-Lodeiro et al., 2014). Therefore, when applying residues with limited amount of amorphous phase to alkali activation, the hardening of the slurry may be affected, thus influencing the gel-casting step. In addition, as already indicated for the recycling of vitrified bottom ash-based

foams, the limited amount of amorphous content upon firing can also affect the densification of the material by viscous flow.

13.2. Experimental procedure

The fine residues powders of partially crystalline residues (polishing stoneware residue or cofalit) were added to an alkaline solution of low molarity and mixed for 3h at 400 rpm. Thereafter, the slurry was submitted to curing, before being foamed by intensive mechanical stirring. 4 wt% Triton was then added to the suspension, which was submitted to intensive mechanical stirring at 2000 rpm. The foamed structure was finally dried at 40 °C, before being demoulded and fired. The firing treatment was done following a heating rate of 10 °C/min and holding time of 1h at 900 °C. The quantity of soda-lime glass added, as well as the composition of the alkaline solution, solid content of the suspension and curing conditions (temperature and time) are presented in Table 13-1. Table 13-1 also indicates the names of each group of samples, in each the numbers corresponds to the quantity of soda-lime glass (SL) mixed with the partially crystallised residue during dissolution.

In the case of the polishing stoneware residues, the addition of 10 wt% soda-lime glass allowed to decrease the molarity of the alkaline solution from 2.5 M to 1 M NaOH. Regarding cofalit, the low molarity of the alkaline solution was maintained, due a high quantity of CaO in the composition of this residue.

Table 13-1. Parameters applied in the production of ceramic foams.

Group of samples	**PWR0SL**	**PWR10SL**	**C10SL**	**C30SL**
Derived foam	**Polishing stoneware residue**		**Cofalit**	
Soda-lime glass addition	0 wt%	10 wt%	10 wt%	30 wt%
Activating solution	2.5 M NaOH	1 M NaOH	1 M NaOH	1 M NaOH
Solid content	63%	63%	60%	60%
Curing before foaming	1h at 75 °C	2h at 75 °C	2h at 20 °C	2h at 20 °C
Firing temperature	900 °C	900 °C	900 °C	900 °C

13.3. Results and discussion

13.3.1. Valorisation of polishing stoneware residues

FTIR analysis (Figure 13-1) were performed on fine powders of polishing stoneware residue and on fired and not fired foams made with this partially crystallised residue. The results indicate that the hardening mechanism of the activated suspensions was related to the formation of hydrated compounds (associated to the O-H stretching and H-OH bending bands), and, mostly to the precipitation of carbonates (Rincon Romero et al., 2018). These bands, as well as the band associated to the addition of the surfactant (C-H_2 stretching) are not present in the

polishing stoneware residue and disappear after firing treatment done at 900 °C (Rincón et al., 2017).

Furthermore, the FTIR spectra of PWR0SL and PWR10SL are quite similar. This indicates that the reduction in molarity passing from 2.5 M (PWR0SL) to 1 M (PWR0SL) was effectively compensated by the addition of 10 wt% soda-lime glass.

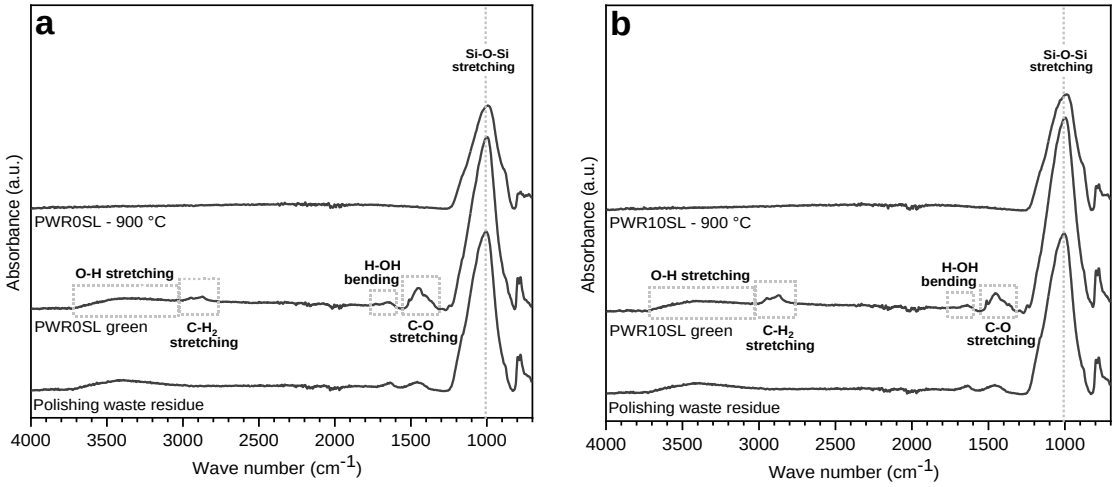

Figure 13-1. FTIR analysis made on polishing stoneware residue and on green and fired foams of PWR0SL (a) and PWR10SL (b).

XRD analyses were performed on polishing stoneware residue and on the not fired foams (Figure 13-2a). Polishing stoneware residues present the following phases: quartz (SiO_2, PDF#85-1054), albite ($Na(AlSi_3O_8)$, PDF#76-0898) and zirconium silicate ($ZrSiO_4$, PDF#71-0991). These phases are also present in the activated residues, and exhibit the same intensity, despite alkali activation and addition of soda-lime glass.

In order to identify the products formed due to alkali activation, it was plotted in Figure 13-2b the difference between the XRD patterns of PWR0SL or PWR10SL and the polishing stoneware residue (as received). This allowed the identification of signals consistent to those of thermonatrite ($Na_2CO_3 \cdot H_2O$, PDF#76-0910), trona ($Na_3(CO_3)(HCO_3) \cdot 2H_2O$, PDF#89-4125, as well as sodium aluminium silicate hydrate (N-A-S-H, $Na_6(AlSiO_4)_6 \cdot (H_2O)_8$, PDF#88-1190) and traces of revdite ($Na_2Si_2O_5 \cdot 5H_2O$, PDF# 00-033-1279). The higher molarity of the alkaline solution promoted the formation of carbonates (trona and thermonatrite), while the addition of soda-lime glass contributed to the precipitation of more hydrated compounds. Furthermore, due to the limited amount of CaO in polishing stoneware residue, it was not possible to detect any Ca-based product, as observed for CaO-rich glasses in the previous chapters. Finally, these results demonstrated that the technique based on alkali activation followed by gel-casting and firing can also be applied in materials with very low content of CaO.

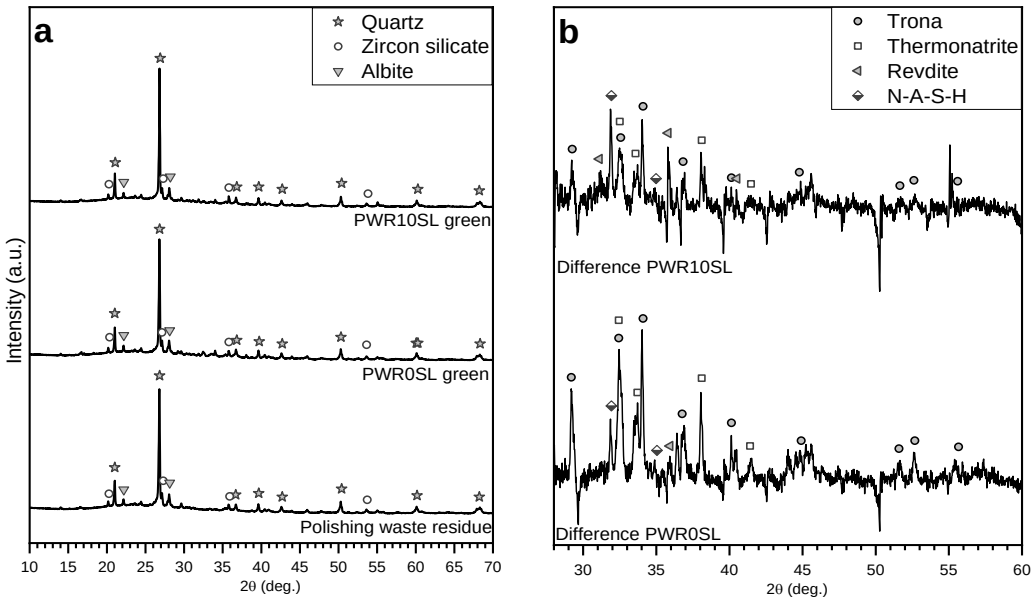

Figure 13-2. XRD patterns of: a) polishing stoneware residue and PWR0SL and PWR10SL (not fired); b) the difference between the XRD patterns of green foams (PWR0SL or PWR10SL) and polishing stoneware residue.

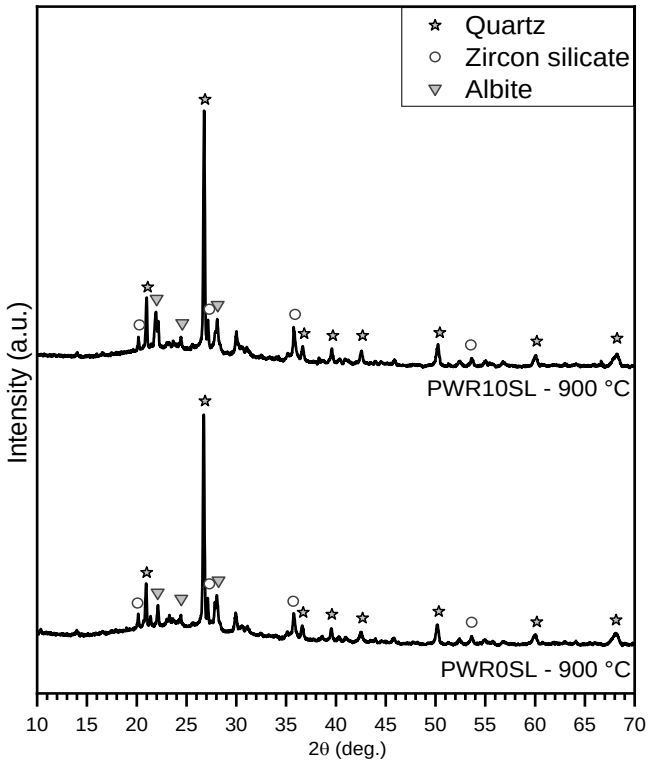

Figure 13-3. XRD patterns of fired foams made with polishing stoneware residue.

The firing of polishing stoneware residue-based foams did not lead to any substantial change in the phase assemblage (Figure 13-3): it was only possible to detect the crystalline

phases already present in the starting material. Moreover, the addition of soda-lime glass promoted only slight changes in the intensity of albite.

The micrographs of the foams (Figure 13-4) show that it was indeed possible to produce highly porous materials with a partially crystallised residue, presenting almost exclusively open-celled morphology. In addition, the firing treatment did not determine a decrease in porosity in the two types of foams. Finally, the addition of 10 wt% soda-lime glass promoted viscous flow, as indicated by the signalled area in Figure 13-4f.

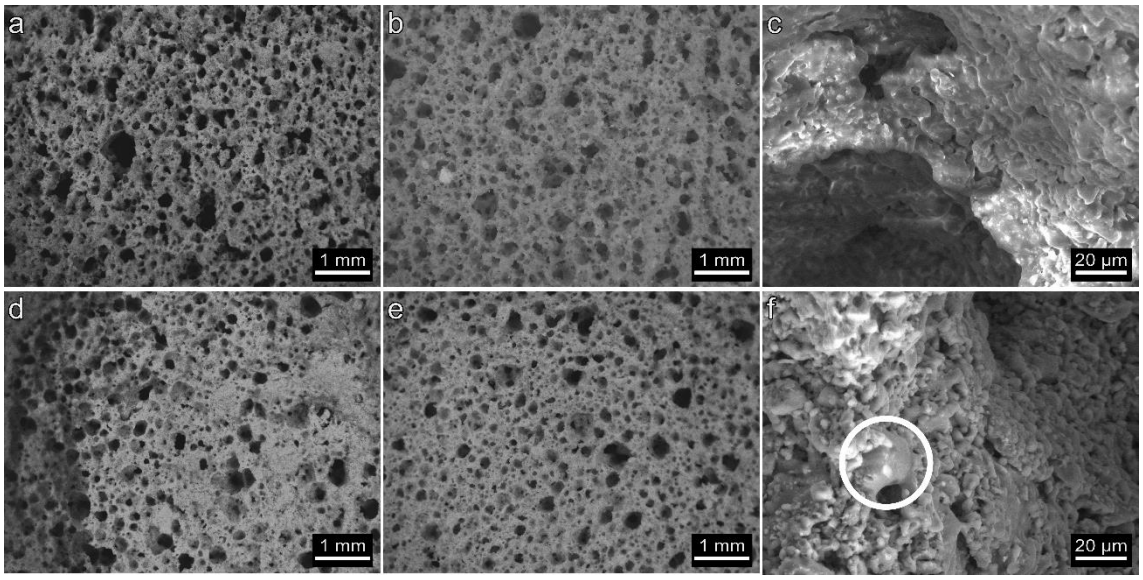

Figure 13-4. Polishing stoneware residue derived foams: a) PWL0SL not fired; b-c) PWL0SL fired; d) PWR10SL not fired; e-f) PWR10SL fired.

Table 13-2 is consistent with the micrographs of the developed foams: both foams PWR0SL and PWR10SL are highly porous (porosity higher than 74 vol%), with porosity mainly open. Furthermore, the foams are also quite strong, especially when one considers their low relative density. The estimated bending strength of the solid phase (σ_{bend}, see Chapter 2) of both foams is above 100 MPa. These estimated values are comparable to the bending strength of ceramic tiles made with polishing stoneware residue (Rambaldi et al., 2007), as well as the strength of dense glass-ceramics made from vitrified mixture of polishing stoneware residue, red mud and fly ash (Bernardo et al., 2009).

The findings of this study show that the two approaches applied to produce PWR0SL and PWR10SL can be potentially employed to valorise polishing stoneware residue into strong and highly porous ceramics, with similar properties. PWR0SL has the advantage to employ a higher amount of polishing stoneware residue in the process, whereas PWR10SL allowed to decrease the molarity of the alkaline solution, thus decreasing costs.

Table 13-2. Physical and mechanical properties data of the partially crystallised porous ceramics.

Group of samples	**PWR0SL**	**PWR10SL**	**C10SL**	**C30SL**
Derived foam	**Polishing stoneware residue**		**Cofalit**	
Soda-lime glass addition	0 wt%	10 wt%	10 wt%	30 wt%
Firing temperature	900 °C	900 °C	900 °C	900 °C
Density determinations				
ρ_{geom} (g/cm^3)	0.66 ± 0.01	0.64 ± 0.02	0.38 ± 0.01	0.57 ± 0.01
$\rho_{apparent}$ (g/cm^3)	2.46 ± 0.04	2.59 ± 0.00	3.02 ± 0.00	2.98 ± 0.00
ρ_{true} (g/cm^3)	2.54 ± 0.00	2.59 ± 0.00	3.02 ± 0.00	2.98 ± 0.00
Porosity distribution				
Total porosity (vol%)	74.0	75.1	87.3	80.9
Open porosity (vol%)	73.1	75.1	87.3	80.9
Closed porosity (vol%)	0.9	0.0	0.0	0.0
Strength determinations				
σ_{comp} (MPa)	3.1 ± 0.6	2.5 ± 0.4	0.2 ± 0.1	2.4 ± 0.2
σ_{bend} (MPa)	118.7	103.5	20.9	147.1

13.3.2. Valorisation of cofalit

Figure 13-5 exhibits the FTIR spectra of C10SL and C30SL:

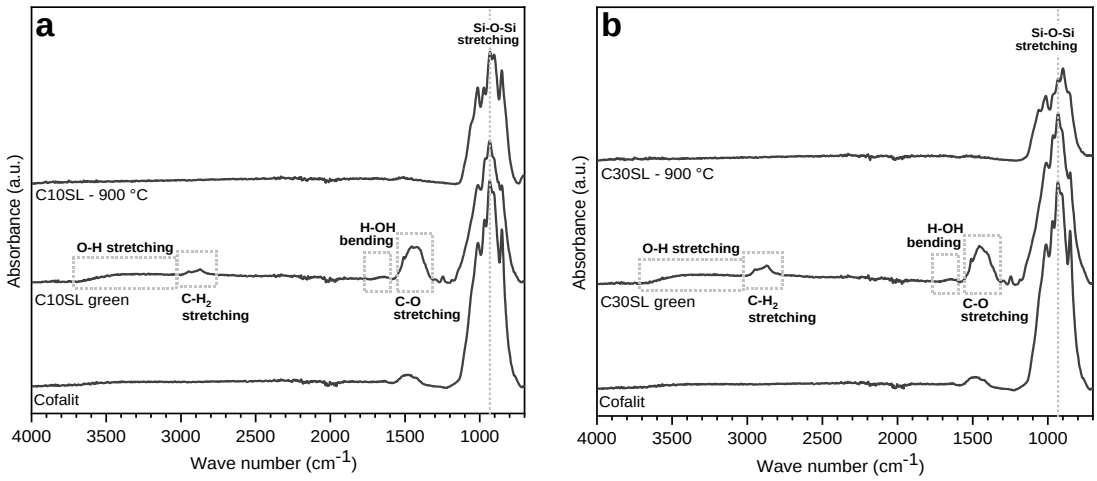

Figure 13-5. FTIR analysis made on cofalit and on C10SL (a) and C30SL (b).

As already observed for the polishing stoneware residue-based foams, the hardening in cofalit-based foams was mainly associated to the precipitations of carbonates (evidenced by the C-O stretching band in Figure 13-5) (Nedeljković et al., 2018). Furthermore, the increase in

soda-lime glass from 10 wt% (C10SL) to 30 wt% (C30SL) apparently did not increase the hardening of the activated slurries, as the FTIR spectra of both green foams were quite similar.

On the other hand, the increase in soda-lime glass passing from 10 wt% (C10SL) to 30 wt% (C30SL) allowed to greatly increase the strength of the foams (see Table 13-2): the estimated bending strength increased in 7 times with the addition of more soda-lime glass. In fact, the estimated bending strength of C30SL foams is even superior than the bending strength of dense glass-ceramics made with remelted cofalit (Bernardo et al., 2011).

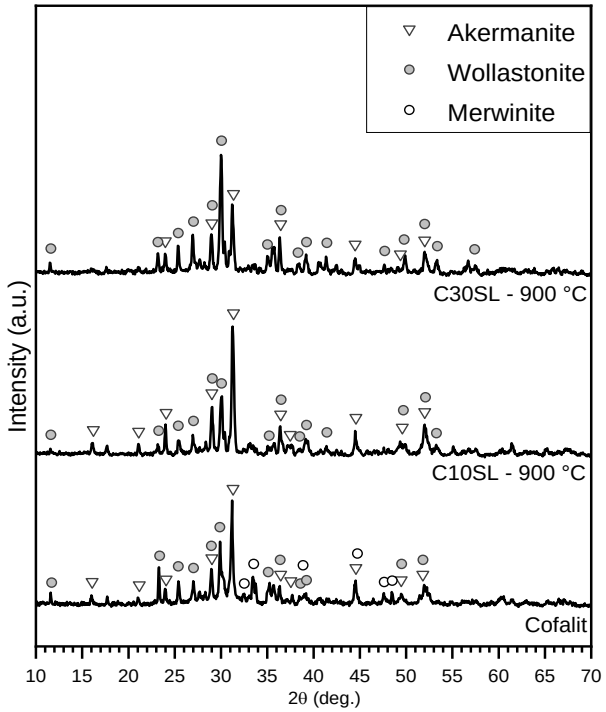

Figure 13-6. XRD patterns of cofalit and fired cofalit-based foams.

The XRD patterns of cofalit and fired cofalit-based foams (Figure 13-6) help to understand the lower mechanical performance of C10SL: cofalit is already quite crystallised, with limited amount of glass phase available for sintering by viscous flow. Therefore, it was necessary to add higher amounts of soda-lime glass to improve densification.

The main crystalline phases detected in cofalit were akermanite ($Ca_2Mg(Si_2O_7)$, PDF#87-0046) and wollastonite ($CaSiO_3$, PDF#00-043-1460). The firing treatment promoted the precipitation of akermanite, whereas the addition of soda-lime glass increased the signals correspondent to wollastonite, as already observed in Plasmastone/soda-lime glass mixtures (Part III). Finally, merwinite ($Ca_3Mg(SiO_4)_2$, PDF#00-035-0591) was also detected, only in traces, in cofalit.

The micrographs of the cofalit-based foams (Figure 13-7) are consistent with Table 13-2, which indicated that the foams were highly porous (porosity higher than 80.9 vol%), with

mainly open porosity. In addition, the pore size distribution is quite homogeneous and similar in foams from different groups.

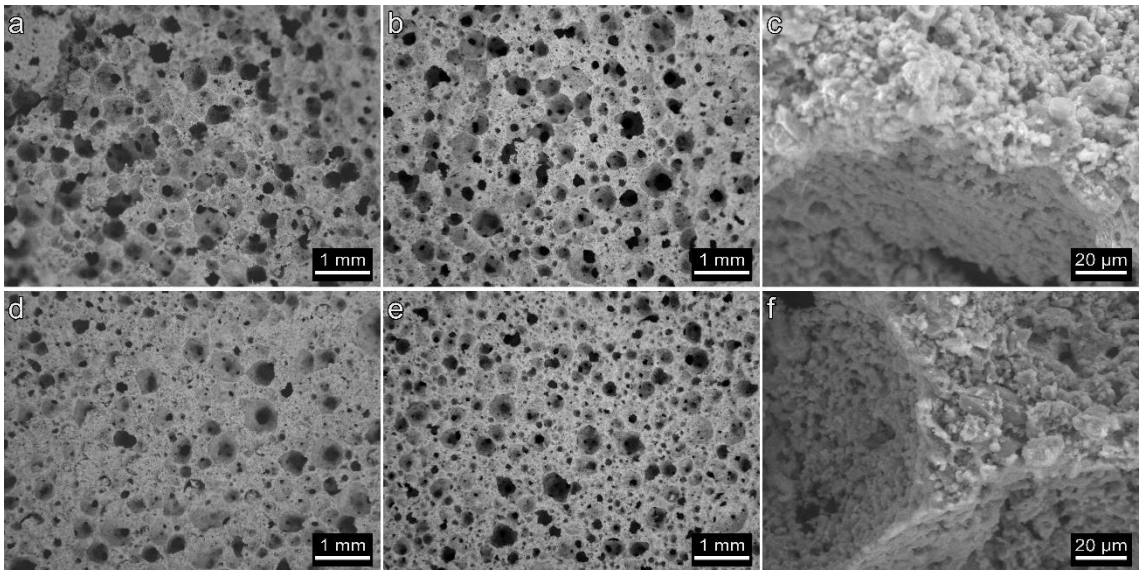

Figure 13-7. Cofalit-based foams: a) C10SL not fired; b-c) C10SL fired; d) C30SL not fired; e-f) C30SL fired.

13.4. Conclusions

The findings of this study suggest the feasibility of developing strong and highly porous ceramic by alkali activation, gel-casting and firing of partially crystallised residues. Soda-lime glass has proven to be helpful in reducing the molarity of the alkaline solution and in improving the strength of the fired foams, especially in the case of plasma processed asbestos-containing waste (‘cofalit’) foams. Furthermore, the valorisation of polishing stoneware residues indicated the possibility of applying alkali activation followed by gel-casting also in materials with very low CaO content. In this case, the XRD analysis indicated that the hardening was associated to the formation of sodium-based hydrated compounds and carbonates.

13.5. References

Bernardo, E., Esposito, L., Rambaldi, E., Tucci, A., 2011. Sintered glass ceramic articles from plasma vitrified asbestos containing waste. Adv. Appl. Ceram. 110, 346–352. https://doi.org/10.1179/1743676111y.0000000020

Bernardo, E., Esposito, L., Rambaldi, E., Tucci, A., Pontikes, Y., Angelopoulos, G.N., 2009. Sintered esseneite-wollastonite-plagioclase glass-ceramics from vitrified waste. J. Eur. Ceram. Soc. 29, 2921–2927. https://doi.org/10.1016/j.jeurceramsoc.2009.05.017

Garcia-Lodeiro, I., Fernández-Jimenez, A., Pena, P., Palomo, A., 2014. Alkaline activation of synthetic aluminosilicate glass. Ceram. Int. 40, 5547–5558. https://doi.org/10.1016/j.ceramint.2013.10.146

Inertam, Asbestos processing and recycling - Inertam, the solution for the final disposal of asbestos waste: http://www.inertam.com/le-traitement-de-lamiante-sa-valorisation/?lang=en

Nedeljković, M., Ghiassi, B., Melzer, S., Kooij, C., van der Laan, S., Ye, G., 2018. CO2 binding capacity of alkali-activated fly ash and slag pastes. Ceram. Int. 44, 19646–19660. https://doi.org/10.1016/j.ceramint.2018.07.216

Rambaldi, E., Esposito, L., Tucci, A., Timellini, G., 2007. Recycling of polishing porcelain stoneware residues in ceramic tiles. J. Eur. Ceram. Soc. 27, 3509–3515. https://doi.org/10.1016/j.jeurceramsoc.2007.01.021

Ramos, G.A., Pelisser, F., Paul Gleize, P.J., Bernardin, A.M., Michel, M.D., 2018. Effect of porcelain tile polishing residue on geopolymer cement. J. Clean. Prod. 191, 297–303. https://doi.org/10.1016/j.jclepro.2018.04.236

Rincón, A., Giacomello, G., Pasetto, M., Bernardo, E., 2017. Novel 'inorganic gel casting' process for the manufacturing of glass foams. J. Eur. Ceram. Soc. 37, 2227–2234. https://doi.org/10.1016/j.jeurceramsoc.2017.01.012

Rincon Romero, A., Salvo, M., Bernardo, E., 2018. Up-cycling of vitrified bottom ash from MSWI into glass-ceramic foams by means of 'inorganic gel casting' and sinter-crystallization. Constr. Build. Mater. 192, 133–140. https://doi.org/10.1016/j.conbuildmat.2018.10.135

Spasiano, D., Pirozzi, F., 2017. Treatments of asbestos containing wastes. J. Environ. Manage. 204, 82–91. https://doi.org/10.1016/j.jenvman.2017.08.038

PART VI - Conclusions and final remarks

The research carried on during the PhD project focused on valorising vitrified or partially crystallised residues into building materials with high-added values. Dense glass-ceramics with properties comparable to those of ceramic tiles could be obtained by the optimisation of the composition and of thermal treatment.

In addition, two types of porous products could be developed based on alkali activation: lightweight aggregates and panels. In the case of lightweight aggregates, their low density was a result of the decomposition of compounds formed due to alkali activation during the heating treatment. The low thermal conductivity of the lightweight mortars indicated the potential of applying the developed lightweight aggregates to increase the thermal insulation of cement-based products.

Regarding the panels, the results of this work demonstrated the feasibility of producing foams made with vitrified or partially crystallised residues by alkali activation, followed by gel-casting and sinter-crystallisation. In specific conditions, soda-lime glass was also added in order to improve hardening and sintering by viscous flow, as in the case of glasses prone to crystallisation (Plasmastone and conditioned bottom ash-red mud) and of partially crystallised residues (plasma processed asbestos-containing waste, polishing stoneware residue and recycled vitrified bottom ash). Furthermore, the introduction of soda-lime glass has also demonstrated to enable the decrease in molarity of the alkaline solution, without affecting the hardening step, as in the case of vitrified bottom ash-based foams and partially crystallised-based foams.

The leachability has proven to be a critical point, especially for waste-derived porous glass-ceramics, due to a higher surface area. In the case of Plasmastone-based foams, this could be adjusted '*a posteriori*' by the addition of boro-alumino-silicate glass, which presents higher stability than soda-lime glass. Furthermore, the stability of foams made with iron-rich glasses (Plasmastone and conditioned bottom ash-red mud) mixed with soda-lime glass could be finally achieved by firing in nitrogen, due to the phase assemblage formed.

In general, the firing treatment or increase in firing temperature enhanced the stabilisation of pollutants, with some exceptions. This was highlighted by the study comparing different processes to produce porous glass-ceramics or alkali-activated materials, which demonstrated that crystallisation increased the chemical stability of glass-ceramic foams when compared to alkali-activated foams. Furthermore, sinter-crystallisation was also responsible to increase the strength of porous glass-ceramics. On the other hand, this research also showed the impact of the firing treatment in the life cycle assessment of ceramic foams. Indeed, this study evidenced that waste-derived glass-ceramics foams should present multiple functionalities in order to justify the firing treatment in terms of costs and environmental impact.

Multifunctional waste-derived glass-ceramics could be produced by firing Plasmastone-based foams at lower temperature or in nitrogen. The different functionalities were related to thermal and acoustic insulation (due to high porosity presented by the foams), combined with

shielding properties (especially for foams fired at lower temperature in nitrogen) or dielectric characteristics (for foams fired at higher temperature in nitrogen).

In addition, the milestones required by the NEW-MINE project were achieved: dense glass-ceramics with specific bending strength above 2 MPa cm^3/g were obtained by cold pressing and sinter-crystallisation of fine powders of Plasmastone, soda-lime glass and kaolin clay. Highly porous glass-ceramics with specific compressive strength above 5 MPa cm^3/g could be finally achieved by valorising vitrified bottom ash into porous glass-ceramics. Indeed, the high strength of vitrified bottom ash-based glass-ceramics was not surprising when one considers the similarities between the chemical composition of this vitrified residue and of slag sitals. Finally, glass-ceramics with magnetic functionality could be established by firing iron-oxide rich glasses at low temperature. The formation of magnetite was maximised by firing at low temperature, especially when coupled with firing in nitrogen.

Finally, a full circularity envisaged by Enhanced Landfill Mining projects can be only achieved by the upcycling of vitreous by-products into building materials with high-added value. Therefore, the overall research carried on could be applied as a guideline regarding the different waste-derived products that could be developed with these residues, as well as techniques to increase the stability and the products value.

List of publications

Journal papers published:

- P. Rabelo Monich, A. Rincon Romero, D. Höllen, E. Bernardo, Porous glass-ceramics from alkali activation and sinter-crystallization of mixtures of waste glass and residues from plasma processing of municipal solid waste, Journal of Cleaner Production, 188, 871-878 (2018). DOI: 10.1016/j.jclepro.2018.03.167
- P. Rabelo Monich, D. Desideri, E. Bernardo, Low temperature upcycling of vitreous byproduct of the MSW plasma processing into multifunctional porous glass-ceramics, Advances in Applied Ceramics, 118, 366-371 (2019). DOI: 10.1080/17436753.2019.1595265
- P. Rabelo Monich, D. Vollprecht, E. Bernardo, Dense glass-ceramics by fast sinter-crystallization of mixtures of waste-derived glasses, International Journal of Applied Ceramic Technology (2019). DOI: 10.1111/ijac.13332
- P. Rabelo Monich, A. Rincon Romero, D. Desideri, E. Bernardo, Waste-derived glass-ceramics fired in nitrogen: stabilization and functionalization, Construction and Building Materials, 232 (2020). DOI: 10.1016/j.conbuildmat.2019.117265

Journal papers accepted:

- P. Rabelo Monich, F. Dogrul, H. Lucas, B. Friedrich, E. Bernardo, Strong porous glass-ceramics from alkali activation and sinter-crystallization of vitrified MSWI bottom ash. Detritus (2019) in press [accepted on 23/07/2019].

Conference papers:

- P. Rabelo Monich, D. Höllen, E. Bernardo, Development and characterisation of dense waste-derived glass-ceramics, Proceedings of the 4th Enhanced Landfill Mining Symposium (ELFM 2018), Mechelen (Belgium), 5-6 February 2018, 291-298.
- A. Rincon Romero, P. Rabelo Monich, E. Bernardo, Recycling of inorganic waste in monolithic and cellular glass-based materials for structural and functional applications, Proceedings of the 4th Enhanced Landfill Mining Symposium (ELFM 2018), Mechelen (Belgium), 5-6 February 2018, 255-270.
- H. Lucas, B. Friedrich, P. R. Monich, E. Bernardo, G. Sauve, K. Van Acker, Sustainable Approach to Valorise Ashes from MSWI, Recy & DepoTech 2018, Leoben (Austria), 07-09 November 2018.
- P. Rabelo Monich, H. Lucas, B. Friedrich, E. Bernardo, Porous glass-ceramics from alkali activation and sinter-crystallisation of vitrified bottom ash, 6th International Slag Valorisation Symposium, Mechelen (Belgium), 01-05 April 2019.

- G. Sauve, H. Lucas, P. Rabelo Monich, E. Bernardo, B. Friedrich, K. Van Acker, Life cycle assessment of novel technical routes to valorise MSWI bottom ash, 6th International Slag Valorisation Symposium, Mechelen (Belgium), 01-05 April 2019.
  2019.
- P. Rabelo Monich, H. Lucas, B. Friedrich, M. Segata, A. Morbi, E. Bernardo, Upcycling of vitrified residues by alkali activation and sinter-crystallization, 17th International Waste Management and Landfill Symposium, Cagliari (Italy), 30 September-04 October 2019.

Presentations given at conferences

- P. Rabelo Monich, A. Rincon Romero, E. Bernardo, Glass-ceramic foams from 'inorganic gel casting' and sinter-crystallization of waste glass mixtures, 15th Conference & Exhibition of the European Ceramic Society (ECerS2017), Budapest, (Hungary), 9-13 July 2017: oral presentation.
- P. Rabelo Monich, E. Bernardo, Optimisation of the sinter-crystallization of waste glass mixtures, 12th International Symposium on Crystallization in Glasses and Liquids (Crystallization 2017), Segovia (Spain), 10-13 September 2017: poster presentation.
- P. Rabelo Monich, D. Höllen, E. Bernardo, Development and characterisation of dense waste-derived glass-ceramics, Proceedings of the 4th Enhanced Landfill Mining Symposium (ELFM 2018), Mechelen (Belgium), 5-6 February 2018, 291-298: pitch presentation.
- P. Rabelo Monich, A. Rincon Romero, D. Höllen, E. Bernardo, Porous glass-ceramics from alkali activation and sinter-crystallization of waste glass mixtures, CIMTEC 2018 - 14th International Ceramics Congress, Perugia (Italy), 10-14 June 2018: oral presentation.
- P. Rabelo Monich, H. Lucas, B. Friedrich, E. Bernardo, High strength cellular glass-ceramics from glass by-products of metal extraction processes applied on MSWI bottom ash, Materials Science and Technology 2018 Technical Meeting and Exhibition (MS&T18), Columbus (USA), 14-18 October 2018: oral presentation.
- P. Rabelo Monich, D. Desideri, E. Bernardo, Upcycling of vitreous by-product of the plasma heating of MSW into multifunctional porous glass-ceramics, Materials Science and Technology 2018 Technical Meeting and Exhibition (MS&T18), Columbus (USA), 14-18 October 2018: oral presentation.
- P. Rabelo Monich, H. Lucas, B. Friedrich, E. Bernardo, Porous glass-ceramics from alkali activation and sinter-crystallisation of vitrified bottom ash, 6th International Slag Valorisation Symposium, Mechelen (Belgium), 01-05 April 2019: oral presentation.
- P. Rabelo Monich, R.E. Murillo Alarcón, H. Lucas, B. Friedrich, Y. Pontikes, E. Bernardo, Upcycling of conditioned MSWI bottom ash into porous ceramics by means of strong or

weak alkali activation, XVI ECerS Conference, Turin (Italy), 16-20 June 2019: oral presentation.

- P. Rabelo Monich, H. Lucas, B. Friedrich, M. Segata, A. Morbi, E. Bernardo, Upcycling of vitrified residues by alkali activation and sinter-crystallization, 17th International Waste Management and Landfill Symposium, Cagliari (Italy), 30 September-04 October 2019: oral presentation.

APPENDIX - Current perspectives

I. Microwave treated MSWI bottom ash-based porous glass-ceramics

This work was conducted in collaboration with NEW-MINE ESR Georgia Flesoura (KU Leuven).

Microwave treated MSWI bottom ash was converted into porous glass-ceramics by alkali activation, followed by gel-casting and sinter-crystallisation. Fine powders of 90 wt% microwave treated MSWI bottom ash and 10 wt% soda-lime glass were added to an alkaline solution of 1 M NaOH and mixed for 3h at 400 rpm. The overall solid content of the suspension was equal to 70 wt%. Thereafter, the slurry was submitted to curing at 75 °C for 3h before being foamed by intensive mechanical stirring. 4 wt% Triton X-100 (polyoxyethylene octyl phenyl ether – $C_{14}H_{22}O(C_2H_4O)_n$, n = 9–10, Sigma-Aldrich, Gillingham, UK) was then added to the 'gelified' suspension, which was submitted to intensive mechanical stirring at 2000 rpm. The foamed structure was finally dried at 40 °C for 2 days, before being demoulded and fired. The firing treatment was performed following a heating rate of 10 °C/min and holding time of 1h. Samples fired at 800 °C correspond to the group 'A', while the ones fired at 900 °C correspond to the group 'B'.

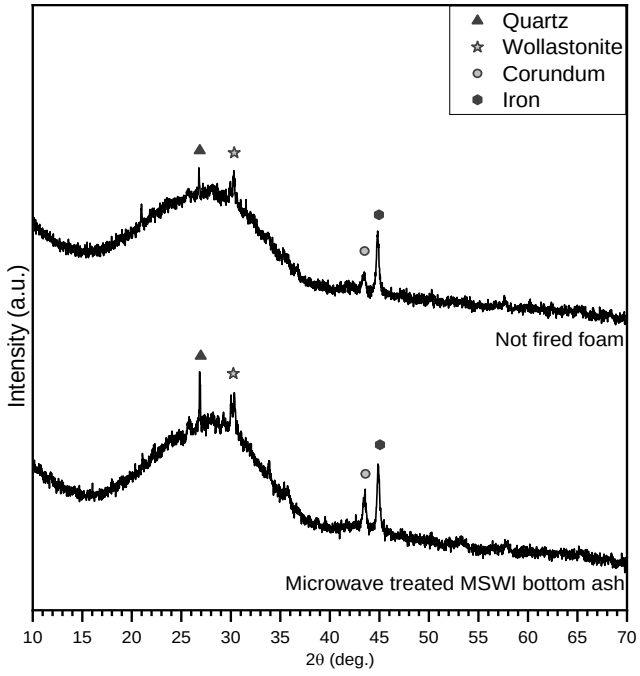

Figure I-1. Mineralogical analysis of the vitrified residue and not fired foams.

X-ray diffraction analysis performed on microwave treated MSWI bottom ash (Figure I-1) indicates the presence, in traces, of quartz, wollastonite, corundum and metallic iron. In addition, the low crystallinity of the vitrified residue is confirmed by the broad 'amorphous

halo' centered at 2θ~28°. The not fired foams also present the previously mentioned crystalline inclusions, in reduced amount. In addition, it was not possible to detect any product due to alkali activation, indicating that the hardening of the slurry was associated to the formation of an amorphous gel.

Firing of vitrified residue-based foams promoted a substantial crystallisation, especially passing from 800 °C to 900 °C (Figure I-2), The peaks are consistent to the phases already detected, in traces, in the starting glass. Furthermore, firing promoted the formation of new phases. Peaks consistent to those of wollastonite ($CaSiO_3$, PDF#76-0925), clinopyroxene ($Ca(Mg_{.6}Fe_{.2}Al_{.2})(Si_{1.5}Al_{.5})O_6$, PDF#72-1379), Na-doped anorthite ($((Ca,Na)(Al,Si)_2Si_2O_8$, PDF#20-0528) and melilite solid solution ($((Ca_{1.96}Na_{.05})(Mg_{.24}Al_{.64}Fe_{.12})(Si_{1.39}Al_{.61}O_7)$, PDF#72-2128) were detected after firing at 800 °C and at 900 °C. Quartz, was only detected in samples fired at 800°C ('group A'), while the formation of iron oxides (hematite, Fe_2O_3, PDF#33-0664) and magnetite (Fe_3O_4, PDF#75-1610)) are most probably associated to the oxidation of the metallic iron. The presence of iron oxides in the glass-ceramic foams could provide novel functionalities to the material, as already discussed in Part III. Indeed, preliminary electric tests performed on foams fired at 800 °C ('group A') indicated particularly high relative permittivity values.

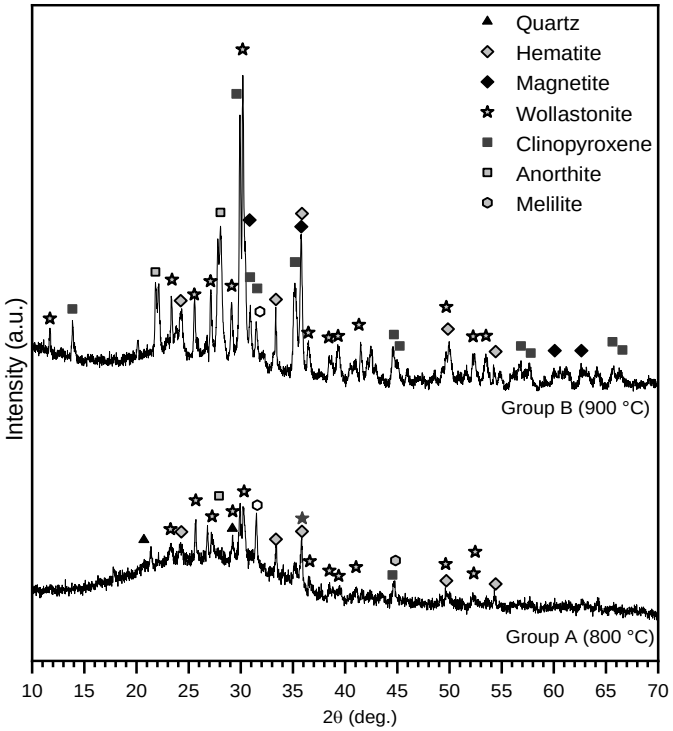

Figure I-2. XRD patterns of foams fired at 800 °C ('group A') or 900 °C ('group B').

Table I-1 reports the physical and mechanical properties of the glass-ceramic foams. The samples are highly porous (porosity above 67 vol%), with only open porosity. Regarding the mechanical properties, the firing treatment at 900 °C ('group B') led to foams exhibiting an estimated bending strength of the solid phase (σ_{bend}) similar to the one of soda-lime glass.

Table I-1. Physical and mechanical properties of the developed glass-ceramics foams.

Group of samples	**A**	**B**
Firing temperature	**800 °C**	**900 °C**
Density determinations		
ρ_{geom} (g/cm^3)	0.89 ± 0.01	0.76 ± 0.26
$\rho_{apparent}$ (g/cm^3)	2.74 ± 0.01	2.74 ± 0.02
ρ_{true} (g/cm^3)	2.74 ± 0.01	2.74 ± 0.02
Total porosity (vol%)	67.5	67.5
Open porosity (vol%)	67.5	67.4
Closed porosity (vol%)	0	0.1
Strength determinations		
σ_{comp} (MPa)	2.1 ± 0.6	2.6 ± 0.7
σ_{bend} (MPa)	57.1	72.1

Table I-2. Results of the leaching test performed on glass-ceramic foams (ppm).

	Limit values		**Fired at 800 °C (Group A)**	**Fired at 900 °C (Group B)**
	Inert waste	**Non-hazardous waste**		
As	**0.5**	2	0.0116	0.0202
Ba	**20**	100	0.0711	0.1061
Cd	**0.04**	1	<0.0002	<0.0002
Cr	**0.5**	10	0.7618*	0.1637
Cu	**2**	50	0.0096	0.0097
Hg	**0.01**	0.2	<0.0004	<0.0004
Mo	**0.5**	10	0.7024*	0.4379
Ni	**0.4**	10	<0.0014	<0.0014
Pb	**0.5**	10	<0.0047	<0.0047
Sb	**0.06**	0.7	0.0328	<0.0099
Se	**0.1**	0.5	<0.0122	<0.0122
Zn	**4**	50	<0.0203	<0.0203

Leaching tests performed on the fired foams (Table I-2) indicate a better stabilisation of heavy metals by increasing the firing temperature to 900 °C (‘group B’). Indeed, only foams from group B can be classified as inert waste. Foams from group A, on the other hand, presented leaching of Cr and Mo above the limits for inert waste, but still below the limits for non-hazardous waste.

II. Conversion of Plasmastone-based alkali-activated materials into glass-ceramics

This work was conducted in collaboration with NEW-MINE ESR Guilherme Ascenção (Italcementi, University of Padova and KU Leuven).

Plasmastone-based alkali-activated materials (porous and dense samples) were produced by NEW-MINE ESR11 by means of a much stronger alkaline solution than the one applied in Part III. The samples were thereafter fired in air at 800 °C, with a heating rate and holding time of 10 °C/min and 1h, respectively. The firing temperature was selected in order to maximise the precipitation of magnetite, based on the findings presented in Chapter 6.

Table II-1. Leaching test results performed on dense and porous samples (ppm).

	Limit values		**Dense samples**		**Porous samples**	
	Inert waste	**Non-hazardous waste**	**Not fired**	**Fired at 800 °C**	**Not fired**	**Fired at 800 °C**
As	**0.5**	2	0.0136	<0.0049	0.0191	0.0256
Ba	**20**	100	0.0017	0.0086	<0.0000	0.0165
Cd	**0.04**	1	0.0007	<0.0002	<0.0002	<0.0002
Cr	**0.5**	10	0.0041	0.0583	0.0409	>3.939*
Cu	**2**	50	0.0148	0.0117	0.0100	<0.0001
Hg	**0.01**	0.2	<0.0004	<0.0004	0.0008	0.001
Mo	**0.5**	10	>2.052*	<0.0033	>2.967*	>2.499*
Ni	**0.4**	10	0.0015	<0.0014	<0.0014	<0.0014
Pb	**0.5**	10	0.0237	<0.0047	<0.0047	<0.0047
Sb	**0.06**	0.7	0.0099	<0.0099	<0.0099	0.0795*
Se	**0.1**	0.5	0.0176	<0.0122	<0.0122	<0.0122
Zn	**4**	50	<0.0203	<0.0203	<0.0203	<0.0203

The chemical stability of the samples (as received and fired) was assessed by means of leaching test (Table II-1) and the eluate values were compared to the values allowed for waste acceptable at landfills for inert waste and non-hazardous waste (Directive 2003/33/EC, 2003). The results regarding the dense samples indicate high leaching of Mo for alkali-activated materials. In contrast, the firing treatment led to a better stabilisation of heavy metals, as indicated by the reduced leachate values, in general, with the firing treatment. In fact, this is the only analysed sample that could be classified as inert waste. The leaching results are in agreement with Chapter 11, which indicated a better stabilisation of heavy metals by firing

alkali-activated materials. In contrast, the results for the porous samples were surprisingly different: the fired samples presented in general higher leachate values than the alkali-activated materials. Nonetheless, the stabilisation of heavy metals may be possibly achieved by firing in nitrogen, as observed in Chapters 7 and 12.

The XRD patterns of the porous samples (Figure II-1) exhibit peaks consistent to calcite ($CaCO_3$, PDF#86-0174) in the alkali-activated materials. On the other hand, the firing treatment at 800 °C led to the formation of kalsilite ($KAlSiO_4$, #85-1413) and calcium silicate, (Ca_2SiO_4, #86-0399). Magnetite (Fe_3O_4, #89-6466) was also detected in the fired sample, which in turn could bring novel functionalities, as shown in Part III. Finally, in order to understand better the relation between the phase assemblage firing and leaching of heavy metals, it is recommended to perform an electron microprobe analysis, as done in Chapters 4 and 5.

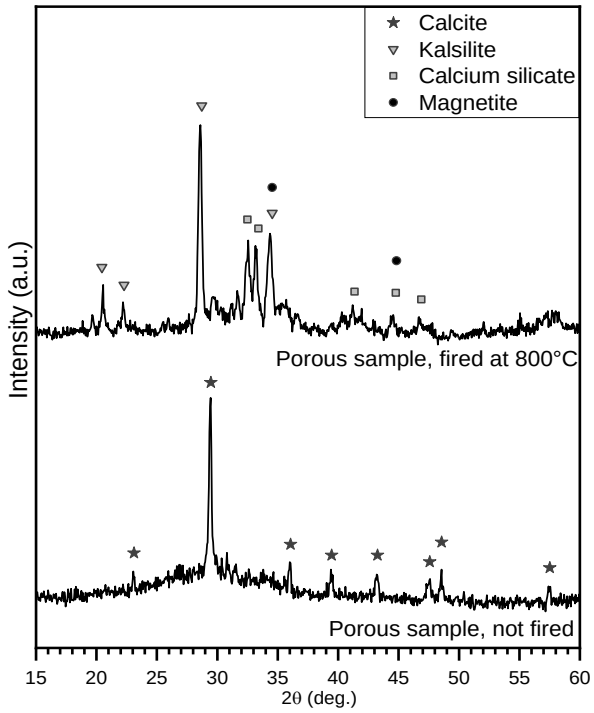

Figure II-1. XRD patterns of the porous samples (fired and not fired).

III. Red-mud/soda-lime glass foams by alkali-activation, gel-casting and firing

Chapter 12 indicated the feasibility of processing conditioned bottom ash-red mud mixtures into porous glass-ceramics. In parallel, another study was conducted regarding the direct valorisation of red mud by applying the same technique. As in Chapter 12, soda-lime glass was also added in order to improve the hardening of the 'gelified' slurries, and, mainly, to improve densification by viscous flow.

Two groups of samples were produced: 70/30 (corresponding to 70 wt% red mud/30 wt% soda-lime glass) and 80/20 (80 wt% red mud/20 wt% soda-lime glass). The foams were made by adding fine powders of red mud and soda-lime glass to an alkaline solution of 2.5 M NaOH. The overall solid content of the suspension was equal to 65 wt%. After 3h of mixing at 400 rpm. the slurry was submitted to curing, at 75 °C (2h for 70/30 and 1h30min for 80/20) before being foamed by intensive mechanical stirring. 4 wt% Triton X-100 (polyoxyethylene octyl phenyl ether – $C_{14}H_{22}O(C_2H_4O)_n$, n = 9–10, Sigma-Aldrich, Gillingham, UK) was then added to the 'gelified' suspension, which was submitted to intensive mechanical stirring at 2000 rpm. The foamed structure was finally dried at 40 °C for 2 days, before being demoulded and fired. The firing treatment was performed at 800 °C in flowing nitrogen atmosphere, following a heating rate of 5 °C/min and holding time of 1h.

Table III-1. Physical and mechanical properties of red mud-based foams.

Group of samples	**80/20**	**70/30**
Soda-lime glass addition	20 wt%	30 wt%
Density determinations		
ρ_{geom} (g/cm^3)	1.07 ± 0.05	1.18 ± 0.04
$\rho_{apparent}$ (g/cm^3)	3.36 ± 0.01	3.32 ± 0.02
ρ_{true} (g/cm^3)	3.38 ± 0.00	3.40 ± 0.00
Porosity		
Total porosity (vol%)	68.4	65.2
Open porosity (vol%)	68.2	64.4
Closed porosity (vol%)	2.0	0.8
Strength determinations		
σ_{comp} (MPa)	1.7 ± 0.3	4.8 ± 0.6
σ_{bend} (MPa)	46.9	116.4

Table III-1 reports the porosity and strength of the developed foams. The foams are highly porous (total porosity above 65.2 vol%), with mainly open porosity. Regarding the strength,

80/20 foams presented quite low mechanical performance: the estimated bending strength (σ_{bend}) was far below the reference bending strength for soda-lime glass (between 70-75 MPa). On the other hand, the estimated σ_{bend} reached very high values for samples made with a higher amount of soda-lime glass ('70/30' group). The low relative density coupled with high strength indicates that these samples could be potentially applied as thermal and acoustic insulators in buildings.

The XRD patterns of red mud (Figure III-1) indicate the presence of mainly hematite (Fe_2O_3, PDF#79-1741), as well as peaks corresponding to those of cristobalite (SiO_2, PDF#76-0934). Moreover, signals corresponding to rutile (TiO_2, PDF#86-0147), calcite ($CaCO_3$), PDF#83-1762), iron oxide (Fe_3O_4, PDF#26-1136), gibbsite ($Al(OH)_3$, PDF#74-1775), boehmite (AlO(OH), PDF#74-1895) were also detected, in traces.

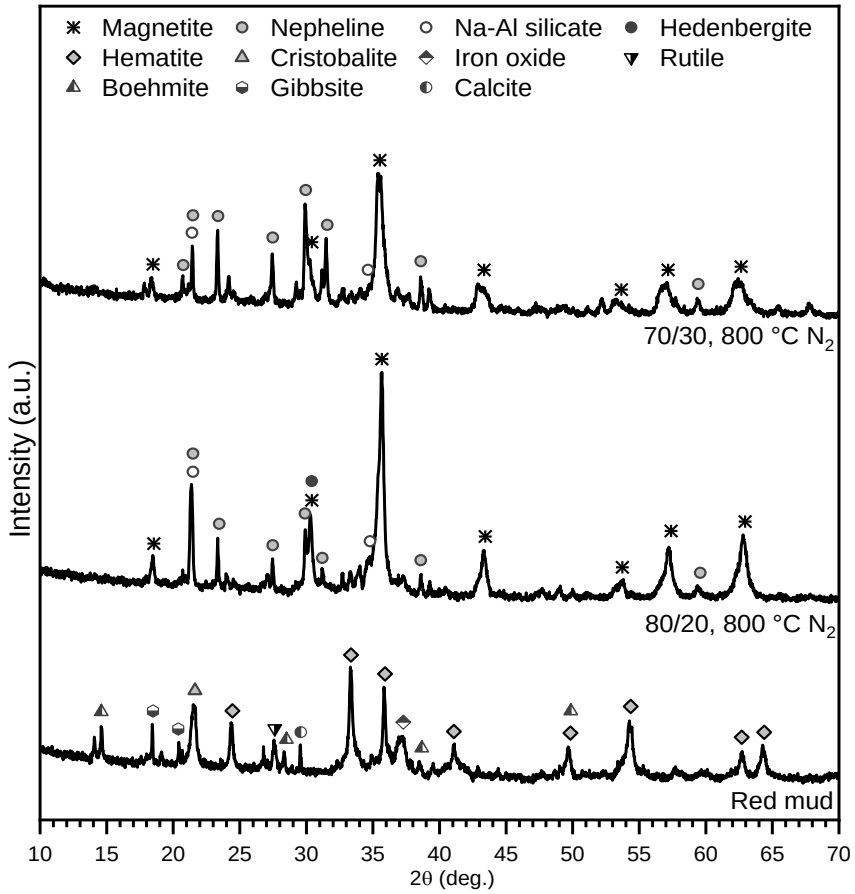

Figure III-1. XRD patterns of red mud and of samples 80/20 and 70/30 fired in nitrogen.

In contrast, the fired foams made with mixtures of red-mud and soda-lime glass presented signals consistent to those of magnetite (Fe_3O_4, PDF#87-2334), nepheline ($Na_{6.65}Al_{6.24}Si_{9.76}O_{32}$, PDF#83-2372) and sodium aluminium silicate ($Na_{1.45}Al_{1.45}Si_{0.55}O_4$, PDF#49-0002). Hedenbergite ($Ca(Fe_{0.821}Al_{0.179})(SiAl_{0.822}Fe_{0.178}O_6)$, PDF#78-1546) was also detected, in traces,

only in 80/20 foams. The addition of a higher quantity of soda-lime glass promoted the formation of nepheline and reduced the amount of magnetite and Na-Al-silicate formed. Finally, the presence of magnetite in both foams could bring novel functionalities to the materials, as shown in Chapters 6 and 7.

Future studies will focus on the assessment of electromagnetic shielding properties and of the chemical stability of the foams.